ISSN 1343-361X

Readout

HORIBA Technical Reports

ENGLISH EDITION
No. 39
September 2012

Europe

HORIBA

http://www.horiba.com/publications/readout/

Readout
HORIBA Technical Reports
English Edition No.39
September 2012

HORIBA Group conducts R&D not only at Japanese Headquarters but also America and European group companies. We hope this issue of HORIBA Readout, featuring the research and technological development in our European companies, shows that HORIBA group is responding to various needs in this fast advancing world, pursing our customers' satisfaction.

In late autumn, I visited Kamikochi, looking for autumn in highland. Yellow autumn leaves of Japanese Larch floating down glistening mountain water along the walking trail stopped my steps for a moment to fully enjoy the autumn there.
-Photographer Hideo MATSUI-
(Member of NIKA Association of Photographers)

Name of the book

This book is named "Readout" in the hope that "the products and technology we have created and developed will be read out and so become widely known".

Europe

Foreword

Innovating in Europe

Michel MARITON
Senior Corporate Officer
HORIBA, Ltd.
President
HORIBA Europe Holding SAS
Ph. D, D. Sc

With its long history, Europe is a powerhouse of science, springing from talented people in many international caliber academic institutions. However this core scientific strength does not convert enough into a business advantage for the region, with products and services able to capture global market share. As industrial competition intensifies to invent answers to tomorrow's consumer requests and social needs, Europe needs to rejuvenate its wealth creation machine in order to sustain its progressive social model and keep the European dream alive.

Faced with a difficult economic period, when imbalanced public budgets cannot be called to the rescue, European entrepreneurs will have to embrace a more open approach to innovation where they can leverage not only academic discoveries but also the capabilities of partners along the value chain. Given the cultural diversity within Europe, this is both a challenge to overcome existing barriers to cooperation and an opportunity to bring to market unique solutions.

In order to support innovation while respecting its budget constraints, the European Union has decided to improve its approach for its next research & technology program, called HORIZON 2020, with the following evolutions:

- emphasize applied research and pre-competitive development work to commute strong

fundamental research into economic value

- focus on key enabling technologies that have the capabilities to transform whole industries (a pan European panel of experts has identified five key enabling technologies as advanced materials, nano-technology, micro-and nano-electronics, biotechnology and photonics).

An important feature of the HORIZON 2020 program will be the use of Public Private Partnership (PPP) as the main channel of the effort. It is expected that the PPPs will enhance the European Union competitiveness and industrial leadership, with commitment of private and public funds under a lean business oriented structure with an open governance. The volume of the HORIZON 2020 framework as presently proposed by the European Commission to the member states is 80 B€ over 2014-2020.

This ambitious innovation drive from the European Union creates a favorable environment for the R&D efforts of HORIBA companies in Europe. This issue of Readout has been organized around our existing business segments, Medical, Automotive Test Systems, Process & Environment, Semiconductor and Scientific, with several papers involving our academic partners. It presents a sample of already active projects that will give us the legitimacy to take an active role in the next period, including the HORIZON 2020 program.

HORIBA in Europe will continue to champion open innovation as a way to bring our best contribution to society.

Review

Interactions and Partnerships with Academic Teams as a Source of Innovation: from Collaborative Research Projects to Open Innovation

Michel MARITON, James THEPOT, Denis CATTELAN, Olivier ACHER

Introduction

HORIBA Jobin Yvon is committed to serving the scientific and spectroscopy communities. These are fast moving communities, and in order to keep a leading position, innovation is a must. The scientific community is also a major innovation source, and as a consequence it is of foremost importance for HORIBA Jobin Yvon to work with academia. The objective of this paper is to present some of our current innovation practices in HORIBA Jobin Yvon, that combine a variety of interactions with academia and internal innovation efforts, to better serve Scientific Instrumentation users.

Development of New Scientific Instruments through Collaboration with Leading Scientists

Formal and Informal Collaboration with Scientists

Collaborating with academic leaders is in the genes of HORIBA Jobin Yvon, from its foundation in 1819 as Ateliers Soleil manufacturing the original lenses of Augustin Fresnel or at the turn of the century when Amédée Jobin built instruments for the famous optician Charles Fabry, the inventor of the ubiquitous "Fabry-Pérot" interferometer. A few other examples of collaborations that proved very successful are the collaboration with astronomer A. Labeyrie on the holographic inscription of gratings, for which HORIBA is now a world champion or the collaboration with Raman pioneer, professor Delhaye, who was amongst the first to envision the coupling between Raman analysis and microscopy, and with Australian scientist Dick Payling, who was amongst the first to envision a broad use for the Glow-Discharge Optical Emission Spectroscopy technique. These long-term collaborations have been key for building the leadership of the company in these fields. Presently, new contacts and interactions are built with scientists

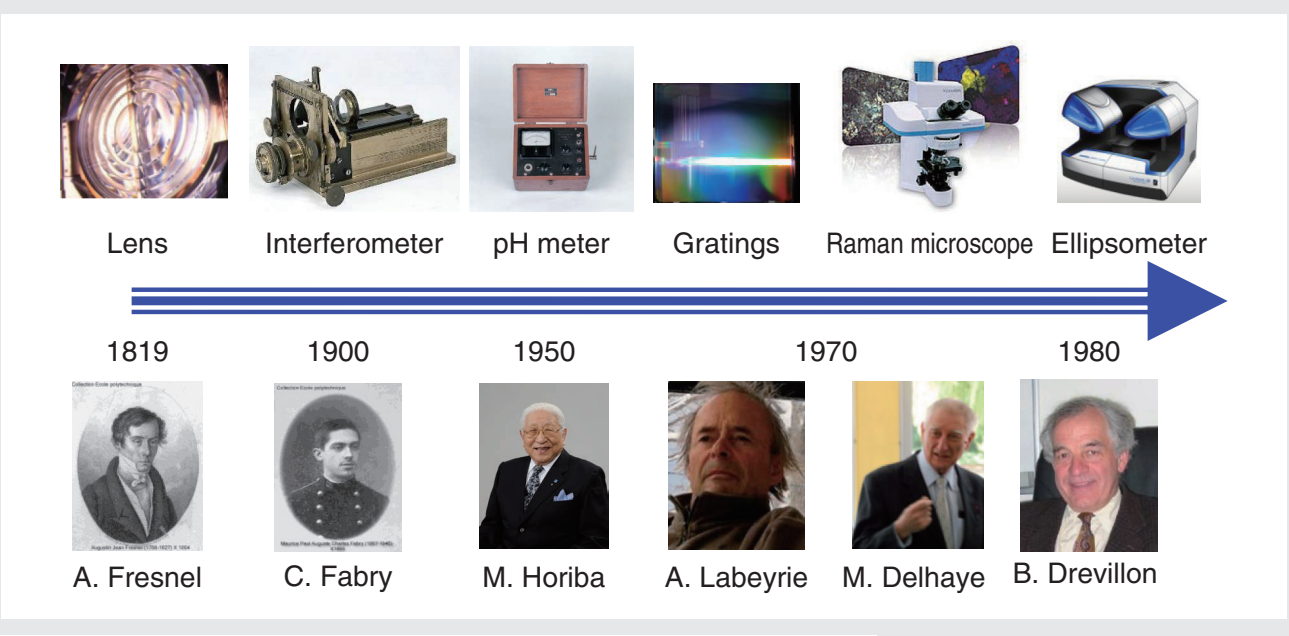

Figure 1 Cooperating with leading researchers worldwide to transform scientific discoveries into scientific instruments

all over the world, and win-win collaborations are developed, with the ambition to provide new technologies and new instruments to the company for the 21st century. (Figure 1)

The company has appointed a handful of scientific advisors, who are scientists with major recognition in their field, who spend several days per year in the company, interacting with both management and technical teams, to help with their expertise and networking ability.

While some decades ago partnership was mainly based on individuals, the present trend is to have more formalized partnerships, that encompass several institutions. An example is the recently-created Institute for PhotoVoltaics in Paris region, denominated IPVF. This institute has been created under the impulse of two major French research institutions (Ecole Polytechnique and CNRS), two very large energy companies (TOTAL and EDF), and has been opened to companies with a more focused interest. HORIBA Jobin Yvon joined this Institute, and anticipates fruitful interaction with high-level scientists in the field of instrumentation for photovoltaics, and more generally for thin film research.

Collaborative Projects

HORIBA Jobin Yvon has been participating to several collaborative projects, either at regional, national, or European level. These projects include one or several academic teams, and in some cases other companies. It is a general trend worldwide that academic teams get an increasing part of their research money through research project grants, after a competitive process of project selection. This is an incentive for scientist to build projects that include industrial partners. Participating to collaborative research projects has

become for HORIBA a useful path for improving our instruments and adapting them to the demand, as well as prototyping brand new solutions.

In some examples, the collaborative project includes a workpackage on instrument improvement. As an example, the "scatteromueller" French collaborative project included one academic team with extensive knowledge in polarimetry (Figure 2), one applied research institute focused in microelectonics, and HORIBA Jobin Yvon. In the course of the project, several improvements have been achieved, such as increased spatial resolution, and higher precision. These improvements have been included in the latest version of the Auto-SE commercial ellipsometer.

Figure 2 The AutoSE ellipsometer benefits from the advances obtained during the "scatteromueller" collaborative program

Another very important aspect of collaborative projects is that it allows us to adapt our current instruments to new fields of science. As an example, the "OLAtronics" project is a multi-partner European project that deals with a field of growing importance (Figure 3), which is plastic electronics. While ellipsometry is well known in the semiconductor community to be a useful tool for research, development, and process control, the interest of this instrument in the context of plastic electronics had yet to be established and documented. HORIBA Jobin Yvon participated to this program, which included the adaptation of an ellipsometer to a Roll to roll unit, on the pilot line of a partner. We were able to demonstrate and publicize the interest of ellipsometry for plastic electronics.
Because scientists use many different instruments to carry on their research, coupling between instruments has become very important. Collaborative projects encourage scientists and companies with different fields of expertise to join forces, and as a consequence they provide very efficient ways of investigating both the technical aspects and scientific impact of coupling between different instruments, in various applicative contexts. As an example, the French-funded "Hybrid Imaging for Oncologic Microscopy"

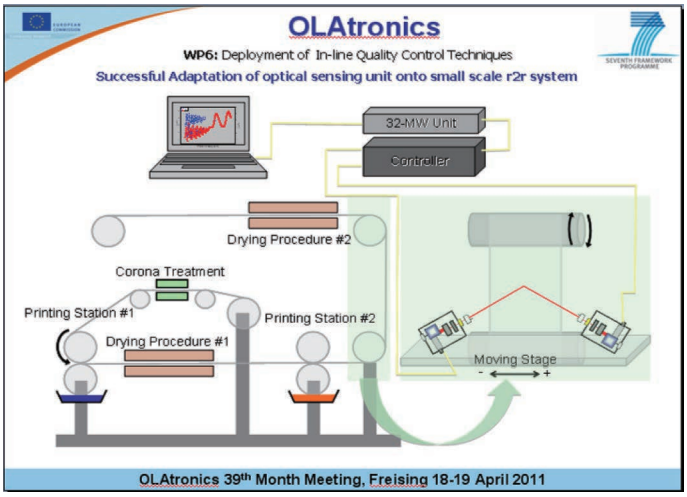

Figure 3 An example of European project in which HORIBA Jobin Yvon participated, and successfully adapted one of our ellipsometers to the field of organic electronics

Figure 4 Special Raman microscope including multispectral imaging ability (left), built within a collaborative program with nine participating partners (logo on the upper right), in order to perform automated classification of luman lymphocytes (bottom right)

(IHMO) project ambitioned to perform automatic classification of human lymphocytes, for health-related applications, based on combined hyperspectral and Raman imaging. This work was carried by nine partners, including two hospitals. HORIBA contributed by building a dedicated version of a Raman microscope that included hyperspectral imaging, and the combination of the two techniques was shown to be very promising. (Figure 4)

The coupling of Raman with AFM, along with new imaging modalities on our Raman and ellipsometric platforms, have also been investigated both in the frame of collaborative projects.

Last but not least, collaborative projects can be a very adequate frame for developing entirely new instruments, based on the vision of one of the partners. This is the case of PP-TOF MS instrument, described in detail by Patrick Chapon and Agnès Tempez in this READOUT.

Open Innovation

The term “Open Innovation” is a term that has been coined in recent years[1] by Professor Chesbrough, to express that companies can tap into innovation resources not only in their R&D and marketing departments, but also in many other places within and outside the company. It also states that some findings of R&D team within a company, can be exploited in a more fruitful

and rewarding way, outside the company, rather then inside the company. The "Open Innovation" movement lead to numerous success stories, featuring cases where the company staff, but also the customers, the industrial partners, or contributors completely unknown to the company, could interact in a win-win situation to create innovation and value. This may be a not so new statement for Horibarians, following the founding principles of Dr. Masao Horiba.[2] Indeed, the OEM activities in the field of gratings and spectrometers, can be seen as an excellent example of Open Innovation practices, though they have been developed long before this term was coined. This is because our OEM activities involve long term win-win relations, with a customer who acknowledges that some part of the system he is designing (the spectroscopy part in our case) could benefit from our guidance and expertise in the design phase, and from our commitment in the production phase.
Open Innovation is useful to a wide range of our activities in addition to OEM. The company has a number of assets for carrying successful Open Innovation approach, as will be discussed below.

Being in the Right Place

While collaborative programs with academics follow very formal procedures once they are engaged, Open Innovation relies on more informal encounters and connections. As a consequence, a key enabling factor for innovation is being connected in a rich environment. Under that respect, the new HORIBA building, at the heart of the Paris Saclay Campus, is a major asset. The Paris Saclay area is a major Science place, hosting some of the most prestigious universities, research centers, and engineering schools in France. In 2008, it represented about 10% of the Public Research in France, 10 000 researchers, and 21 000 students. By 2016, 7 new engineering schools and 3 major research institutions will move to the Paris Saclay area, increasing the number of researchers by 3000, and nearly doubling the number of students. The new HORIBA Building in Paris Saclay is an asset not only because of the quality of its technical facilities, not only because it is conveniently located in a major hub for HORIBA Scientific customers, but also because it will facilitate interactions with innovative researchers, visionary customers, highly creative and motivated students. It is our responsibility to make the best out of this situation. (Figure 5)

Sharing Knowledge and Experience

The "Open Innovation" paradigm underlines the importance of cross-fertilization. Cross-fertilization begins inside the company, and the monthly 1-hour seminar is one of the opportunities for that. As an example, the presentations in that seminar given by Dr. Benferhat on "Serving the Chineese Scientific market", and by Dr. Ayasse on "Serving the Brasilian market", were very well attended and appreciated. It participates to the shared knowledge within the company, and this knowledge is expected to contribute to the success of one of our products specifically designed to cope with specific requirement of Chinese customers. It is to be noted that the innovation in this product has not so much to do with technical features, but

Figure 5 New HORIBA building in Palaiseau, at the heart of Paris Saclay Campus: Artist's rendering (left); building work in progress (right); Map of the research and high education places located nearby the HORIBA building on the Paris Saclay Campus

rather with sales and delivery aspects. This is consistent with the Open Innovation motto, that innovation is not something specific to R&D.
Scientific and professional societies are also useful for networking and promoting fruitful encounters. HORIBA Jobin Yvon is active in the SFO and EOS, which are the scientific societies at the national and European level; in the French Optics and Photonics industrial association (AFOP), presently headed by HJY President; and in European-scale European Photonic Industry Consortium (EPIC).

Tapping into the Company's Creativity

In 2009, HJY organized an Innovation challenge in France, where employees were encouraged to suggest ideas for innovative products or improvements. This challenge was conducted in two steps: in the first step, a very short description of the innovation was required, so that it was possible to participate even with little extra-work from the individual or the team that carried the proposition. The Strategic Committee selected the propositions that appeared as the most relevant, and asked more details. In the second round, the person or the team that carried a nominated proposition presented the idea in an oral form to the Strategic committee, allowing a direct interaction. The most promising suggestions were prized and investigated in more detail through cooperation between the proposer, the HJY Innovation

team, and in some case an academic partner. With a three-year distance, it is now possible to draw some conclusion of the impact of the challenge and subsequent actions. One of the most ambitious proposition issued during this challenge has turned into an ongoing instrumentation project, with the first beta users to be served in possibly less than a year. It should be mentioned that at the time of the challenge, this proposition had appeared as a desirable but unrealistic dream, and as a consequence it had been rejected by the Strategic Committee. But the Innovation challenge had made it possible to share the dream, and some time later other people in the company found some ways so that the dream could became reality. Building connections and initiating cooperation between people who would not have worked together otherwise, has been another positive outcome of the challenge. In 2010 a challenge was carried in the German branch, focusing both on sales practices and innovative products.

Acting Swiftly to Seize Opportunities

Having nice ideas is not sufficient to carry on innovation projects, since it may require some time and resources that do not fit within existing plans. Making bottom-up initiative possible, allowing people to spend some time and resource for it, and providing recognition for the most promising ones, is therefore necessary. The BlackJack contest is one of the useful paths to it for all Horibarians, and the IP challenge is also very useful in that respect. In order to seize opportunities that require significant time and effort to be pursued, the creation of the Innovation team in 2009 has made possible the investigation of several projects. These projects were started from suggestions coming from different parts of the company, and from academic teams. Some of these projects are expected to go into development phase by the end of the year.

Conclusion

HORIBA Jobin Yvon has been using many of the Open Innovation best practices, such as combining fruitful interaction with academic partners, with the vision and the contribution of many different people within the company. The new implantation at the heart of the Paris Saclay Campus is an asset not only to be closer to some of our major clients, but also to maximize interactions with academia, as a source of innovation.

References

[1] "Open innovation" , Henry W. CHESBROUGH, Harvard Business School Press (2003)
[2] «JOY and FUN», Dr. Masao HORIBA, Published by «JOY and FUN» publication project (1998)

Michel MARITON
Senior Corporate Office
HORIBA, Ltd.
President
HORIBA Europe Holding SAS
Ph. D D. Sc

James THEPOT
C.O.O.
HORIBA Jobin Yvon SAS

Denis CATTELAN
Director of R&D
HORIBA Jobin Yvon SAS

Olivier ACHER
Director of Innovation
HORIBA Jobin Yvon SAS
Ph. D

Review

HORIBA Medical in Europe: Evolution of Technologies for White Blood Cell Differential at HORIBA Medical

Philippe NERIN

This article retraces the evolution of technologies for leucocyte differential, which is a key feature of hematology analyzers. It is emphasized here the way HORIBA Medical started using simple and robust technologies, based on CIS (Cell Impedance Signal) for 3 part DIFF, and then evolved toward more sophisticated bio-photonics designs including cut edge technologies, considered as pioneering works in the field of flow cytometry. This article was presented by myself at ISLH 2012, in Nice, France, at the luncheon session attended by about 200 worldwide customers.

Introduction

It is worth pointing out that the first attempts in automatic measurements of blood cells go back to the mid twentieth century, when two techniques were developed in parallel: impedance measurement (the so-called electronic gate) and the first optical scattering detector. Improved year after year along with specific reagents, the electrical and optical methods allowed considerable projections in the field of hematology since, in most cases, the main cellular populations (examined early back by a photonic microscope) are differentiated and taken into account with acceptable accuracy.

Nowadays, a hematology analyzer is a complex system involving various disciplines and technologies such as biology, biochemistry, chemistry, fluidics, optics, electronics, data acquisition and statistical data processing.[1] Basically, a hematology analyzer is a fully automated device able to sample the blood through a hermetic stopper, dilute the sample, add a specific reagent for single or multiple cell parameters detection, carry the cells within a flow stream toward one or several sensors, acquire and store the information resulting from several physical mechanisms, and finally process the raw data by using a classification algorithm. What definitely differentiates this new analyzer from a classic flow cytometer is it capacity to accurately manage whole blood volumes (traditionally per mm^3 or per µl) added to its high level of automation. Although all HORIBA ABX analyzers provide platelet, red blood cell and leukocyte measurement, this article will focus on leukocyte differential, pointing out the evolution of technologies from the beginning of HORIBA ABX products toward the last generation of apparatuses. Prior to this, it is necessary to point out that leukocyte differentiation and counting are strongly related to hematopoiesis. Any cell in circulating blood arises from a single cell, the stem cell, originating from

bone marrow.

The bone marrow is one of the most complex tissues in the body. Distributed as red marrow all over the skeleton, but mainly situated in the pelvis area, the sternum and the vertebrae, an adult weighing 70 kg has roughly 1.5 kg hematopoietic tissue. This comes in addition to 5-6 liters of blood, of which more than 2 kg consist of red blood cells.

The main process for blood production is:

(1) A few stem cells produce a large number of progeny cells. This goes on continuously, and a single stem cell may, in a week or two, have up to 10^6 descendants. The stem cells also maintain their own numbers by additional cell division, as showed in Figure 1.
(2) Immature cells become mature blood cells which are able to perform specialized functions in the body.
(3) A limited number of cell divisions occur in parallel with maturation, with a final stage where mature cells lose their ability to divide (erythrocytes)
(4) Mature cells are stored for a while in the bone marrow until they enter the bloodstream to perform their specialized functions in blood or tissues
(5) The multipotent stem cells have the ability to direct their development into all subclasses of hematopoietic cell types, including erythrocytes, granulocytes (neutrophils, eosinophils and basophils), mast cells, monocytes and macrophages, megakaryocytes and platelets, as well as the different types of lymphocytes, including B, T, and NK cells.

A few images of such cells are shown on Figure 1. The main objective of leukocyte differentiation is automatic classifying and counting of the lineages according to their morphology, size or more advanced criteria such

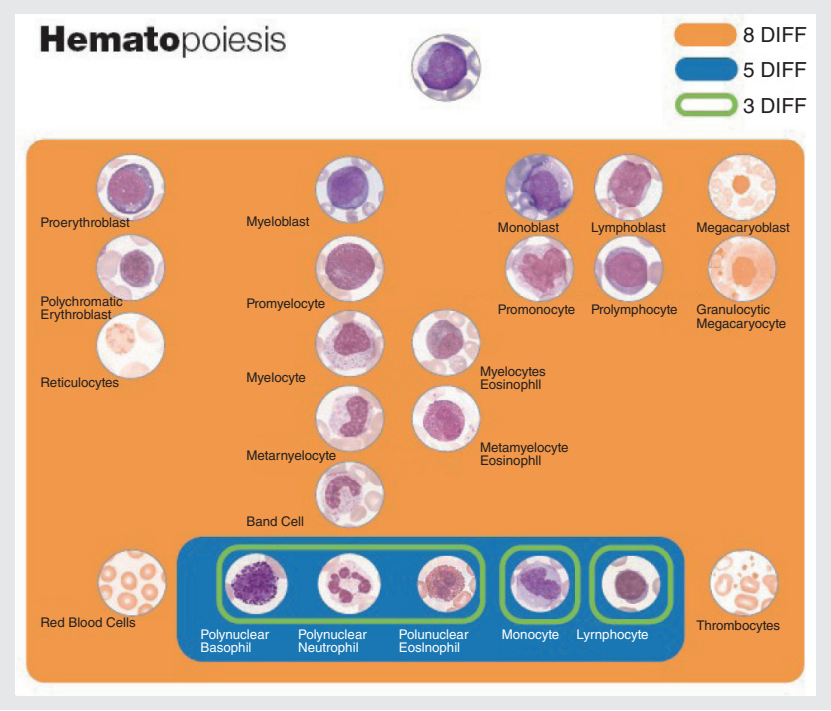

Figure 1 Leukocyte subsets according 3 DIFF, 5 DIFF and 8 DIFF definitions.

as the expression of some molecules like trans-membrane proteins or RNA/DNA content. In the area of automatic diagnosis, leukocyte classification has been organized according the following definitions:

3 DIFF: classification of three lineages of leukocytes (Lymphocytes, Monocytes and Granulocytes), so–called LMG classification.

5 DIFF: classification of five lineages of leukocytes (Lymphocytes, Monocytes, Neutrophils, Eosinophils, Basophils).

Extended-5 DIFF: classification of five lineages of leukocytes (Lymphocytes, Monocytes, Neutrophils, Eosinophils, Basophils) including the count of Large Immature Cells, the LIC parameter with a specific differential including IMM (Immature Monocytes), IML (Immature Lymphocytes) and IMG (Immature Granulocytes). The LIC parameter being used to flag samples containing abnormal leucocytes.

8 DIFF: classification of eight lineages of blood cells (Lymphocytes, Monocytes, Neutrophils, Eosinophils, Basophils, Blasts, Immature Granulocytes, Erythroblasts)

Today, manufacturers of *in vitro* diagnostic instruments are facing a dilemma: developing systems which enable ever more complex analyses for a more accurate and affordable diagnosis, providing robust and reliable methods to flag abnormal samples, while ensuring easily interpreted results for increased laboratory productivity, with a minimal false positive results thus reducing useless slides or flow cytometry reviews. The progress from 3 DIFF to 8 DIFF illustrates partly how technologies have been evolving during the last 10 years, pointing out how challenges have been taken up in terms of accuracy, throughput and reagent consumption, and how these advances have improved efficiency in the laboratory.

CIS for 3 Part Differential

This measurement principle relies on an electronic gate designed to detect and generate an electronic pulse: the CIS (Cell Impedance Signal) related to the overall particle volume. According to Figure 2, an electric field is generated inside a micro-aperture placed inside a chamber, in which the particle, a blood cell, is pulled through by aspiration. Two electrodes are placed on either side of the aperture producing a continuous electric current through the aperture. A blood cell, when passing through the aperture, creates an obstacle to the electrical current and, therefore, increases the micro-aperture impedance. It can be experimentally shown that pulse current amplitude varies in accordance with cell volume, as long as the biological cell can be considered as slightly insulating. From the electronic point of view, a constant current source converts such current variations into pulsed voltage signals, measurable across the gate. A constant voltage supplies a basic network composed of a polarization resistor Rs, a shunt resistor R and feedback resistors R1 & R2. All of these resistors are

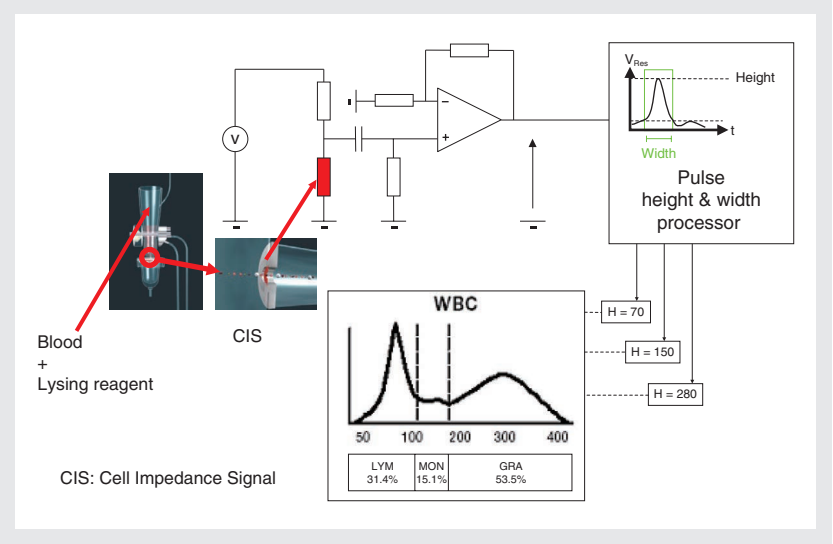

Figure 2 Principle of CIS for 3 Part Differential

optimized to simultaneously gain stable operation against temperature changes of the gate resistance Ra and they are set to optimize the electronic signal to noise ratio. The output signal is measured by using a specific electronic circuit designed to determine gate pulse parameters, namely their heights and widths.

It is worth noting that, whereas pulse heights inform about cell volume, widths of the pulses are used to filter the signal, rejecting undesirable pulses corresponding, for example, to simultaneous crossing of the gate by two cells.
The MICROS analyzer uses CIS technology. For 3 part DIFF, a specific reagent lyses red blood cells, but it preserves and prepares WBC membrane to react differentially according to cell features:

- When the lyse reacts with lymphocyte cytoplasmic membranes, it allows release of water-soluble cytoplasm and shrinks the cell membrane around the nucleus.
- When the lyse reacts with monocyte cytoplasmic membranes, it has an intermediate reaction, maintaining its large size in comparison to lymphocytes.
- When the lyse reacts with granulocyte cytoplasmic membranes, it has a limited reaction due to a molecule in their cytoplasmic structure which protects them from the shrinking action of the lyse. This limited reaction makes granulocytes the largest of the sub-populations in cell differentiation.

After the differential lysing action, the machine analyses the height of each pulse as cells pass through the electronic gate. These pulses are then digitized, grouped according to their size (30 fL to 450 fL), and mathematically processed to create the WBC distribution curve, which is also known as the WBC histogram.

The 3 sub-populations of WBCs are charted and classified according to the

following classes:
Lymphocytes (30 fL to 100 fL)
Monocytes (100 fL to 150 fL)
Granulocytes (150 fL to 450 fL)

This classification is also known as LMG. Results are printed according to a histogram as reported on Figure 2, specifying the percentage of each sub-population.

FROM 3 to 5 Part DIFF

The LMG differential lyse provides an efficient technique to separate Lymphocytes, Monocytes and Granulocytes. An improved diagnostic can be formulated if granulocytes are discriminated between themselves. For example, eosinophilia occurs in a wide range of conditions. In modern countries, its commonest causes are allergic diseases such as asthma and hay fever, whereas worldwide, the main cause is parasitic infection. It can also occur in relation to common skin diseases and drug reactions. Other rarer causes include: lung diseases, eg Loeffler's syndrome, vasculitis (inflammation of blood vessels), eg Churg-Strauss syndrome, some tumors, eg lymphoma, liver cirrhosis, some antibody deficiencies (not typically AIDS), other rare skin diseases, eg dermatitis herpetiformis and other unknown causes, labeled hypereosinophilic syndrome.

From a technological point of view, a new step was accomplished through simultaneous measurement of electronic volume and optical signature of cells travelling through an optical gate placed just above the electronic gate, Figure 3.
Each blood cell experiences a travel from the CIS sensor toward an optical gate where it interacts with the light beam, causing an optical power loss (the so-called optical extinction) measured by a photoreceptor. Different situations are depicted on Figure 2. When no cell crosses the optical gate, the light beam is totally transmitted, producing a stationary electrical signal called "the baseline". The light source (not represented on the Figure) is a thermal or semiconductor lamp. Usually, a non-coherent optical source is tailored by a beam shaper into a rectangular window with uniform illumination (the so-called optical gate) projected inside the flow cell.

HORIBA Medical instruments use a specific flow cytometer based on hydrofocusing to combine Cell Impedance Signal (CIS) and Optical Extinction. In this apparatus, cells are described by two parameters (volume and optical extinction) and displayed in a matrix where several sub-populations are identified by a specific algorithm. Low optical extinction corresponds to lymphocytes and monocytes which are poorly scattering particles whereas neutrophils and eosinophils produce high optical extinction corresponding to highly scattering particles. In this method, whole blood is mixed with a specific lytic reagent containing Chlorazol black as a stain reinforcing optical extinction, even if we have to recognize that the main contribution to optical extinction is scattering.

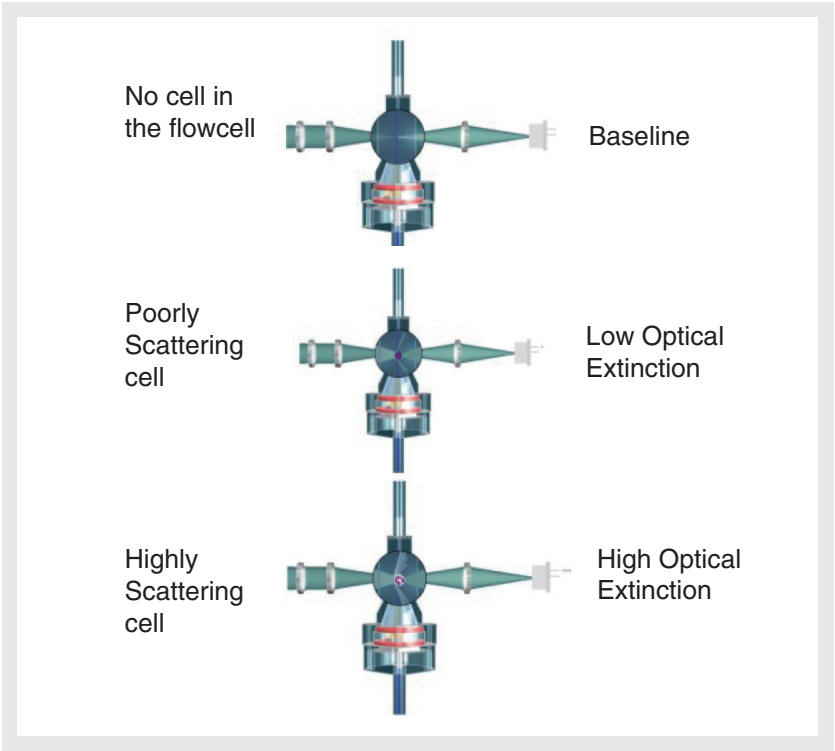

Figure 3 Schematic representation of the optical response to a travelling cell through the optical gate to work out the 5 part DIFF.

The Optical Extinction Phenomenon

While a cell crosses the optical gate, the optical detector is designed to provide a sensitive response to light losses including scattering and absorption.

It is worth to analyse, from a physics point of view, the process of optical extinction as a unique feature in HORIBA Medical blood analyzers. Optical extinction is the capability of any particle to remove light from an original beam. This light removal produces power variation in the transmitted light beam. Two independant mechanisms, absorption and scattering, are responsible for optical extinction. Absorption is mostly a non radiative process reinforced by cytochemistry, most often converting light to thermal energy. Whereas scattering is a very complex phenomenon, involving specific features of the particle itself. For blood cells, optical thickness is so

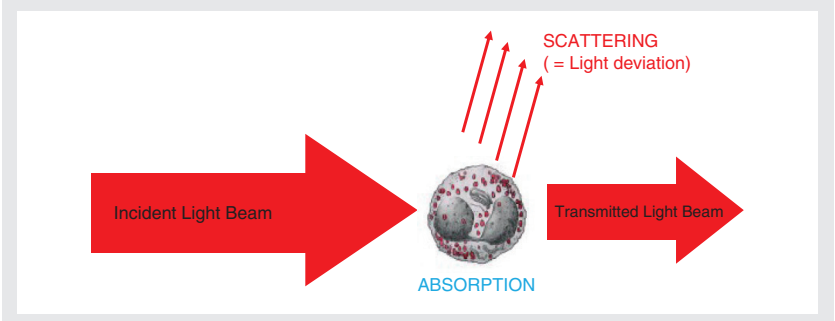

Figure 4 Optical Extinction Definition

small that absorption is often negligeable in comparison to scattering. Scattering by a perfect sphere has been definitely solved by Gustave Mie in 1907. Since then, a lot of progresses have been done using extensive computer calculations. A biological cell is a pseudo random particle with different compartments, each having a specific refractive index.

These refractive indexes have been measured by several research teams for cytoplasms, mitochondria and others biological species as reported in the left side of Figure 5. On the right side , top and bottom graphs represent computer calculations of light scattering versus scatter angle for a semi realistic cell , wherein nucleus, cytoplasm and granule refractive indexes have been taken into account.[2] These curves show that light scattering is dependant on cell granule or organelle concentration: higher concentration produces significant effect mainly at high scatter angle, more than 20 degrees, whereas forward scattering is not dependant on this organelle content. On the other hand, side scattering is dependant on nucleus size whereas forward scattering is not. Design tradeoffs involving parameters, such as optical numerical aperture of illumination/detection and light wavelength, are very important since they balance absorption and scattering strength responsible for the performance of the analyzer. Each cell being probed optically and electronically is identified by its two components X: impedance measurement, Y: optical extinction measurement.

According to Figure 6, the blue cluster represents Lymphocytes which are very small round shaped cells with condensed cytoplasm and large nucleus. These cells are normally positioned in the lower part of the optical Y-axis as well as the lower part of the volume X-axis because of their small volume. The far left side of the lymphocyte zone (LL) should normally be empty. Any detection of cells in the (LL) zone indicates small lymphocytes, Platelet aggregates, NRBCs (Nucleated Red Blood Cells), or improperly adjusted flow cell alignment. Background noise may also be detected in this zone if

Cell Component	Index	Reference
Cytoplasm, rat liver cells	1.38	(Beuthan et al., 1996)
Mitochondria, rat liver cells	1.40	(Beuthan et al., 1996)
Lipid	1.48	(Beuthan et al., 1996)
Cytoplasm	1.35	(Kohl and Cope, 1994)
Protein	1.50	(Kohl and Cope, 1994)
Cytoplasm, hamster ovary cells	1.37	(Brunsting and Mullaney, 1974)
Mitochondria, rat liver	1.42	(Liu et al., 1996)
Melanin	1.7	(Vitkin et al., 1994)
Cytoplasm	1.358-1.374	(Lanni et al., 1985)[2]
Cortical cytoplasm	1.353-1.368	(Bereiter -Han et al., 1979)
Dried protein	1.58	(Barer and Joseph, 1954)

From « Optics of Biological Particles » NATO Science Series vol. 238

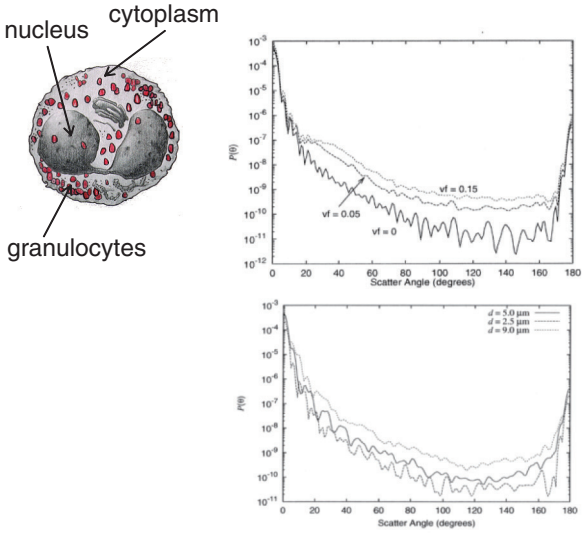

Figure 5 Refractive indexes of biological coumponds (left hand side) , a pseudo realistic model of cell (center), and numerical results of scattering diagrams for a simplified cell model taking into account inner granule concentration (top) and nucleus size (bottom).

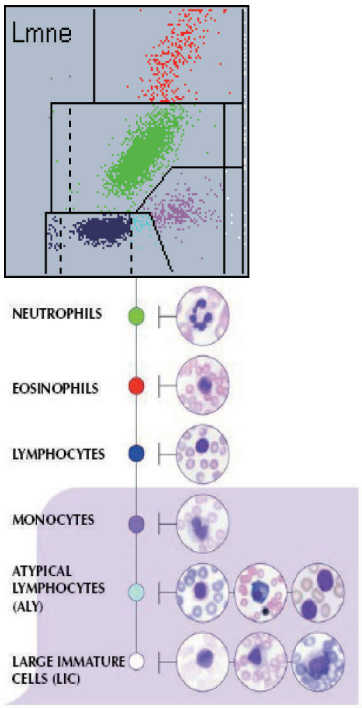

Figure 6 LMNE matrix representation according to CIS and optical extinction measurement.

biological interference takes place in a significant way.

As represented in Figure 6, optical extinction (Y-axis) is plotted against volumes (X-axis) to form an image with several "clusters" identified as follows:

The blue cluster represents Lymphocytes which are very small round shaped cells with condensed cytoplasm and large nucleus. These cells are normally positioned in the lower part of the optical Y-axis as well as the lower part of the volume X-axis because of their small volume. The far left side of the lymphocyte zone (LL) should normally be empty. Any detection of cells in the (LL) zone indicates small lymphocytes, Platelet aggregates, NRBCs (Nucleated Red Blood Cells), or improperly adjusted flow cell alignment. Background noise may also be detected in this zone if biological interference takes place in a significant way.

The purple cluster represents Monocytes which are very large irregular shaped cells with large convoluted nuclei. The nucleus contains folds and sometimes vacuoles. The cytoplasm is also large with non-granular intra-cellular material. These cells will not scatter or absorb a large amount of light when passing through the optical gate. They will therefore be positioned in the lower part of the optical Y-axis. Because monocytes are large cells, they will be placed on the right side of the volume X-axis.

The green cluster represents Neutrophils which are larger in size than lymphocytes. Neutrophils contain granular material in their cytoplasm along

with a segmented nucleus. Due to these cellular features, more light will be scattered as they pass through the optical gate, spreading up the cloud to higher values of the Y-axis depending on their granule concentration, and then spreading up along the X-axis according to their maturity. Hyper segmentation and increased granule content will place these cells higher on the optical Y-axis.

The red cluster represents Eosinophils which are somehow like neutrophils. They contain granular material and segmented nuclei within the cytoplasm. Because they scatter more light than other cells, they are placed at the top of the image. Hyper-segmentation of the nucleus and increased granule/ organelle content will spread this population across the right side of the matrix.

Additional parameters, ALY (Atypical Lymphocytes) and LIC (Large Immature Cells), are other cells identified in pathologic blood, they complete the matrix spectrum of leukocytes.

Basophils are rare cells, they are embedded in the LMNE matrix. To detect this rare population, a specific reagent is used (ABX BASOLYSE II) in order to lyse erythrocytes and shrink leukocytes except basophils which cytoplasm remains shaped. Based on cytochemistry of basophils, this process allows a basophil measurement based on CIS reading for volumetric analysis of the sample. An improvement was made in OCTRA technology where CIS and Optical Extinction are combined for basophil detection.

Side Scattering (SSC) versus Optical Extinction (EXT)

SSC versus EXT was investigated at HORIBA Medical using a customized flow cytometer measuring simultaneously Side Scattering and Optical

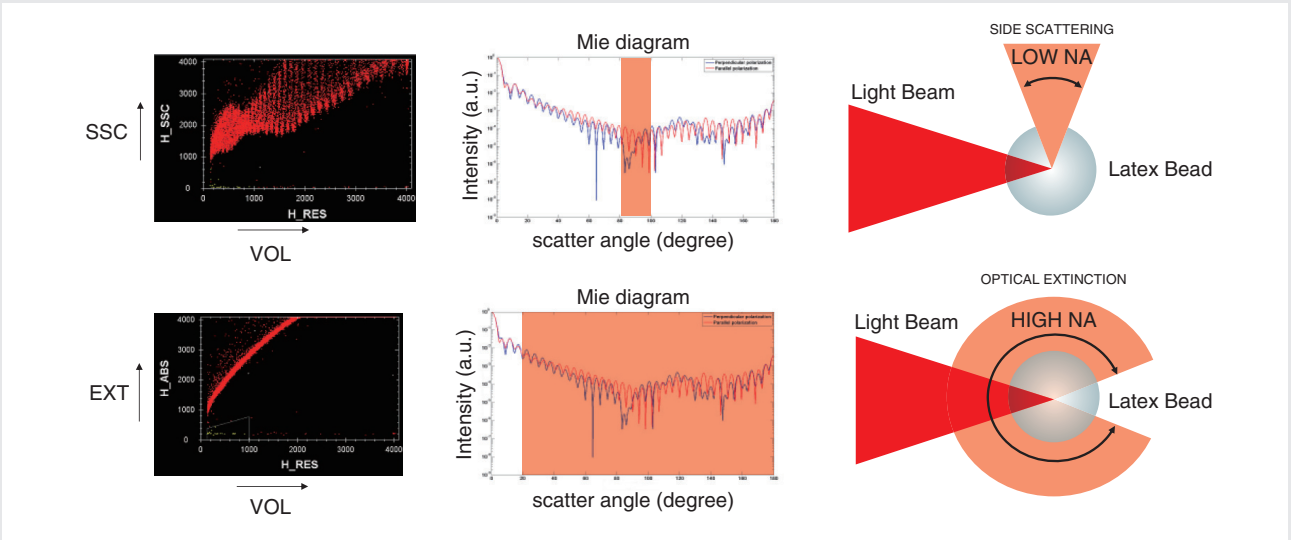

Figure 7 Comparison of Side Scattering Detector (SSC) placed at right angle of the light beam (top image) producing a relatively low numerical aperture (LOW NA) in comparison with optical Extinction (EXT) which provides High Numerical aperture (High NA) filtering therefore the Scattering profile derived from Mie Theory for both TE and TM polarizations.

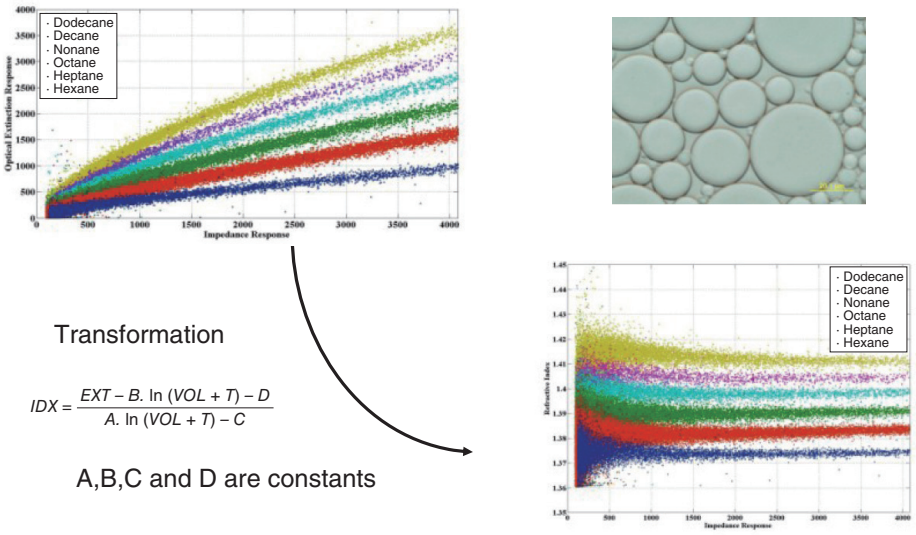

Figure 8 Calibration of bi-parametric representation CIS x EXT to determine a new mapping involving VOL x INDEX. The calibration process is based on emulsions of organic solvents: hexane (marine blue), heptane (red), octane (green), nonane (blue), decane (purple), dodecane (yellow).

Extinction. Figure 7 is an amazing demonstration of side scattering and extinction behaviors for polydisperse polystyrene beads, diameters ranging from 1 to 20 µm.

The horizontal axis represents particle volume and the vertical axis optical response. Side Scattering detector (SSC) produces a very strange behavior with strong oscillations whereas Optical extinction (EXT) has a smooth like response. Explanations of these results come from Mie theory where it is derived that scattering of a perfect sphere is an oscillating function of size parameter or scatter angle. In SSC, these oscillations are weakly filtered by the low numerical aperture of side optics (pink color). On the other hand, optical extinction takes place over a large numerical aperture, causing an

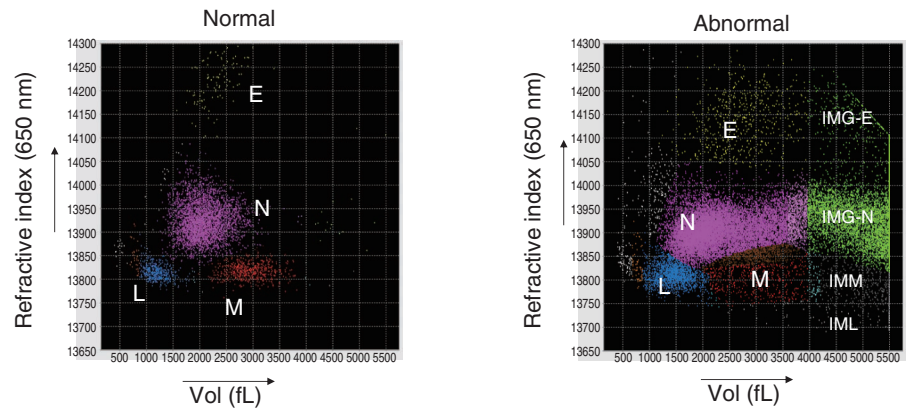

Figure 9 Normal (left) and Abnormal samples (right) according to orthogonal representation volume x refractive index.
This classification process was compared to microscopic examination of blood smears, and algorithms were optimized to match manual counts as much as possible. More specifically, we defined thresholds to identify immature granulocytes (green color), monoblasts (grey color) and lymphoblasts (blue color). These fundamental results were the starting point for flags on Pentra DX analyzer. Accordingly, ten years ago, HORIBA Medical introduced the extended 5 part diff comprising Immature Granulocyte, Monoblast and Lymphoblast counts based on volume and optical extinction measurements. The sum of IML, IMM and IMG is called Large Immature Cells parameter or LIC parameter.

efficient filtering process of optical oscillations, producing therefore a smooth response in comparison to a standard side scattering detector.

These considerations have been applied to calibrate VOL x EXT using specific emulsions made from organic solvants (hexane, heptane, etc..). In Figure 8, each emulsion have a specific refractive index, increasing from the bottom (blue) to the top (green). As you can see on this picture, each fluidic particle is a perfect sphere with a specific volume and refractive index represented in the matrix as a colored dot. Each refractive index isoline can be transformed into another one where volume dependence is removed to produce an orthogonal mapping of volumes and refractive indexes.
In this new orthogonal representation, normal and abnormal blood can be displayed and each cell can be identified by its volume and its average refractive index.

Pentra DX and Nexus: the LIC Parameter

Pictures, in Figure 10, illustrate some Leucograms of Pentra DX and Nexus blood analyzers. Acute and chronic leukemias, displayed respectively on the left and on the right hand sides, show the LIC parameter including a differential count of IML, IMM, IMG. Many other blood diseases have been investigated by biologists in European laboratories and the LIC (Large Immature Cells) parameter was compared to cytology counts showing acceptable correlations between automatic and manual counts. The LIC parameter was therefore definitively used for flag purpose.
We recently investigated the capability of these analyzers to detect abnormal samples at Bordeaux Hospital. The experiment was based upon a total of 218 patients including 152 abnormal samples. These samples were selected to provide a large spectra of abnormal cells containing different etiologies for immature granulocytes and blasts. Within the scope of this study, sensitivity and specificity of the LIC parameter were investigated versus IG + BLAST

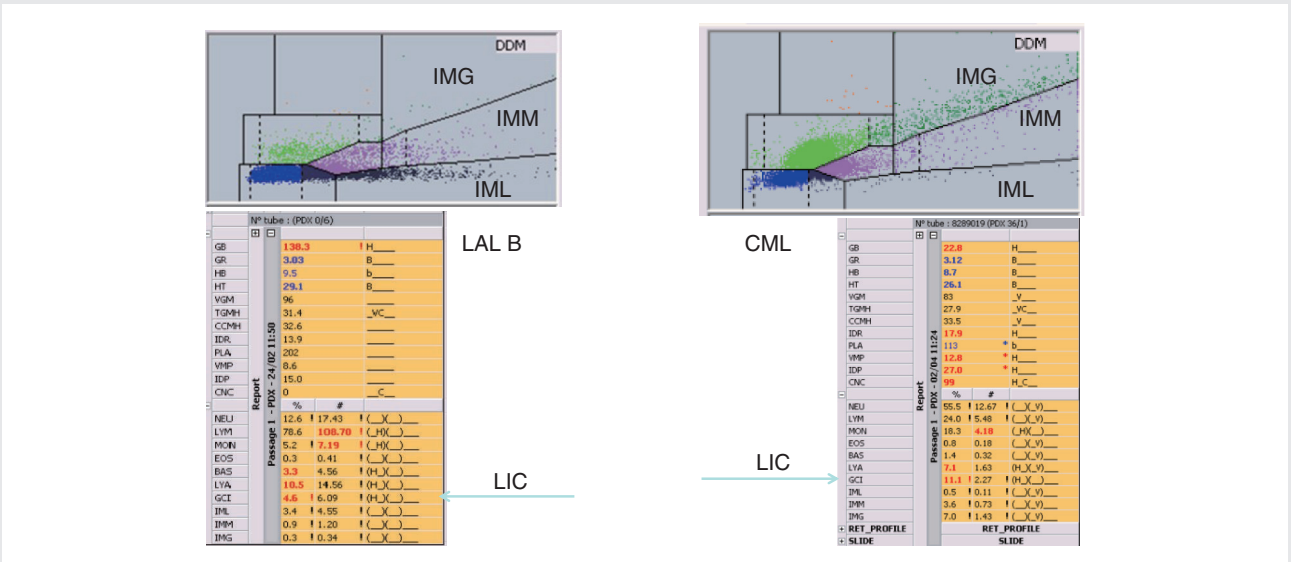

Figure 10 Example of two abnormal samples from leukemia patients: LAL B (left) and CML (right). LIC parameter is derived as the summation of IML, IMM and IMG events falling in corresponding boxes.

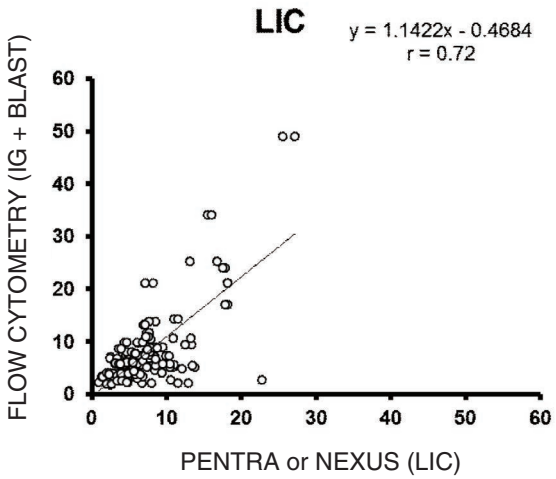

Sensitivity	0,94
Specificity	0,83
PV-	0,89
PV+	0,88

Figure 11 IG + BLAST derived by flow cytometry versus LIC derived by PENTRA and NEXUS.

derived from flow cytometry based on CD16, CHTR2, CD45 and CD11b (standard protocol used at Bordeaux Hospital). We reported that Pentra DX and NEXUS analyzers had a sensitivity of 94 % and a specificity of 83% to flag samples, with a negative predictive value of 89% and a positive predictive value of 88%.

For routine purpose, these results are highly satisfactory since we reported that the rate of false negative is lower than 10 %. In addition, it is worth pointing out that the absolute count of Immature cells can be derived by mulytiplying the LIC % parameter by the total count of white blood cells; nevertheless we have to recognize that this parameter is mainly designed to detect and flag abnormal cells in the sample. From a biophysics point of view, it is worth noting that despite the fact that measuring principles are far from each other, analysis being based on volume x refractive index measurements, Pentra DX and Nexus instruments deliver highly correlated results in comparison to flow cytometry immunomarking. (Figure 11)

FROM 5 to 8 Part DIFF: OCTRA Technology.

To reduce some discrepancies between routine and CD marker analyses, mainly for absolute count of immature cells and its interference with other leucocyte sub-populations, we recently developped a unique optical device, depicted in Figure 12. In addition to previous physical parameters (CIS, SSC and EXT), the cell signature is enriched by fluorescence measurement of RNA / DNA content. Based on this strategy, called OCTRA technology, we were looking for an improved method of detecting and counting immature cells including immature granulocytes, blasts and erythroblasts.

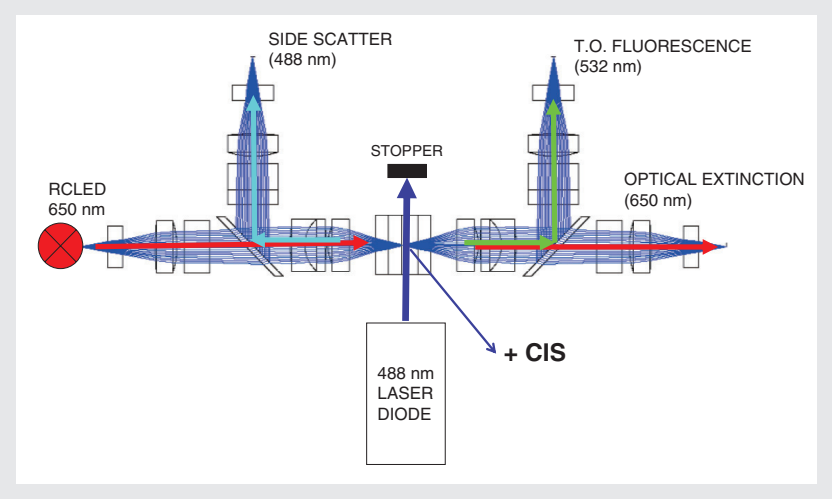

Figure 12 Schematic representation of the optical principle used in OCTRA Technology.

OCTRA Technology combines two optical beams in the flow cell. The red light beam passing through the flow chamber is used for optical extinction measurement. The Blue Laser diode is used to induce both scattering and fluorescence optical signals of cells. These three optical measurements are combined to Cell Impedance Signal (CIS) measurement. Optical Extinction, Fluorescence, Scattering and Cell Impedance measurements form a fourth dimensional space analysis where each blood cell signature is digitized by an electronic processor.

Analytical techniques based on fluorescence detection are very popular because of their high sensitivity and selectivity, together with advantages of spatial and temporal resolution. The principle of fluorescence relies on absorption and re-emission of light by a molecule, see Figure 13. Once the molecule is excited by absorption of a photon at 488 nm, it returns to the ground state with emission of a new photon at 530 nm. In OCTRA technology, the Thiazol Orange dye[3] is used and replaces the Chlorazol Black used in the Pentra Analyzer. Free in solution, the two aromatic cycles rotate about the Carbon-Carbon bound and absorbed photons are converted to mechanical motion: there is no significant fluorescence. On the other hand, this molecular compound fluoresces strongly when rotation is blocked by hybridization to DNA / RNA strands.
Early stages of blood cell maturation, normally occurring in bone marrow only, are denoted by their nucleic content. Nucleic acids (RNA and DNA) are therefore found in larger amounts in these immature cells. Mature leukocytes also exhibit different levels of nucleic acids depending on their nature and activity. The level of nucleic acid concentration can be measured through the use of Thiazole Orange (TO), as exemplified in the next section.

Leukocyte Classification in OCTRA Technology.

In OCTRA technology, whole blood is mixed with a specific reagent performing simultaneously the following operations:
- Removal of erythrocyte by lytic action

- Chemical poration of nucleated cells for fast staining purpose, while maintaining membrane voltage to accelerate penetration of Thiazole Orange (electropositive ion).
- Staining of intra cellular nucleic acids by TO, which is an intercalative dye, highly specific to nucleic acids.

Once incubation completed (a few seconds), the cell suspension is pulled through a flow chamber equipped with the electro-optical device depicted in Figure 12.

In OCTRA technology, multiple cells crossing through CIS or EXT gates are detected by pulse width measurements: undesirable events are filtered based on pulse/height ratio information. The four space analysis is used to design algorithms in a self-learning approach, after intensive testing based on a large spectrum of blood samples including normal and abnormal. In addition to the standard matrix CIS x EXT available in the Pentra instrument, OCTRA technology provides a new matrix where ERB, BASOPHILS, IG and HRC cells are identified.

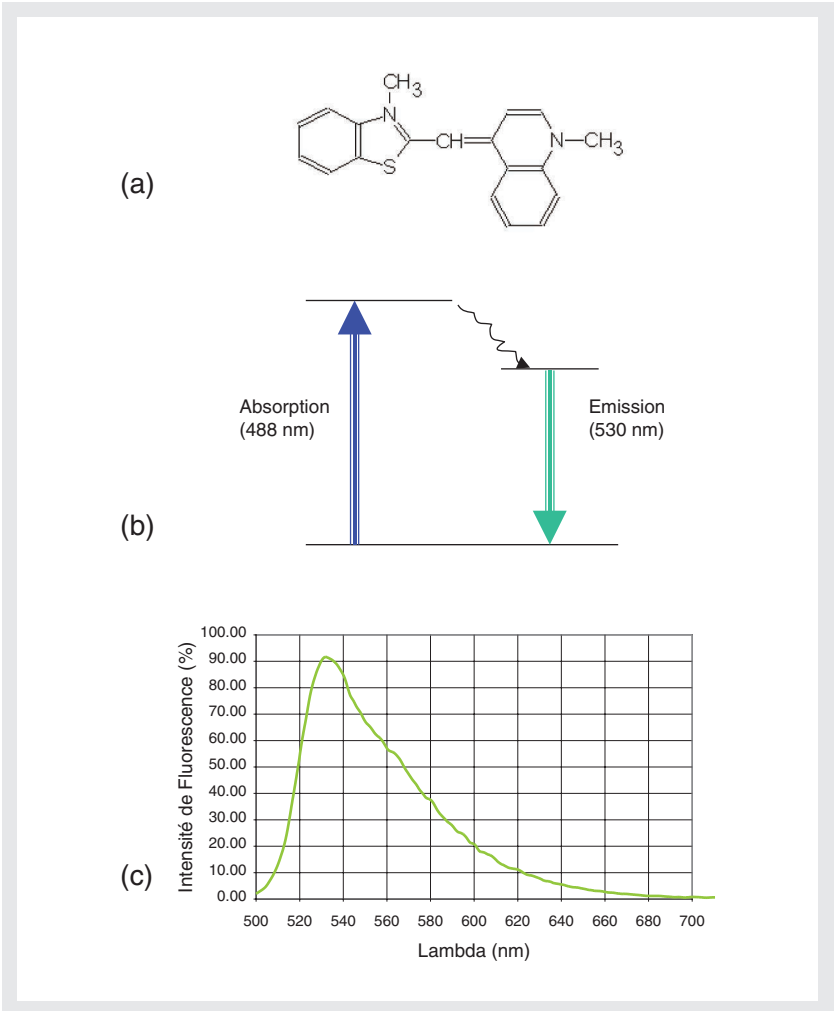

Figure 13 Simplified Jablonsky diagram of Thiazole Orange dye
(a) and associated fluorescence spectra (c) for λ_{ex} = 488 nm.

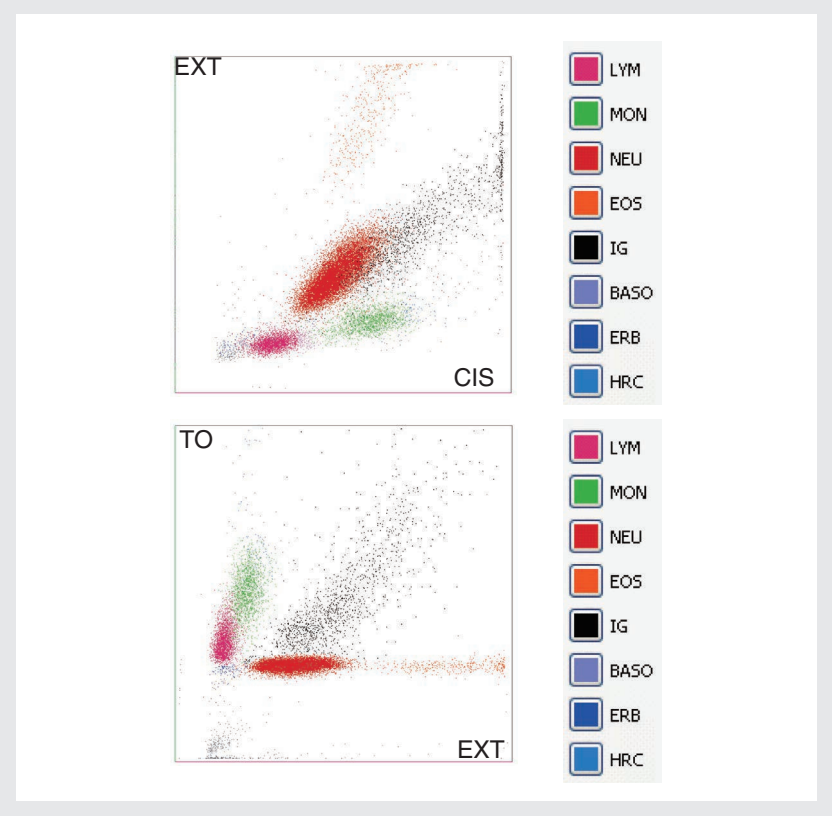

Figure 14 Standard bi-parametric representation in OCTRA technology involving CIS x EXT and EXT x TO images.

Figure 14 displays a representation using standard parameters CIS x EXT and EXT x TO.

Stromas, platelet aggregates and other fragments (grey color), having no genetic material, are easily separated by their poor level of TO fluorescence. Platelet aggregates are themselves denoted by their higher SSC response.

Being lysed in the same way as erythrocytes, the remaining part of Nucleated Red Blood Cells (marine blue), which have small nucleuses; produce weak level of signals in the four measurement spaces.

Lymphocytes (purple color) are larger in size than NRBC. Being mono-nucleated, and having small cytoplasm, they produce a bigger response for EXT and SSC. Depending on their maturation and their activation state, they produce a weak or high level of CIS and TO fluorescence.

Basophils (blue color) have roughly the same size as that of lymphocytes, but being poly-nucleated, they produce higher SSC levels. On the other hand, the TO level remains weak like other granulocytes. Neutrophils (violet) and eosinophils (pink) also produce this TO level, but being bigger, they produce medium RES and EXT levels; being more complex, they exhibit a much higher SSC response. Due to their granule size, Eosinophils produce a higher EXT response than neutrophils with respect to their volume (CIS). We have to point out that mature granulocytes produce a TO baseline from which the

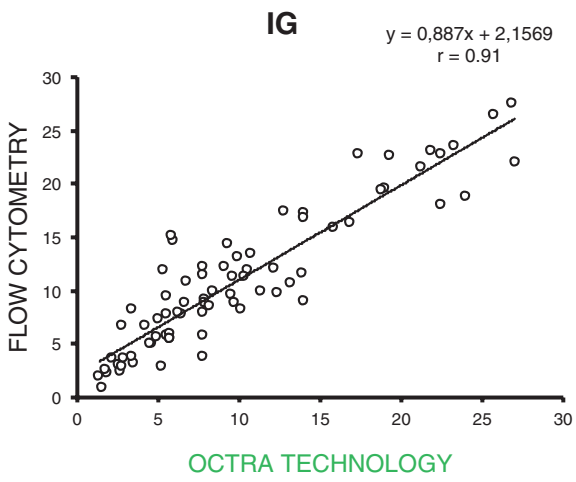

Sensitivity	0,95
Specificity	0,8
PV-	0,88
PV+	0,85

Figure 15 Immature Granulocyte parameter derived from OCTRA technology in comparison with four color cyometry for CD16, CHTR2, CD45 and CD11b.

immature cells are detected.

Immature granulocytes (black) show higher TO level than mature granulocytes, and high EXT. High CIS responses are produced because of their large volumes. Other large leukocytes are HRC (High ARN Content) (sky blue), which produce high CIS and TO responses. These cells have a high TO level due to their high RNA content.

Monocytes (green), being mono-nucleated and having no granules, produce a weak to medium SSC level and a medium to high EXT, TO and CIS levels.

In OCTRA Technology, the HRC box gathers lymphoblast, monoblast and plasma cells.

We investigated the capability of OCTRA technology to detect abnormal samples containing immature granulocytes. The experiment included 196 patients, selected to provide a large spectrum of abnormal cells containing different etiologies for immature granulocytes, blasts and atypical lymphocytes. Within the scope of this study, sensitivity and specificity of the IG parameter and its flag capability, were investigated versus IG derived from flow cytometry based on CD16, CHTR2, CD45 and CD11b (standard protocol used at Bordeaux Hospital). Based on a cut-off of IG (Octra) > 2% and IG (Flow cytometry) > 2%, we reported that OCTRA technology had a sensitivity of 95% and a specificity of 80% to recognize and flag samples containing immature granulocytes, with a negative predictive value of 88%

and a positive predictive value of 85%. These results are highly satisfactory for routine application, and it is worth noting that RNA / DNA expression measurements of leucocytes provide an exceptionally simple and affordable technique to meet flow cytometry standards both for detecting and counting IG cells as reported in Figure 15.

Biomolecule Detection for Leucocyte Recognition and Counting

Many membrane or cytoplasmic proteins of leukocytes have been studied at laboratory level.[4] Availability of monoclonal antibodies directed against

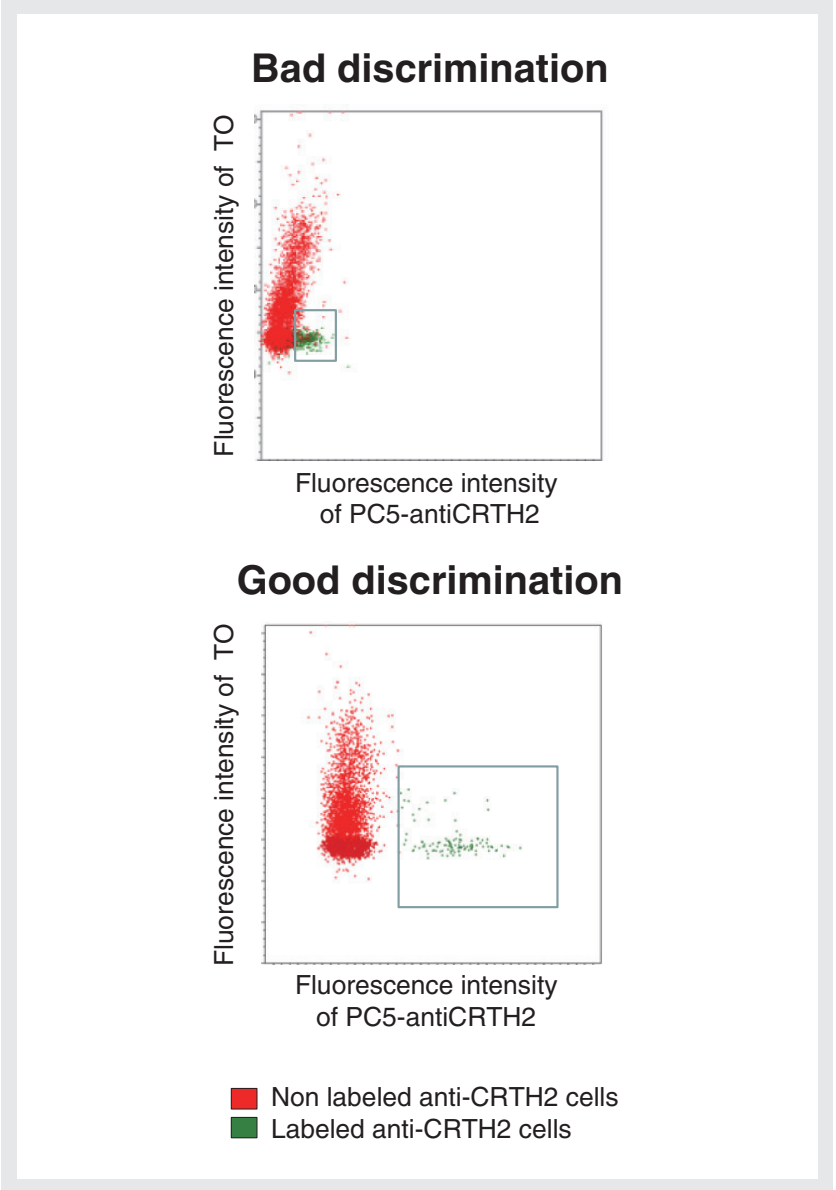

Figure 16 Top: demonstration of a single wavelength LIF experiment based on PC5 –CRTH2 and TO –RNA/DNA showing poor separation of labeled and non-labeled cells. Bottom: dual wavelength LIF experiment where PC-antiCRTH2 is correctly measured despite unbalanced biomolecule expression.

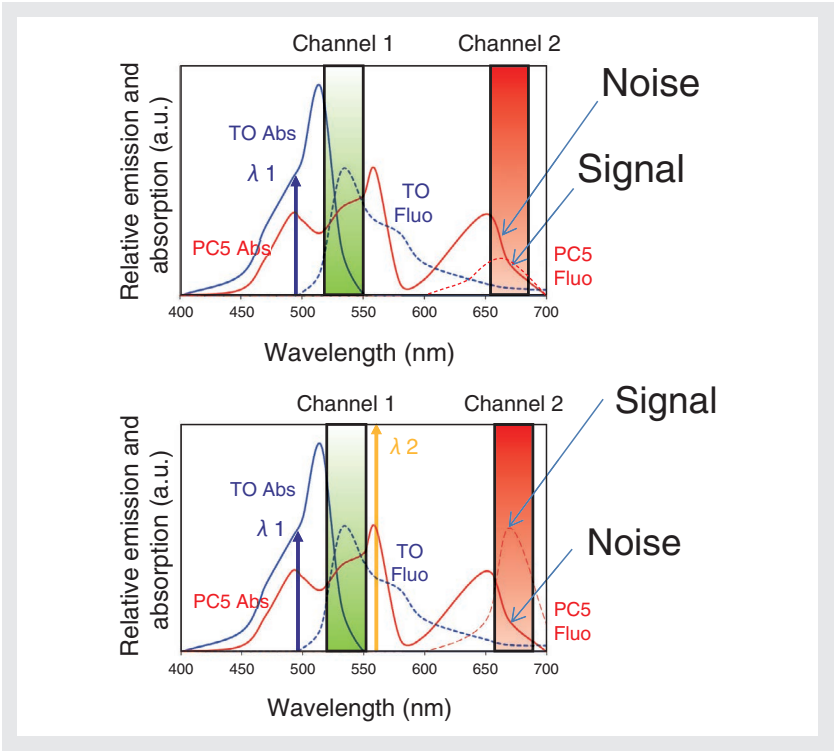

Figure 17 Illustration of spectral overlaps, single (top) and dual (bottom) LIF experiments.

these proteins allows flow cytometric analysis of leukocyte lineages, mainly based on fluorescence immuno-markers.[5] In this context, the standard diagram is replaced by a similar diagram, where cells are fully described by their antigenic expression. A specific cell is described by a set of CD markers, each having a specific expression. Obviously, this concerns the field of standard flow cytometry, except that at HORIBA Medical, we took into account limitations and drawbacks existing in marketed flow cytometers.[6] A first limitation comes from detection of unbalanced fluorescence signals measured in a multi-channel flow cytometer. To illustrate this pitfall, we carried out an experiment where a weak fluorescence (Phycoerythrin Cyanine 5 coupled to an antibody denoted PC5-antibody) is investigated in the presence of a strong fluorescence background (TO from DNA / RNA). In Figure 16, the situation of PC5-antiCRTH2 is reported here whereas several other combinations were investigated.[6]

Figure 16 (top) reports an experiment using a single wavelength operation showing that anti-CRTH2 is weakly detected in presence of TO fluorescence, while Figure 16 (bottom) reports a dual wavelength excitation exhibiting a larger fluorescence for labeled anti-CHRTH2 cells.

At the top of Figure 17, blue and red curves are respectively the absorption spectrum of TO and that of PC5. Dashed lines are respectively the fluorescence spectrum of TO and that of PC5. Using one wavelength illumination, overlap of TO spectrum in channel 2 induces a background optical signal producing quantum noise for PC5 fluorescence measurement. At the bottom of Figure 17, a second wave is added in the flow chamber at 565 nm reinforcing significantly the PC5 fluorescence strength independently

of the TO fluorescence, thus improving to some extent the signal to noise ratio for channel 2.

Wavelength Multiplexing: A Flow Cytometry Paradigm.

A generalisation of the previous concept is depicted in Figure 18. Here, multi-wavelength illumination is proposed to improve the signal to noise ratio for multi color flow cytometry measurements with spectral overlaps.[6]

Looking at Figure 18, let's consider a fifth channel flow cytometer designed to adress the following fluorochormes: Alexa Fluor 405 (AF405 blue) for channel 1 (CH1) , Cyanine 2 (marine blue) for channel 2 (CH2), Cyanine 3 (orange) for channel 3, Cyanine 5 (red) for channel 4 (CH4) and Cyanine 5.5(brown) for channel 5, each coupled to a monoclonal antibody. This general scheme can be used for unbalanced CD expression measurements involving, for example, CD16, CRTH2, CD45, CD11b and CD34 as a standard protocol for leucocyte differentiation purpose. In this set-up, the wave λ 1 excites AF405. The wave λ 2 excites CY3. The wave λ 3 excites CY4. The wave λ 4 excites CY5 and the wave λ 5 excites CY5.5. This scheme is a generalisation of our principle for which each antibody is associated to a specific wave and a specific channel.

Thus, this set-up requires multi-wavelength operation. Each CD marker being adressed by a specific wave of defined wavelength and amplitude. To provide flexibility on multi-wavelength operation and selection, HORIBA Medical promoted the development of a specific laser based on non linear optics inside crystal fibers.[7, 8]

Figure 18 shows the set-up investigated at research level and corresponding

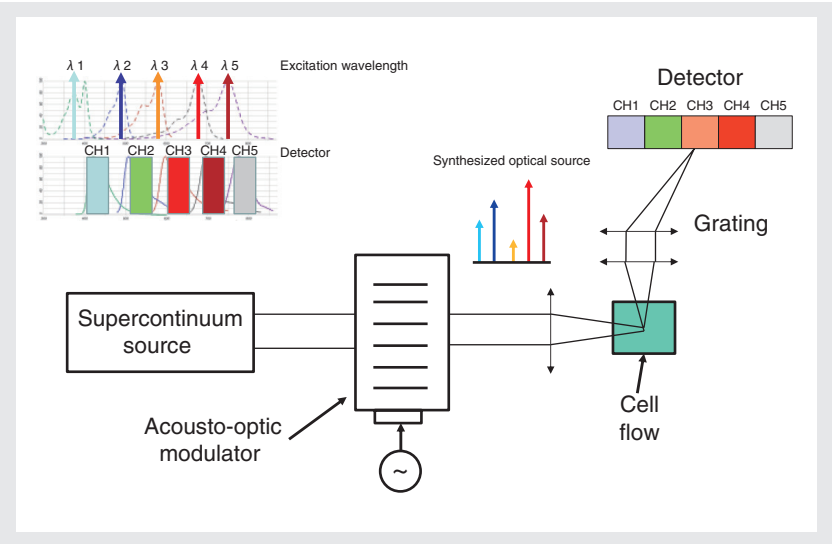

Figure 18 Design principle of a multiwavelength and multispectral detection architecture based on supercontinuum optical source.

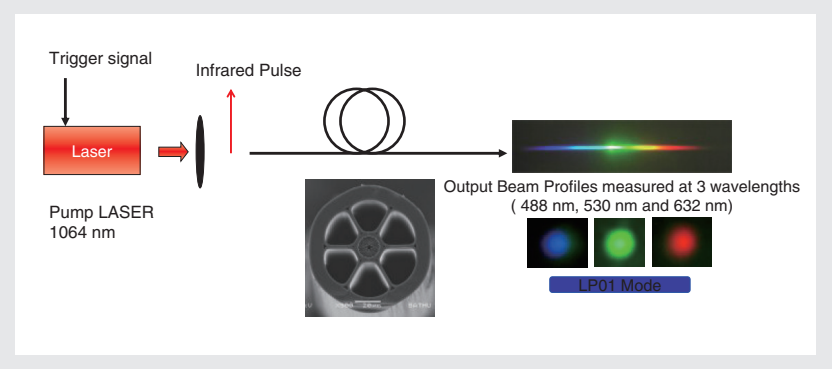

Figure 19 The supercontinuum optical source principle used at HORIBA Medical

to a compact solid-state flow cytometer with multiplexing-demultiplexing capabilities for CD expression measurements. Somewhere, it stands as a paradigm in the field of flow cytometry since the device is expected to be fully programmable thanks to a wavelength selector acting as an optical synthesizer tailoring both wavelength and wave amplitude for CD marker expression measurement. Preliminary results of this promising technology have been accepted for publication.[9]

In Figure 19, the optical source is depicted. It is based on a crystal fiber is composed of a small silica core surrounded by air galeries. Non linear effect takes place when an optical infrared pulse is sent into the tiny optical fiber core. When the pulse matches some technical conditions defined by the fiber itself, non linear optical processes convert the original pulse to a supercontinuum light source comprising all wavelengths, from the visible range to the short infrared. The beam emerging from this optical source looks like a white laser with a high spatial coherence. This rainbow-like image corresponds to dispersion of the beam by an optical grating. Thus, the white laser beam can be filtered at specific wavelengths providing LP01 modes identically to a conventional laser beam.

Conclusions

WBC differential technology covers a wide range of products at HORIBA Medical, depending on needs, habits and laboratory organization. Micros and Pentra analyzers provide flexible, accurate and reliable solutions for routine hematology, with satisfactory correlations with many references such as manual counts or cross correlated instruments based on physical measurements. We have to point out that incoming OCTRA technology will bring higher insight with improved correlations to flow cytometry «gold standards».

In addition to continuous improvement in biophysical measurement principles applied in routine analysis, HORIBA Medical explores the way cellular immunophenotypes can be carried out using optical wavelength multiplexing. This methodology is expected to fulfill requirements for multiple measurement of biomolecules, both improving cell identification and accuracy. To some extent, wavelength multiplexing alleviates software compensations applied in standard flow cytometers, which are the root cause

of inaccurate measurements in clinical applications, including diagnosis of hematology disorders or Minimal Residual Disease (MRD) monitoring. MRD is part of the concept of chronic disease follow-up requiring an accurate and sensitive methodology to monitore patients all along their lives. We are expecting that routine and innovative technologies will improve sensitivity and efficiency of clinical care and preventive medicine, which are the driving guidelines for the WHO and European Community in their fight against chronic disease while promoting active and healthy aging.

About the author: Philippe NERIN (MSc, PhD) is author of about 20 peer reviewed publications and inventor of about 25 patents. He has a 20 years experience in Applied research encompassing Measuring Science, Biophysics and Biophotonics. Since 2003, he is leading the Research and Innovation at HORIBA Medical, Montpellier.

References

[1] P. Nerin, D. Lefevre, Blood Cell Biology, Optics and Related Technologies, *HORIBA Technical Reports*, English Edition N° 8, 2004, p. 26-37.

[2] Andrew K. Dunn in A. Hoekstra, V. Maltsev and G. Videen, *Optics of Biological Particles*, Springer, 2007, p. 19-29.

[3] J. Nygren, N. Svanvik, M. Kubista, "The interactions between the fluorescent Dye Thiazole Orange and DNA, *Biopolymers*, Vol. 46, 1998, p. 39-51.

[4] M. Brown and Carl Wittwer, Flow Cytometry: Principles and clinical Applications in Hematology, *Clinical Chimestry* vol. 46, 2000, p.1221-1229.

[5] C. Arnoulet, M. C. Béné, F. Durrieu, J. Feuillard, C. Fossat, B. Husson, H. Jouault, M. Maynadié, Francis Lacombe, Four- and five-color flow cytometry analysis of leukocyte differentiation pathways in normal bone marrow: A reference document based on a systematic approach by the GTLLF and GEIL

[6] N. Rongeat, P. Brunel, JP. Gineys, D. Cremien, V. Couderc, P. Nérin, Wavelength encoding technique for particle analyses in hematology analyzer. *Optics Express*, Vol. 19 Issue 15, pp.14076-14082 (2011)

[7] M. Andreana, A. Bertrand, Y. Hernandez, P. Nerin and Col. Adjustable supercontinuum laser source with low coherence length and low timing jitter, Proceedings of SPIE, *the International Society for Optical Engineering A*. 2010, vol. 7714.

[8] PA. Champert, V. Couderc, P. Leproux, S. Février, V. Tombelaine, L. Labonté, P. Roy, C. Froehly, P. Nérin, White-light supercontinuum generation in normally dispersive optical fiber using original multi-wavelength pumping system. Optics Express, Vol. 12 Issue 19, pp.4366-4371 (2004)

[9] N. Rongeat, P. Leproux, V. Couderc, P. Brunel, S. Ledroit, D. Cremien,S. Hilaire, G. Huss, P. Nérin, Flow Cytometer Based on a Triggered Supercontiuum Laser Illumination, accepted for publication in Cytometry Part A, (2012).

Philippe NERIN
Research Director.
HORIBA ABX SAS
PhD.

Guest Forum

Investigation of Brake Wear Particles

Klaus AUGSBURG
Department Automotive Engineering
Technical University Ilmenau, Germany
Prof. Dr.-Ing.

Hannes SACHSE
Department Automotive Engineering
Technical University Ilmenau, Germany

Stefan KRISCHOK
Institute for Micro- und Nanotechnologies
Technical University of Ilmenau
Ph. D

Rüdiger HORN
Department Automotive Engineering
Technical University Ilmenau, Germany

Marcus RIEKER
Director Academic Affairs
HORIBA Europe GmbH
Prof. Dr. Sc. Hum

Uwe DIERKS
HORIBA Europe GmbH

Over the last years, brake dust has become a topic in different fields. The first research to brake dust after the abolishment of asbestos was done to understand the staining of the wheel. Since then, several attempts were made to understand the synthesis, composition and distribution of brake dust because of the growing awareness of environmental and health effects, for example with antimony and copper in the brake pads. The published measurements for the number and size of brake particles vary widely.[1-5] This is mainly because of the complex and susceptible characteristics of a brake system and the limited resolution of many measurement systems. With every change in temperature, braking speed, braking pressure, pad formulation, brake type and history of the friction partner, differences in the properties of brake dust particles will be recognizable. One approach to measure the size of the particles is to analyze a sample of collected brake dust in a scanning electron microscope. The handicap of this method is the characteristic of the debris to agglomerate and to deposit dependent on the particle size. A precise analysis of airborne particulate matter requires a more complex methodology which is known from the combustion engine particle measurement. HORIBA offers equipment to detect the particle size from ~2 nm up to 600 nm, for example the MEXA-2100SPCS*1 with a DMA*2 3081 classifier and a CPC*3 3776.

過去数年間に渡り，ブレーキダストは様々な分野で話題になっている。アスベストの使用廃止後，ブレーキダストの最初の研究はホイールを汚すことを理解するためであった。その時以降，例えばブレーキパッドのアンチモンと銅のような元素の環境，健康に対する影響への意識が高まり，ブレーキダストの合成，組成，および分散について理解するためにいくつかの試みが行われた。ブレーキ摩擦微粒子の数とサイズについて公表された測定値は非常にばらつきが大きい[1-5]。これは主としてブレーキシステムの複雑な動作条件と多くの測定装置での限定された分解能等の分析性能による。温度，ブレーキ速度，ブレーキ圧，パッド配合，ブレーキタイプ，および摩耗ペアの履歴が変化するたびに，ブレーキダストの特性の違いが見られる。微粒子のサイズの計測の1つの方法は，集められたブレーキダストの試料を走査型電子顕微鏡で分析することである。この方法の不利な点は，ダストが凝集し易い事と粒径により堆積する事が挙げられる。空中に浮遊する粒状物質の正確な分析には，燃焼機関の粒子測定で知られる，より複雑な方法が必要である。HORIBAは約2 nmから600 nmの粒子サイズまでを測定できる，例えばDMA*2 3081およびCPC*3 3776装置と共に用いるMexa-2100SPCS*1といった測定装置を提供している。

*1: Solid Particle Counter System（固形粒子数計測システム）
*2: Differential Mobility Analyzer（微分型移動度分析装置）
*3: Condensation Particle Counter（凝縮粒子カウンター）

Introduction

Beside combustion particles the wheel brake is the main emitter of nano-sized particles of passenger cars. The environmental problems of brake dust were reviewed in previous scientific works, e.g. “Method for visualization and handling of brake dust emissions” by Audi AG and TU Ilmenau, chassis.tech 2010 and “Brake dust measurement” by HORIBA Europe and TU Ilmenau at the Eurobrake 2012. Especially copper is known to harm the environment. Therefore the State of California introduced a law for the ban of copper in brake pads. Several papers proved a wide size distribution from a few nanometers to few micrometers. Another key fact to understand the effects of brake dust is the material composition of the emitted particles. The friction system of a brake is a complex structure which contains more than a dozen substances. With a combination of different measurement techniques the emissions can be characterized on a brake dynamometer. Brake dust from the surface of a wheel has been analyzed by SEM*4-EDX*5 to find out the physical properties and the chemical structure. Properties of the particles vary widely dependent on the braking temperature, rotating speed, braking pressure and the friction partners.

*4: Scanning Electron Microscope
*5: Energy Dispersive X-ray Spectroscopy

Scanning Electron Microscope

A quick method to measure the size of the particles is to generate images of collected brake dust in a scanning electron microscope. A drawback of this method is the characteristic of the debris to agglomerate and to deposit dependent on the particle size and their electric charge. If a sample of brake dust is collected on a sample holder it will never exactly have the size distribution of the airborne particles behind the brake caliper. Differences can also be demonstrated in the particle mass which is

deposited on a wheel fixed to a brake dynamometer setup and a wheel which lies next to the brake setup. This shows the effect of the electric charge.

This airborne fraction can be measured with available particle counters and particle size measuring devices. This equipment is often based on the light dispersion of laser light through the particles. Tests on a brake dynamometer were successful as the results were repeatable and it was detectable, that brake emissions increase exponentially with braking energy. The particle size and the number of particles for brake emissions show similar behavior compared to the emission of combustion engines. An additional parameter for the brake system is the substantial composition of the brake dust, considering that the material of a brake pad can contain a wide range of substances. An analysis with SEM-EDX shows the distribution of elements in the brake debris, while there is still no possibility to detect the accurate molecular formation. EDX showed an equal composition of the brake dust to the brake pads, only with a higher amount of iron, coming from the brake disc. The main ingredients of brake pads are e.g. iron, copper, silicon, aluminum, manganese and others. The exact chemical bond was also examined by XRD[*6], which can detect crystallographic materials. The outcome was a distribution with high rates of iron oxides, graphite, silicon oxide, copper, potassium oxide and corundum. In their different chemical compounds these ingredients are converted to micro and nanoparticles. In an accumulation process after the generation, particles tend to adhere together. The result is a mixture of all brake dust ingredients to small clustered particles. Current research aims towards an understanding of the exact composition of brake wear particles and their effects on mechanical components and human health.

The particle size and amount of particles depend on several factors, mostly the rotational speed of the disc and the applied brake pressure. First, the particle size was measured optically by collecting brake dust on a wheel surface and using a SEM subsequently. It was possible to compare several brake scenarios by the amount of brake dust on the surface as well as the method offered an estimation of the particle size. (Figure 1)

*6: X-Ray Diffraction

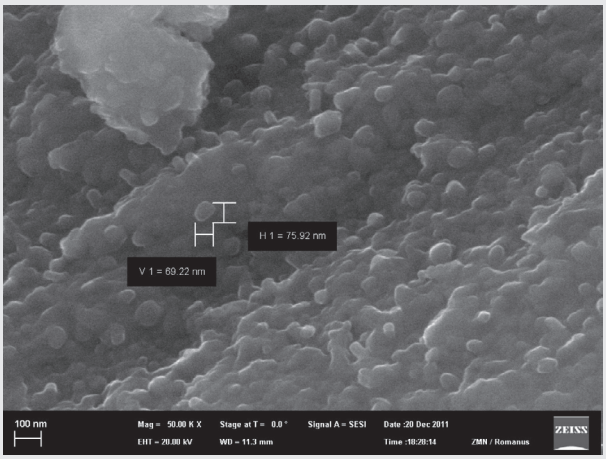

Figure 1 SEM Image of collected Brake Dust

HORIBA Solid Particle Counter System

Previous investigations with the SEM showed that simple systems for particle detection would not be sufficient to characterize the amount and size distribution of brake dust.

The brake dust can be collected with a HORIBA SPCS directly after the caliper and goes through a heated tube to the analyzer unit. (Figure 2, Figure 3) Result is a reliable size distribution for airborne brake dust particles. A drawback to the results is the minimal measurement time of 120 seconds for correct results. This requires a

Figure 2 HORIBA SPCS

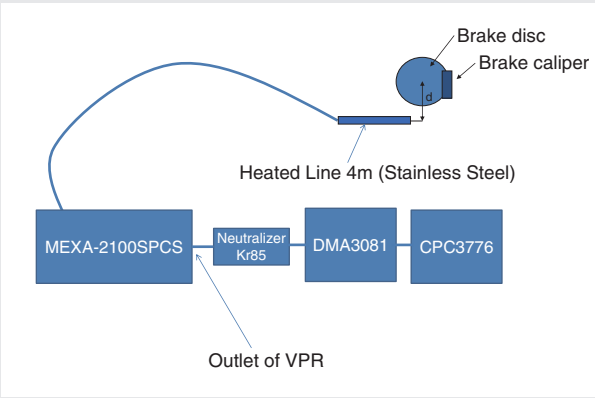

Figure 3 Schematic Measurement setup SMPS*7

long brake-on time in drag mode to generate a constant particle flow which is limited representative for a usual braking scenario. A difficulty for particle size measurement is the complex behavior of the debris. It runs through several processes, in which the particles agglomerate and condensate:

Emission → Transport → Transformation → Immission → Deposition[8]

This is what makes it complicated to get reliable numbers for a size distribution. The analysis with the HORIBA SMPS (Figure 4) showed that brake dust particles appear in a size range similar to diesel engine exhaust. So the size range of diesel particles will mostly be covered by the wider size range of the brake wear particles except for the smallest diesel fraction. (Figure 5) The measurements took place on a brake dynamometer at different speeds, brake pressures and cooling air speeds. In previous measurements with CPCs it was shown that the amount of particles is strongly connected to the braking energy. Compared to a highway braking scenario with a deceleration of 0.4 g and a change in speed of 150 km/h to 80 km/h, a city braking scenario with 0.25 g from 50 km/h to zero generates less than 5% of the brake wear debris weight.

For future measurements, smaller size measurement ranges would allow shorter brake activation and also higher brake pressure. These experiments with specific measurement systems have already showed that the airborne particle size is smaller than the assumed sizes from the research with scanning electron microscope. There were also previous attempts for measuring the particle size with specialized devices like ELPI*8 oder MOUDI*9 impactors. This research was done by Paul Sanders at Ford Motor Co. In his publications he describes size and mass measurements of brake wear particles from different pad qualities. One of his conclusions is particle number peaks for a size under 1 µm.[6], [7]

*7: Scanning Mobility Particle Sizer
*8: Electrical Low Pressure Impactor
*9: Micro-Orifice Uniform Deposit Impactor

Particle Image Velocimetry

A Particle Image Velocimetry (PIV) system is used to visualize the particulate matter. This allows a snapshot view of the emitted particle during the on-brake scenario. This offers an impression of the amount of emitted particles and how they move. PIV requires at least one camera and a triggered laser which produces a highlighted area in the image plane of the camera. The strong laser light allows short exposure times for the camera, which is required to take a picture of fast moving particles.

The particle mass emitted during a braking scenario can be evaluated with the PIV and digital image processing. This information is helpful for particle measurement as it

Figure 4 SMPS System with DMA and CPC

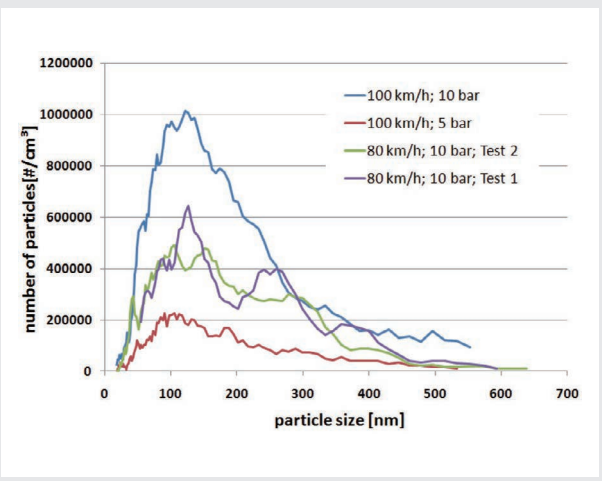

Figure 5 Size Distribution of Wear Particles

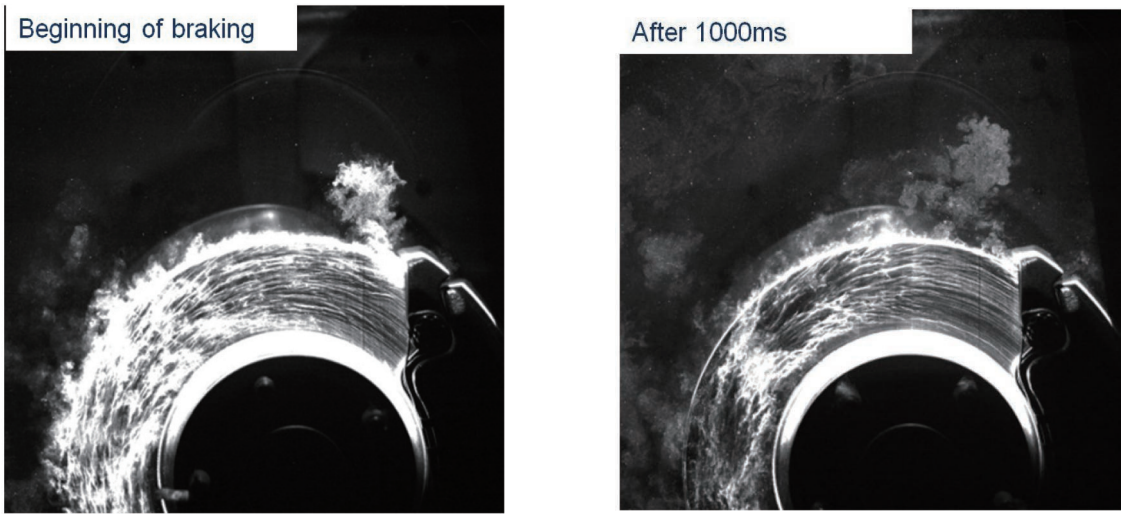

Figure 6 Particles around disc brake with laser sectioning method from PIV

will show where the probe tube of the SPCS has to be installed near the brake. (Figure 6)

CONCLUSION

With a combination of measurement techniques, the emissions of a friction brake were characterized on a brake dynamometer. Several previous publications proved a wide size distribution from a few nanometers to a few micrometers. Measurements with a HORIBA SMPS demonstrated that if a Gaussian distribution is assumed, the peak of the size distribution is below 250 nm. This is still larger than diesel exhaust particles but there is nevertheless a certain fraction of ultrafine particles. Simpler measurement systems mostly detect only particles larger than 300 nm so the main fraction of brake particles is not taken into account.

The friction system of a brake is a complex structure which contains more than a dozen substances. Properties of the particles vary widely and depend on the brake temperature, braking power and friction partners.

For future measurements there is room for improvement regarding the measuring time. To measure the size distribution with a SMPS takes usually more time than a single braking process. A drag braking setup was used for the present size distributions, so the rotational speed and the pressure were kept constant. This does not completely match with the properties of a real driving cycle braking scenario.

References

[1] "Toxic effects of brake wear particles on epithelial lung cells in vitro"; M. Gasser, M. Riediker, L. Mueller, A. Perrenoud, F. Blank, P. Gehr, B. Rothen-Rutishauser; Institute for Anatomy, Division of Histology, University of Bern, Bern, Switzerland; Institute for Work and Health; University of Lausanne and Geneva, Lausanne, Switzerland, 2009

[2] "Airborne Brake Wear Debris: Size Distributions, Composition, and a Comparison of Dynamometer and Vehicle Tests", P. Sanders et. al., Environ. *Sci. Technol*. 37, 2003

[3] "On Airborne Nano/Micro-sized Particles Released from Low-metallic Automotive Brakes", J. Kukutschováa, P. Moravecb, V. Tomášeka, V. Matějkaa, J. Smolíkb, J. Schwarzb, J. Seidlerováa, K. Šafářováca, V. Roubiceka, P. Filipd, Technical University Ostrava, Institute of Chemical Process Fundamentals ASCR Prag, Department of Experimental Physics Olomouc Czech Republic, SIU at Carbondale USA, 2010

[4] "Characteristics and morphology of wear particles from laboratory testing of disk brake materials", M. Mosleh, P.J. Blau, D. Dumitrescu, Howard University Washington, DC, USA, 2003

[5] "The Influence of Brake Wear Debris Chemical Proberties on Wheel Dust", T. Kikudome, Y. Yoshida, M. Unno, Hitachi Chemical Co., Ltd. Japan, *SAE* 2009-01-3020, 2009

[6] "Brake Dynamometer Measurement of Airborne Brake Wear Debris", P. Sanders et. al., *SAE Technical Paper Series* 2002-01-1280, 2002

[7] "Wheel Dust Measurement and Root Cause Assessment", P. Sanders et. al., *SAE Technical Paper Series* 2003-01-3341, 2003

[8] Bergmann, Maik: Entwicklung und Anwendung neuartiger Messverfahren zur Charakterisierung partikelförmiger Emissionen moderner Kraftfahrzeuge, Dissertation, Wuppertal, 2008

Guest Forum

Nitric Oxide Emissions from Soils
— Field and Laboratory Measurements with HORIBA's APNA

Cornelius OERTEL
Radiation protection officer
Chair for Geochemistry
and Earth System Science (Geoecology)
Institut of Mineralogy
Dipl.-Geoecol.

Kurt HERKLOTZ
Research group biology / ecology
TU Bergakademie Freiberg
Dipl.-Chem.

Jörg MATSCHULLAT
Chair for Geochemistry
and Earth System Science (Geoecology)
Institut of Mineralogy
Prof. Dr. Rer. Nat.

Nitrogen Oxides (NOx) are climate relevant trace gases in the atmosphere and are involved in acidic precipitation as well as in ozone formation and destruction. NOx originates from natural processes like thunderstorms and especially soil microbial activity next to anthropogenic emissions (mainly combustion processes). The gases play a crucial role in soil-atmosphere feedback processes. Our research aims to investigate NOx-emissions from soils under different land use, geographical and meteorological conditions. Such emissions could be quantified in both field and laboratory experiments with a closed static chamber in combination with HORIBA's NOx-analyser APNA-360. The instrument showed its ability to reliably measure nitrogen oxide soil emissions.

窒素酸化物(NOx)は，酸性雨やオゾンの形成と破壊に関わる重要な大気中の微量ガスである。NOxは人為的な排気ガス(主として燃焼過程から)で大気に放出され，その他には雷雨のような自然過程や，特に土壌中微生物活動が原因となって発生する。これらのガスは，土壌-大気のガス成分の循環に重要な役割を果たす。我々の研究は，様々な利用方法，地理的条件，および気象条件下での土地のNOx排出を調査することを目的としている。このような土壌からの放出は，HORIBAのNOx分析器APNA-360を使った閉鎖系によるフィールドおよび試験室両方での実験により定量化が可能である。この測定装置は土壌からの窒素酸化物放出を確実に測定できることを示した。

Introduction

Nitric Oxide (NOx) emissions play an important role in atmospheric sciences. They contribute to acidic precipitation, global warming, ozone formation and destruction.[1] Next to anthropogenic sources such as the combustion of fossil fuels, natural NO-emissions from soils are very important with a global annual rate of about

13–21 Tg N a^{-1}.[2] Due to the high reactivity of NO, related soil emissions are kept within the troposphere; leading to a short atmospheric life time.[3]

NO-emissions from soils are basically regulated by microbial denitrification and nitrification. NO from denitrification is negligible compared with the produced rate from nitrification.[4] Important parameters, further controlling NO soil emissions, are soil humidity, soil temperature and nutrient availability. Since nitrification is governed by aerobic microbes, soils with low Water-Filled Pore Space (WFPS) show higher NO-emissions and increasing temperatures also lead to higher emissions.[5] To determine NO-soil-emissions in the field, mostly "closed dynamic chambers" or "closed static chambers" are used. These methods can measure hourly emission values.[6] Laboratory experiments have been performed next to field experiments to analyse NO-emissions from soils.[7]

We combined field determinations with laboratory experiments. In the field, emissions from different soils under ambient conditions were analysed. The same soils as in the field determinations were used for laboratory experiments. The key objective was to better understand the behaviour of soil emissions under different temperatures as a contribution to regional climate change research. For this study, we used HORIBA's APNA 360 generation in combination with a closed static chamber system. This report provides some important results from soil NO-emission measurements and details about the measurement set up with APNA-analysers.

Materials and Methods

Site Description

The experimental field sites were situated on grassland and in a spruce forest in Saxony, central eastern Germany. The grassland is part of the campus of TU Bergakademie Freiberg in the Erzgebirge foreland (397 m a.s.l.; coordinates: 50°55'30"N, 13°19'52"E; loamy brown soil; avg. annual temperature 7.7 °C; avg. annual precipitation 764 mm a^{-1}, 1961–1990 DWD). The spruce forest site lies close to Oberbärenburg in the upper Erzgebirge on the atmospheric and forest ecosystem research station of TU Bergakademie Freiberg and TU Dresden (740 m a.s.l.; coordinates: 50°47'16"N, 13°43'22"E; loamy podsol; avg. annual temperature 5.5 °C; avg. annual precipitation 996 mm a^{-1}). This site lies about 30 km southeast from the grassland site. The vegetation is dominated by Norway spruce (*Picea abies*). Due to their dense stand, direct sunlight is limited and undergrowth missing. Soil samples for the laboratory experiments were taken at both sites and additionally at an agricultural site north of Freiberg (369 m a.s.l.; coordinates: 50°56'25"N, 13°19'42"E; loamy brown soil).

Experimental Setup

Field experiments

To sample NO emitted by soil, we use acrylic glass chambers with variable volumes, which are installed on the soil. To measure meteorological parameters and to control the influence of the chamber system onto the soil, the chamber is equipped inside and on the outside with sensors for air temperature, air pressure and air humidity. Additionally, a CO_2-sensor (GMP 343, Vaisala, Finland) and sensors for soil temperature und soil humidity can be found inside the chamber (Figure 1). The chamber systems are connected via tubes to the NOx-analyser (HORIBA, model APNA 360, detection limit 2σ: 0.5 ppb_v, reproducibility: ± 1% F.S).

Accumulation time for the emitted gas was 10–30 minutes and was set to fit the measuring range of the NOx-analyser, the volume of the chamber system and the expected emission values. Air from the chamber was pumped into the NOx-analyser after each accumulation interval. Values were averaged, based on 1-minute intervals, over a total time of 5-minutes. Following each data acquisition series, ambient air was pumped into the chamber for five minutes to restore ambient conditions. Thereafter, a new accumulation phase started. Ambient NO-concentrations were determined during this accumulation phase. The measuring flux was rerouted with a commercial magnetic valve. The average value of this measurement was subtracted from the subsequent soil emission measurement.

Laboratory experiments

Laboratory experiments were performed in a climate chamber (VC 4034, Vötsch Industrietechnik, Germany) with soil temperature and air humidity regulation. Disturbed soil samples from the uppermost 10 cm of the soil profile were used for the analysis. The chamber system was placed inside and the NOx-spectrometer outside of the climate chamber. Gas tubes were run through an opening into the climate chamber to take air samples. Soil temperatures were adjusted in a range from ~ 0 to 60 °C, and temperatures increased in 5 K steps to measure emissions. Following each measurement,

Figure 1 Measuring Setup to Analyse NO-Emissions from Soils.[5]
1) pumps to restore ambient conditions in the chamber; 3) acrylic measuring chamber with 2) GMP 343 CO_2-sensor and 4) sensorbox; 5) sampling tube connected to 7) NOx-analyser; 6) magnetic valve to switch between sampling of ambient and chamber air

conditions in the chamber were restored. The NO-concentration value in the climate chamber was subtracted from the NO-value determined in the chamber system.

Results and Discussion

Field Measurements

Meadow

NO-emission values and air temperature values of the eight-day experimental period are shown in Figure 2(a). This period was characterized by zero precipitation and an average air temperature of 17.2 °C. The average NO-emission was 6.1 µg NO-N m^{-2} h^{-1}, with the highest values in the afternoon (maximum 18.3 µg NO-N m^{-2} h^{-1}). The lowest values occurred after midnight and in the early morning (minimum 2.0 µg NO-N m^{-2} h^{-1}). On the seventh day, air temperatures were low in comparison to previous days, and no NO-peak occurred. The following and last day delivered the highest air temperatures, but not the highest NO-emission values, since soil temperatures react delayed on air temperature changes. The highest daily average value occurred on the fourth day (7.6 µg NO-N m^{-2} h^{-1}), and the lowest average value (1.6 µg NO-N m^{-2} h^{-1}) on the second day.

Figure 2(a) shows that NO-emission-values are correlated with air temperature. The Spearman-correlation-coefficient (0.68) delivered a significant positive correlation (slightly exponential) between air temperature and NO-emission. High temperatures lead to high NO-soil emission-values. The relation between both factors was slightly exponential, since NO is produced mainly by nitrification – a temperature-dependent process. Since vegetation had been removed from the measuring plot, obtained NO-emission values are too high. This bias is due to higher warming of the naked soil and decrease of

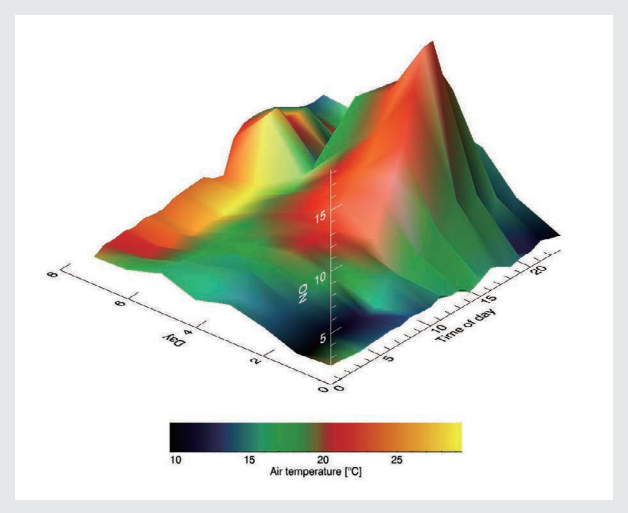

Figure 2(a) Grassland soil NO-degassing in an IDL surface-diagram. X-axis: time of day; Y-axis: measuring day; Z-axis: NO-degassing in µg NO-N m^{-2} h^{-1}. The surface colour of the 3D-object shows air temperature (field experiment)[5]

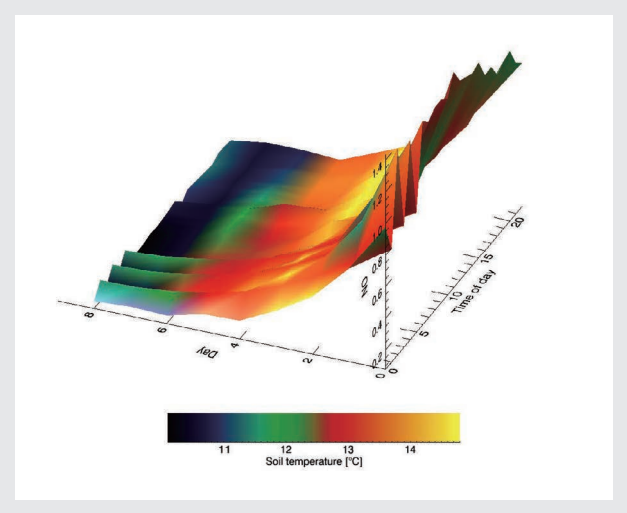

Figure 2(b) Forest soil NO-degassing in an IDL surface-diagram. X-axis: time of day; Y-axis: measuring day; Z-axis: NO-degassing in µg NO-N m^{-2} h^{-1}. The surface colour of the 3D-object shows soil temperature (field experiment)[5]

soil moisture. Both positively influence NO-emission, if soil moisture stays above 10%.[8]

HORIBA's APNA-360 worked very well for these measurements. All values were above the detection limit (~ 0.15 µg NO-N m^{-2} h^{-1}). The noise level of the system (~ 0.3 NO-N m^{-2} h^{-1}) was low enough to clearly distinguish between different emission values.

Forest

Data from the forest site (eight days) are presented in Figure 2(b). The average air temperature was 13.6 °C and the precipitation sum 72.5 mm. The largest precipitation amount (49.5 mm) occurred during the seventh day. No effect of this event onto NO-emissions was observed, since soil moisture already increased up to field capacity after a 28.5 mm precipitation event one day before the NO-measuring period. Soil temperatures decreased (ΔT~ 2 K) as of the first day, and so did NO-values. Minor changes of NO-emissions occurred during the day. These small changes were below the resolution of the detection system. Consequently, the highest NO-values were determined in the first days (maximum 1.5 µg NO-N m^{-2} h^{-1} and maximum average day-time value 1.3 µg NO-N m^{-2} h^{-1}). The minimum values occurred after a continuous decrease during the last days and were below the detection limit of the system, just like the lowest average day-time value. A significant positive correlation between NO-emissions and soil temperature (Spearman correlation 0.47) and a smaller one between NO-emissions and air temperature (Spearman correlation 0.22) were found. No significant correlation between NO-emissions and precipitation can be shown. The low soil temperature changes explain that no exponential correlation between NO-emissions and soil temperature could be found.

Different behaviour of NO-soil emissions at Oberbärenburg, as compared with the grassland measurements in Freiberg were caused by the dense vegetation cover at this site. Solar radiation is inhibited to penetrate to the soil and only small diurnal variations of the soil temperatures (1–2 K) could occur, leading to small daily variations in soil NO-emissions. The lower average temperatures accompanied with continuous small rain events in Oberbärenburg, explainable with the different orography, lead to the clearly lower daily average values of NO-emissions in comparison to the grassland in Freiberg. Very low NO-emissions at this spruce forest site could not be detected. This problem can be solved with longer accumulation times. However, the use of HORIBA's APNA-generation is suitable for spruce forest sites too, since German spruce forests deliver an average value of 1.3–608.9 µg NO-N m^{-2} h^{-1}.[9] This range can be easily detected with APNA measurement system.

Laboratory experiments

Disturbed soil samples from an agricultural site, a grassland and a forest were analysed in a climate chamber (Figure 3(a)-(c)). Strong exponential correlations with highly significant correlation R-squares (agricultural soil: 0.99; grassland: 0.93; forest: 0.95) were observed for all three soil types between NO-emissions and temperature and were much higher than for field measurements. In the agricultural soil, a temperature increase from 10 to 50 °C led to 15 times higher NO-emissions. A strong NO-emission increase started at a soil temperature of about 30

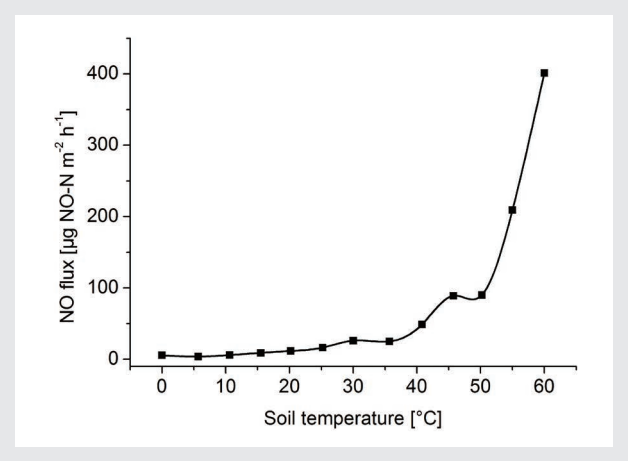

Figure 3(a) Agricultural soil NO-Eissions (climate chamber experiment)[5]

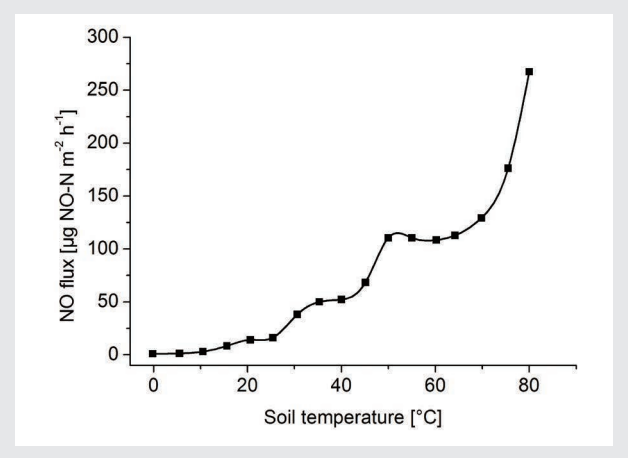

Figure 3(b) Grassland soil NO-Eissions (climate chamber experiment)[5]

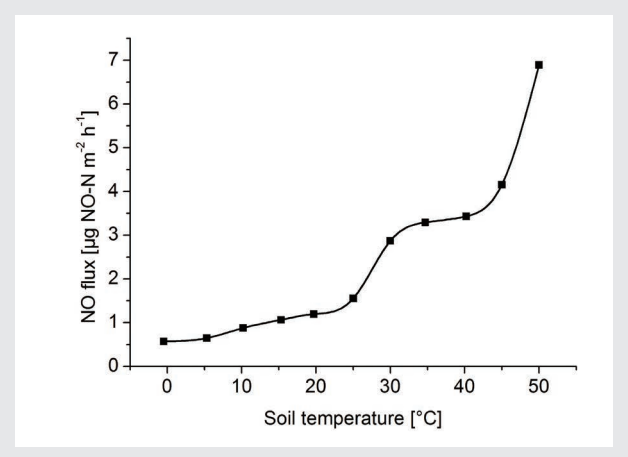

Figure 3(c) Forest soil NO-Eissions (climate chamber experiment)[5]

°C. Temperature changes below 30 °C had little influence on soil emission, in full agreement with the field experiments at Oberbärenburg. The exponential growth is interrupted at two points for each curve. There, NO-emissions do not follow the soil temperature increase. This can be explained by the nitrification driven by different groups of bacteria, which all have different temperature optima. The temperature optimum of five bacterial groups ends at a temperature of 30 °C.[10] A first plateau of NO-emission occurred at about 30 °C for all three samples. The remaining bacterial groups cannot increase soil emissions. Above soil temperatures of 40 °C, NO-emissions were strongly increasing again. This strong increase could be a result of chemo-denitrification. Urease activity is also supposed to be responsible for high NO-emission values at high soil temperatures. Urease decomposes urea to ammonium. Since ammonium is a precursor of nitrification, high urease activity can lead to higher NO-emissions. The temperature optimum of urease is about 70 °C. Accordingly more ammonium is formed at high soil temperatures.

The highest NO-emission was found at soil temperatures above 60 °C; an unrealistic value even for dark soils of this climate zone. The highest values occurred with the agricultural soil (maximum values above 400 µg NO-N m^{-2} h^{-1}), followed by the grassland. The lowest values were found for the forest soil. For a soil temperature of 40 °C, an average sequence emerged: agricultural soil 49 µg NO-N m^{-2} h^{-1}; grassland soil 14 µg NO-N m^{-2} h^{-1}, and forest soil 3 µg NO-N m^{-2} h^{-1}. Measured NO-values seem to overestimate the true soil response due to disturbed soil samples and low soil humidity in the climate chamber. In consequence, higher NO-emissions result from better aeration. NO-emission values for the agricultural soil should be most realistic, since plant cover is low and the management practices can lead to similarly disturbed soil. In general, measurements of NO-emissions under laboratory conditions seem to be more comparable with natural conditions in comparison with laboratory experiments for soil emissions of CO_2 or N_2O, since NO is mainly produced in the uppermost centimetres of the soil cover.[11] (Figure 3(d))

All NO-emission values, even for low soil temperatures, of the climate chamber measurements were above the detection limit of the APNA-measurement system. Since NO-values were generally higher than values for field experiments, the APNA-analyser is well suitable for these measurements. It has to be mentioned, that air samples have to be dried for the climate chamber measurements, since high temperature gradients can occur between climate chamber and outside, where the NOx-analyser is

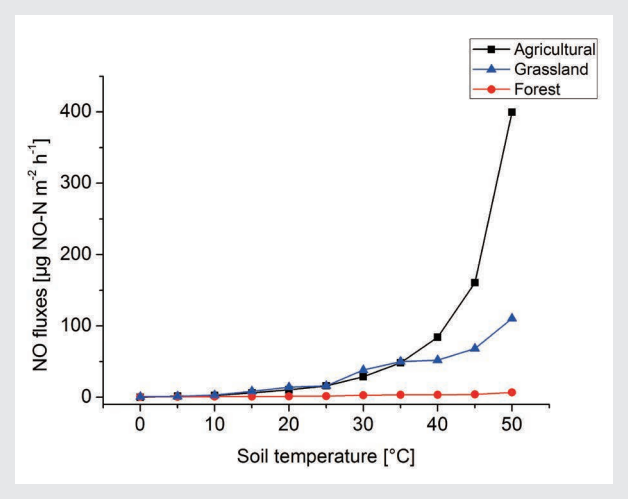

Figure 3(d) Comparison of the degassing responses from agricultural, forest and grassland soils from Figure 2(a)-(c) (climate chamber experiments) measured with APNA-360[5]

placed. Without drying, water may form through condensation and get into the NOx-analyser.

Conclusions

In combination with chamber systems HORIBA APNA-analysers are a sensitive tool to measure NO-emissions from soils. Excluding very low NO concentrations, which are not relevant for global budgets, the system could detect the soil emissions very well and has showed a fine cost-performance ratio. Further development of our automatic chamber systems will improve detection of NO-emissions from soils. Accordingly the quality of global and regional estimations of NO-emissions from soils could be further improved.

Acknowledgments

We thankfully acknowledge financial support of this project by the Air Liquide Foundation. The authors also wish to thank Prof. Gerhard Heide for generous access to his climate chamber.

References

[1] Kampfl G, Kristof K, Algaidi AA, Bayoumi Hamuda HEAF, Heltai G (2007) Study of NOx and CO_2 production of cultivated soil in closed microcosm experimental system. *Microchem* J 85 (1 Spec. issue): 31-38. doi:10.1016/j.microc.2006.05.003

[2] Butterbach-Bahl K, Kahl M, Mykhayliv L, Werner C, Kiese R, Li C (2008) A European-wide inventory of soil NO emissions using the biogeochemical models DNDC/forest DNDC. *Atmos Environ* 43: 1392-1402. doi:10.1016/j.atmosenv.2008.02.008

[3] Davidson EA, Kingerlee W (1997) A global inventory of nitric oxide emissions from soils. *Nutr Cycling Agroecosyst* 48 (1-2): 37-50. doi:10.1023/A:1009738715891

[4] Brümmer C, Brüggemann N, Butterbach-Bahl K, Falk U, Szarzynski J, Vielhauer K, Wassmann R, Papen H (2008) Soil-atmosphere exchange of N_2O and NO in near-natural savanna and agricultural land in Burkina Faso (W. Africa). *Ecosystems* 11 (4): 582-600. doi:10.1007/s10021-008-9144-1

[5] Oertel C, Herklotz K, Matschullat J, Zimmermann F (2011) Nitric oxide emissions from soils: a case study with temperate soils from Saxony, Germany. *Environ Earth Sci*. doi 10.1007/s12665-011-1456-3

[6] Abdalla M, Jones M, Ambus P, Williams M (2009) Emissions of nitrous oxide from Irish arable soils: effects of tillage and reduced N input. *Nutr Cycling Agroecosyst* 86 (1): 1-13. doi:10.1016/S0038-0717(00)00042-0

[7] Van Dijk SM, Gut A, Kirkman GA, Meixner FX, Andreae MO, Gomes BM (2002) Biogenic NO emissions from forest and pasture soils: Relating laboratory studies to field measurements. *J Geophys Res Atmos* 107 (20): 25-21-25-11. doi:10.1029/2001JD000358

[8] Ludwig J, Meixner FX, Vogel B, Förstner J (2001) Soil-air exchange of nitric oxide: An overview of processes, environmental factors, and modeling studies. Biogeochemistry 52 (3): 225-257. doi:10.1023/A:1006424330555

[9] Pilegaard K, Skiba U, Ambus P, Beier C, Brüggemann N, Butterbach-Bahl K, Dick J, Dorsey J, Duyzer J, Gallagher M, Gasche R, Horvath L, Kitzler B, Leip A, Pihlatie MK, Rosenkranz P, Seufert G, Vesala T, Westrate H, Zechmeister-Boltenstern S (2006) Factors controlling regional differences in forest soil emission of nitrogeNOxides (NO and N_2O). *Biogeosci* 3 (4): 651-661. doi:10.5194/bg-3-651-2006

[10] Coyne MS (1999) Soil Microbiology: An Exploratory Approach. Delmar Publishers, Albany, Bonn, Boston, Cincinnati

[11] Venterea RT, rolston DE, Cardon ZG (2005) Effects of soil moisture, physical, and chemical characteristics on abiotic nitric oxide production. *Nutr Cycl Agroecosys* 72 (1): 27-40. doi: 10.1007/s10705-004-7351-5

Guest Forum

Multiparameter Immunophenotyping by Flow Cytometry in Multiple Myeloma: Advantages for Diagnosis and Minimal Residual Disease Monitoring

Guilhem REQUIRAND
Institute of Research in Biotherapy,CHU Montpellier
INSERM, U1040

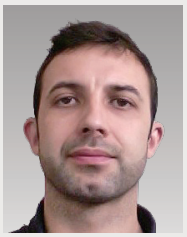

Jérôme MOREAUX
Institute of Research in Biotherapy
CHU Montpellier
INSERM, U1040

Anouk CARAUX
INSERM, U1040

Sébastien RAIMBAULT
Research Dept
HORIBA Medical

Bernard KLEIN
Institute of Research in Biotherapy,
CHU Montpellier
Université MONTPELLIER1,
UFR Médecine
INSERM, U1040

Multiple Myeloma (MM) is a B cell neoplasia characterized by the accumulation of malignant cells in the bone marrow. Immunophenotyping has become a critical tool in the management of hematological malignancies including Multiple Myeloma (MM) with an increasingly importance with diagnosis and monitoring of Minimal Residual Disease (MRD). Here, we review the advantages of Multiparameter Flow Cytometry (MFC) to distinguish normal and malignant plasma cells, for treatment response assessment, prognostic classification and treatment management.

多発性骨髄腫(Multiple Myeloma=MM)は，悪性細胞が骨髄に蓄積するB細胞の異常増殖である。免疫型検査は，微小残留性病変(MRD)の診断とモニタリングがますます重要になってきているの伴い，MRDなどの血液病理学的の管理における重要なツールとなった。ここで我々は，治療反応評価，予後分類および治療管理のために，正常と悪性の形質細胞を区別するマルチパラメータフローサイトメトリー(MFC)の利点について検討する。

Introduction

Multiple Myeloma (MM) is a Plasma Cell (PC) neoplasm characterized by the Accumulation of Malignant PCs (MMCs) within the Bone Marrow (BM). Numerous studies have pointed out the heterogeneity of both the phenotype (CD20, CD28, CD56, CD117) and chromosomal abnormalities of MMCs in association with patient outcome.[1-3] Evaluation of MM disease is based on a variety of laboratory techniques, including BM morphology and immunophenotyping, analysis of serum and urine M-component and free light chains, hematological and biochemical parameters, cytogenetics,[4] DNA ploidy, and measurement of PC proliferative activity. These investigations are important to support the diagnosis of MM, to guide the therapy, to provide prognostic information, and to monitor treatment efficacy.[4] Many studies have shown high clinical sensitivity of flow cytometry in the analysis of MMCs when compared to conventional morphology.[5-7] This article combines a review of the literature concerning the advantages of Multiparameter Flow Cytometry (MFC) for diagnosis and Minimal Residual Disease (MRD) monitoring in MM as well as practical guidelines.

Role of Multiparameter Flow Cytometry in Multiple Myeloma

In MM, the use of MFC in clinical diagnostic laboratories becomes mandatory for the diagnosis and monitoring of the disease. MFC presents several advantages for the differential diagnosis between Monoclonal Gammopathy of Undetermined Significance (MGUS), MM and reactive conditions, the monitoring of MM patients, the assessment of prognostic markers expression, the detection of MRD after treatment and the determination of a stringent Complete Response (CR).[8], [9] MFC allows the simultaneous assessment of MM markers on rare populations of PCs as well as determination of the monoclonality. The initial studies utilized four-color MFC with a limited sensitivity.[10] More recently MFC using six-color analysis (including CD138/CD38/CD45/CD19/cytoplasmic Igκ/cytoplasmic Igλ) enables increased sensitivity, has a lower requirement of samples for detection of MMC, and ensures routine diagnosis in MM.[11], [12]

Delineation of normal and malignant plasma cells

MMCs express various markers aberrantly, compared to Normal PCs (N-PCs), and a combination of several markers is necessary to delineate optimally MMCs from N-PCs. The antigens used for detecting N-PCs and MMCs include CD19, CD56, CD20, CD117, CD28, CD33, CD27, CD81, CD31, CD39, CD40 and CD44.[5]

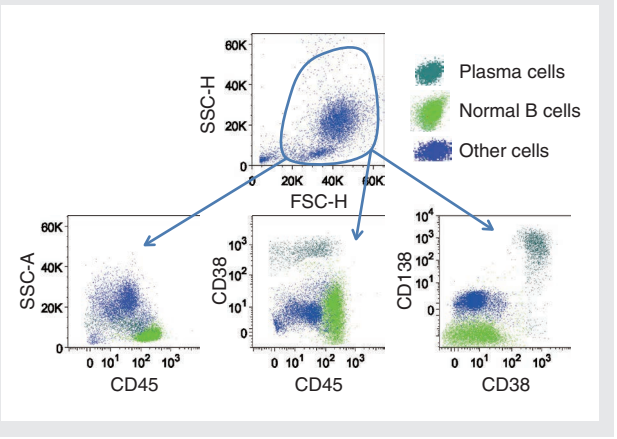

Figure 1 Primary gating strategy for plasma cells analysis
We used a combination CD38, CD138, CD45 and light scatter characteristic to identify total plasma cells ($CD38^{high}$ $CD138^{high}$ $CD45^{+}$).

The European Myeloma Network has recommended using CD38, CD138 and CD45 together with CD19 and CD56 to identify MMCs.[5] Primary gating strategy to identify PCs uses a combination of CD38, CD138, CD45 and light scatter characteristic (Figure 1). Contrary to N-PCs, MMCs from a majority of patients do not express CD19 and CD27, express at low level CD45 and express aberrantly CD56, CD28, CD81 and CD200 (Figure 2(A) and 2(B)).

Increased expression of CD20 and CD117 was also reported in a small proportion of patients (Table 1). Given these antigens are not specific to plasma cells and can yield to false plasma cell identification in case of low counts, we have developed recently a methodology to identify plasma cells based on their unique biological function: the production of immunoglobulins.[13], [14] Cells are first labelled for membrane antigens with fluorochrome-conjugated antibodies, then permeabilized and labelled with fluorochrome-conjugated kappa or lambda Ig light chain antibodies. As shown in Figure 2, plasma cells display a 10-fold higher fluorescence intensity for anti-Ig light chain antibodies than B lymphocytes (Figure. 2(A)). Using the MMC specific markers discussed above and the monoclonality of MMCs, producing either κ or λ Ig light chains, this methodology is powerful to discriminate MMCs from N-PCs, even in cases where few aberrant markers are expressed by MMCs (Figure 2(B) and 3).

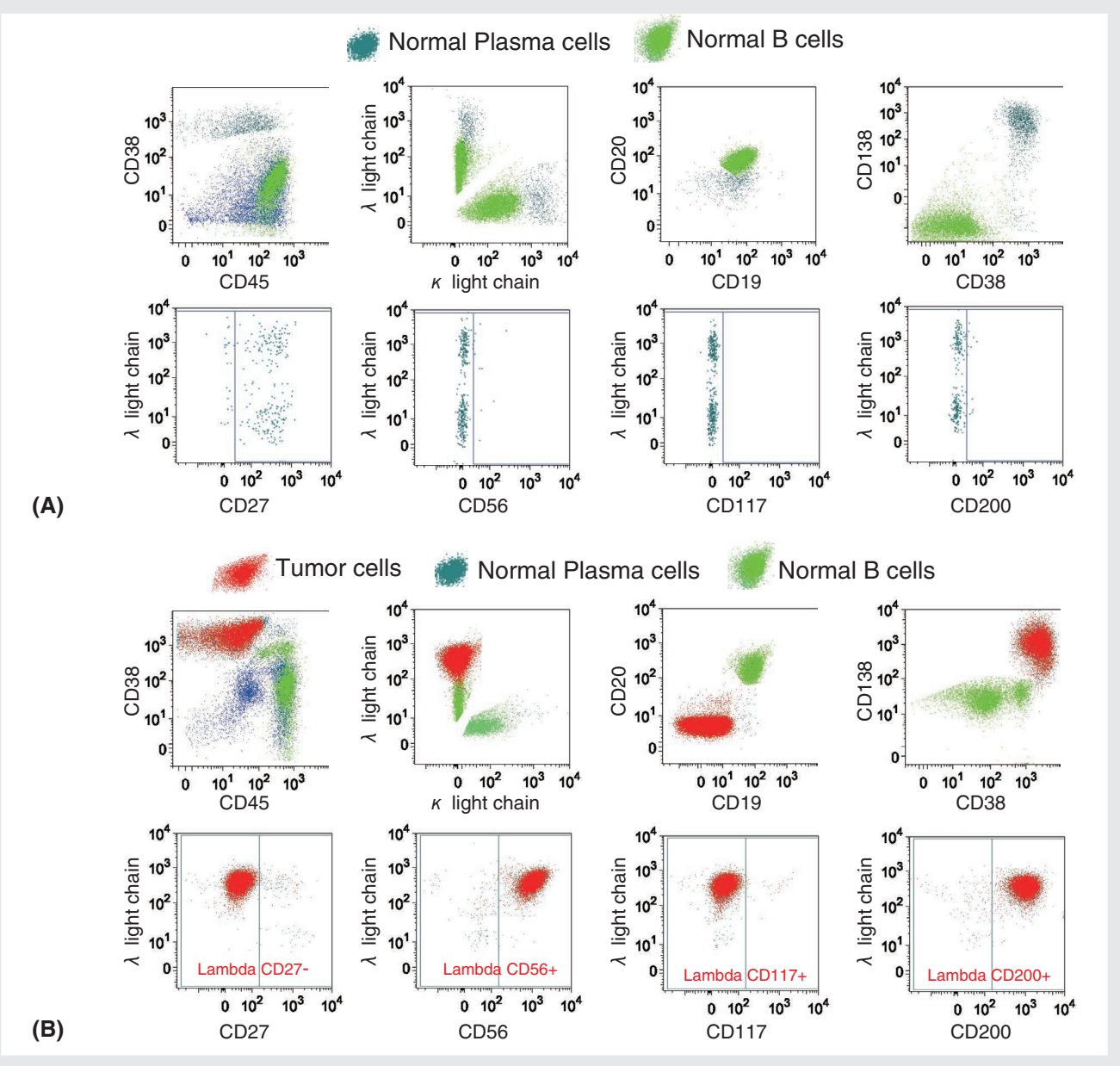

Figure 2 Immunophenotyping of normal and malignant plasma cells

(A) Cells phenotype was analyzed by gating on $CD38^{++}$, $CD45^{+}$ plasma cells (normal plasma cells in dark blue). Dotplots show FACS labeling of cytoplasmic kappa and lambda light chains, of CD19, CD20, CD138, CD27, CD56, CD117 and CD200. Normal polyclonal plasma cells are $CD38^{high}$, $CD138^{+}$, $CD45^{+}$, $CD27^{+}$, $CD19^{+}$, $CD20^{-}$, $CD56^{-}$, $CD117^{-}$ and $CD200^{-}$.

(B) Cells phenotype of malignant plasma cells was analyzed using the same gating strategy. In this patient, monoclonal (lambda light chain) malignant plasma cells are $CD38^{high}$, $CD45^{-}$, $CD19^{-}$, $CD20^{-}$, $CD138^{+}$, $CD27^{-}$, $CD56^{+}$, $CD117^{-}$ and $CD200^{+}$.

Table1 List most useful antigens for the detection of malignant plasma cells in multiple myeloma.[1], [2]* data obtained in our cohort of 70 MM patients at diagnosis.

Antigen	Expression profile on normal plasma cells	Abnormal myeloma expression profile	Percentage of MM patients with abnormal expression	Necessity for diagnosis and minimal residual disease follow-up
CD200	Negative	Strongly positive	73%*	Critical
CD56	Negative	Strongly positive	73%*	Critical
CD19	Positive	Negative	95%	Critical
CD27	Positive	Negative	50-80%	Critical
CD117	Negative	Positive	28%	Recommended
CD81	Positive	Negative	45%	Recommended
CD20	Negative	Positive	20-30%	Recommended

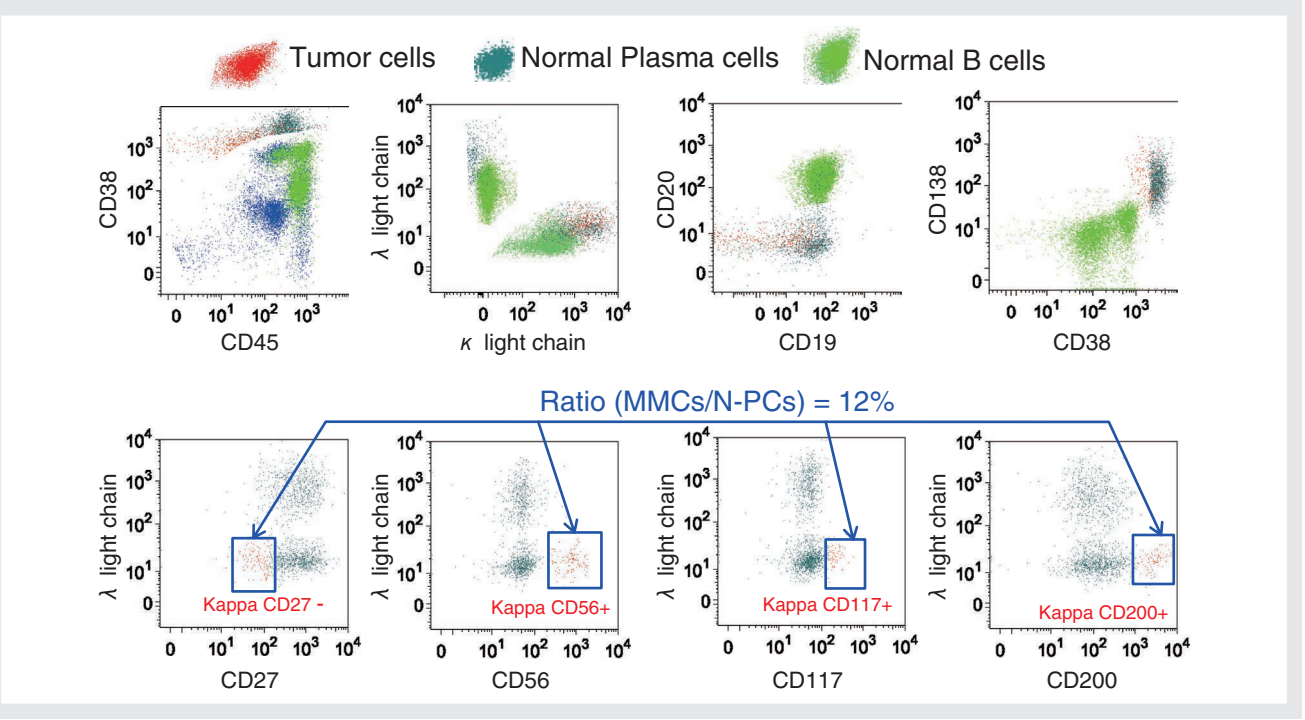

Figure 3 Detection of minimal residual disease
As previously described, malignant plasma cells were identified with the same gating strategy. In this example, we detect a small contingent of malignant plasma cells ($CD27^-$, $CD56^+$, $CD117^+$, $CD200^+$ expression with monoclonality kappa in this case) one year after allograft with a sensitivity 1/10000 (ratio: 1200 tumor cells /10000 total plasma cells in this case).

Prognostic Markers in Multiple Myeloma

CD56

CD56 (NCAM-Neural cell adhesion molecule) is a homophilic binding protein expressed on surface of neurons, glia, skeletal muscle and natural killer cells. It is aberrantly expressed on MMCs of 73% of patients, while N-PCs are negative. A poor prognosis was described to be associated with CD56 expression in previous studies including patients treated with conventional therapies. However, no prognostic value of CD56 expression was reported in patients treated with high-dose chemotherapy supported by Autologous Stem Cell Transplantation (ASCT). Modulation of CD56 expression may be involved in PCs homing since CD56 negative patients present a higher incidence of extramedullary disease. And, CD56 expression was reported to be inversely correlated with the presence of circulating MMCs.[15], [16]

CD45

CD45 is a high-molecular weight glycoprotein uniquely expressed on the surface of all leukocytes and their hematopoietic progenitors that plays a key role in lymphocyte activation.[17] In healthy individuals, CD45 is expressed on early PCs and decrease with maturation[18] while in MM patients, MMCs present a heterogeneous expression pattern with a mixture of CD45 negative and positive.[18], [19] In a study including 95 patients treated by High-Dose Chemotherapy (HDT) and ASCT, loss of CD45 expression at the surface of MMC was associated with poor survival.[20] It was reported that IL-6 is able to stimulate both $CD45^+$ and $CD45^-$ MMCs. Other growth factors including IGF-1, HGF, FGF and HBEGF stimulate the growth of $CD45^-$ MMCs.[21] More recently, Sprynski *et al.* reported an autocrine IGF-1 loop in $CD45^-$ MMCs promoting autonomous survival. At the opposite, $CD45^+$ MMCs could not survive without addition of myeloma growth factors.[22]

CD28

CD28 is a major costimulatory molecule on T cells. Its expression is aberrant in neoplastic PCs.[23] $CD28^+$ PCs are identified in 9% of patients with MGUS, 26% with newly-diagnosed MM, 59% with relapsing MM, 93% with extramedullary relapse and 100% with a secondary PCs leukemia.[24] CD28 could support the angiogenesis by the up-regulation of interleukine-8 gene transcription.[25] Whereas our group found no functional role for CD28 in MMCs [26] a recent study demonstrated CD28 is involved in interaction of MMCs and dendritic cells expressing CD80/CD86, which delivers a pro-survival signal to MMCs. This interaction induces the production of IL-6 and of the suppressive enzyme IDO by dendritic cells.[27]

CD27

CD27 is a member of tumor necrosis factor receptor superfamily found on most T-lymphocytes. CD27 expression is uniformly observed in N-PCs whereas loss of CD27 was reported in 45% of MM patients.[28], [5] And CD27 loss is associated with disease progression and shorter overall survival (OAS) in MM patients.[28], [29] Furthermore, CD27 expression is significantly lower on primary PCs leukemia compared to MMCs. And low CD27 expression correlates with plasmocytoma progression to MM.[30]

CD200

CD200 is type 1a transmembrane protein, related to the B7 family of costimulatory receptors, with immunosuppressive functions. CD200 was not expressed at the surface of N-PCs.[31], [4] We previously reported that patients with $CD200^{absent}$ MMCs have an increased event-free survival compared with patients with $CD200^{present}$ MMCs, after high-dose therapy (HDT) and stem cell transplantation.[31] These data were confirmed at protein level with a significant shorter EFS in $CD200^{+}$ patients compared to $CD200^{-}$ patients treated by HDT/ASCT (15 vs. 37 months).[32] Of note CD200 expression and International Staging System (ISS) remain independent prognostic factors for EFS in multivariate Cox proportional hazard regression model.[32]

Response Assessment and Minimal Residual Disease Follow-up

MFC has become a useful tool for MRD monitoring in MM.[33] The major reasons are that MFC could be used for MRD monitoring in 98% of the patients with a high sensitivity (detection of one MMCs among 10000 total PCs). The sensitivity is one Log less sensitive than quantitative PCR measuring MMC-specific mutated Ig genes, but it is easily applicable in almost all patients.[9]
Three months after ASCT, the detection of minimal residual MMCs is associated with shorter progression free survival (PFS).[8] The detection of MMCs by MFC in 27% patients with immunofixation negative complete response predicted a shorter PFS.[8] Furthermore, patients with at least 30% of N-PCs after treatment had a significantly longer PFS than patients with less than 30 % of N-PCs/total PCs.[34] Another retrospective study has shown that detection of more than 1.8% of MMCs prior ASCT significantly correlated with poorer PFS in MM patients.[35] More recently, Paiva *et al*. demonstrated that the MRD status 3 months after ASCT is the most powerful prognostic factor in MM patients.[36] Patients with ≤ 5% N-PCs among total bone marrow PCs had a significantly lower PFS (median 42 vs. 54 months) and OAS (median 89 months vs. not reached) than patients with > 5% N-PCs.[36] Another study on 685 newly-diagnosed patients treated by GEM 2000 protocol (HDT supported with ASCT) shows an impact of antigen expression on patient's survival. Based on CD28 and CD117 expression, MM patients with CD28 positive and CD117 negative expression had a high risk of progression and shorter survival.[2] In a study including MM newly diagnosed patients over 65 years treated according to the GEM05 PETHEMA/GEM trail, MRD monitoring by MFC is stringent to assess complete response than conventional criteria.[37] Patients with a negative immunofixation, but a positive MRD by MFC showed an early reappearance of M-component.[37] In a recent analysis combining detection of cytogenetics abnormalities by Fluorescence In Situ Hybridation (FISH) and MRD by MFC, Paiva *et al*. established a predictive score allowing delineation of three risk groups with significant different rates of disease progression in MM patients in CR after HDT/ASCT.[38] This score is also significantly predictive for OAS of patients in CR at day +100 after ASCT.[38]
All these studies have shown the advantages of MFC in the evaluation of the MRD in MM. The current challenge is the standardization of acquisition and analysis procedures[30]. The sensitivity of MFC to detect early relapse and for assessment of CR after treatment could be helpful for the follow-up of MM patients after allograft (Figure 3). MRD monitoring by MFC emerges as a promising tool for the management of treatment including donor lymphocyte infusion and/or novel agents such as Bortezomib or Immuno-Modulatory Drugs (IMiDs) in relapsed or refractory MM patients after allograft.

Assessment of Plasma Cell Proliferation

Proliferating PCs, i.e. the growth fraction of MM cells, have been evaluated by the detection of DNA synthesis using techniques including assessment of DNA content after flow cytometry or uptake of tritiated thymidine or Bromodeoxyuridine (BrdU).[40-42] The so-called PC Labelling Index (PCLI) has been shown to be a powerful and independent predictor of survival in MM[43] or flow-cytometric cell-cycle analysis using propidium iodide[44]

or assessment of Ki-67 expression.[45] Assessment of proliferation in MM is of special interest, as proliferating MMCs can be targeted by available treatments and upcoming therapeutic treatment options (e.g. aurora kinase inhibitors).[46] In our group, we combine MFC with BrdU incorporation to assess specifically the proliferation rate of MMCs at diagnosis and at the follow-up with a high sensitivity (Figure 4).

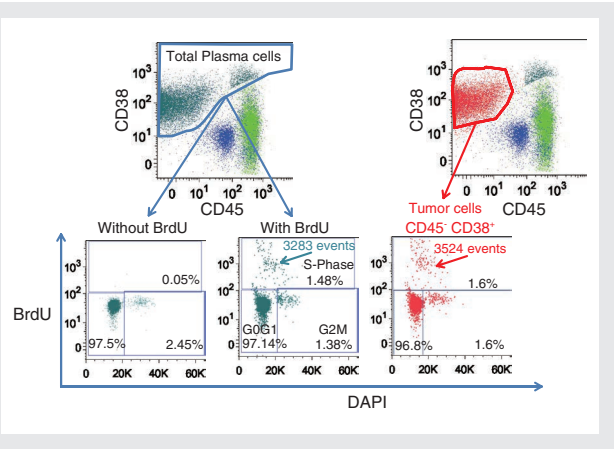

Figure 4 Assessment of plasma cell proliferation
Monoclonal plasma cell proliferation in MM patients was assessed using BrdU incorporation. Dotplots show FACS labeling of incorporated BrdU vs. DAPI (dye staining which stoichiometrically binds to DNA) in (A) total plasma cells ($CD138^+$, $CD38^{high}$, $CD45^+$ and $CD45^-$; S phase = 1.48%) and in (B) malignant plasma cells ($CD138^+$, $CD38^{++}$, $CD45^-$ in red color; S phase = 1.6%).

Individualized MRD monitoring including proliferation assessment combined with whole genome DNA copy number and gene expression profiling provide the major tools to predict the outcome of patients and to guide therapeutic management of MM patients, in particular to develop personalized medicine.

High Throughput, Highly Sensitive and Specific Automatic Flow Device for Rare Cells Detection and MRD Monitoring

Flow cytometry techniques are efficient for rare cells detection and therefore for MRD monitoring. However, MRD monitoring is a time-consuming task requiring expertized people for preparation, processing, and analysis, making this monitoring expensive.
HORIBA Medical, having a long experience in automation for hematology analyzers, can bring higher insight to deliver competitive and affordable solutions for automated specialized flow cytometry. Our company is involved in a five years collaborative project (Dat@diag) with IRB to develop prototype dedicated solutions for MRD monitoring. There are many technical challenges to be addressed, especially due to the high cell throughput required for measuring rare events.
These include leading edge technologies such as biophotonics based on supercontinuum laser source,[47] wavelength encoding as an alternative to compensation,[48] high speed acquisition systems and automatic multidimensionnal classification algorithms.[49]
This project is expected to provide fully automatic analyzers that would make MRD monitoring faster and less expensive, so that it can be widely used for Mutliple Myeloma patients.

References

[1] Fonseca, R., et al., Genetics and cytogenetics of multiple myeloma: a workshop report. *Cancer Res*, 2004. 64(4): p. 1546-58.
[2] Mateo, G., et al., Prognostic value of immunophenotyping in multiple myeloma: a study by the PETHEMA/GEM cooperative study groups on patients uniformly treated with high-dose therapy. *J Clin Oncol*, 2008. 26(16): p. 2737-44.
[3] Avet-Loiseau, H., et al., Genetic abnormalities and survival in multiple myeloma: the experience of the Intergroupe Francophone du Myelome. *Blood*, 2007. 109(8): p. 3489-95.
[4] Cannizzo, E., et al., Multiparameter immunophenotyping by flow cytometry in multiple myeloma: The diagnostic utility of defining ranges of normal antigenic expression in comparison to histology. *Cytometry B Clin Cytom*, 2010. 78(4): p. 231-8.
[5] Rawstron, A.C., et al., Report of the European Myeloma Network on multiparametric flow cytometry in multiple myeloma and related disorders. *Haematologica*, 2008. 93(3): p. 431-8.
[6] Kumar, S., T. Kimlinger, and W. Morice, Immunophenotyping in multiple myeloma and related plasma cell disorders. *Best Pract Res Clin Haematol*, 2010. 23(3): p. 433-51.
[7] Paiva, B., et al., Utility of flow cytometry immunophenotyping in multiple myeloma and other clonal plasma cell-related disorders. *Cytometry B Clin Cytom*, 2010. 78(4): p. 239-52.
[8] Rawstron, A.C., et al., Flow cytometric disease monitoring in multiple myeloma: the relationship between normal and neoplastic plasma cells predicts outcome after transplantation. *Blood*, 2002. 100(9): p. 3095-100.
[9] de Tute, R.M., et al., A single-tube six-colour flow cytometry screening assay for the detection of minimal residual disease in myeloma. *Leukemia*, 2007. 21(9): p. 2046-9.
[10] Marsee, D.K., B. Li, and D.M. Dorfman, Single tube, six-color flow cytometric analysis is a sensitive and cost-effective technique for assaying clonal plasma cells. *Am J Clin Pathol*, 2010. 133(5): p. 694-9.
[11] Morice, W.G., et al., Novel multi-parameter flow cytometry sensitively detects phenotypically distinct plasma cell subsets in plasma cell proliferative disorders. *Leukemia*, 2007. 21(9): p. 2043-6.
[12] Domingo, E., et al., Enhanced sensitivity of flow cytometry for routine assessment of minimal residual disease. *Haematologica*, 2010. 95(4): p. 691-2.
[13] Caraux, A., et al., Circulating human B and plasma cells. Age-associated changes in counts and detailed characterization of circulating normal CD138- and CD138+ plasma cells. *Haematologica*, 2010. 95(6): p. 1016-20.
[14] Caraux, A., et al., Mobilization of plasma cells in healthy individuals treated with granulocyte colony-stimulating factor for haematopoietic stem cell collection. *Immunology*, 2011. 132(2): p. 266-72.

[15] Pellat-Deceunynck, C., et al., Adhesion molecules on human myeloma cells: significant changes in expression related to malignancy, tumor spreading, and immortalization. *Cancer Res*, 1995. 55(16): p. 3647-53.
[16] Dahl, I.M., et al., Differential expression of CD56 and CD44 in the evolution of extramedullary myeloma. *Br J Haematol*, 2002. 116(2): p. 273-7.
[17] Ledbetter, J.A., et al., CD45 regulates signal transduction and lymphocyte activation by specific association with receptor molecules on T or B cells. *Proc Natl Acad Sci U S A*, 1988. 85(22): p. 8628-32.
[18] Pellat-Deceunynck, C. and R. Bataille, Normal and malignant human plasma cells: proliferation, differentiation, and expansions in relation to CD45 expression. *Blood Cells Mol Dis*, 2004. 32(2): p. 293-301.
[19] Asosingh, K., et al., Multiple myeloma tumor progression in the 5T2MM murine model is a multistage and dynamic process of differentiation, proliferation, invasion, and apoptosis. *Blood*, 2003. 101(8): p. 3136-41.
[20] Moreau, P., et al., Patients with CD45 negative multiple myeloma receiving high-dose therapy have a shorter survival than those with CD45 positive multiple myeloma. *Haematologica*, 2004. 89(5): p. 547-51.
[21] Collette, M., et al., Crucial role of phosphatase CD45 in determining signaling and proliferation of human myeloma cells. *Eur Cytokine Netw*, 2007. 18(3): p. 120-6.
[22] Sprynski, A.C., et al., The role of IGF-1 as a major growth factor for myeloma cell lines and the prognostic relevance of the expression of its receptor. *Blood*, 2009. 113(19): p. 4614-26.
[23] Pellat-Deceunynck, C., et al., Expression of CD28 and CD40 in human myeloma cells: a comparative study with normal plasma cells. *Blood*, 1994. 84(8): p. 2597-603.
[24] Robillard, N., et al., CD28, a marker associated with tumoral expansion in multiple myeloma. *Clin Cancer Res*, 1998. 4(6): p. 1521-6.
[25] Shapiro, V.S., M.N. Mollenauer, and A. Weiss, Endogenous CD28 expressed on myeloma cells up-regulates interleukin-8 production: implications for multiple myeloma progression. *Blood*, 2001. 98(1): p. 187-93.
[26] Zhang, X.G., et al., Malignant plasma cell lines express a functional CD28 molecule. *Leukemia*, 1998. 12(4): p. 610-8.
[27] Nair, J.R., et al., CD28 expressed on malignant plasma cells induces a prosurvival and immunosuppressive microenvironment. *J Immunol*, 2011. 187(3): p. 1243-53.
[28] Guikema JE, et al., CD27 is heterogeneously expressed in multiple myeloma: low CD27 expression in patients with high-risk disease. *Br J Haematol*., 2003. 121(1): p. 36-43.
[29] Moreau, P., et al., Lack of CD27 in myeloma delineates different presentation and outcome. *Br J Haematol*, 2006. 132(2): p. 168-70.
[30] Morgan, T.K., et al., Low CD27 expression in plasma cell dyscrasias correlates with high-risk disease: an immunohistochemical analysis. *Am J Clin Pathol*, 2006. 126(4): p. 545-51.
[31] Moreaux, J., et al., CD200 is a new prognostic factor in multiple myeloma. *Blood*, 2006. 108(13): p. 4194-7.
[32] Olteanu, H., et al., CD200 expression in plasma cell myeloma. *Br J Haematol*, 2011. 153(3): p. 408-11.
[33] Rawstron, A.C., et al., Circulating plasma cells in multiple myeloma: characterization and correlation with disease stage. *Br J Haematol*, 1997. 97(1): p. 46-55.
[34] San Miguel, J.F., et al., Immunophenotypic evaluation of the plasma cell compartment in multiple myeloma: a tool for comparing the efficacy of different treatment strategies and predicting outcome. *Blood*, 2002. 99(5): p. 1853-6.
[35] Liu, H., et al., Flow cytometric minimal residual disease monitoring in patients with multiple myeloma undergoing autologous stem cell transplantation: a retrospective study. *Leuk Lymphoma*, 2008. 49(2): p. 306-14.
[36] Paiva, B., et al., Multiparameter flow cytometric remission is the most relevant prognostic factor for multiple myeloma patients who undergo autologous stem cell transplantation. *Blood*, 2008. 112(10): p. 4017-23.
[37] Paiva, B., et al., Comparison of immunofixation, serum free light chain, and immunophenotyping for response evaluation and prognostication in multiple myeloma. *J Clin Oncol*, 2011. 29(12): p. 1627-33.
[38] Paiva, B., et al., High-risk cytogenetics and persistent minimal residual disease by multiparameter flow cytometry predict unsustained complete response after autologous stem cell transplantation in multiple myeloma. *Blood*, 2012. 119(3): p. 687-91.
[39] Hart, A.J., et al., Minimal Residual Disease in Myeloma: Are We There Yet? *Biol Blood Marrow Transplant*, 2012.
[40] Maurer, H.R., Potential pitfalls of [3H]thymidine techniques to measure cell proliferation. *Cell Tissue Kinet*, 1981. 14(2): p. 111-20.
[41] Neckers, L.M., et al., Significant non-S-phase DNA synthesis visualized by flow cytometry in activated and in malignant human lymphoid cells. *Exp Cell Res*, 1985. 156(2): p. 429-38.
[42] Falini, B., et al., Immunocytochemical evaluation of the percentage of proliferating cells in pathological bone marrow and peripheral blood samples with the Ki-67 and anti-bromo-deoxyuridine monoclonal antibodies. *Br J Haematol*, 1988. 69(3): p. 311-20.
[43] Greipp, P.R., et al., Value of beta 2-microglobulin level and plasma cell labeling indices as prognostic factors in patients with newly diagnosed myeloma. *Blood*, 1988. 72(1): p. 219-23.
[44] San Miguel, J.F., et al., A new staging system for multiple myeloma based on the number of S-phase plasma cells. *Blood*, 1995. 85(2): p. 448-55.
[45] Alexandrakis, M.G., et al., The relation between bone marrow angiogenesis and the proliferation index Ki-67 in multiple myeloma. *J Clin Pathol*, 2004. 57(8): p. 856-60.
[46] Hose, D., et al., Inhibition of aurora kinases for tailored risk-adapted treatment of multiple myeloma. *Blood*, 2009. 113(18): p. 4331-40.
[47] Rongeat, N., et al., Flow Cytometer Based on a Triggered Supercontiuum Laser Illumination. *Cytometry Part A*, 2012.
[48] Rongeat, N., et al., Wavelength encoding technique for particle analyses in hematology analyzer. *Opt Express*, 2011. 19(15): p. 14076-82.
[49] Raimbault, S., *Patent WO/2010/026328 – PCT/FR2009/051559*. 2008.

Guest Forum

High Performance Shafts for Engine and Powertrain Test Beds based on Glass or Carbon Fiber Polymer Composites.

Barbara HÖRING
The Institute of Leightweight Design
Darmstadt University of Technology

Helmut SCHÜRMANN
The Institute of Leightweight Design
Darmstadt University of Technology
Prof. Ph. D

Jürgen PITZ
HORIBA Europe GmbH
Ph. D

In engine, powertrain or e-motor test applications electrical dynamometers connected by shafts to the specimen have to simulate or replicate the load the specimen would see in the real world. Increasing demands on measurements signal quality, speed range and acceleration rates on one side and significant improvements in dynamometer performance on the other side caused the shaft connection becoming a key limiting factor. Therefore HORIBA Europe GmbH has started a research project together with the Institute of Lightweight Design of the TU Darmstadt with the support of public funding by the Hessen Agentur GmbH. The article gives a short introduction to the application and to fiber polymer composites and reveals some differences to metal constructions. Furthermore it discusses the main aspects of the carbon shaft design as well as the construction of the first prototype.

ダイナモメータは，試験対象のエンジン，パワートレイン，電気モーター等と連結軸で繋がり，実際の負荷をシミュレートし確実に再現しなければならない。一方で測定信号品質，速度範囲，および加速率に対する応答性の要求が高まり，他方ではダイナモメータの性能の著しい向上により連結軸が，負荷の再現を阻害する主要な制限要因となってきた。そのためホリバ・ヨーロッパ社(ドイツ)はダルムシュタット工科大学の軽量設計研究所と共に，Hessen Agentur GmbHからの公的資金の支援を得て研究プロジェクトを立ち上げた。本論文ではこの用途および繊維・ポリマー複合材料についての簡単な説明を行い，金属構造とのいくつかの相違について明らかにする。さらに，カーボン軸の設計ならびに最初のプロトタイプの構造に関する主要な点について述べる。

Application Requirements

When testing powertrain components the loads of the missing parts in the environment of a test bed compared to the real world vehicle have to be replicated or simulated. In case of an engine test bed an electrical dynamometer is connected to the flywheel of the unit under test by a shaft connection. The dynamometer has to simulate the load the engine would see in the real world. In case of a transmission test bed multiple dynamometers are connected by shafts to the input and outputs of the transmission. The unit under test, the dynamometers and the elastic shaft connections are forming a multiple mass-spring system with a number of natural frequencies with low damping. It cannot be avoided that these natural frequencies are excited by the firing frequency of the combustion engine, rotational frequencies of the dynamometer, not ideal balanced test bed components, pitch errors or just gear shifting. This will at least cause low quality measurements results of torque and speed signals, but may also result in unrealistic wear of the specimen or in the worst case will cause damage of the specimen and/or test bed components. When designing a test bed it is targeted to move the natural frequencies into "not dangerous" operating ranges by selecting the right shaft connections with dedicated spring rate and damping rate. For example engine test beds are designed in a way that the natural frequency is excited only in the range between starting speed and idle speed, which was not really a normal operating range. However with the introduction of start-stop systems starting and stopping the engine has become a regular test scenario as well. Additionally improvements in the dynamometer technology allow manufacturing of very low inertia dynamometers. These dynamometers provide an extended operating range of test beds with increased demands on measurement signal quality and the inertia of the existing shaft technology is no longer negligible compared to the dynamometer inertia. The shaft inertia is in the same range as the dynamometer inertia. E-motor and hybrid applications require testing at a high speed of more than 15000 rpm. At these speeds the allowed overhang masses are very limited and high weight shafts cannot be used.

Therefore it is a must to develop a new generation of shafts which meets the future requirements and allow HORIBA to remain competitive.

State of the art is using shafts made of steel, Titan or aluminum combined with rubber plates which define stiffness and damping. The rubber plates do have significant damping, but caused by the production process the variance of the stiffness is quite high. Target of the research project together with the University of Technology of Darmstadt is to develop shafts with defined damping and stiffness and at the same time low weight and inertia.

Key to meet the design targets was to use a carbon fiber reinforced shaft combined with a diaphragm coupling flange. (Figure 1) Carbon fiber reinforced shafts already exist on the market however together with steel couplings at the end which have to provide the flexibility. The weight of these shafts is therefore still quite high. The main targets of the project were:

- minimizing the weight by designing the flexible coupling as well out of fiber polymer composites
- defined low stiffness
- high damping rate

The project is supported by the Hessen Agentur GmbH an organization of the Hessen Government to promote the local economy.

Short introduction to fiber polymer composites

Fiber polymer composites provide very high stiffness and strength in relation to their mass density, which is known to be one of the main characteristics of lightweight

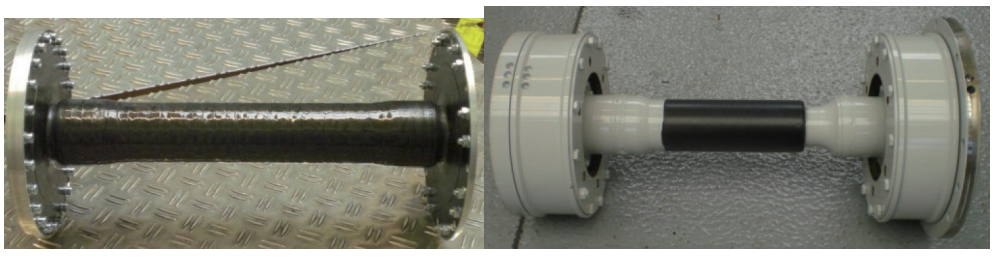

(a) (b)

Figure1 (a) Carbon Fiber Shaft and (b) Küsel Coupling

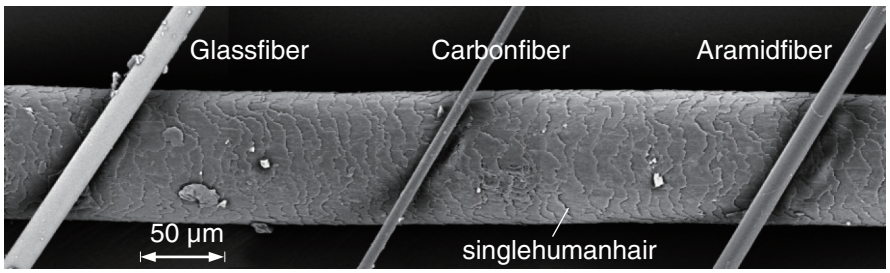

Figure 2 The commonly used fiber types in comparison to a single human hair[1]

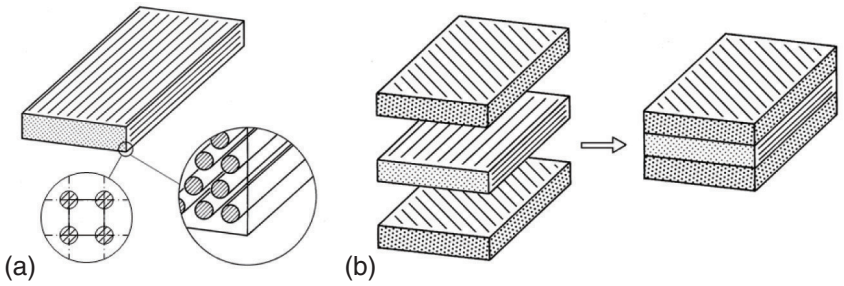

Figure 3 (a) Unidirectional layer (b) Multi-layer composite consisting of single layers[1]

construction materials. This is achieved by combining fibers and matrix in a way that yields material properties which the single components by themselves could not attain. Most commonly carbon or glass fibers are used glued together with an epoxy resin. (Figure 2)

The designer of fiber polymer composites has to handle much more parameters than the designer of metal parts, which makes design much more complex. For example: In a single layer or unidirectional layer (UD) the fibers are oriented parallel in one direction as shown in Figure 3(a). As a result the UD shows, in contrast to metals, orthotropic material properties. In this case there are 3 plains of symmetry that are orientated orthogonally to each other. Instead of 2 engineering constants - stiffness modulus (E) and Poisson's ratio (ν) as for isotropic metals, there are 9 engineering constants - 3 stiffness moduli (E_1, E_2, E_3), 3 shear moduli (G_{12}, G_{13}, G_{23} and 3 Poisson's ratios (ν_{12}, ν_{12}, ν_{23}) - needed to fully describe the fiber polymer constitutive law. Due to the fact that load cases are mostly multiaxial, the load-bearing fibers need to be arranged in different directions, which are quantified by angles. These can be achieved by stacking several UD-layers together building a multi-layer composite, called laminate (Figure 3(b)). These different angles represent another important design parameter.

Choosing different angles between the UD also varies the stiffness and strength of the composite. Hence, the outer strains of the laminate do not line up with the orthotropic coordinate system any longer; therefore 2 coordinate systems are used as shown in Figure 4. The x,y-coordinate system shows the laminate coordinate system which is fixed. The 1,2-coordinate system of the UD-layer is orientated in an angle α in relation to the laminate

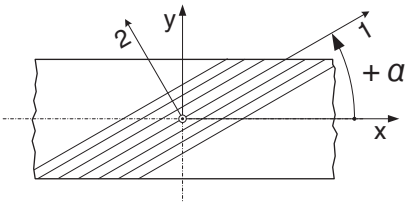

Figure 4 1,2-coordinate system of the UD-layer and x,y-coordinate system of the laminate[1]

coordinate system.
Mechanical properties and strains of the laminate can be calculated using the Classical Laminate Theory (CLT). For further details please see [2] and [3].

Shaft construction

Shaft construction includes several aspects that need to be considered and which can cause conflict of objectives:
1. Strength
2. Stiffness: torsion stiffness and bending stiffness
3. Buckling stability
4. Damping
5. Natural harmonics: torsion harmonics and bending harmonics

The following discusses each aspect of the previously mentioned objectives:

Strength: Highest composite strength can be achieved by placing the fibers in the main load case direction I, II. The load case of the shaft is torsional shear. Figure 5 shows an element under shear load. In this case the main axes lie in an angle of 45°. From this it is determined that using a ±45° ply is the best construction in terms of lightweight design.

Stiffness: The highest torsional stiffness can be reached by using a fiber angle of 45°. The more angles differ from 45° the lower the torsional stiffness will be. On the other hand a fiber orientation of 0° which is the axial direction of the shaft provides the highest bending stiffness.

Torsional buckling: Besides strength failure, shafts can also show buckling failure. To prevent a shaft from buckling a steep fiber angle around 65°-85° should be used in the outer layer.

Damping: Fibers are very stiff and therefore do not provide good damping properties. In contrast the matrix with its viscoelastic properties shows good damping properties. In order to attain damping in the laminate loads have to be guided through the matrix. This can be achieved by choosing fibers angles which are not too close to 45°.

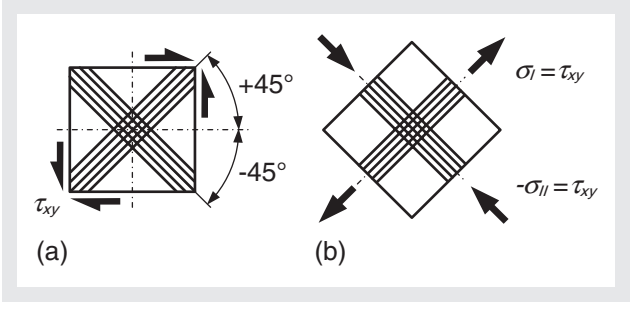

Figure 5 (a) Element under shear load
(b) Shear load transformed to the main axes[1]

Natural harmonic: Especially bending harmonics can limit the revolutions per minute. Therefore it is important to provide sufficient bending stiffness.

Taking all the above mentioned aspects into consideration the optimal construction of the carbon shaft turns out to be as shown in Table 1. Fiber angles differ from 45° to provide damping and low torsional stiffness. The layer with a 15° angle produces bending stiffness and the layer with 65° yields a high buckling moment.

Table 1 Carbon fiber shaft laminate design and lay up

Layer thickness	Fiber angle
0.8 mm	±65°
1.0 mm	±15°
0.8 mm	±65°

The shaft is connected by a carbon fiber diaphragm coupling to the engine and the dynamometer. The diaphragm design is based on specific fiber arrangement which allows the diaphragm to be flexible in axial direction as well as angular movement. Table 2 summarizes the result of the shaft including diaphragm and aluminum adapters for centering on the engine and the dynamometer. Weight and inertia are about 10 times lower as conventional steel shafts.

Table 2 Results in Summery

Parameter	Value
max. torsional impact moment M_{max}	2400 Nm
torsional failure moment M_F	3000 Nm
axial movement U	1.2 mm for 20 kg
	1.8 mm for 40 kg
crit. revolution per minute n_{crit}	> 12000 rpm
torsional stiffness c_T	13723 Nm/rad
mass m	2030 g

Status

The first prototype based on this design was manufactured and tested in 2011 (Figure 6). Based on the results an improved 2nd generation was designed and manufactured. Testing is still in progress.

Especially the design of the diaphragm has turned out to be critical as there is only a small window which provides sufficient strength on one side and elasticity to

Figure 6 Handover of the carbon shaft

compensate misalignment and axial movement on the other side. Furthermore other constructions for optimized damping properties in the shaft are in the planning process. It can be also imagined instead of running the shaft supercritical to increase torsional stiffness in a way which allows having it work subcritical. In this case the shaft does not go through resonance.

References

[1] SCHÜRMANN, Helmut: Konstruieren mit Faser-Kunststoff-Verbunden. Berlin Heidelberg New-York: Springer Verlag, 2007

[2] CHAWLA, Krishan Kumar: Composite Materials: Science and Engineering. New York: Springer Verlag, 1987

[3] PHILLIPS, Leslie N: Design with Advanced Composite Materials. London: The Design Council, 1989

Feature Article

— Malaria Infection Diagnostic Tests —
Predictive Flags in Hematology Analyzers and Quantification of Parasitized Red Blood Cells.

Manuela PASTORE, Sylvie VERIAC, Laurence CHAUVET, Alexandra URANKAR, Sylvain LEDROIT, Patrick BRUNEL, Sébastien LEGRAS, Christophe DUROUX, *Veronique SINOU, *Daniel PARZY

We present here the advances that HORIBA Medical R&D implemented in its hematology analyzers to progress against malaria. On one hand we describe the utilization of the Microsemi CRP for the screening of novel malaria infections in the field thanks to the combination of platelet count and CRP measure. On the other hand we present the application of DNA staining technology integrated into an ABX Pentra 60 derivative system for the precise measure of parasitemia. Based on HORIBA Medical reagent specificity, the simultaneous use of two fluorochromes was adapted to direct dilution and automation. This analytic method allows enumeration of parasitized red blood cells.

Introduction

Malaria represents a global health problem, causing disease and death in several tropical and subtropical areas: there are still 106 countries where the disease is endemic according to the WHO 2011 Report.[1]
Malaria is a protozoan infection of erythrocytes caused by five species of the genus *Plasmodium* (*P. falciparum*, *P. vivax*, *P. ovale*, *P. malariae*, and *P. knowlesi*). Two are most common. *Plasmodium falciparum*, present globally but mainly in Africa and Asia, is the most aggressive species. *Plasmodium vivax*, ranges widely throughout Asia, Africa, the Middle East, Oceania, the Americas and in Eastern Europe. The parasite is transmitted to human by the bite of infected *Anopheles* mosquitoes, but the infections can also occurs through the exposure to infected blood products (transfusion malaria) and by congenital transmission ,[2] (Figure 1).
The clinical symptoms are primarily due to schizont rupture and destruction of red blood cells; these allow the release of parasites and free hemoglobin into the bloodstream. Malaria can have gradual or a fulminant course with nonspecific symptoms that often remind of common viral infections: fever, chills, headaches, profuse perspiration. Other common and nonspecific symptoms include dizziness, malaise, myalgia, abdominal pain, nausea, vomiting, mild diarrhea, and dry cough. Alterations of hematological and biochemical parameters are well documented as well as inflammation and infection markers. However, as the clinical symptoms, laboratory findings are not really malaria specific and can be more or less predictive according to the context and if

* from the UMR-MD3 (Host-Parasite relationships, Pharmacology and Therapeutic), Aix-Marseille University- France.

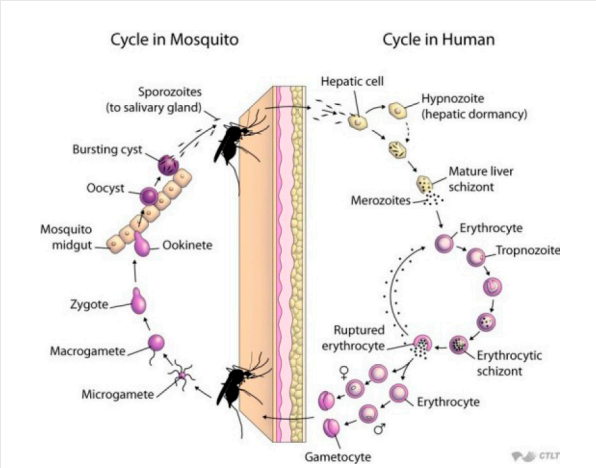

Figure 1 The Malaria Parasite Cycle in Mosquito and Human.
Johns Hopkins Bloomberg School of Public Health's OPENCOURSEWARE (OCW): http://ocw.jhsph.edu.

combined together.[3]

The gold standard for confirmation of malaria diagnosis remains light microscopy examination of thick or thin stained blood smear allowing identification and determination of parasitemia with a detection threshold of 4 to 100 parasites /µl. However, its accuracy depends on the quality of the reagents and microscope as well as the experience of the microscopist.[4] Rapid and accurate diagnosis of malaria is necessary to appropriate treatment and therapeutic follow-up of patients, thus preventing infection spread and drug resistance. A reliable detection method for malaria, incorporated into the routine Complete Blood Count (CBC), would be of great help to detect cases earlier and potentially reduce adverse outcomes related to malaria infection. In addition, these instruments would have the benefit of being already available even where diagnostic tools are limited.

We present here two different diagnostic approaches that HORIBA Medical developed to contribute to the diagnosis of malaria. In the first part of the article we present an application of current hematology analyzers for the screening of suspected patients. In the second part of the article we present a high sensitive method for detection and quantification of parasitized red blood cells.

Predictive Flags in Hematology Analyzers

Introduction and Purpose

Identification of peripheral blood biomarkers that could help identify malaria infection in the absence or with low patient peripheral parasitemia would be of great value since they would accelerate the process for definitive diagnosis, could minimize unnecessary drug treatment and thus improve patient outcomes. Following this reasoning, we wanted to verify the hematology analyzer performances in field conditions and to test if we could select some hematology parameters that would allow creating a flag to help the screening and diagnosis of malaria. Alterations of hematological and biochemical parameters are well documented in malaria. Thrombocytopenia is the most common laboratory abnormality, followed by hyper-bilirubinemia, anemia and elevated hepatic aminotransferase levels, whereas the leukocyte count may be normal or decreased.[3] Although anemia can be often found in malaria, it is not always a reliable marker. Indeed in countries where the social-economic situation is more difficult, the status of general health is also degraded and malnutrition and iron-deficiency are common. When malaria infection installs, anemia becomes more severe and consequently it becomes a good predictor for malaria. This applies to Africa, but for example it does not correspond to the reality of Vietnam. Here, the population has a better general health. Moreover, people consult the doctor as soon as fever arises and they do not wait to be in severe condition before asking medical help. Therefore the severe anemia caused by a concealed anemia and a subsequent malaria infection is less common, making this finding low sensitive for malaria screening and therefore useless. Inflammation and infection markers (erythro-sedimentation rate, C-Reactive Protein (CRP), procalcitonin are also commonly modified. However, as well as clinical symptoms, laboratory findings are not really malaria specific and can be more or less predictive according to the context and if combined together.[4], [6] In particular we decided to focus on combining hematology parameters and CRP to create a dedicated malaria alarm. For this purpose we planned a study in collaboration with the UMR-MD3 (Host-Parasite relationships, Pharmacology and Therapeutic), Aix-Marseille University- France.

Study Plan and Methods

A test campaign was conducted in endemic regions of Vietnam (Binh Phuoc in the South of Vietnam) for two months as part of a collaboration between the French and Vietnamese army health services. The Microsemi CRP and the ABX Pentra 60, both instruments from HORIBA Medical, were installed in a dispensary, a basic outpatient health facility providing primary healthcare services in a rural community. This location had double advantage (1) it offered a perfect setting to test the behavior of the hematology analyzers in rude utilization conditions for temperature and hygrometry and (2) it permitted

recruitment of blood samples directly in an endemic country at the time when propagation by the mosquitos is most frequent. A total of 119 whole blood specimens were collected from patients presenting with fever at the dispensary and after they had given their informed consent. All samples were tested in parallel on the ABX Pentra 60, on the Microsemi CRP and compared with the microscopic examination on thick blood film stained with RAL555 (RAL DIAGNOSTICS, France), a fast acting variation of May-Grünwald Giemsa Staining.

Results and Conclusions

The first step was to verify the proper functioning of the instruments in these adverse environmental conditions. In particular all the analytical alarm flags that were triggered in the ABX Pentra 60 were identified and analyzed:
NOISE (informing about the presence of noise in certain count channels): 6 times.
LMNE-(meaning that the two counts of white cells performed by two distinct channels are not identical/in agreement): 5
LMNE+ (as for the previous, meaning that the two counts of white cells performed by two distinct channels are not identical/in agreement: 7.
A total of 14 (11.7%) specimens triggered one or multiple flags. There were no flag related to incorrect working conditions, proving that the instrument was not disturbed by the environmental situation of high temperature and hygrometry. Indeed those alarms didn't appear in series but they were triggered from time to time without any pattern. We consider that all generated alarms were related to the peculiar features of the specimens and not to the instability of the instrument.
The criteria for the selection of patients were the presence of fever and the fact that he/she had spent sometime in the forest. Among these patients, 61 (51.3%) were diagnosed with uncomplicated malaria by microscope-based analysis that was used as reference diagnostic method.
The hematology parameters obtained for each sample with the ABX Pentra 60 and the Microsemi CRP were analyzed in order to extrapolate those that would be discriminative for malaria diagnosis.
The two analyzers showed comparable results (data not shown).
The machines were used in normal working conditions (standard pathology ranges). However for post-analytical data treatment we considered the following thresholds on relevant parameters:
Platelet absolute count. Alarm threshold < $150 \times 10^3/mm^3$;
Neutrophil absolute count. Alarm threshold > $7.5 \times 10^3/mm^3$ and < $2 \times 10^3/mm^3$;
Lymphocyte absolute count. Alarm threshold > $4 \times 10^3/mm^3$ and < $1 \times 10^3/mm^3$;
Monocyte absolute count. Alarm threshold > $1 \times 10^3/mm^3$ and < $0.2 \times 10^3/mm^3$;
Eosinophil absolute count. Alarm threshold > $0.5 \times 10^3/mm^3$;
Basophil absolute count. Alarm threshold > $0.2 \times 10^3/mm^3$;
Hemoglobin concentration. Alarm threshold > 17 g/dL and < 11.5 g/dL;
C-reactive protein concentration. Alarm threshold > 16 mg/L.

The relationship between parasitemia and each of the above parameters was established from the calculation of Sensitivity, Specificity, Positive Predictive Value (PPV) and Negative Predictive Value (NPV) (Figure 2).

Out of 119 samples, only 19 samples were out of normal range for monocyte count, 8 for eosinophil count and 3 for the basophil count. Therefore these three parameters were not taken into account as potential candidates. Also neutrophils, lymphocyte and monocyte showed low sensitivity and therefore they were discarded as well. On the other side the platelets and the CRP presented a good sensitivity, but the specificity was not satisfactory. In order to improve the specificity the PLT and CRP alarm have been combined (Figure 2). When PLT (< $150 \times 10^3/mm^3$) and CRP (> 16 mg/L) were both altered we obtained an alarm with 79.8% of sensitivity and 76.9% of specificity, with a positive predictive value of 82% and a negative predictive value of 73.2%. The thresholds were selected in order to optimize the identification of malaria cases. In particular for the CRP, the limit was chosen in order to have guiding criteria for diagnosis of malaria which needs a rapid confirmation by a specific test. Indeed, the treatment of malaria access is an emergency treatment. These results suggest that a dedicated flag incorporated in a hematology analyzer triggered when both the PLT and CRP are out of range would be a reliable screening method allowing decrease of the time-lapse between early symptoms and definitive diagnosis, thus potentially reducing adverse outcomes related to malaria infections. Further studies should be planned to confirm these encouraging preliminary results.

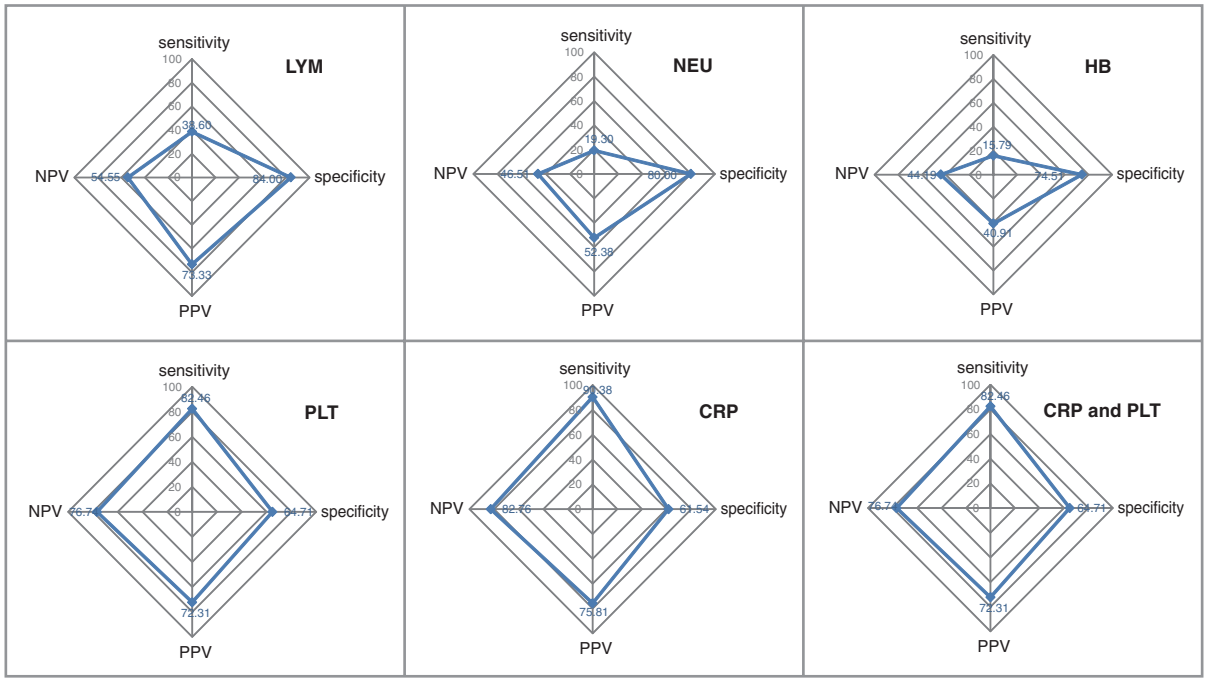

Figure 2 Sensitivity, Specificity, Positive Predictive Value (PPV), Negative Predictive Value (NPV) calculated on single relevant parameters and in the combination of CRP and PLT.

Detection and Quantification of Parasitized Red Blood Cells.

Background

Flow cytometry has a high rate cell counting potential that is associated with low levels fluorescence detection system. This technology has been shown to be the most appropriate, robust and flexible to detect low concentration and size of parasitic forms in peripheral blood. Flow cytometry is a technology for individual, quantitative and qualitative characterization of particles suspended into a liquid and based upon the analysis of optical or other physical signal, emitted by a particle crossing the light beam of a laser. Particle characteristics such as structure, size and shape are given by the intrinsic optical properties of the particle. Identification of main cellular structures or functions needs specific chemical tags like fluorescent probes. Efficiency of flow cytometry for detection, characterization, and counting of malaria parasites, reported by Shapiro et al,[7] dates back to the 1970s. Acridine orange for example was used for staining in an apparatus with 488 nm laser sources, whereas Hoechst dyes,[8] which are more DNA-selective, were preferred where UV excitation was available. The study done by Grimberg et al.[9] described the results obtained by two fluorescent probes for the differentiation of parasitized red blood cells (Hoescht 33342) from other nucleic acid elements present in blood (Thiazole orange).

The fluorescent dye Thiazole Orange (TO) allows the suppression of the main interference susceptible to reduce infected blood cells determination. As TO is present into some HORIBA Medical reagents*, the hematology analyzer fluorescent technology already proper to HORIBA Medical could be integrated efficiently into a malaria diagnosis automatic procedure.

*(*ex.: Fluocyte ™ dedicated to reticulocyte determination of the HORIBA Medical Pentra DX120 Hematology system)*

Experiments

An experimental analytic device was developed for this application. It includes a specific optical bench (Figure 3) integrated into a HORIBA Medical ABX Pentra 60 analyzer. The preparation of the sample is direct and automatic, including dilution and treatment of the blood by fluorescent chemical reagents. The design incorporates a focus nozzle and three light sources. The first source, a Low Temporal Coherence (LED), sets the optical axis. Associated with this light source measurement is the measurement of the optical extinction. The detection is done in a light background. The other two sources, located at 90° to the optical axis of the source S1, are monochromatic (laser) at 375 nm and 488 nm respectively. They are associated with the FL1 and FL2 fluorescence measurements. A black background is used for detection. With such a device, four parameters are associated with

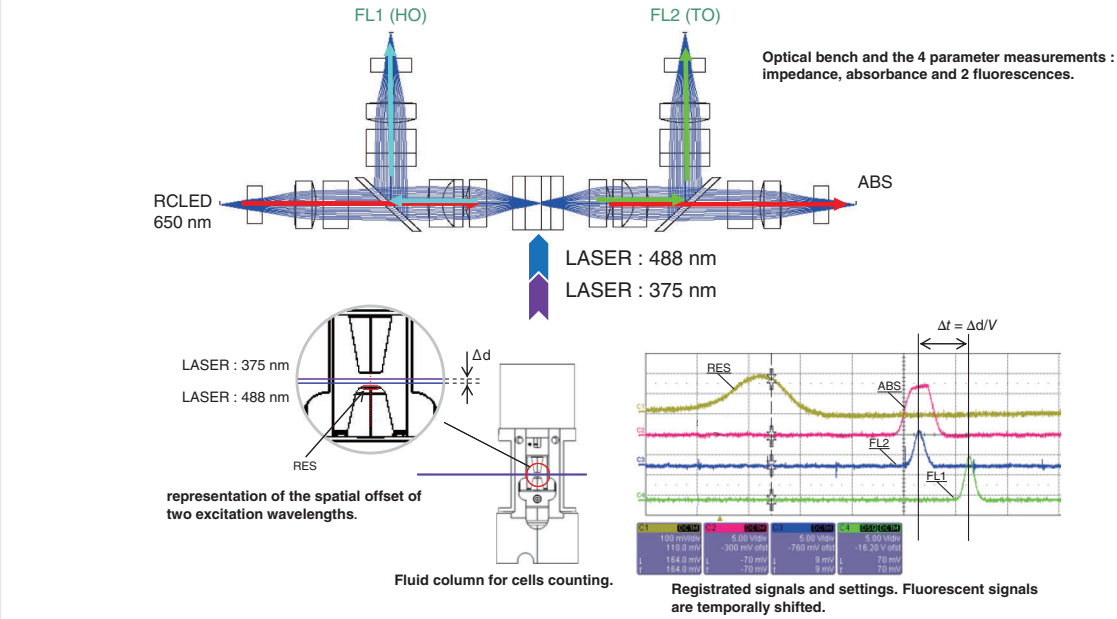

Figure 3 Optical Bench.

each red cell measured:

1- impedance measurement for a volumetric classification of each cell.
2- measure of the extinction at λ_{em}. 650 nm for cell refractive/diffractive effects.
3- measure of fluorescence FL1 at λ_{em}. 480 nm for the DNA parasite determination within red blood cells by the specific dye - Hoescht 33342 .
4- measure of fluorescence FL2 at λ_{em}. 530 nm for determination of reticulocytes (young red blood cells) by RNA content measurement.

Experiments were carried out with cultured infected red blood cells and human whole blood infected samples. Culture cells and human samples are provided by the research unit "Host-Parasite relationships, Pharmacology and Therapeutic" (UMR-MD3-Marseille).[10] The material used for analysis was a flow cytometer LSR type (from Becton Dikinson) equipped with argon laser (20 mW) and UV laser (Helium-Cadmium 8mW) and the prototype previously described. The flow cytometry method was optimized and adapted to the automatic analyzer constraints. Based on HORIBA Medical reagent specificity, the simultaneous use of the two fluorochromes TO and Hoescht-33342 (HO) was adapted to direct dilution and automation. Moreover, the initial incubation time of 75 minutes was drastically decreased to 30

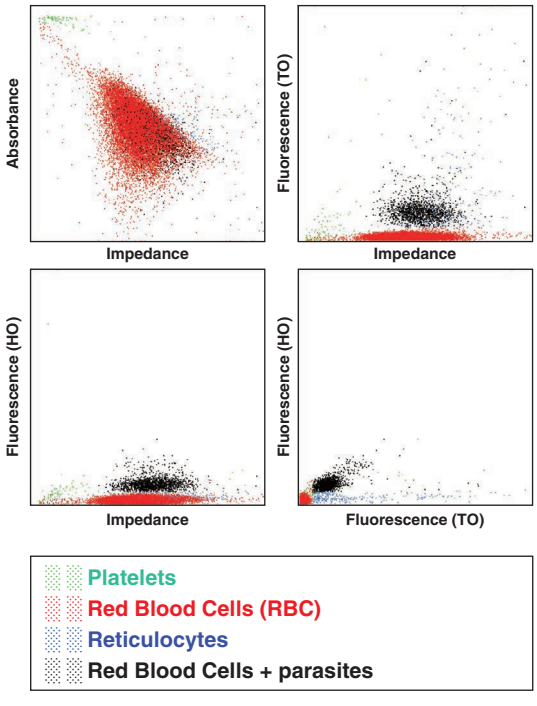

Figure 4 Determination of Parasitic DNA into Red Blood Cells by Four Parameter Analysis.
The 4 parameters are absorbance, impedance and two.

seconds, mainly thanks to the permeabilization control of parasite and red blood cell membranes. This analytic method allows the identification and quantification of parasitized red blood cells (Figure 4).

TO fluorescence (λ_{em} 530 nm) allows specific identification of RNA present in immature red blood cells (Reticulocytes). HO fluorescence (λ_{em}. 480 nm) allows specific identification of DNA present in parasites.

The results of the developed parasite staining methodology are compared to the flow-cytometric reference method (Grimberg et al.), as shown in Figure 5. The percentage of parasitized red blood cells is equivalently determinated with both methods ($r^2 = 0.99$, no bias). A detection threshold of 0.008% infected erythrocytes for this set of analysis has been demonstrated.
The determination of the parasitemia obtained with the prototype is presented in Figure 6. The automatic analysis results are compared to the results of the gold standard method, the microscopic smear examination. A good correlation was obtained between test and reference results with 28 infected human blood samples.

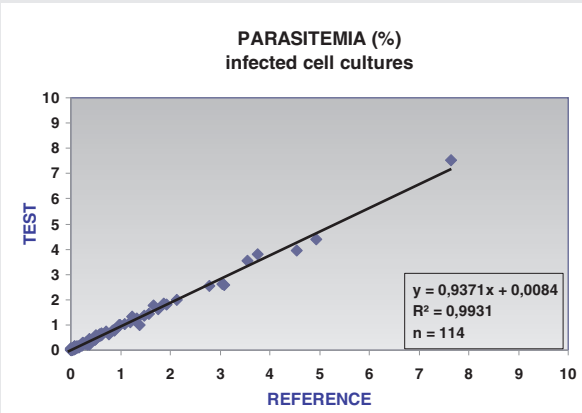

Figure 5 Accuracy Evaluation of the Fluorescent Method.
Samples of cultured infected red blood cells (n=114) were analysed by flow cytometry; the prototype method (TEST) and the flow cytometry reference method are compared.

Conclusion

The goal of this project was to define a strategy to upgrade the current instrument and obtain a dedicated device with good detection specificity of infected red blood cells to diagnose malaria. The fluorescent method presented here based on nucleic acid differentiation (DNA versus DNA/RNA) is rapid (30 sec./sample) and sensitive (~ 0.01% infected erythrocytes). In association with some CBC parameters, a specific and reliable diagnostic tool could be proposed and could participate to the malaria medical efforts.

Perspectives

The implementation of an automatic flag, in the Microsemi CRP, based on Platelets count and C-reactive protein level, would contribute to the improvement of detection capacity at local level, in agreement with the needs emphasized by the recent literature. Indeed this compact hematology analyzer provides first-line tests generally prescribed for patients presenting with fever. This makes the Microsemi CRP an affordable and robust device for malaria screening able to reach isolated and poor areas. The second solution, presented above, is the logic complement to the process of malaria infection diagnosis. This module, derived from the ABX Pentra 60, is highly sensitive but user-friendly as a routine hematology analyzer. It has the advantage of providing quantitative and reproducible results without the need of a well-trained technologist for microscopic examination and definitive malaria diagnosis and follow-up.
The solutions presented here are in line with the WHO recommendations that highlight the importance of using locally appropriate intervention for malaria prevention and case management to reduce adverse outcomes related to this infection.

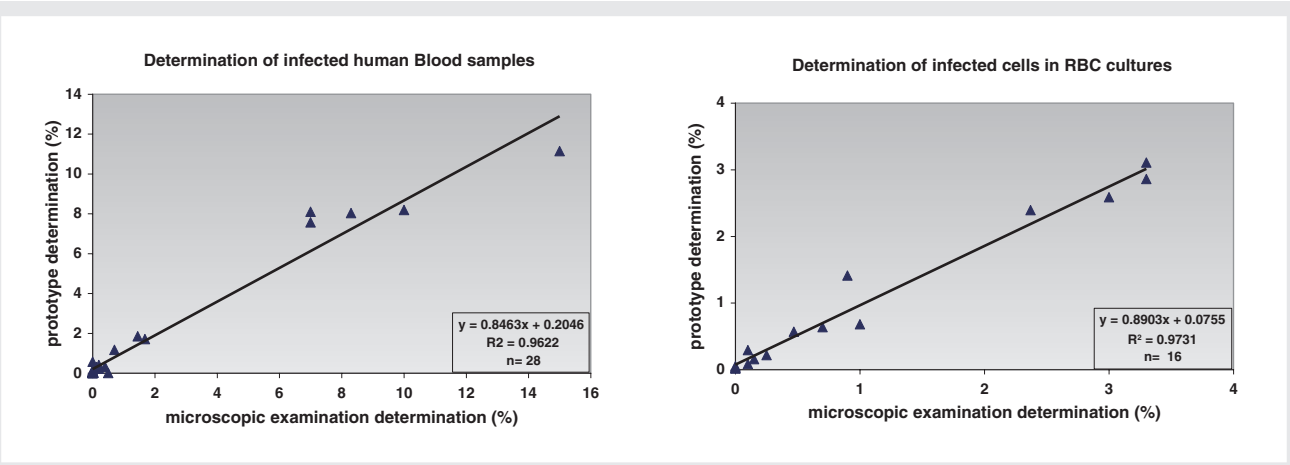

Figure 6 Determination of infected red blood cells (%) with the prototyped analytical device.
(left) Samples of malaria infected human whole blood - (right) Samples of malaria infected cultures of red blood cells.

References

[1] World malaria report: 2011. World Health Organization 2011. http://www.who.int/malaria/world_malaria_report_2011/9789241564403_eng.pdf

[2] Crawley J, Chu C, Mtove G, Nosten F. *Lancet*. 2010 Apr 24; 375(9724):1468-81.

[3] Trampuz A, Jereb M, Muzlovic I, Prabhu RM. *Crit Care*. 2003 Aug;7(4):315-23.

[4] Campuzano-Zuluaga et al. Malaria Journal 2010, 9:346.

[5] Schwake L, Streit JP, Edler L, Encke J, Stremmel W, Junghanss T. *Crit Care*. 2008; 12(1):R22.

[6] Conroy AL, Liles WC, Molyneux ME, Rogerson SJ, Kain KC. *PLoS One*. 2011; 6(12):e28540.

[7] Shapiro H.M., Mandy F. Cytometry Part A. 71A: 643_645, 2007.

[8] Howard RJ, Battye FL, Mitchell GF. *J Histochem Cytochem* 1979; 27 : 803–813.

[9] Grimberg BT, Erickson JJ, Sramkoski RM, Jacobberger JW., et al. *Cytometry A*. 2008; 73(6):546-54.

[10] Parzy D., Sinou V. Malaria research at the IMTSSA le Pharo. *Med. Trop*. 2001; 61(1):11-4.

Manuela PASTORE
Scientific Manager,
Marketing Dept.
HORIBA ABX SAS
Ph. D

Sylvie VERIAC
Hematology Research Reagent Manager,
R&D Dpt.
HORIBA ABX, SAS.
Ph. D

Laurence CHAUVET
Hematology Research Reagent Team,
R&D Dpt.
HORIBA ABX, SAS.

Alexandra URANKAR
Digital Systems Engineer,
R&D Dpt.
HORIBA ABX, SAS.

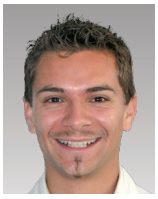

Sylvain LEDROIT
Integration Technician,
R&D Dpt.
HORIBA ABX, SAS.

Patrick BRUNEL
Integration Manager,
R&D Dpt.
HORIBA ABX, SAS.

Sébastien LEGRAS
International Service Engineer,
HORIBA ABX SAS

Christophe DUROUX
International area Manager / Asia Pacific,
HORIBA ABX DIAGNOSTICS (THAILAND) Ltd

Veronique SINOU
Host-Parasite relationships, Pharmacology
and Therapeutic Dpt.
Aix-Marseille University.
PhD.

Daniel PARZY
Host-Parasite relationships, Pharmacology
and Therapeutic Dpt.
Aix-Marseille University.
MD.

Feature Article

Fast Reading of C-Reactive Protein in Whole Blood in Hematology Analyzers

Gilles CAUET, Jean-Philippe GINEYS, Nevzat TEMUROK,
Aurélien DAYNES, Philippe NERIN

A new homogeneous immunoassay of whole blood C-reactive protein based on the use of magnetic field-assisted agglutination of polyclonal anti-CRP coated superparamagnetic particles is described. These particles self-organize into linear chains under an appropriate magnetic field which considerably increase the colliding frequency and thus, the probability to form links between ligand and receptor. Therefore, reaction rates are highly accelerated so that results are obtained well before the system has reached equilibrium. This immunoassay can be adapted to perform high sensitivity as well as high speed assays depending on analyte concentration. The high capabilities of magnetic agglutination immunoassay allow the integration of a whole blood CRP immunoassay to an existing high speed hematology analyzer. The feasibility of such a concept is reported with a prototype that combines the sampling process of a hematology analyzer with an immunodetection module. As a result, a complete whole blood CRP analysis cycle is achieved in less than one minute. The successful application of these investigations should reinforce the competitiveness and leading position of HORIBA medical in whole blood immunoassay.

Introduction

C-Reactive Protein (CRP) is a well-established biomarker in clinical laboratories for the diagnosis of infection or inflammation. It is an acute-phase protein whose concentration increases rapidly in response to various stimuli including bacterial infection, inflammation, trauma, surgery. Many commercially available CRP immunoassays performed on plasma or serum samples are mainly based on particle-enhanced turbidimetry or nephelometry using latex microbeads.[1] This technology has been further adapted to whole blood samples by HORIBA Medical. Actually, C-reactive protein assay in whole blood where blood cells are present (leucocytes, erythrocytes, thrombocytes) has led to specific developments in HORIBA Medical.[2] For example, an analyzer such as ABX MicrosCRP200 provides biologists with efficient equipment which allows performing in less than 5 minutes a Complete Blood Count (CBC) including the determination of 18 parameters together with a CRP immunoassay in the range 2-200 mg/L. The determination of all these parameters on a unique blood sample which avoids separation of plasma or serum from blood cells, constitutes an important procedure simplification and reduction of analysis time. This was made possible by use of an infrared light source for which cell debris and hemoglobin diffusion/absorption is negligible with respect to the specific signal due to particle aggregates formation in response to the presence of CRP. With latex beads, formation of aggregates results roughly from two events, capture of the antigen by the beads and formation of links between beads. However, the agglutination rate which obviously depends on antigen concentration and antibody surface density, is also limited by particles diffusion. The technique proposed in this article, first described by Baudry et al.[3] and further developed by HORIBA Medical for blood proteins, allows a considerable reduction of reaction time between particles due to the use of superparamagnetic particles whose aggregation is accelerated by a magnetic field.

This article describes the adaptation of a magnetic agglutination assay to whole blood CRP which combines high analytical sensitivity and fast reading. This technique fast enough to be integrated to a high speed hematology analyzer (60-120 tests/h), will offer new opportunities for HORIBA Medical within routine high throughput hematology analyzers.

Magnetic Agglutination Assay:

Magnetic agglutination assay is a homogeneous assay like usual Latex Agglutination Assay (LAA) used in many diagnostic assays.[4] In LAA, particles grafted with a specific antibody self-aggregate in the presence of the antigen. However aggregation rate is limited by diffusion time. In the case of magnetic particles assay, aggregates formation is accelerated by submitting the particle suspension to a homogeneous magnetic field reducing the diffusion time. Actually, a colloidal suspension of superparamagnetic particles can form linear chains under an appropriate magnetic field. This chaining process brings the particles together, considerably increasing colliding frequencies between adjacent particles, which leads to a substantial increase of antibody-antigen bond formation rate. Upon release of the magnetic field, unreacted particles and aggregates rapidly diffuse in the solution (Figure 1). Aggregates are then detected by light scattering, the signal is expressed as the difference in optical density at 650 nm (OD650 nm) measured before and after application of the magnetic field. Whereas analytical sensitivity is in the nanomolar range for LAA, it drops to the picomolar range for magnetic agglutination assay which makes it comparable to heterogeneous approach such as ELISA (enzyme-linked immunosorbent assay) in terms of sensitivity, but much faster.

The accelerating effect of magnetic field is illustrated on Figure 2. Progress curves obtained for magnetic particles grafted with an anti-CRP antibody in the presence of 14 picomoles/L of C-reactive protein (CRP) with and without several pulses of a magnetic field of 20 mTesla (mT), were compared. In the absence of magnetic field, no significant change in the optical density was observed indicating that nearly no reaction occurs between particles. On the contrary, under a field, particles aggregation took place, causing a progressive increase of optical density which demonstrates the extent of the accelerating effect induced by the magnetic field. Typical aggregation kinetics is shown on Figure 3. Repeated pulses of magnetic field corresponding to alternating particles chaining and relaxation phases lead to a progressive increase of suspension turbidity. Particles chaining starts when magnetic field is on. In the first 100 msec, a drop of OD is observed which corresponds to the orientation of already formed aggregates in the direction of the field, and then the chaining process itself occurs, resulting in a slow decrease of OD. When magnetic field is off, relaxation of the system takes place. Disruption of chains leads to an almost instantaneous increase of turbidity. This rapid phase is followed by a slow decrease of OD which corresponds to the breakdown of non-specific aggregates,

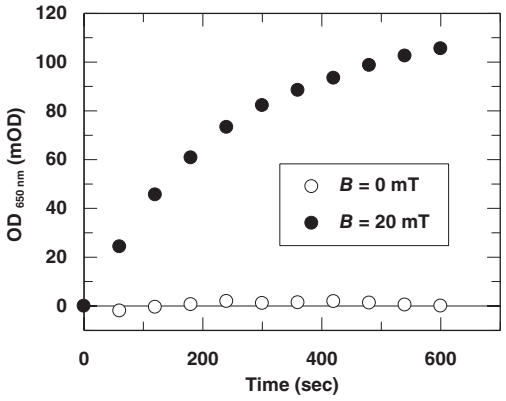

Figure 2 Progress curves obtained with magnetic particles (200 nm) grafted with an anti-CRP antibody in the presence of 14 pM of CRP, with or without pulses of a magnetic field of 20 mT.

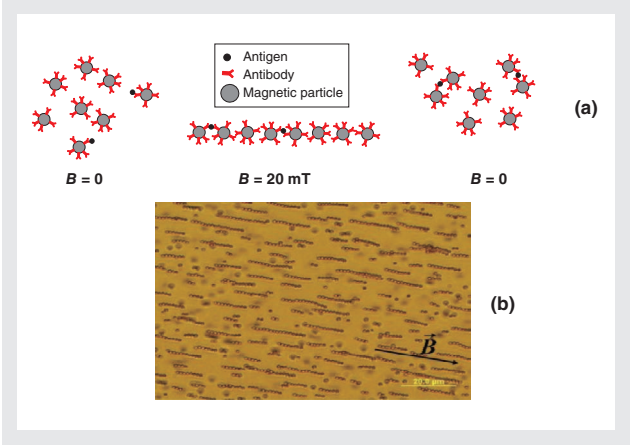

Figure 1 Principle of magnetic agglutination assay.
(a) Chaining process; (b) Linear chains of magnetic particles (1 µm, Dynal) under a magnetic field (*B*). The arrow indicates field direction.

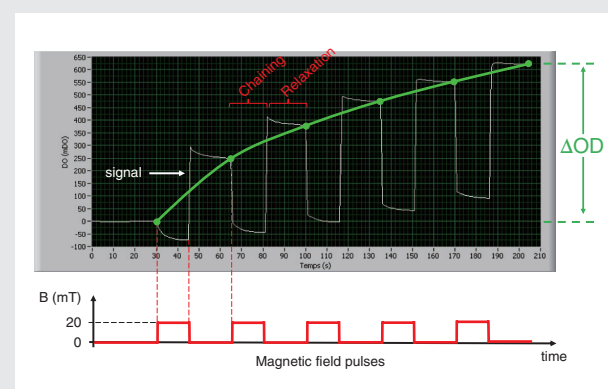

Figure 3 Optical density variation during field-induced aggregation of magnetic particles (200 nm) grafted with an anti-CRP antibody in the presence of CRP. Magnetic field was 20 mT.

and finally a plateau is reached whose level is proportional to the number of stable bonds formed between particles.

C-Reactive Protein Assay in Whole Blood

First results were obtained with an in-house built magneto-optical device described in Figure 4(a). This device included a disposable spectrophotometric cuvette surrounded by an electromagnet able to deliver a roughly homogeneous field, a LED emitting at 650 nm as a light source and a photodiode. Sample illumination and light collection were performed by optical fibers. Carboxyl-modified superparamagnetic particle of 200 nm diameter (Ademtech, Pessac France) were covalently coated with a goat polyclonal antibody directed against human CRP (Meridian life sciences, Memphis, USA) using a carbodiimide coupling chemistry. Before mixing with particles, blood sample was first diluted in a buffer containing saponin in order to disrupt blood cells. Then the diluted sample was mixed with particles in the measuring cell, and 3 pulses of 30 sec of magnetization at 20 mT followed by 30 sec of relaxation, were applied. Aggregation kinetics was monitored at 650 nm, ΔOD was plotted against CRP concentration (Figure 4(b)). For CRP concentrations less than 20 mg/L, ΔOD is directly proportional to the amount of CRP. This linear relationship corresponds mainly to the formation of only doublets. Then the slope of the curve decreases progressively and for CRP concentrations higher than 200 mg/L, ΔOD finally decreases slightly. In LAA, this is usually explained by a progressive saturation of grafted antibodies by excess antigen or "hook effect" which is characterized by a bell-shaped curve. Rather, the curve profile obtained in the conditions described above for the magnetic agglutination assay could mainly result from an optical effect due to formation of large aggregates when CRP exceeds 20 mg/L[5]. High dilution of blood sample together with detection at a wavelength where hemoglobin absorption is minimal allowed a drastic reduction of interferences due to cell debris and hemoglobin. Dynamic range and analytical sensitivity can be modulated through modification of either dilution factor or total magnetization time, or both. This is illustrated in Figure 5. When blood sample was diluted 150 times and magnetization time was 105 sec, dynamic range was approximately from 0.1 to 10 mg/L. With a 1:1500 dilution and magnetization time of 10 sec, dynamic range was approximately from 2 to 200 mg/L. Thus, with simple modifications of sample treatment and conditions of magnetization, a dynamic range of about three orders of magnitude could be explored in whole blood.

Fast Reading Automated Assay

Our objective is to combine an immunoassay module to an existing high speed hematology unit such as Pentra80 or Pentra120 in order to perform simultaneous biochemical and hematology analyses without impairing hematology analyses rate. Fast CRP immunoassay described above should fulfill the conditions to reach this goal. The flow diagram of such a machine is reported in Figure 6. A transfer module including a sampling valve

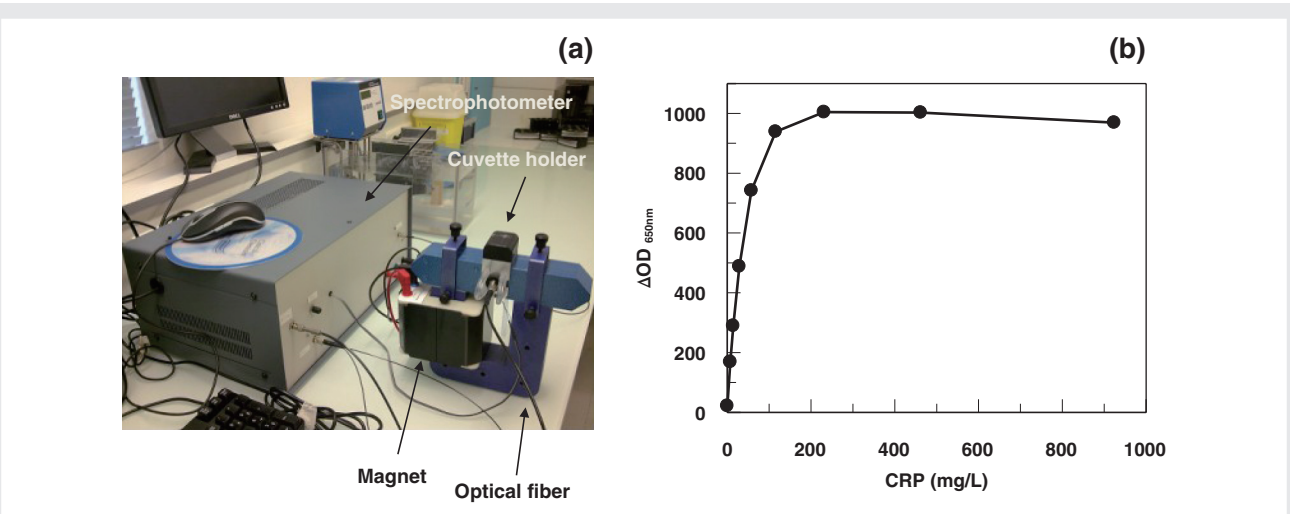

Figure 4 Whole blood CRP immunoassay.
(a) Magneto-optical device.
(b) Dose-response curve obtained using magnetic particles (200 nm) grafted with a polyclonal anti- human CRP with 3 × 30 sec of a field of 20 mT. Final sample dilution is 1:1500.

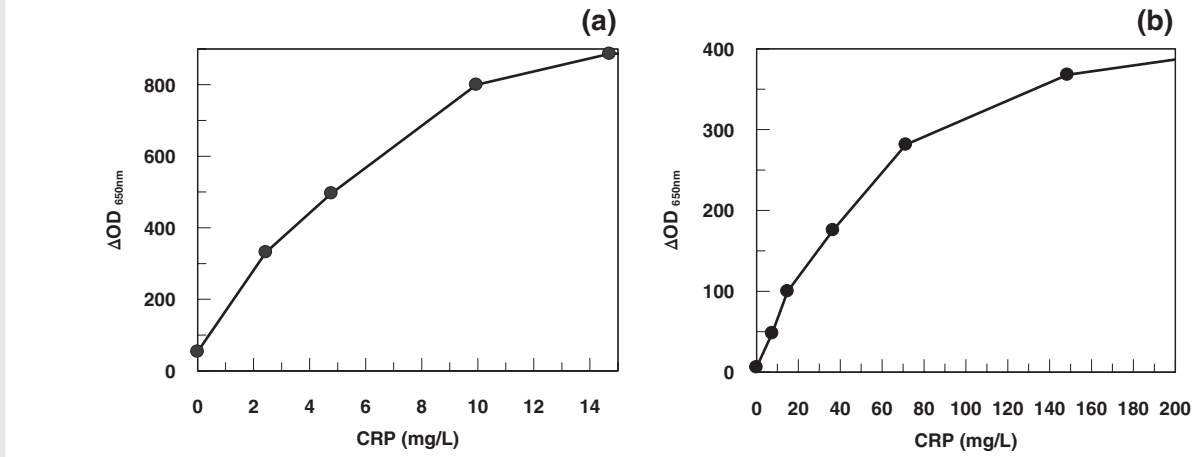

Figure 5 Dose-response curves of whole blood CRP in different conditions.
(a) Dilution factor 150, total magnetization time 105 sec, (b) Dilution factor 1500, magnetization time 10 sec

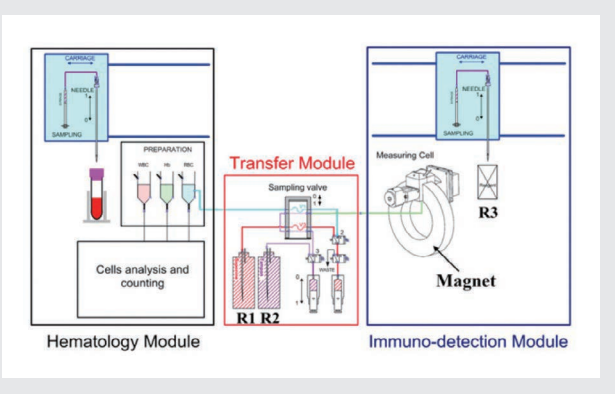

Figure 6

and two syringes for R1 (Saponin solution) and R2 (Buffer solution) will constitute an interface between hematology and immunodetection modules. The hematology module will typically comprise a sampling needle, preparation tanks for hemoglobin determination, and blood cell analyses, and a counting device. The immunodetection module will include measuring cell, magnet, optical unit and sampling needle for R3 (magnetic beads). In this approach, there will not be a specific pre-dilution tank for CRP analysis; the immunodetection module will use a pre-diluted blood sample from one of the preparation tanks of the hematology module. This configuration will allow simultaneous cell counting and CRP immunoassay at high speed (patent pending).

With this goal in mind, preliminary results were obtained with a prototype built in a Pentra60 frame which simulated such a configuration, i.e. only the sampling and dilution sections of a hematology module associated with the transfer and immunodetection modules.

The sequence of events was as follows

First step: a blood sample was taken and subsequently prediluted (1:40) in Eosinofix which is the reagent used in hematology analyzers such as Pentra80 for white blood cell analysis. In the meantime, the sampling valve of the transfer module was loaded with R1 and R2

Second step: diluted sample was loaded in the sampling valve while R3 was taken by the needle of the immunodetection module.

Third step: the diluted sample, R1 and R2 were transferred from the transfer module to the immunodetection module, added to the measuring cell together with R3 and rapidly mixed by air bubbling. Magnetization cycle then began including 7 sec of magnetization, and 3 sec of relaxation after which OD was recorded. Total reaction volume was 500 µL. Final sample dilution was 1:1500.

The complete cycle was achieved in 45 sec before next sample analysis. These conditions should be fully compatible with analysis rate of a P80, i.e. 80 samples analyzed per hour.

The imprecision profile of the assay obtained with various amounts of serum CRP indicated that CVs were less than 5% from 1 to 250 mg/L, and less than 3% from 2.5 to 100 mg/L. Detection limit determined on blood samples was less than 1 mg/L(*) and no “hook effect” was observed for blood CRP up to 1 g/L.

A preliminary correlation study was performed against the ABX MicrosCRP200 with 25 samples constituted of a pool of human EDTA-blood spiked with various amounts of purified human CRP (Euromedex, France) (Figure 7). Prototype calibration was performed with ABX Pentra400 serum CRP calibrators (ABX Pentra CRP Cal, HORIBA Medical). Measured blood CRP concentrations were corrected with hematocrit value (HCT) determined on ABX Micros CRP200.

Although very preliminary, these results were quite

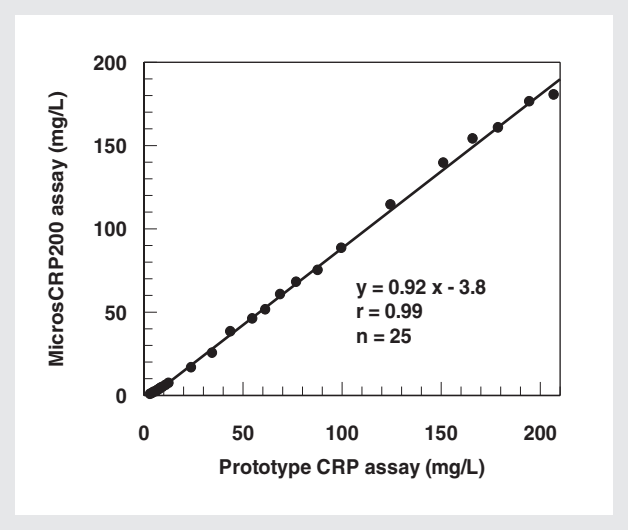

Figure 7 Correlation between prototype and HORIBA MicrosCRP200 using EDTA-blood samples spiked with purified human CRP. Concentrations were corrected with HCT.

satisfactory and promising. The high y-intercept value of the correlation curve was essentially due to not corrected differences in optical density observed between blood CRP and the serum CRP calibrators used for the prototype. These differences are related to a "matrix effect". Actually, we found that the presence in normal blood (or serum) of high molecular weight proteins caused some non-specific interactions between magnetic beads. Surprisingly, these interfering proteins are absent from the CRP calibrators used, probably eliminated by a chemical or physical treatment of serum during the production process. This matrix effect is considerably reduced by addition of an appropriate concentration of saponin or other related detergents to the reaction mixture. However, in the example reported here, it is possible that the prototype did not deliver the right quantity of saponin. Efforts are underway to improve this particular point and the overall analytical performances of the prototype. We are also focusing on the reduction of reaction volume to 300 µL in order to limit reagent consumption and waste.

Conclusion

Magnetic agglutination assay is a very sensitive and flexible technique. One can perform high sensitivity assays in few minutes or fast medium sensitivity assays in few seconds. This allows determination of low abundant blood proteins (~ 10-100 µg/L) as well as high throughput assays of more abundant proteins (>1 mg/L) such as C-reactive protein. Work is underway to adapt this technology to Pentra hematology analyzers. Throughout these investigations and results, the uniqueness and competitiveness of HORIBA Medical in the field should be maintained over years, taking into account these last achievements.

However, despite its sensitivity, the method is limited to the detection of few picomoles/L of an antigen. There are different causes for this limitation; one comes from the optical detection system itself, i.e. turbidity measurement for which the limit of resolution is higher than a 1% intensity variation (3). We are currently working on a different optical approach that should lower the detection limits down to a few hundreds of femtomoles/L.

(*) Detection limit was determined empirically and represents the lowest CRP concentration at which the mean value minus2 sigma does not overlap with blank mean value plus 2 sigma.

References

[1] Roberts WL., Moulton I., Law T.C., Farrow G., Cooper-Anderson M., Savory J., and Rifai N. (2001) *Evaluation of Nine Automated High-Sensitivity C-Reactive Protein Methods: Implications for Clinical and Epidemiological Applications. Part 2* Clin Chem, 47: 418-425

[2] Oku N., and Yamao Y., *Blood cell count/immunoassay apparatus using whole blood* EP0905514B1 (priority 1997)

[3] Baudry J., Rouzeau C., Goubault C., Robic C., Cohen-Tanoudji L., Koenig A., Bertrand E., and Bibette J. (2003) *Acceleration of the recognition rate between grafted ligands and receptors with magnetic forces* Proc Natl Acad Sci USA 103:16076-16078.

[4] Newman DJ., Henneberry H., and Price CP(1992) *Particle enhanced light scattering immunoassay* Ann Clin Biochem, 29: 22-42

[5] Daynes A., Manuscript in preparation

Gilles CAUET
Head of Biochemistry group
R&D dept.
HORIBA ABX SAS,
Ph. D

Jean-Philippe GINEYS
Measurement System Designer
Research Dept.
HORIBA ABX SAS

Nevzat TEMUROK
Technician, Biochemistry group,
R&D dept.,
HORIBA ABX SAS

Aurélien DAYNÈS
Biochemistry group,
R&D dept.,
HORIBA ABX SAS,
Thesis Student

Philippe NERIN
Research Director.
HORIBA ABX SAS
Ph. D

Feature Article

Numerical Simulation of Particle Dynamics in an Orifice-Electrode System. Application to Counting and Sizing by Impedance Measurement

Damien ISEBE, Jean-Philippe GINEYS

This paper describes how to numerically tackle the problem of counting and sizing particles by impedance measurement in an orifice-electrode system. The model allows to simulate the particle dynamics submitted to strong hydrodynamic stresses through a microorifice and to compute the voltage pulses generated by the modification of the inner dielectric medium. This approach gives important information about particles size distribution and allows to quantify the role of trajectory and orientation of particles on the size measurement.

Introduction

Counting and sizing of biological cells are often based on electrical gating through a micro aperture-electrode system. A voltage drop, generated by the particle flowing through the aperture allows to determine the volume of the particle. We expose here a complete numerical approach based on fluidic and electrical cross linked simulations coupled to an equivalent electrical circuit model to Figure a realistic operation of cell impedance measurement of blood cells. The model allows to compute the exact particle size distribution by taking into account trajectory and orientation of the particles through the micro-aperture. For a given particle flow, we also compute full particle size distributions for systems with and without sample hydrodynamic focusing where volume measurement errors can be derived. These numerical results are also compared to experimental measurements.

Impedance Gating and Particle Sizing Principles

Figure 1(a) depicts the considered orifice-electrode system with hydrodynamic focusing for the sample flow. The micro-aperture is a cylindrical aperture of length L and diameter D_0 and is made of electrical insulator material. The two electrodes, placed on each side, are platinum made with anode voltage fixed to V_1 Volt. The sample arrives by an injector of diameter D_i and an external sheath flow is used to focus the sample at the center of the aperture

Counting and sizing of biological cells are determined by an impedance variation measurement. This is the most popular technology, based on the well-known *Coulter Principle*, for volume measurement in the hematology field.[1]

More precisely, counting is done by an electrical measurement through a micro-aperture. When a particle passes through the orifice, a voltage and/or voltage drop appears in the electrical field. The resistance of the medium is changed and this impedance variation generates an electrical pulse which is directly linked to cell volume (See Figure 1(b)). Unfortunately, for a given particle, volume measurement can be distorted by its trajectory and its orientation and produce overestimations:

- Concerning the impact of particle trajectories, it is obvious that the electrical field experienced by the particle is not the same if the particle flows at the center or close to the edges (respectively streamlines S_1 and S_2 in the Figure 2(a)). Actually, in such a system, the electrical field is non-homogeneous and increases

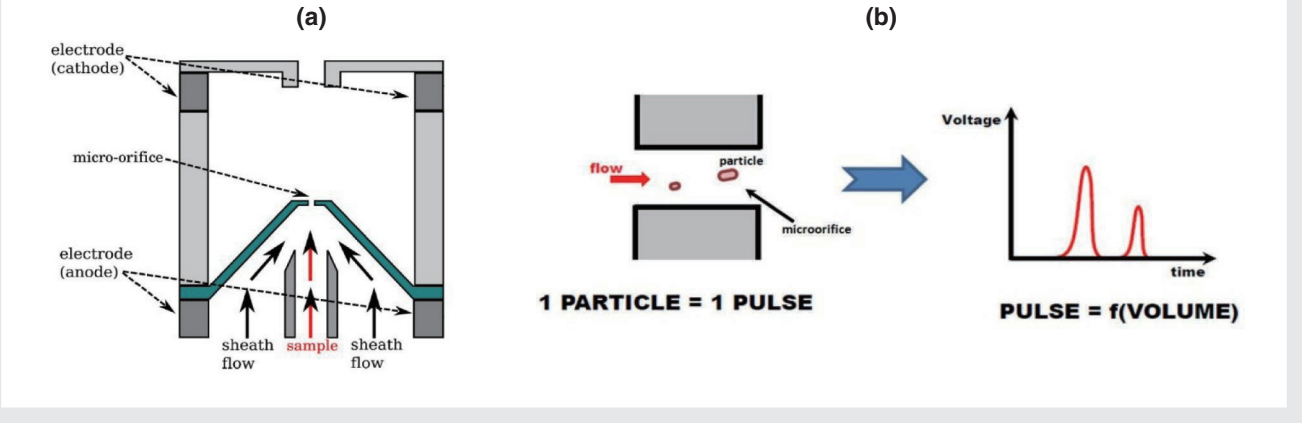

Figure 1 (a) Scheme of the orifice-electrode system; (b) - Principle of impedance measurement

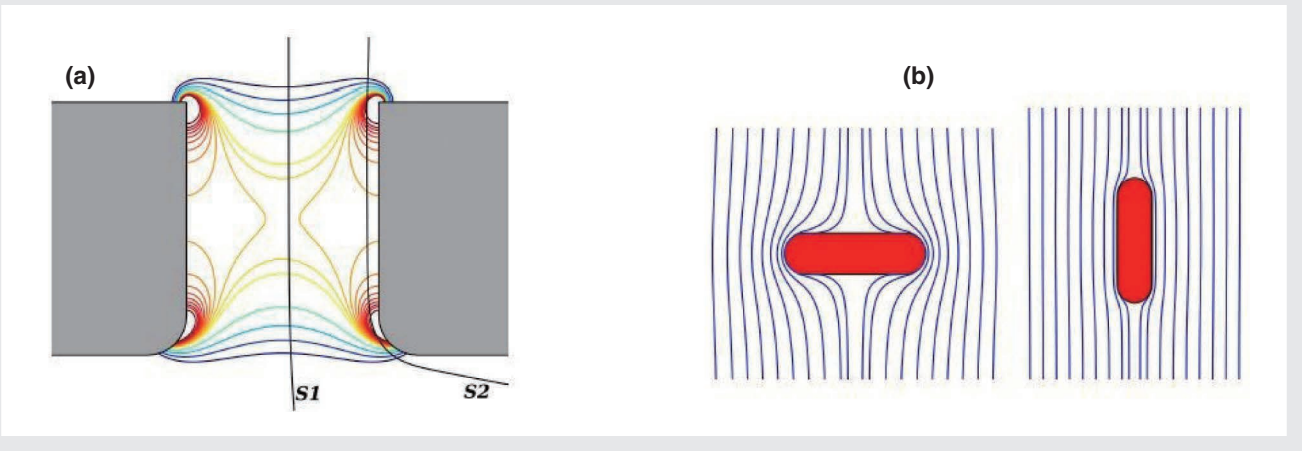

Figure 2 (a) Isovalues of electrical field inside the orifice. Velocity streamline S1 and S2 representing 2 different particle trajectories; (b) Effect of an insulating particle on electrical streamlines: particle flows perpendicular (left) and parallel (right) to streamlines

dramatically close to the edges of the orifice. Along the central axis, electrical isolines are almost parallel.

- Moreover, the orientation of the particle through the orifice impacts more or less electrical streamlines. More precisely, when an insulating particle passes through the orifice, the resistance of the medium increases proportionally to particle volume. In practice, depending the particle's orientation, electrical streamline is more or less deflected, and so the particle may appear bigger than it really is.

Numerical Method to Compute Measured Voltage Pulses

The aim of this paper is to take advantage of simulation techniques to tackle the problem of counting and sizing particles. This complete numerical approach is fully innovative in diagnostics engineering and allows to understand and optimize physical processes that we don't experimentally apprehend.

Framework and Assumptions

The domain used for simulation is an orifice-electrodes system as in Figure 1 where the orifice aspect ratio D_0/L corresponds to practical instruments from HORIBA Medical. The model is developed in two dimensions as an approximation of plane flow devices. The particles considered here are shaped like capsules, defined by a central rectangle of length nR and width 2R and two half-circles of radius R at both extremities. At each time step, position of the particle is given by coordinates of its center of gravity C_p and its orientation is controlled by angle θ. Also, particles are supposed to be rigid and totally insulating. The size ratio $2R/D_0$ is comprised between 0.05 and 0.15 corresponding to small size particles as compared with the size of the orifice.

Flow model, particle transport and electrostatic: To simulate the dynamics of suspended particles, the numerical model solves a fluid-structure interaction problem (the flow affects particle movement and vice versa). Velocity field u and pressure *p* in the system are

solutions to Navier-Stokes equations (the fluid is assumed to be incompressible and Newtonian and effects of Brownian motion and gravity are ignored). Particle velocity v_p is a sum of a translational velocity v_{tr} and a rotational velocity v_{rot}. To compute these two components, we use fluidic parameters (u, p) to determine Hydrodynamic Force F_{hyd} and Torque T applied on the particle boundary. The force and torque exerted by the fluid are found by integrating the stress tensor over the particle surface.[2] Electrical field E is defined by $E=\nabla . V$ where V is the voltage potential (∇ is the gradient operator), solution of a Laplace's equation for electrostatics. Electric displacement D is defined by $D=\varepsilon E$ where ε is the absolute permittivity (the particle is supposed to be totally insulating so absolute permittivity of the medium is taken eighty times higher than absolute permittivity of the particle).

Computation of physical voltage pulses: The total energy W(t) [J] is given by integrating the energy density on the domain as follows : $W(t) = \int_\Omega (1/2)\varepsilon ||E||^2$.
For a small time interval $\Delta t = t_2 - t_1$, the instantaneous power P [J/s] in the system is defined by

$$p = \frac{\Delta W}{\Delta t}$$

On the other hand, the instantaneous electrical power P is given by $P(t) = U(t).I(t)$ where U(t) [V] is the voltage dropt and I(t) [A] the current in the system (In our case, the current I(t) is maintained constant thanks to a constant current generator, so I(t) = I for each time t.
Then, the physical voltage pulse U_p is computed for each time t in the interval $[t_1, t_2]$ by

$$U_p(t) = \frac{W(t_2) - W(t_1)}{(\Delta t).\bar{I}} \text{ where } t = \frac{t_1 + t_2}{2}$$

Equivalent electrical model for the orifice-electrode system and for an RBC-type cell:
In practice, voltage pulses U_m measured by the electronic card have twice lower amplitude than physical pulses U_p, particularly owing to polarization resistance and temperature compensation. To model and compute mathematically the measured voltage pulses, the idea consists in developing an equivalent electrical model for the system and switching between temporal and frequential spaces by Fourier transform in order to filter pulses by transfer function H of the system. More precisely, in the first step, we sample physical pulse $U_p(t)$ and compute its spectrum $F(U_p)=F(U_p)(\nu)$ by Discrete Fourier Transform. Then, we multiply $F(U_p)$ (ν) by the transfer function of the sensor $H(\nu)$ and we finally recover measured voltage pulse U_m by Inverse Discrete Fourier Transform such as

$$U_m(t) = F^{-1}[H(\nu).F(U_p)(\nu)](t).$$

To determine the transfer function of the orifice-electrode system, we establish the corresponding equivalent electrical model. In such system, total resistance R_g is concentrated very close to the orifice and we assume that R_g is channeled inside this one (the value R_g is determined by the numerical electrostatic model). In the presence of cell in the orifice, we thus consider the equivalent electrical model described in Figure 3. The incoming voltage is first distributed in the whole space when it penetrates into the orifice; the voltage is then split up in two parts: around the cell and through the cell (the equivalent electrical impedance of this area is called Z_{eq}). Finally, the voltage is distributed again in the whole space to the outlet.

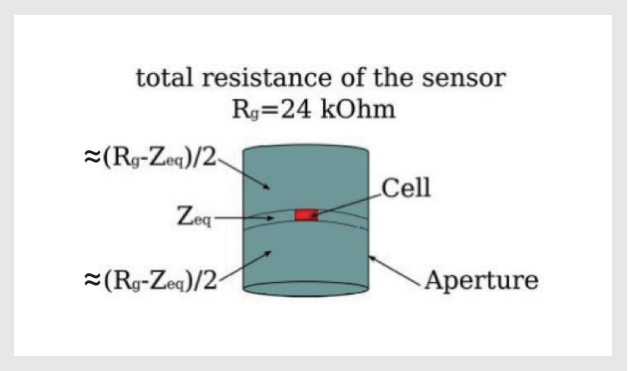

Figure 3 Scheme of the orifice including a cell

Taking into account the parasitic capacity of sensor Cg and insolator resistance R_{iso}, the equivalent electrical model for the orifice-electrode system described is given in Figure 4(a). Equivalent electrical model Z_{eq} can be seen as a resistance R_p, resistance of the area around the cell, in parallel with impedance Z_{cel}, the equivalent electrical model for the cell. In the absence of cell, Z_{cel} can be changed by resistance R_0 equal to the resistance of the cell's volume filled of sheath liquid (see Figure 4(b)). In the presence of cell, Z_{cel} is changed by the equivalent electrical model of an RBC-type cell. In this case, the membrane can be modeled by resistance R_m in parallel with capacity C_m, and the cellular content by resistance R_i. Thus, the cell can be seen as a membrane connected in series with cellular content and connected again in series

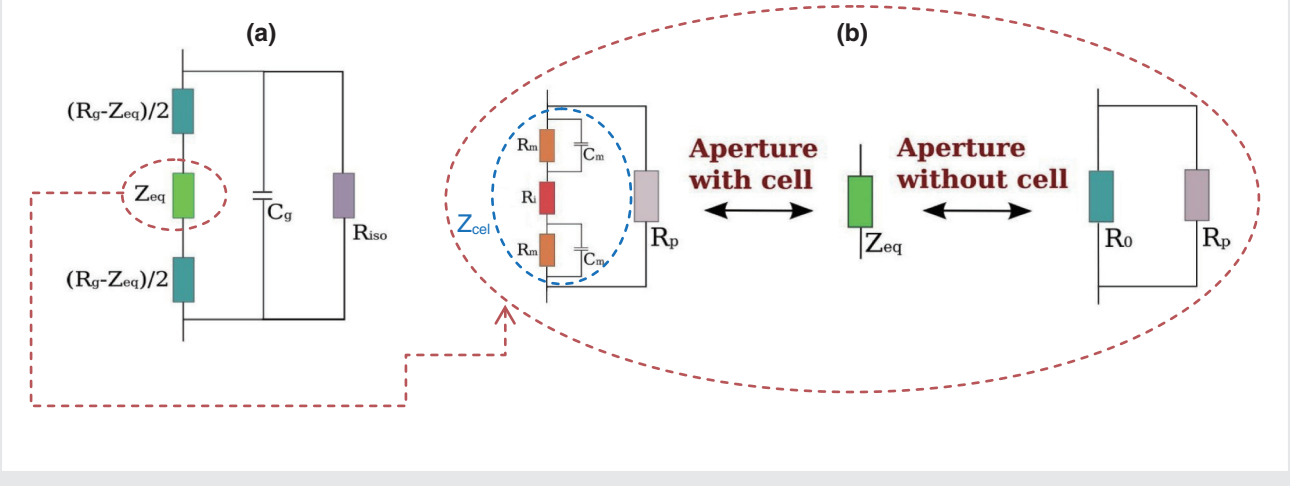

Figure 4 Equivalent electrical model for (a) the general orifice-electrode system; (b) the resistance Zeq

with opposed membrane (see Figure 4(b)). So, the two transfer functions (with or without cell in the system) are then given by the following expressions:

$$H_{cell}(\nu) = \frac{2R_mR_p + R_iR_p(1 + 2\pi\nu C_mR_mJ)}{2R_m + (R_i + R_p)(1 + 2\pi\nu C_mR_mJ)}$$

and $$H_{no\ cell}(\nu) = \frac{R_oR_p}{(R_o + R_p)}$$

Computation of Measured Voltage Pulses

Thanks to the above mentioned numerical method, we can exactly compute measured voltage pulses obtained with an orifice-electrode system. We consider two particles passing through the micro-aperture along velocity streamlines S1 and S2 described in Figure 2(a). In Figure 5(a), we expose physical (raw) voltage density U_p a long a streamline computed by multiphysics numerical simulation (flow model, particle transport and electrostatic). The *blue* pulse refers to a particle passing at the center of the micro-aperture and the *red* pulse to a particle passing close to the edges. Figure 5(b) shows spectral magnitude $F(U_p)$ of these two physical pulses. The spectral magnitude referring to cells passing close the edges is non-null for high frequency. This highlights fast intensity changes in physical pulses due to electrical field peaks at the edges of the gate. The use of band pass filter in the electronic card should smooth the magnitude for high frequencies. Figure 5(c) exposes the corresponding measured filtered voltage pulses.

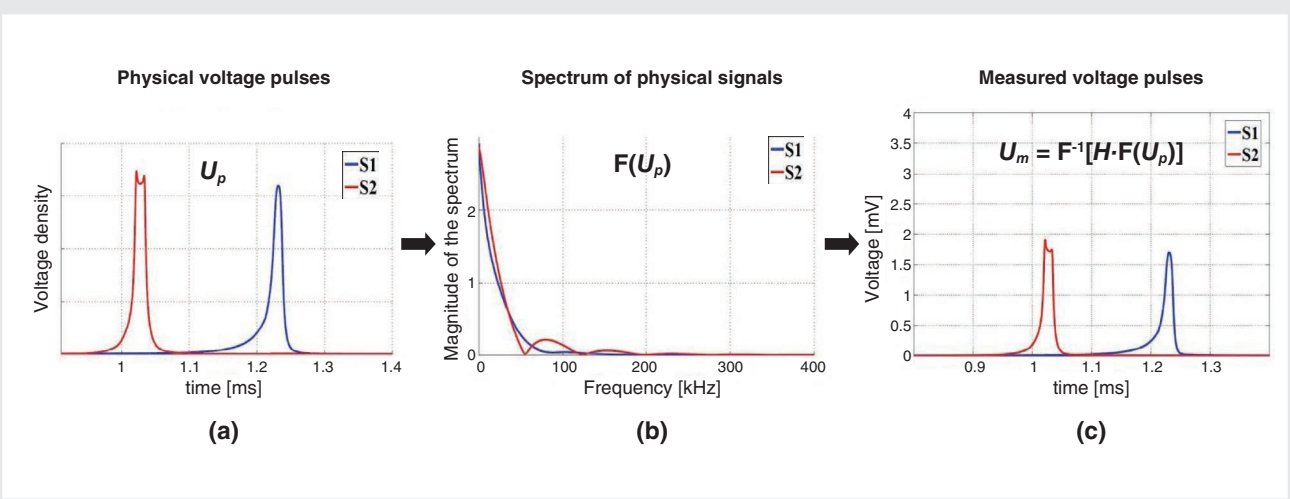

Figure 5 (a) physical voltage pulses (viewed by a particle along a streamline); (b) the spectrum of the two physical voltage pulses; (c) measured voltage pulses (after electronic amplification).

Effect of Size, Trajectory and Particle Orientation on Voltage Pulses

The numerical method presented in the previous section is used to numerically solve the problem of counting and sizing particles in an orifice-electrode system. The results below quantify the effect of the trajectory, orientation and dimensions of the particle on measured voltage pulse and on particle size distribution.

Effect of particle size: We have seen that the impedance measurement allows to determine the size of the particle. We first simulate the direct effect of particle size on generated voltage pulses. We consider an experimental micro-aperture with an aspect ratio $D_0/L=0.4$. Mean velocity through the orifice is around 7.6 m/s and voltage at the anode is fixed to 6 V. Radius R of the particle is fixed to 1 µm. Size parameter is nR (0.5, 1, 2 and 4 µm). In Figure 6, we display electrical voltage pulses corresponding to 4 particles with different nR. Clearly, we see that the bigger the particle, the higher the peak of the resulting voltage pulse. More precisely, the maximum level of voltage pulses is linearly correlated to size parameter nR and particle size can be directly determined by using a peak detection algorithm for the voltage pulse.

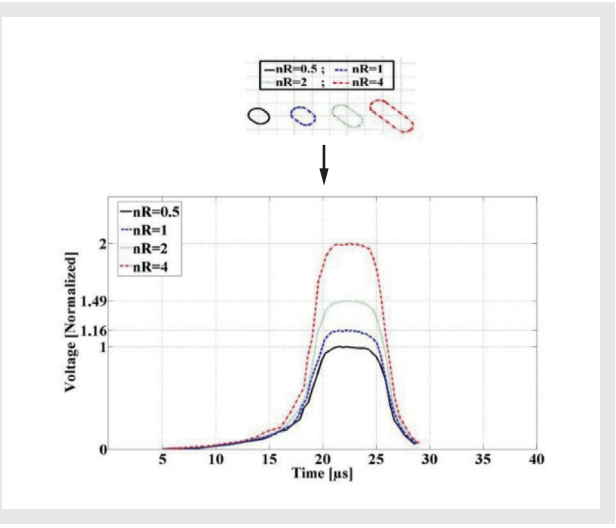

Figure 6 Voltage pulses generated by 4 particles with different size.

Effect of particle trajectory: Here, we study the effect of particle trajectories on resulting voltage pulses. Dimensions of the orifice are L=65 µm and D_0=50 µm. Mean velocity through the orifice is around 4.25 m/s and voltage is fixed to 7.6 V. Radius R of the particle is fixed to 2.5 µm and nR=2.15 µm. The trajectory, and the resulting voltage pulse, of the particle are computed for a particle passing at the center of the orifice and a particle passing close to the edges of the orifice (see Figure 2(a) for corresponding velocity streamlines S_1 and S_2). Figure 7(a) shows two voltage pulses corresponding to particles passing through the orifice along velocity streamlines S_1 and S_2. Along the central axis of the orifice (streamline S_1), the generated voltage pulse is of the Gaussian type. In this case, peak detection is quite easy and the size of the particle can be precisely determined. On the other hand, a particle passing close to the edges of the orifice (streamline S_2) is submitted to high electrical values and the resulting voltage pulse has a distorted shape on its apex. This produces erroneous peak values and computation of particle sizes produces false estimations (until 8% of the maximum of voltage pulse depending on electronic configuration). Figure 7(b) exposes series of experimental voltage pulses obtained with an orifice-electrode prototype developed by HORIBA Medical. It is interesting to see that the two types of voltage pulses are experimentally obtained. For identical configurations, amplitude of pulses obtained numerically is similar to the experimental case.

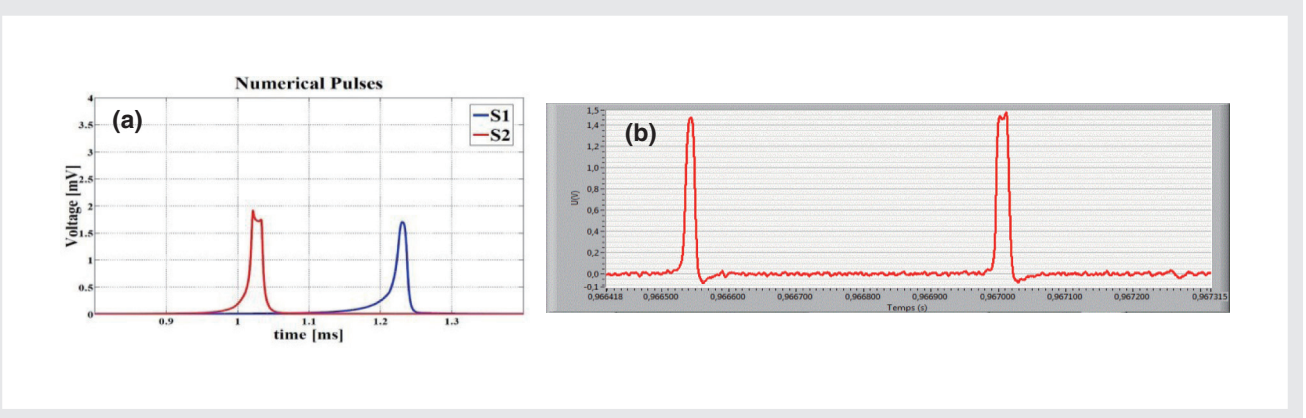

Figure 7 (a) Numerical voltage pulses for two different particle trajectories; (b) Series of experimental pulses.

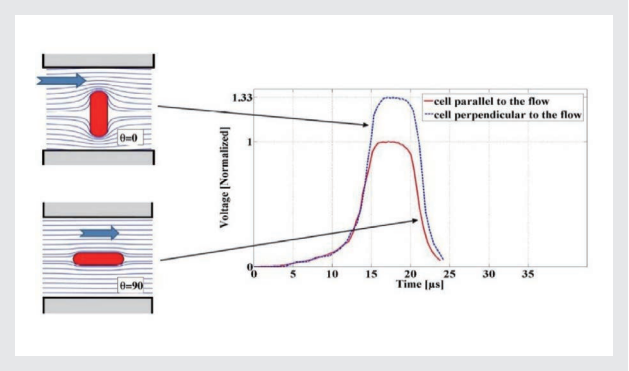

Figure 8 Two voltage pulses generated by a particle with the same size but different orientations through the aperture.

Effect of particle orientation: To quantify the effect of particle orientation on voltage pulses (and therefore on particle size measurement), we force a particle to pass through the orifice with a fixed orientation of θ=90° first, and with a fixed orientation θ=0° secondly. We consider an experimental micro-aperture with an aspect ratio D_0/L=0.4. Radius R of the particle is fixed to 1 µm and nR=1 µm. Results show that, in this mechanical and fluidic configurations, the particle passing perpendicular to the flow (θ=0°) generates a voltage pulse 33% higher than a particle passing parallel to the flow (θ=90°). Voltage pulses are exposed in Figure 8. Controlling this phenomenon allows to avoid erroneous size measurement due to particle orientation through the orifice.

Statistic Particle Size Distribution: Role of Hydrodynamic Focusing

Given the previous results, we can compute the size of particles immerged in a liquid suspension. Dimensions of the orifice are L=65 µm and D_0=50 µm. Mean velocity is approximately 4.25 m/s and voltage is fixed to 7.6 V. We consider a sample flow containing same spherical particles of radius equal to 2 µm (to take into account manufacturing tolerances for simulation, we consider random radius to be comprised between R-ϵ and R+ϵ for a small ϵ << 1 µm). The mean volume of the particle is 113 μm^3. For each particle, we compute transport through the orifice and detect the peak of generated voltage pulse. Finally, we can construct statistic particle size distribution of the total sample. Here, we study and compare particle size distribution for two fluidic configurations: 1) the classical case where particle sample is evenly distributed in the whole micro-aperture; 2) the hydrodynamic focusing case where sample rate inside the micro-aperture is controlled by a sheath flow in order to direct the particle sample flow through the gate along the central axis. We will see that, due to inhomogeneous electric field and particle trajectory, computation of the mean size is more precise when we use a hydrodynamic focusing for the sample.

The classical case: Historically, counting and sizing of biological particles in an orifice-electrode system is done for sample evenly distributed in the system. It means that the sample is present in the whole orifice and the part passing close to the edges is subject to strong electric field variations as we said. Thus, as we can see in Figure 10(a), numerical particle size distribution is a right-skewed distribution (the mass of the distribution is concentrated on the left and the right tail is longer). So, due to edge effect, the base of the size distribution is abnormally wide around the real particle size and mean particle size value can be distorted. In Figure 10(c), we expose experimental size distribution obtained for the same configuration. In practice, we also observe a distortion due to statistical doublets. Thus, numerical distribution shape is close to the experimental distribution shape.

Improvement by sample hydrodynamic focusing: To increase resolution of particle sizing measurement by electrical gating, a sample hydrodynamic focusing can be integrated in the orifice-electrode system (see HORIBA Medical patent[3]). More precisely, the sample rate inside the orifice is controlled by a sheath flow in order to direct the sample flow along the central axis of the orifice.
This allows to avoid peaks of electrical field due to edge effects. Figure 9 shows sample concentration with hydrodynamic focusing and its distribution in the orifice. Figure 10(b) exposes particle size distribution in the case of sample hydrodynamic focusing. In Figure 10(d), we expose experimental size distribution obtained for the same configuration. Contrary to the classical case, this distribution tends to be a centered Gaussian distribution, and computation of mean particle size value is more precise.
More precisely, if we compare numerical and experimental statistical distributions for the two cases, we estimate that hydrofocused flow chamber is twice more accurate than in non-hydrofocused method. In particular,

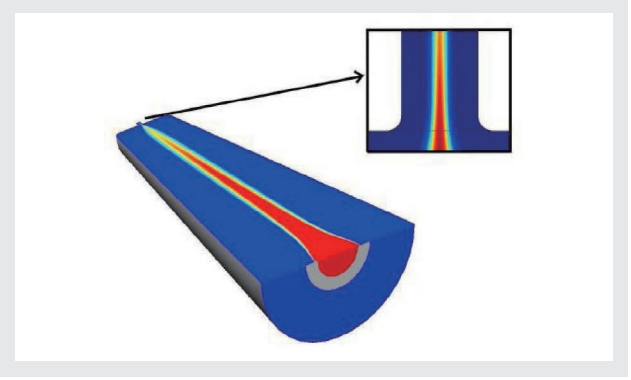

Figure 9 Hydrofocused sample transport.

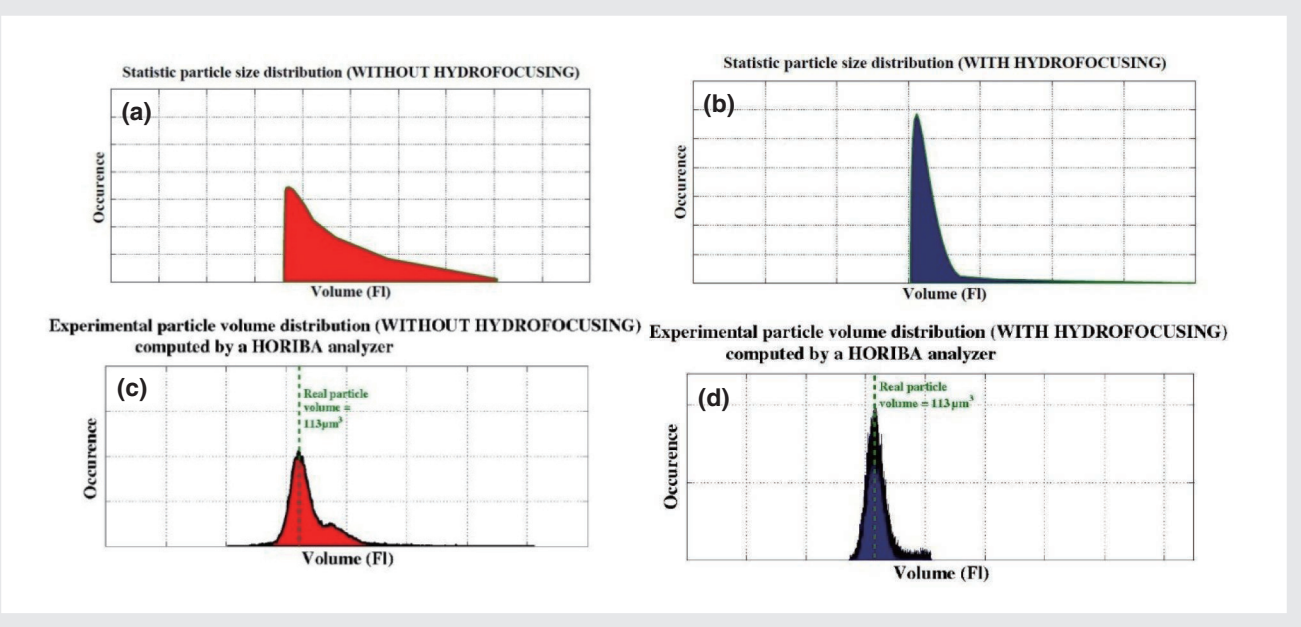

Figure 10 (UP) Numerical Particle Size Distribution (a) classical case, (b) with sample hydrodynamic focusing; (DOWN) Experimental Particle Size Distribution (c) classical case, (d) with hydrodynamic focusing

the variation coefficient for the hydrofocused method is twice smaller than the one obtained without hydrodynamic focusing.

Conclusion and Perspective

A complete numerical approach was developed to tackle the problem of counting and sizing particles by electrical measurement in an orifice-electrode system. The results, in line with experimental tests, highlight the crucial role of trajectory and orientation of particles in generated voltage pulses. This general method can be used to perform particle sizing measurement, in particular by optimizing shape design or fluidic conditions. We are currently working on substantial improvements on the particle transport model, notably including three dimensional processing and deformability of particles under hydrodynamic stresses.

References

[1] Kachel V., Electrical Resistance Pulse Sizing: Coulter Sizing. *Flow Cytometry & Sorting, Second Edition*, J. Wiley & Sons, 1990; p45-80.

[2] Al Quddus N, Moussa W.A and Bhattacharjee S., Motion of a spherical particle in a cylindrical channel using arbitrary Lagrangian-Eulerian method., *J. Colloid and Interface Science*, 2008; 317: 620-630.

[3] European patent EP 0 425 381, Apparatus for counting and determination of at least one leucocyte-subpopulation. - Filing date: 25 octobre 1990; Lefevre D.; Champseix H.; Champseix S.

Damien ISEBE

Scientific Computing Engineer
Research Dept.
HORIBA ABX SAS

Jean-Philippe GINEYS

Measurement System Designer
Research Dept.
HORIBA ABX SAS

Feature Article

Biomarker Discovery using Surface Plasmon Resonance Imaging

Elodie LY-MORIN, Sophie BELLON, Géraldine MÉLIZZI, Chiraz FRYDMAN

Surface Plasmon Resonance (SPR) is an optical technique used to follow molecular interactions (binding) in real time without labeling. It provides information on kinetic processes (association and dissociation rates), binding affinity, analyte concentration and real time molecule detection. This article describes the principle of SPR imaging for high-throughput measurements. An example of a clinical application for the capture and characterization of a potential biomarker of breast cancer is illustrated.

Introduction

Surface Plasmon Resonance (SPR)-based biosensors are used to monitor biomolecular interactions in real time. SPR is an optical technique sensitive to variations of the refractive index near the surface of the sensor (or biochip), thus it does not require the use of labels (fluorescent tag for example) to follow the interaction between a molecule immobilized on the biochip (ligand) and one passed over the surface (analyte). Real time measurements give access to the evaluation of the kinetic parameters of the interaction (association rate, dissociation rate and affinity/avidity).

Physical Principle of Surface Plasmon Resonance

The notion of evanescent wave is at the core of SPR. Let's consider the interface between two media 1 and 2 (glass and liquid for example), with refractive indexes of n_1 and n_2 respectively ($n_1 > n_2$). If the incident angle of the light is superior to the critical angle, the incident light is totally reflected and no light is refracted in medium 2 (Snell – Descartes' law). An evanescent wave is created at the interface. An evanescent wave is non-propagating and its intensity decays exponentially with the distance to the interface. This phenomenon is called total internal reflection. Because the evanescent wave remains confined to the interface of the two media, it is only sensitive to perturbations occurring at the vicinity of the interface. Evanescent waves are thus useful tools to measure in real time modifications of refractive index, layer thickness or molecular adsorption on a surface.

If a golden surface is between the glass and liquid, surface plasmons (= collective oscillations of conduction electrons) of the metal can interact strongly with light to produce a surface plasmon wave. In a total internal reflection situation, surface plasmons can couple with the evanescent wave and resonate. The conditions to reach the resonance of surface plasmons depend on the wavelength, polarization and incident angle of the incoming light, but also on the properties of the metallic layer and the medium above the surface.

How is the SPR Signal Measured?

If the intensity of the reflected light after the biochip in a total internal reflection configuration is measured for different incident angles using a CCD camera for example, it will go through a minimum (Figure 1). This curve is called a plasmon curve. The angle at which the loss of intensity is maximum is called the resonance angle. It corresponds to the resonance of surface plasmons

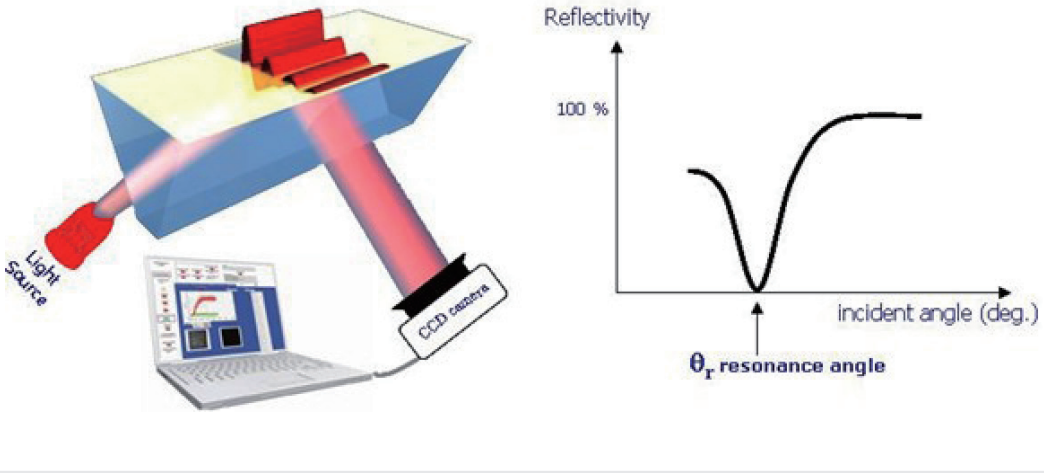

Figure 1 The Dip of Reflectivity in the Plasmon Curve. The intensity of the reflected light reaches a minimum at the resonance angle.

of the gold layer. The position of the resonance angle is characteristic of the metal surface and the medium above it. For example, changes of refractive indexes of the medium above the biochip will induce changes of the position of the resonance angle.

SPR can be used to monitor changes of the refractive index at the vicinity of the biochip surface. For example, a binding event (or mass accumulation) between ligands immobilized on the gold surface and analytes flowing on the surface will induce a change of refractive index and a shift of the plasmon curve, hence the position of the resonance angle. This shift can be monitored in real time. Most SPR-based biosensors retrieve the SPR signal by either following

- the position of the resonance angle versus time ($\Delta\theta$)
- the variation of reflectivity at a fixed angle position versus time (ΔR)

Principle of Surface Plasmon Resonance Imaging

Surface Plasmon Resonance imaging (SPRi) is adding an imaging capacity to SPR. It combines the strength of SPR to monitor label-free biomolecular interactions to the throughput of microarrays. It is thus possible to measure several dozen to several hundred interactions in parallel (multiplexing). Imaging allows monitoring simultaneously the resonance conditions on the whole surface of the biochip. If the biochip contains different immobilized molecules (array of spots), potential interactions on those different molecules can be monitored in parallel. In addition, the real time image of the biochip surface is also retrieved. The "difference image" shows interacting spots when the analyte solution is injected. Our systems are based on prism-coupled SPR (Figure 2). A collimated beam is sent towards the functionalized gold surface through the prism in order to illuminate the entire surface of the biochip (there is no need to perform a 2D scan). After reflection on the biochip, the reflected beam is collected by a CCD array (2D matrix) where each pixel corresponds to a given location on the biochip. The proprietary optical configuration enables a simple yet very precise imaging system without any moving part but a scanning mirror. The rotation of this mirror allows the selection of the working angle relatively to the resonance angle for kinetic measurements. The working angle (position at which kinetic curves will be recorded) is chosen at the highest slope of the plasmon curve. Kinetic measurements consist in monitoring reflectivity variations against time simultaneously on up to several hundred spots (regions of interest).

SPRi is used to monitor changes of the refractive index occurring at the surface of the biochip. A binding event (or mass accumulation) will induce a change of refractive

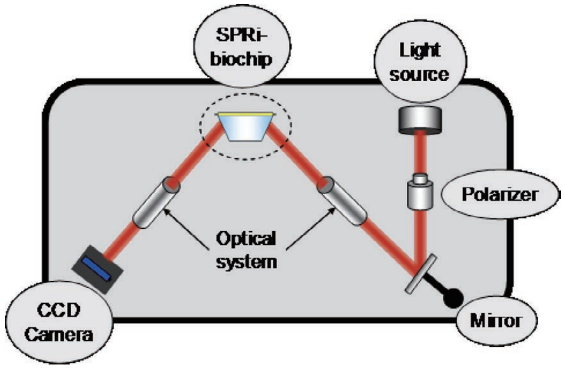

Figure 2 SPRi System Configuration

index and a shift of the position of the resonance angle. SPRi follows the variations of reflectivity occurring at a fixed angle (working angle). The working angle is chosen at the highest slope of the plasmon curves. The principle is described in Figure 3:

- Step A: The ligands are immobilized in an array format on the biochip surface.
- Step B: When the sample solution enters the flow cell (interaction chamber), molecular binding can occur. This induces a shift of the plasmon curves and a variation of reflectivity. The kinetic curves show the variations of reflectivity versus time. The process can also be monitored on the SPRi difference images. White spots correspond to interacting areas of the biochip.
- Step C: When the sample solution leaves the flow cell, the ligand-analyte complex dissociates. This induces a shift of the plasmon curves and a variation of reflectivity. The kinetic curves show the variations of reflectivity versus time. The process can also be monitored on the SPRi difference images as interacting spots become darker.
- Step D: When the ligand-analyte complex is fully dissociated (using a regeneration solution sometimes), the plasmon curves and the kinetic curves return to the initial state. The SPRi difference image is black.

Coupling of SPRi to Mass Spectrometry

The coupling of SPRi biosensors and matrix-assisted laser desorption ionization mass spectrometry (MALDI-MS) is an innovative approach for biomarker discovery in biological fluids. It permits analytes captured by SPRi to be identified and characterized by MS from their molecular weight and peptide sequence. SPRi-MS opens a new method of detection, quantification and structural characterization of proteins of interest. In the future, it could help better discriminate between sub-species within a family of biomarkers. In this context, the complexity lies in the coupling of both techniques.[1] Most strategies require the elution of the bound analyte and its analysis by ESI- (electrospay ionisation) or MALDI-MS. This procedure has many drawbacks (analysis time, no multiplexing capabilities, decreased sensitivity, additional cross-contamination risks, etc...) which delayed the development of SPR-MS in the diagnostic field. The open format of our instruments makes MS coupling easier and faster. The possibility of direct MS analysis on the SPRi sensor was recently shown.[2] The biochip used for SPRi (SPRi-Slide™) is directly transferred to the MS

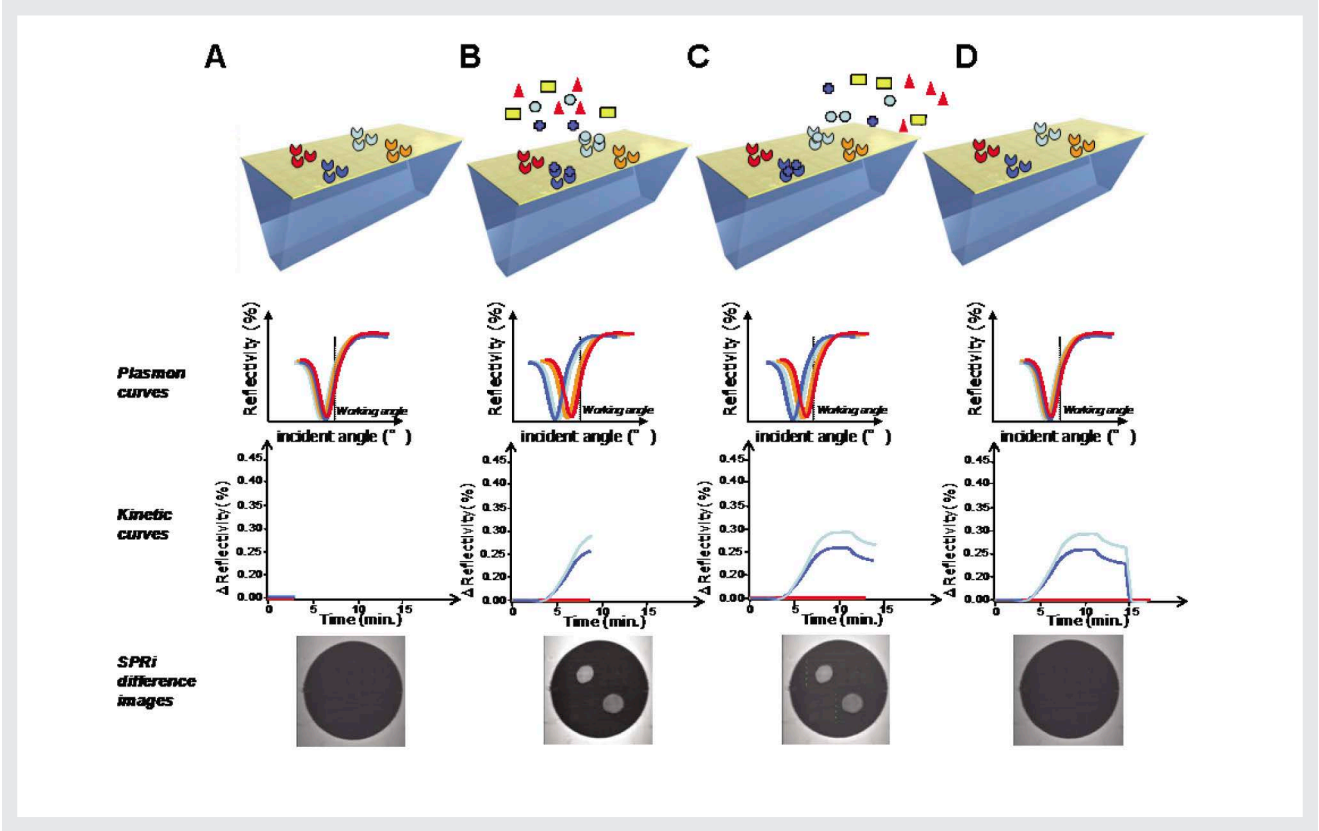

Figure 3 Monitoring of Biomolecular Interactions by SPRi

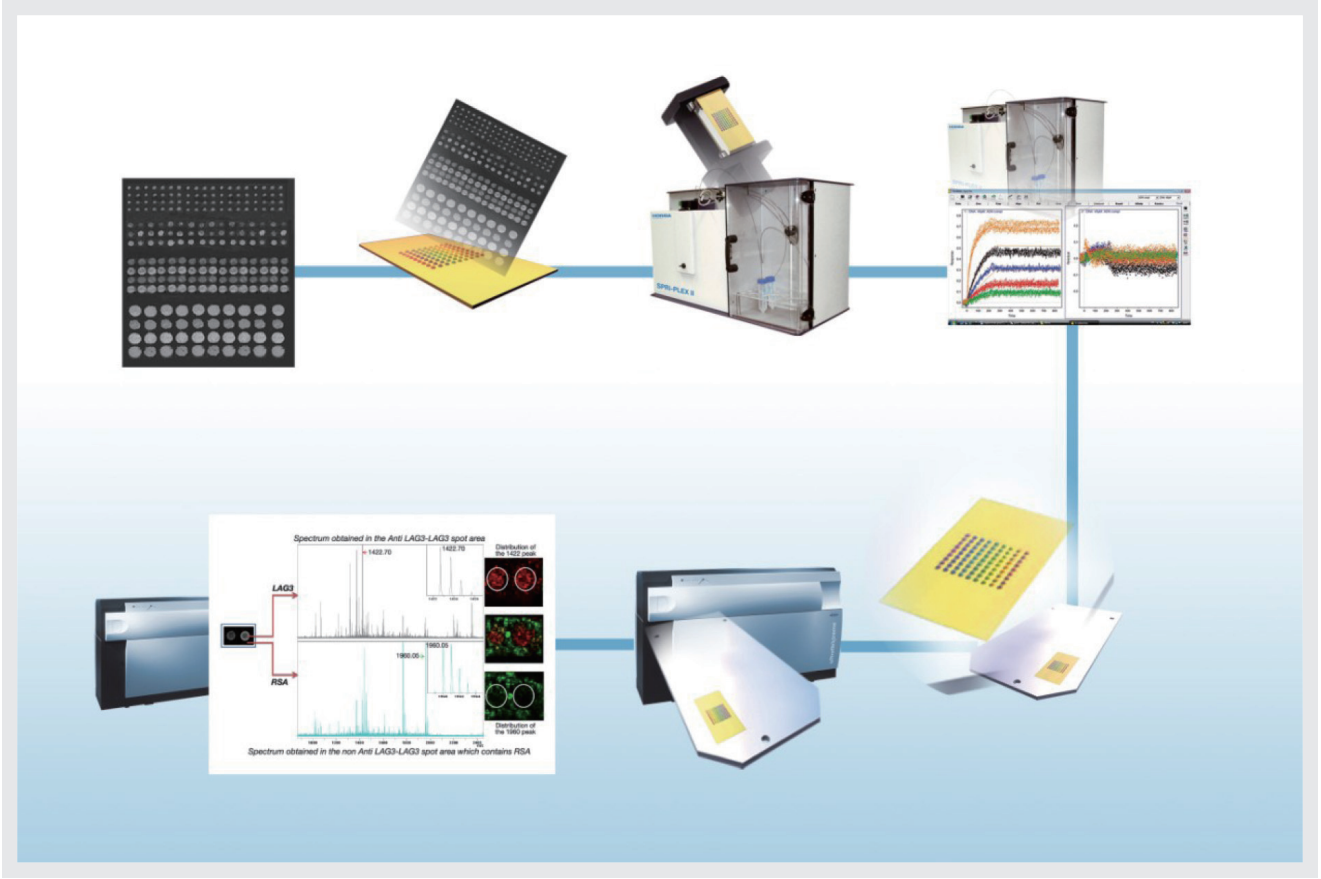

Figure 4 The Coupling of SPRi to MALDI-MS

instrument. There is no need to either elute or re-deposit the bound analyte. The MS enzymatic digestion and the deposition of the MALDI matrix are performed directly on the SPRi-Slide™. The latter is then directly placed on the MS plate holder (Figure 4).

Biomarker Capture and Identification

A proof-of-concept study of SPRi-MS imaging coupling was performed for the detection of LAG3 recombinant protein in plasma. The solution fraction of this protein is a potential biomarker for breast cancer.[3] For this purpose, a mouse antibody (IgG2A) directed against LAG3 was immobilized on a SPRi-Slide™ using a dedicated surface chemistry compatible with MS analysis (NHS chemistry). Before injecting LAG3, rat serum albumin (RSA) was used to avoid non-specific binding on the surface of the biochip. Then, the specific interaction of LAG3 (added in plasma) and IgG2A was monitored using SPRi and images of the interaction were studied. Several femtomoles/mm² of LAG3 proteins were captured by SPRi. After direct processing on the biochip surface (enzymatic digestion and matrix deposition), the SPRi-Slide™ was analyzed using a MALDI-MS imager (Ultraflex, Bruker Daltonics). By showing the distribution of MS peaks specific of LAG3 and RSA respectively, it was possible to build the MS image of LAG3 spots (Figure 5) directly on the SPRi-Slide™. This application pioneers the combination of SPR imaging and MS imaging (MSi). It offers the possibility to gain spatially resolved information on the capture, sequence and molecular weight of clinical biomarkers.

Conclusion

Multiplexed SPRi analysis provides rapid and high-throughput information in real time from up to several hundreds interactions in parallel. The technology is sensitive and does not require the use of labels. It can speed-up the workflow and reduce consumable costs during optimization processes. The coupling with MS analysis is straightforward and easier, which makes it a valuable tool for biomarker identification.

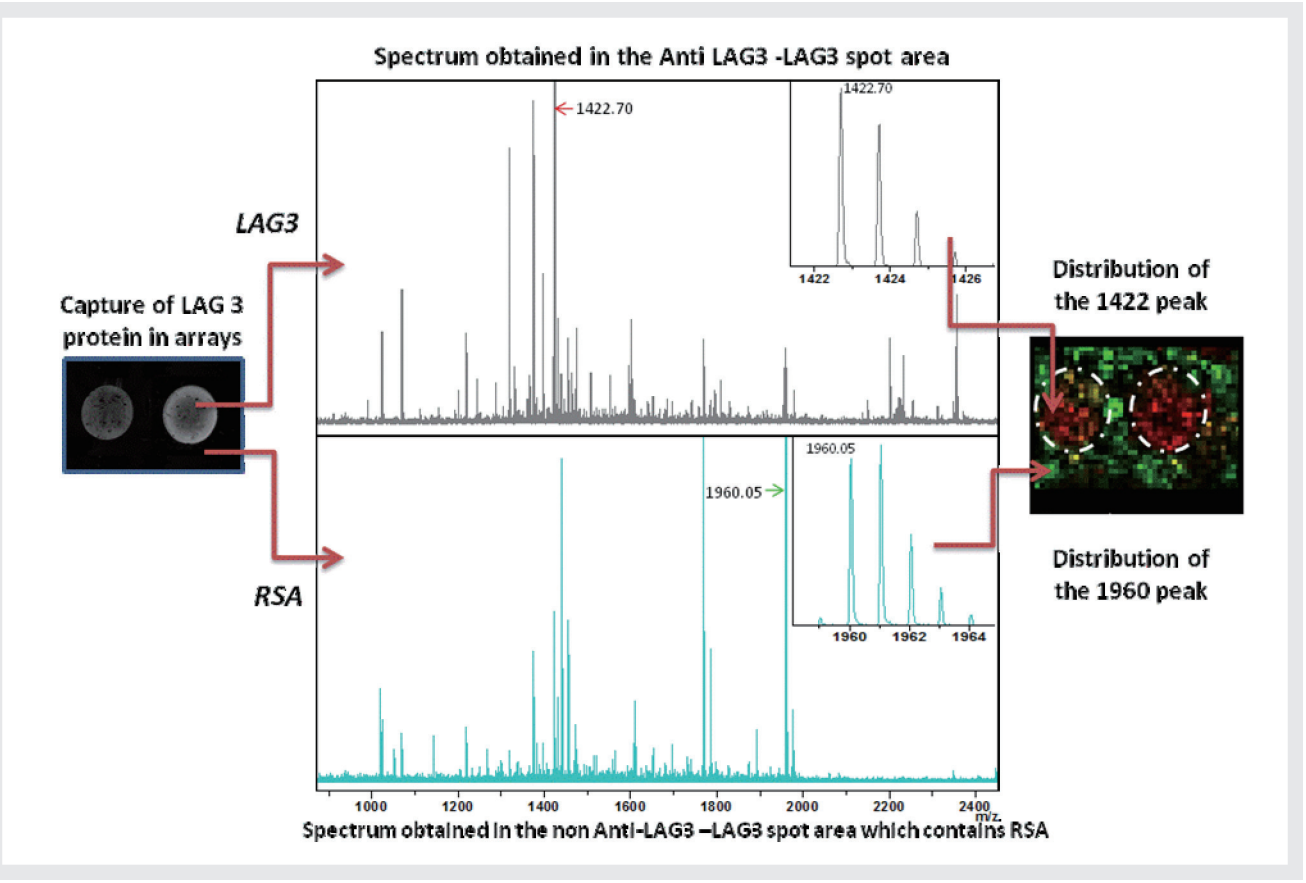

Figure 5 On-a-chip detection, identification and imaging of LAG3 protein (potential marker of breast cancer) at 10 nM in human plasma

References

[1] Boireau and al. (2009) Revisited BIA-MS combination: Entire "on-a-chip" processing leading to the proteins identification at low femtomole to sub-femtomole leveks. *Biosensors and Bioelectronics 24*: 1121-1127

[2] Bellon and al (2009) Hyphenation of Surface Plasmon Resonance Imaging to Matrix-Assisted Laser Desorption Ionization Mass Spectrometry by On-Chip Mass Spectrometry and Tandem Mass Spectrometry Analysis. *Anal. Chem*. 81: 7695-7702

[3] Triebel and al (2006) A soluble lymphocyte activation gene-3 (sLAG-3) protein as a prognostic factor in human breast cancer expressing estrogen or progesterone receptors. *Cancer Letters*. 235(1):147-53.

Elodie LY-MORIN
Bio Sales Engineer
HORIBA Jobin Yvon SAS
Ph. D

Sophie BELLON
Bio Application Lab Manager
HORIBA Jobin Yvon SAS
Ph. D

Géraldine MÉLIZZI
R&D Projet Manager
HORIBA Jobin Yvon SAS

Chiraz FRYDMAN
Product Manager
HORIBA Jobin Yvon SAS
Ph. D

Feature Article

New Developments in GD Spectrometries for Advanced Materials Characterisation

Patrick CHAPON, Agnès TEMPEZ

Over than 70% of recent papers published with GD data refer to HORIBA Jobin Yvon instruments and several key patents give us a world leading position in the field. In this article we will illustrate the latest developments in GD Spectrometries through a survey of recently published articles. Pulsed RF Glow Discharge OES and Plasma Profiling TOFMS provide rapid depth profile composition of thin and thick layers of conductive and non conductive layers with excellent depth resolution, sensitivity and multi-element capability. Thus, they contribute to the development of new advanced materials and, being fast and easy to operate, they are changing the way people consider surface analysis.

Introduction

RF Glow Discharge Optical Emission Spectrometry (RF GD-OES) and the new Plasma Profiling Time of Flight Mass Spectrometry (PP-TOFMS™) developed within a EU project[1] coordinated by HORIBA Jobin Yvon contribute to provide fundamental and strategic information for advanced material's development. Over than 70% of recent papers published with GD data refer to our instruments and several key patents give to HJY a world leading position in the field.

GD Spectrometries rely on the controlled sputtering (Figure 1) of a representative area (2-8 mm) of the

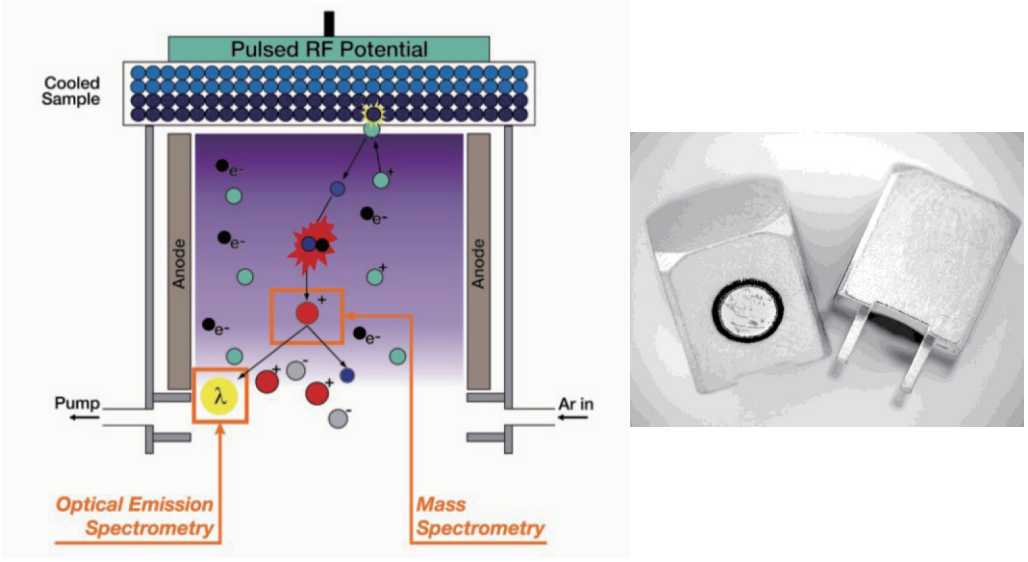

Figure 1 Principle of GD and sputtered crater

material of interest by a high density (10^{14} cm^{-3}) and low energy RF plasma and the parallel detection of the sputtered species excited or ionised in the plasma with a spectrometer. The unique characteristics of the GD plasma allow very fast erosion (2-10 nm/s, several microns per minute) with nanometre depth resolution, absence of charge effect and induced heat and with minimum surface damage (as the incident particles have an average energy of about 50 eV). The spectrometers match the speed of erosion and measure all elements simultaneously at any depth.

The latest developments in GD spectrometries (OES & TOFMS), most of them patented, will be presented through published results covering new materials or coatings applications (nano-scale and upward).

Deuterium and other Isotopes

Access to transport mechanisms within materials can be studied through isotopic depth profiles. With OES, only Deuterium (D) can be measured, with TOFMS all isotopes are readily available. D in OES is measured at the wavelength 121.534 nm and is well separated from the most intense H line at 121.567 nm. D can be accessed from H using the Polyscan™ function (patent 2 651 575A1) or measured simultaneously to H using multiple orders of the diffraction grating. The capability to detect D together with H and all other elements in a depth profile is crucial as it provides unambiguous determination not affected by residual background and is used notably for corrosion studies of fusion reactors materials. In a recent paper[2] Nakamura *et al* have studied with GD-OES the deuterium behaviour at the interface of different metals (SS304, F82H and nickel) oxidized under high temperature heavy water.

PP-TOFMS™ measures all masses at any depth in a depth profile from H (mass 1), D (mass 2) to U (238/235) and beyond (for molecular fragments) and is therefore ideal for obtaining isotopic depth profiles. Baron Wiechec *et al*[3] have looked with PP-TOFMS™ at amorphous anodic alumina permeated by linear pores using ^{18}O tracers. Another example from a paper by Tempez et al[4] is given here with thin anodic Ta_2O_5 layers, material of interest in electronics: ^{18}O enriched layers have been prepared in ^{18}O enriched H_2O. The graph in the figure 2 below is the depth profile of a sample consisting of three bilayers of ^{18}O enriched Ta_2O_5/ non-enriched Ta_2O_5, each Ta_2O_5 layer being 50 nm thick.

Lithium (Li) Batteries

Intense research is conducted on Li-ion batteries used in electric or hybrid vehicles and electric power tools. Both positive[5] and negative[6] electrodes have been studied with GD, with research notably conducted on degradation mechanisms and coatings for thermal stability and cyclic performance. Li cannot be measured with X Ray-based techniques but it is very sensitive both in OES (measured at wavelength 670.791 nm) and MS (Li has 2 stable isotopes, most abundant at mass 7).

The GD source does not require UHV and sample handling is usually straightforward as the specimen is simply placed against an O-ring sealing the discharge chamber. However this ease of use, generally an advantage, might be a drawback for some Li based materials where contact with air should be minimized or prevented. A transparent dedicated chamber has therefore been designed and patented (P 2001-197308) allowing easy sample handling to the instrument and GD analysis under Ar inert gas atmosphere.

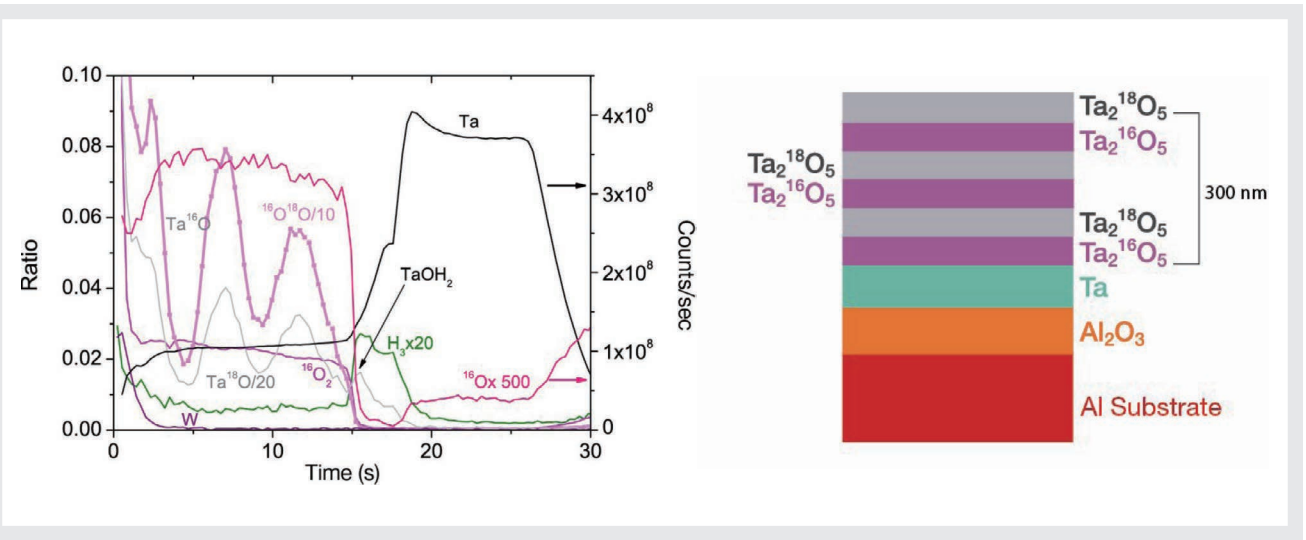

Figure 2 Isotopic Depth Profile with PP-TOFMS

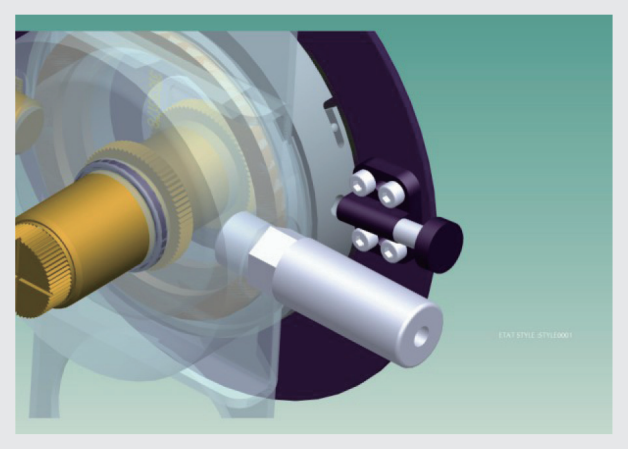

Figure 3 Patented "Li bell"

A similar concept was used by Lobo et al for PP-TOFMS[7] and shown to minimize residual air background.

Plasma Cleaning Strategies

A specific way of tuning the RF GD plasma with very soft conditions (typical power less than 3 W and pulsed mode) has been described by Molchan et al[8] and used to clean sample surfaces prior to depth profile analysis – a strong reduction of surface C notably was observed in OES and TOFMS.

With slightly stronger conditions, pulsed mode and very short erosion time, GD plasma can be used to structure surfaces at the nano-scale and upward or, as demonstrated by Shimizu et al,[9] to prepare sample surfaces for SEM observation (patent EP 1715504A2, 2006) – not only by eliminating residuals of polishing or removing a superficial oxide layer but also by revealing the grain structure or the phases within the material under investigation due to preferential sputtering over the large sputtered area. (Figure 5)

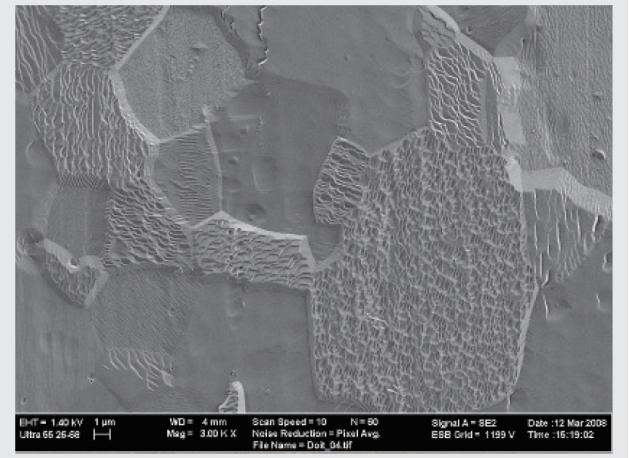

Figure 4 SEM View after GD Sputtering, Grain Structure is revealed

Pulsed Operation

The patented development of a pulsed RF source (patent 10 52883, 2010) having the speed and capability of matching impedance changes in pulsed mode has represented a major step forward for many applications. Pulsed operation allows minimizing the average power (and so the thermal constraints) while keeping high instantaneous power for sensitivity. Pulsed operation is also beneficial for the precise control of the crater shape offering enhanced depth resolution.[10]

Depth Resolution

The following example illustrates the enhanced depth resolution offered by the pulsed RF operation – here with OES detection. The sample is a mirror for X-ray and features 60 stacks each with Si/B_4C/Mo multilayers. Each layer is less than 7 nm thick. (Figure 5)

In addition, in the case of TOFMS detection and RF pulsed mode a significant enhancement of the ion signals after the pulse ends is observed linked to the ionisation mechanisms. Such effect (not observed in OES) was central to the work done within the EU project EMDPA due to its analytical benefits and for the information it provides on plasma physics and plasma surface interactions; following this work all EMDPA partners were invited to contribute to the chapter on thin/thick films in a new Handbook of Mass Spectrometry[11] where most findings are summarized.

The orthogonal configuration in the PP-TOFMS and the speed of TOFMS detection allows for monitoring the transient signals over the ms period of the pulsed RF source with a high duty cycle. So not only the full mass spectrum is obtained at each depth within a depth profile but also at each time during the pulses (the so called "source profile") offering the possibilities to select for each element optimum time region for intense signals, high signal to noise, and time separation of isobaric interferences which greatly enhances analytical results. (Figure 6)

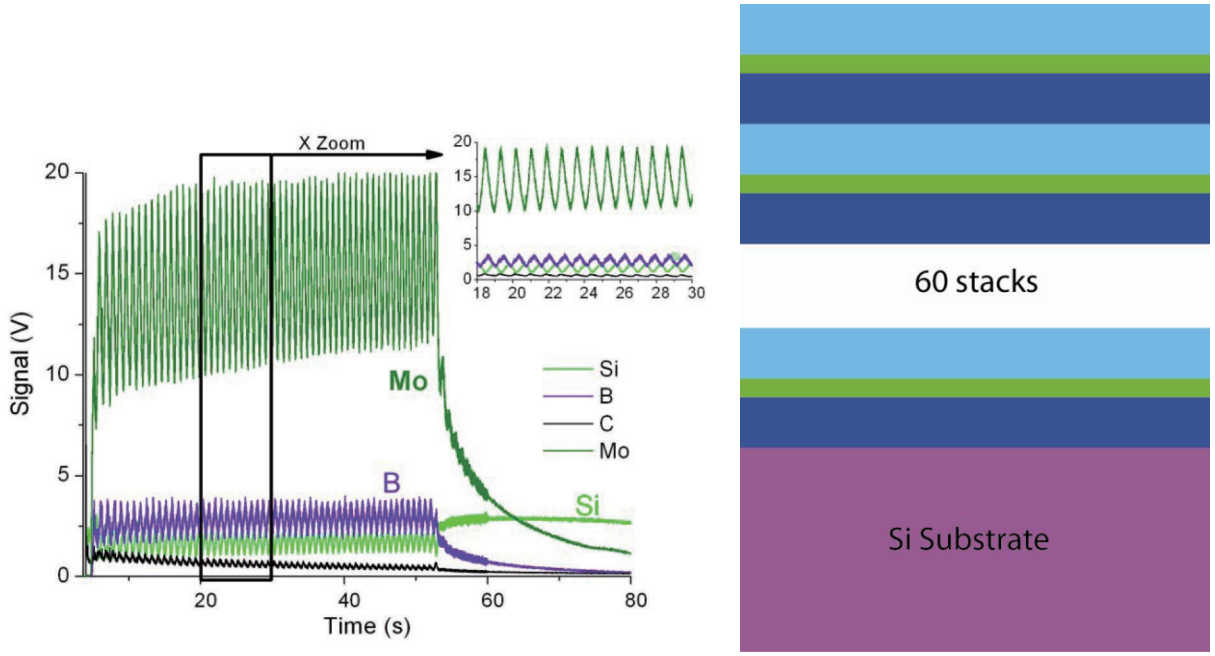

Figure 5

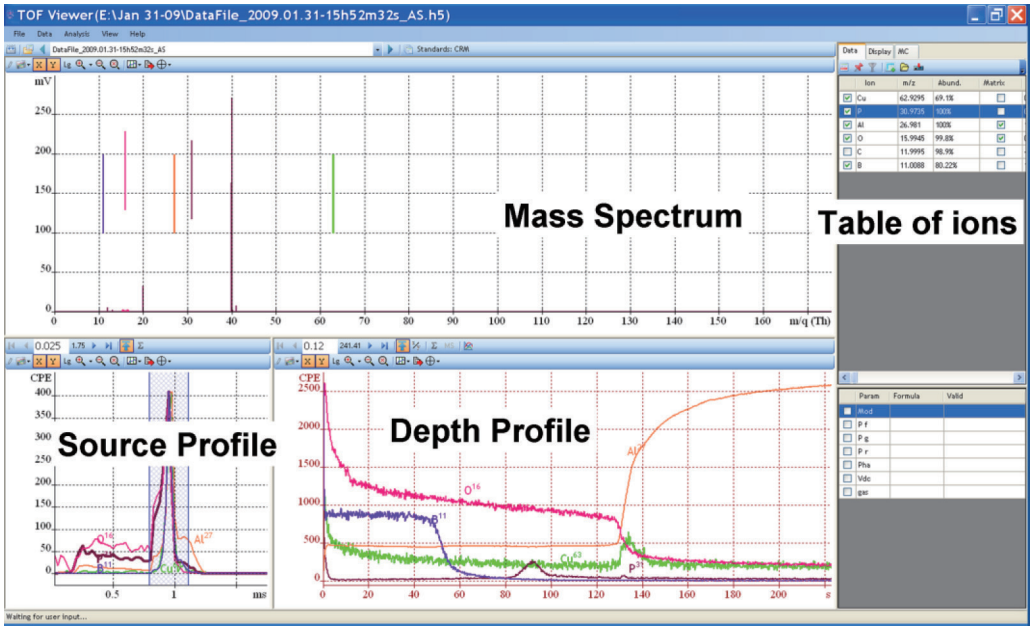

Figure 6

Polymers

Many advanced materials feature polymer layers or substrates.

GD-OES provides elemental depth profile analysis. However the emission spectrum includes some regions featuring emission bands from molecular origin that can be detected. They are often found at the surface (hydroxide OH band at 306 nm, good tracer of humidity[12]) or when polymers are to be measured. They indirectly indicate that the GD plasma may content some information of interest beyond the elemental composition. Simply the nature of the detection (OES) is not suitable to

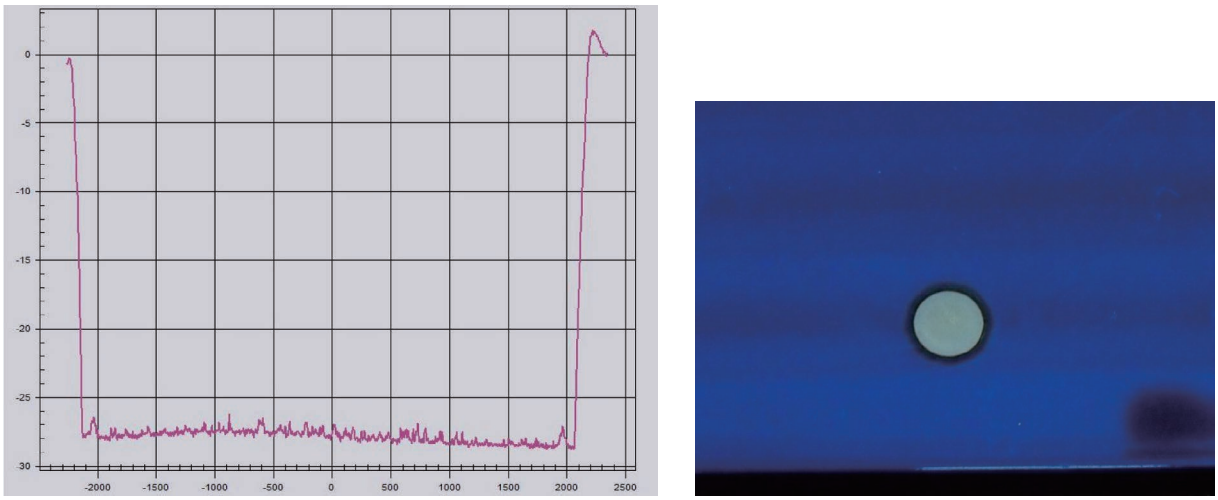

Figure 7 GD crater obtained on a car part covered with an organic layer – over 25 microns were sputtered in 3 minutes

interpret this information correctly and as such, bands do not provide any insight on the chemistry of the molecules as compared to Raman spectroscopy and they are more considered as a nuisance for the measurements of elemental lines in their vicinity.[13]

With PP-TOFMS however, when a polymer is sputtered with soft conditions some significant fragments can be detected if they are ionized in the afterglow region of the pulse. The paper written by Tuccitto *et al* on this topic within EMDPA was awarded the RCM Beynon Prize for best paper published in 2009/2010.[14]
By selecting the adequate source profile region after the RF pulse, so called "molecular depth profile" could be obtained which might allow for instances to distinguish different polymers in an organic solar cell.

However in many cases, polymer layers can be extremely thick (10-100 µm) and as the sputtering of polymers has to be done very slowly, with soft operating conditions in order to minimize unwanted sample degradation this leads to long analysis times and often poor crater shapes affecting the depth resolution and limiting the practical use of the techniques for these applications. To take an example from automotive industry, it is known that painted car bodies for instances have to be sputtered for nearly 2 hours[15] before the metallic coatings below the paint can be reached, where for comparison inorganic multilayers can be profiled in minutes. (Figure 7)

The most recent development made by both French and Japanese HORIBA GD labs (patent 1057722, 2010) completely solves this drawback and has already brought substantial benefits (orders, retrofits and invitations to participate to some R&D projects). This new method allows for ultra fast and uniform sputtering (minutes) of organic layers and is therefore ideal for observing embedded layers with nanometre depth resolution. This new invention has already been successfully applied to painted car bodies, protecting layers on cardboards used in packaging, DVDs etc.

PV Photovoltaics

HJY GD references in PV include world leading companies such as First Solar (US), Nanosolar (US), Solar Frontier (Japan) as well as major research institutes such as ZSW (Germany).
We are coordinating a new project with Ecole Polytechnique (France) for PP-TOFMS. In addition, we have been asked to participate in two national RD and one EU FP7 projects by leading laboratories in the field.
There is therefore a growing interest in the capabilities of GD for PV applications [16], [17] due to the fact that technologies for PV evolve very rapidly with a definitive trend towards thin-films – the driving force of all research is cost reduction for which thin-film technologies are promising.

PV films can be based on Si with various dopants, CdTe (as for First Solar), CIGS (quaternary CuInGaSe2 - as for Solar Frontier and others, Figure 8), or organic films.

Hybrid configurations are also subject to intense research with for instance, layers made of Si nanowires coupled to organic layers or nanoparticles deposited inside the layers. Investigations are also made on alternative substrates to bulk glass to create flexible cells. However, even if materials evolve and change rapidly needs for characterisation and control are now well identified. Thin-film technologies involve a number of operations to be performed and key parameters to be followed carefully (including time, temperature etc – any variation to the optimum conditions inducing major defects in the final product). Therefore rapid characterisation to assess efficiency and provide immediate feedback to the process by measuring depth distribution of major, traces, and contaminations and aspect ratio in thin to thick films (most cells have now a total thickness of 3-5 µm with most layers being less than 1 µm thick) are crucial.

The GD spectrometries have therefore the potential to be recognised as the metrological companion to solar cells elaboration and applied worldwide.

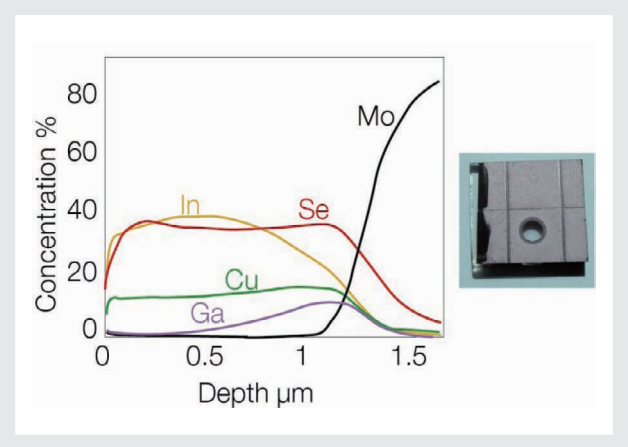

Figure 8

Conclusion

More patents have been awarded, notably some related to the use of magnetic fields in TOFMS and OES (0950848 & WO_2010_092301) and several new papers from on going researches are in preparation.
The 6th international GD day (http://www.horiba.com/fr/scientific/products/atomic-emission-spectroscopy/6th-gd-day/) will be the occasion of a review of new results and applications (e.g. bio compatible or nano-structured materials, PV, hard disks etc) and a special issue of the Journal of Analytical Methods in Chemistry will then be published associated to this GD day. Finally a GD group has just been created through LinkedIn with the ambition to gather GD' friends world wide.

References

[1] www.emdpa.eu
[2] H. Nakamura, et al, "Deuterium behavior at the interface of oxidized metal under high temperature heavy water", *Fusion Eng.* Des. (2012), doi:10.1016/j.fusengdes.2012.02.044
[3] A. Baron Wiechec et al, "18O distributions in porous anodic alumina by plasma profiling time-of-flight mass pectrometry and nuclear reaction analysis", *Surface and Interface Analysis* (2012) doi 10.1002/sia.5032
[4] A. Tempez, et al, "$^{18}O/^{16}O$ isotopic separation in anodic tantala films by glow discharge time-of-flight mass spectrometry", *Surface and Interface Analysis* (2009), 41, 966-973
[5] Y.Saito et al, "Investigation of positive electrodes after cycle testing of high-power Li-ion battery cells IV. An approach to the power fading mechanism by depth profile analysis of electrodes using glow discharge optical emission spectroscopy", *Journal of Power Sources* 174 (2007) 877–882
[6] H. Gab.Song et al, "The effects of LaPO4 coating on the electrochemical properties of Li[Ni0.5Co0.2Mn0.3]O2 cathode material" (2012) doi:10.1016/j.ssi.2011.12.014
[7] L. Lobo et al, "A purged argon pre-chamber for analytical glow discharge—time of flight mass spectrometry applications", *Journal of Analytical Atomic Spectrometry* (2011) 26, 798-803
[8] I. Molchan et al, "The concept of plasma cleaning in glow discharge spectrometry", *J. Anal. At. Spectrom*., (2009), 24, 734–741
[9] K. Shimizu, T. Mitani. "New Horizons of Applied Scanning Electron Microscopy". Springer (2010).
[10] Ph. Belenguer et al, "Pulsed glow discharge for analytical applications", *Spectrochemica Acta* B, 64, (2009), 623-641
[11] P. Le Coustumer, P. Chapon, A. Tempez et al. "Thin and thick films analysis" chapter 41 of Applied Handbook of Mass Spectrometry. Wiley (May 2012)
[12] N. Fukumuro et al, "Confirmation of hydroxide in electroless cobalt alloy films by GDOES", *Transactions of the Institute of Metal Finishing*, 2007, vol 85, N°2
[13] T. Nelis, R. Payling. "Practical Guide to Glow Discharge Optical Emission Spectrometry". RSC 2003
[14] N. Tuccitto et al, "Time-of-flight pulsed radio frequency glow discharge mass spectrometry for molecular depth profiling of polymer-based films", *Rapid Communications in Mass Spectrometry*, 23, 549–556 (2009). *Paper awarded the RCM Beynon Prize for best paper published in 2009/2010*
[15] T. Torok, J Pallosi et al, "Characterizing Coatings of Car Body Sheets by GD OES" chap 11 of High Performance Coatings for Automotive and Aerospace Industries, Nova Science Publishers (2011)
[16] J . Pisonero et al, "Quantitative depth profile analysis of boron implanted silicon by pulsed radiofrequency-Glow Discharge-Time of Flight Mass Spectrometry", Solar Energy Materials and Solar Cells, 94, 1352-1357 (2010).
[17] S.W. Schmitt et al, "Chemical and optical characterisation of atomic layer deposition aluminium doped ZnO films for photovoltaics by glow discharge optical emission spectrometry", J. *Anal. At. Spectrom* DOI: 10.1039/c0ja00158a

Feature Article New Developments in GD Spectrometries for Advanced Materials Characterisation

Patrick CHAPON

GD Product Manager
HORIBA Jobin Yvon SAS

Agnès TEMPEZ

PP-TOFMS Product Manager
HORIBA Jobin Yvon SAS
PhD

Feature Article

High Performances Diffraction Gratings for Scientific Applications

Arnaud COTEL, Pierre PICHON, Audrey LIARD, Yann BERNARD, Frédéric DESSEROUER, Olivier NICOLLE

High performances diffraction gratings are usually key components for many scientific applications. Diffraction gratings are used in scientific studies to analyze, measure, propagate or tailor the light sources issued from nature, laser radiation or synchrotron radiation. The three main scientific applications we present are based on three different grating types: *Laser Pulse Compression Gratings, Space Flight Gratings* and *XUV Synchrotron Gratings*. These high performances diffraction gratings for scientific applications are designed and manufactured by HORIBA Jobin Yvon SAS (HJY part of HORIBA Scientific) at Longjumeau (France) in the Optical Components Division.

Introduction

The history of HJY can be traced back to 1819, and began with the collaboration of famous physicists such as Augustin FRESNEL and François ARAGO. Committed to excellence and high performances in optics from its very beginning, it has consistently been one of the leading innovators of state-of-the-art diffraction gratings. In 1968, HJY introduced the first commercially available holographic diffraction grating opening the door to new scientific experiments and applications. Projects are typically identified well in advance since gratings represent a key component for these major facilities and/or projects and such programs may last for 3 or 4 years before the final gratings are needed.

In the laser field, HJY provided the first large gold-coated gratings for the demonstration of the Chirped Pulse Amplification[1] (CPA) technique in 1983. Since this date, HJY pulse compression gratings are widely used by scientists in laser facilities worldwide to produce ultra-short pulses in the femtosecond regime (1 femtosecond = 10^{-15} second) and ultra-high peak power (Petawatt regime = 10^{15} Watt) and intensity up to 10^{20} W/cm^2. Such ultrahigh-peak-power laser systems are used in fundamental research areas, such as high-field physics and the generation of ultra-short energetic electrons and ions. One of the main applications of ultra-intense lasers using HJY pulse compression gratings is the particle acceleration. Scientists develop very compact particles accelerators by laser-plasma interaction. The goal of these compact particles accelerators is to accelerate electrons to very high energies (1 GeV, or a billion electron volts) in a distance of centimeters rather than hundreds of meters with classical accelerator.

Synchrotron facilities and XUV beamlines require for radiation instrumentation very high performances diffraction gratings. HORIBA Jobin Yvon's holographic ion-etched lamellar gratings exhibit ultra-low stray light levels, making them ideal for synchrotron and VUV to soft X-ray applications. These gratings are fully compatible with the latest synchrotron systems, as they are fully engraved in the substrate material and can therefore withstand high thermal loads. A recent innovation developed by HJY in collaboration with SOLEIL Synchrotron is the Variable Groove Depth (VGD) grating we present here.

For space flight missions, HJY is often selected by NASA

or ESA agencies for their most demanding experiments. For example, HJY supplied the first 400×400 mm 6000 gr/mm aberration-corrected grating for the Lyman Fuse mission. Similarly, the Hubble Telescope is equipped with an imaging spectrograph, STIS whose gratings are from HJY. In 2000, the company received a rare NASA award in recognition of the holographic gratings for the Cosmic Origin Spectrograph (COS) instrument that will enable a new generation of scientific exploration for the Hubble Space Telescope. More recently, in 2006, NASA Jet Propulsion Laboratory, Organized an award ceremony to acknowledge the on-time delivery of 3 «remarkable» gratings from the HJY production team for the Orbiting Carbon Observatory (OCO) satellite. The OCO satellite's mission consists in accurately measuring the CO_2 content in the atmosphere, in order to evaluate the effect of human activity on our climate and global warming. In 2009-2011, both projects Jovian InfraRed Auroral Mapper (JIRAM) conducted by NASA and Visible Infrared Hyperspectral Imager (VIHI) conducted by ESA, we present here were a great challenge for HORIBA Jobin Yvon grating team. The very high performances gratings produced for these projects were among the most difficult and challenging we have ever produced.

Laser Pulse Compression Gratings Application

Particles Acceleration by Laser-Plasma Interaction

One of the main applications of ultra-intense lasers using HJY Pulse Compression Gratings (PCG) is the particle acceleration. Scientists develop very compact particles accelerators by laser-plasma interaction. The goal of these compact particles accelerators is to accelerate electrons to very high energies (1 GeV, or a billion electron volts) in a distance of centimeters rather than hundreds of meters with classical accelerator. Such ultra-intense lasers are developed worldwide, as for example the BELLA Petawatt laser developed by THALES company for Lawrence Berkeley National Laboratory (LBNL) or the PULSER Petawatt laser developed by Gwangju Institute of Science & Technology - Advanced Photonics Research Institute (GIST-APRI, South Korea).

The use of the Chirped Pulse Amplification (CPA) is widely employed to produce high-energy laser pulses in the femtosecond and picosecond regimes. The basic scheme of a high-intense femtosecond laser is presented on Figure 1. A femtosecond oscillator generates an ultra-short laser light in the near-IR, nanojoule energy, MHz repetition rate. By using only the femtosecond oscillator, the scientific applications are really limited, so an increase of the laser energy and intensity is needed. To increase the laser intensity, the laser pulses need to be stretched from femtosecond to nanosecond duration to avoid damages in optical components. Then, several stages of optical amplifiers allow achieving the Joule energy level. The final stage and the most critical part of the laser is the gratings pulse compressor. The compressor stage is based on a pair or a quadruplet of reflection diffraction gratings; associated with the need to have large gratings with high efficiency, laser-induced damage threshold remains the main limiting factor towards generating higher-energy

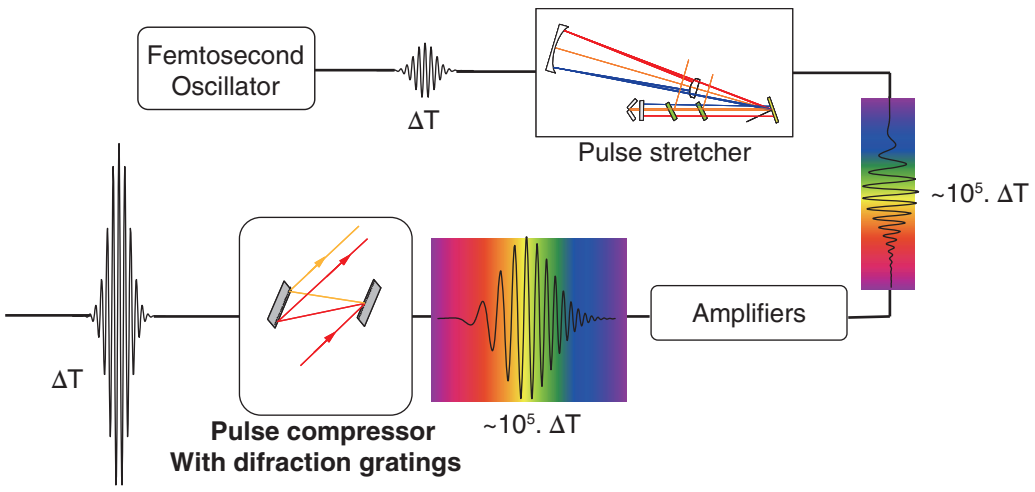

Figure 1 Chirped Pulse Amplification (CPA) technique using high performances diffraction gratings for pulse compression

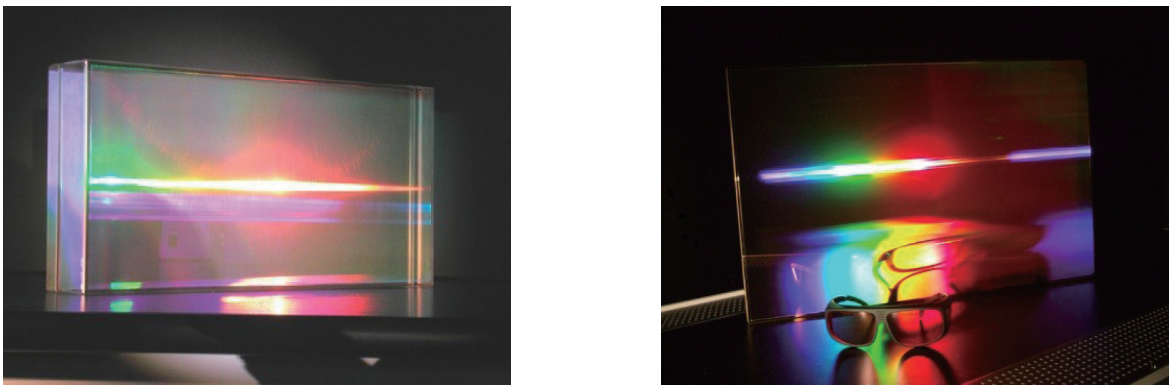

Figure 2 Picture of Multi-Layer Dielectric (MLD) grating (left) and Gold-coated grating (right)

compressed pulses.

In the pulse compressor, two or four large pulse compression holographic gratings (gold-coated or ion-etched on multi-layer dielectric coating represented on Figure 2) are installed in a vacuum chamber to generate a peak power in the range of the Petawatt (10^{15} W) and an achievable intensity up to 10^{20} - 10^{22} W/cm^2.

To achieve these performances, HJY has continuously improved the process and capabilities to be able to propose now to the laser community very large gratings (up to H360×W565×T40 mm). Manufacturing processes and characterization of such pulse compression gratings (PCG) are extremely long and complex.

By installing HJY large pulse compression gratings in the laser system, GIST-APRI team in Korea has succeeded to compress femtosecond pulses up to 1 Petawatt at 0.1 Hz repetation rate[2] which is the world record of peak power at this repetition rate. In parallel, the objective of the BELLA laser, developed by THALES company for LBNL, is to generate 1.3 PW at 1 Hz repetition rate.[3] The large pulse compression gratings manufactured by HJY have been installed in 2011 in a large vacuum chamber to allow the generation of high peak power (Figure 3).

Figure 3 Pulse Compressor vacuum chamber with four HJY gold-coated diffraction gratings

Pulse Compression Gratings manufactured by HJY achieve very high-performances:

- High diffraction efficiency better than 90% to transmit the precious amplified energy,
- Broadband efficiency over 150-200 nm to preserve the amplified spectrum and recompress to the Fourier transform-limit pulse duration,
- High wavefront quality to be able to focus in a diffraction-limited spot,
- High laser damage threshold (LDT) to resist to the highest energy and intensity in the laser system,
- Compatible with air and vacuum,
- Long life time in a pulse compressor.

These gratings can be customized to be adapted to various laser configurations.

XUV Gratings for Synchrotron Application

Synchrotron facilities and XUV beamlines requires for radiation instrumentation very high performances diffraction gratings. HORIBA Jobin Yvon's holographic ion-etched lamellar gratings exhibit very high performances in terms of stray light, diffraction efficiency and by reducing the harmonics contamination. Depending on the application, different types of VUV gratings can be manufactured with various shape (plane, spherical, cylindrical, toroidal), groove density (constant, aberration corrected or Variable Line Spacing (VLS) type)

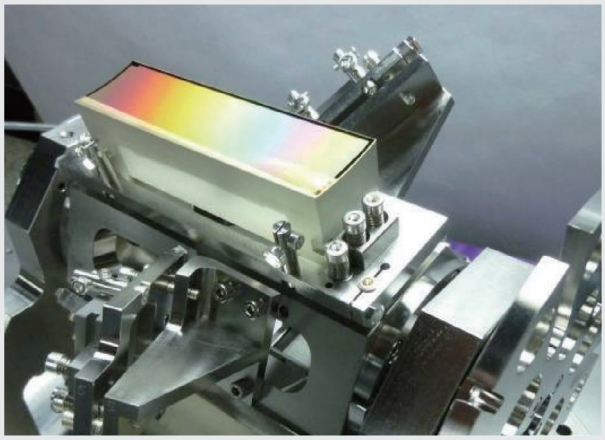

Figure 4 VUV Synchrotron Grating

(Figure 4). The Variable Line Spacing grating displays a groove density variation that is defined by a polynomial law. This type of grating is commonly used in synchrotron beamline designs to correct for the defocusing of a grating monochromator. HORIBA Jobin Yvon and the synchrotron community together have developed software tools to define holographic recording geometries for VLS gratings, which allow us to produce gratings according to an arbitrary polynomial VLS law.

In the VUV gratings field, HJY took part of a major innovation: the Variable Groove Depth (VGD) grating type. The VGD grating type, developed in collaboration with SOLEIL Synchrotron (France), consists in tuning the groove depth of the VUV grating (Figure 5).

By tuning the groove depth from h_{min} to h_{max} (~ 3 or 4 h_{min}), VGD gratings allow a continuous blaze wavelength adjustment and harmonic contamination adjustment, with the same dispersion (same groove density). So, the groove depth is continuously varying from one edge of the ruled area to the other edge. As a result, the grating energy range is enlarged only by translating the VGD grating and all the other high performances of classical HJY ion-etched holographic VUV gratings are conserved. As it is shown on the Figure 5, for different value of groove depth (*h*), the maximum efficiency can be shifted in the energy range.

Space Flight Gratings

HORIBA Jobin Yvon manufactures since a long time space flight gratings either holographic or ruled, in reflection and in transmission. In the past two years, two main projects drove us beyond what we thought being our limits for the manufacture of ruled gratings.

A Grating for JIRAM – Jovian InfraRed Auroral Mapper

The goal of the first one, the NASA JUNO mission, was to obtain a high resolution image of the Jupiter atmosphere and to retrieve its spectral properties in the 2-5 µm spectral range. The JIRAM instrument, for which a low density and low blaze angle grating had to be made, was one of the instruments of this mission. Such a ruled grating is difficult to obtain because of the heavy load on the diamond, which corresponds to tons per cm^2. This makes all the characteristics inherent to ruled gratings more difficult to obtain than for more conventional ones (medium density – few hundreds gr/mm and medium blaze angle). Groove profile (giving the efficiency) and

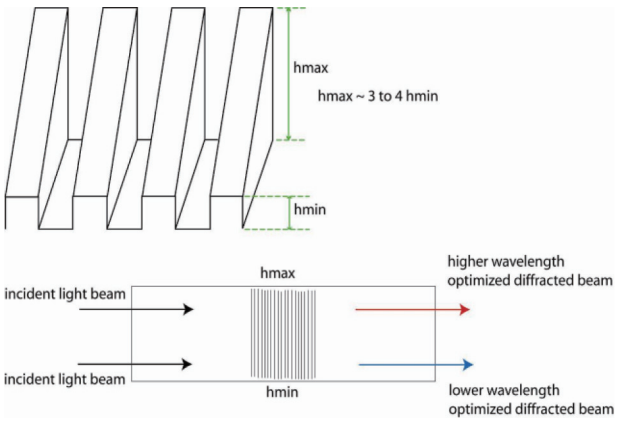

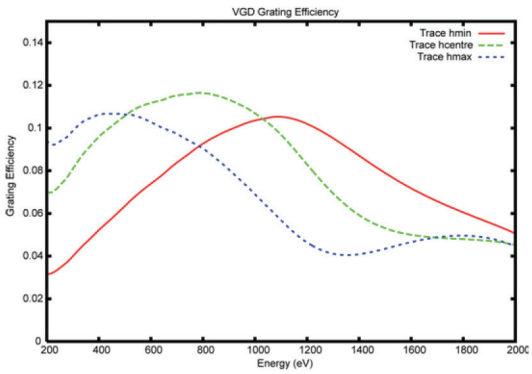

Figure 5 Variable Groove Depth (VGD) grating

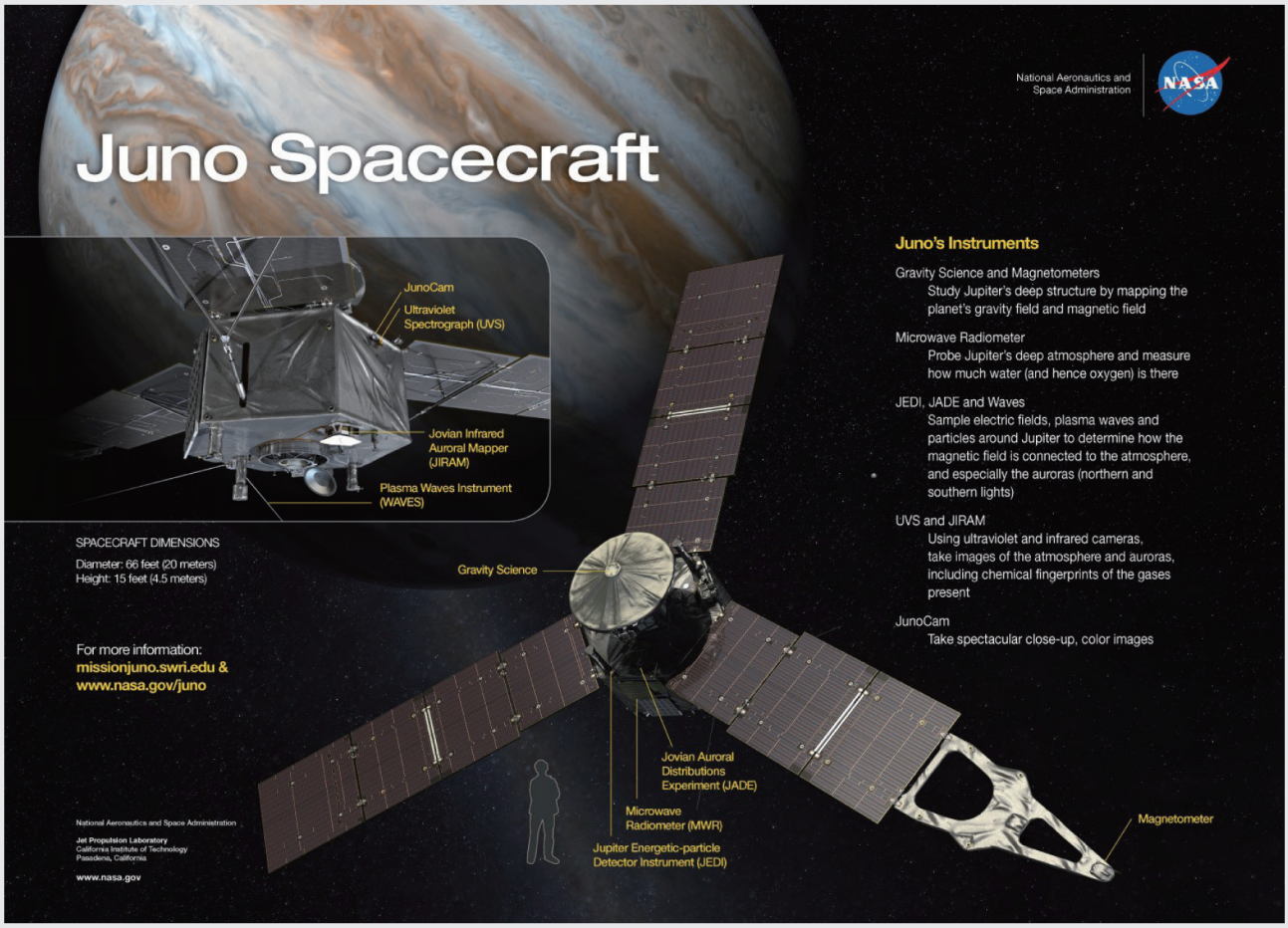

Figure 6 Picture of the JUNO Spacecraft including the HJY grating in the JIRAM instrument

straightness of the grooves (giving the wavefront deviation) are the most critical. The grating, 60×32 mm in dimensions, has 30.3 gr/mm and a very small blaze angle. A relative efficiency of 50% at the peak expected by our customer was raised to more than 90% absolute for the flight model and 85% absolute for the qualification model. The total amount of stray light, mainly due to random groove position errors as low as 18 nm RMS, was also a good surprise for the customer who expected much more from a ruled grating. The permitted wavefront deviation of λ was crushed to λ/8.

All these performances were maintained after severe environmental tests: thermal cycling between 70 °C and -175 °C and 24 h at 50 °C and 95% relative humidity did affect neither optical properties nor aspect, proving that our masters can undergo space conditions. The 4 tons Juno spacecraft was launched August 5, 2011 on an Atlas V rocket from Cape Canaveral and its arrival above Jupiter is expected for July 2016.[4]

A Grating for VIHI – Visible Infrared Hyperspectral Imager

After the success of JIRAM, the customer came back to HJY, asking for a more challenging grating, with a low blaze angle, low groove density and very large spectral range.

The instrument called VIHI (Visible Infrared Hyperspectral Imager) was part of numerous instruments of an international mission Bepi Colombo for Mercury surface observation. Composed of a telescope and spectrometer, the optical configuration of VIHI permits to obtain hyperspectral imaging of the planetary surface in the spectral range 400 - 2000 nm (spectral sampling of 6.25 nm), with a spatial sampling down to 100 m at the periherm. The challenge was to make a single grating with the highest efficiency at the opposite sides of the spectrum were the wavelengths of interest were situated. Finally neglecting the middle of the spectrum, we designed and fabricated a grating with almost twice the

efficiency expected by the customer at 400 nm and 50% above the one expected at 2000 nm. As for JIRAM, the gratings succeeded all the environmental tests without any degradation of the optical properties, proving once again the quality of our processes. The launch of the spacecraft is programmed for 2015 by an Ariane V launcher for an arrival in orbit in 2022.[5]

References

[1] D. Strickland, and G. Mourou, *Opt. Comm*. 56, 219 (1985).

[2] J. H. Sung, S. K. Lee, T. J. Yu, T. M. Jeong, and J. Lee, *Opt. Letters*, 3021-3023, vol.35, No.18 (2010).

[3] S. Laux *et al, Opt. Letters*, 1913-1915, vol.37, No. 11 (2012).

[4] http://www.nasa.gov/mission_pages/juno/main/index.html

[5] http://sci.esa.int/science-e/www/area/index.cfm?fareaid=30

Arnaud COTEL

Scientific Gratings Technical Sales & Marketing Manager
HORIBA Jobin Yvon SAS
Ph. D

Pierre PICHON

Diffraction Gratings R&D Engineer
Optical Component Division
HORIBA Jobin Yvon SAS
Ph. D

Audray LIARD

Diffraction Gratings Production Manager
Optical Component Division
HORIBA Jobin Yvon SAS

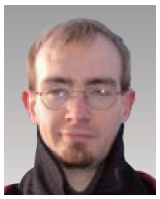

Yann BERNARD

Project Manager
Optical Component Division
HORIBA Jobin Yvon SAS

Frédéric DESSEROUER

Scientific Gratings Engineering Manager
Optical Component Division
HORIBA Jobin Yvon S.A.S.

Olivier NICOLLE

Director of the Optical Component Division
HORIBA Jobin Yvon SAS

Feature Article

Quantum Cascade Lasers in Test Benches
— Tracing Additional Exhaust Components using the Latest Measurement Equipment under Test Bench Conditions —

Daniel SCHEDER, Matthias SCHRÖDER,
Marcus RIEKER, Hiroshi KAWAMURA

Proposed legislation as well as new after-treatment devices that comply with recent regulations lead to the need for further analysis capabilities in terms of nitrogen exhaust components such as NO and NO_2, NH_3 and N_2O. This study compares conventional methods, which face difficulties when measuring these compounds, with a new analyzer utilizing Quantum Cascade Lasers (QCL). After a short description of optical absorption spectroscopy in general and the QCL technology in particular, system setup and sample handling with a QCL analyzer are described. The second part covers a variety of tests conducted at different locations within the HORIBA Group and at different end user laboratories. Subjects discussed include synthetic gas tests that verify the viability of the QCL analyzer as well as engine tests that show the analyzer in comparison with conventional methods for measuring nitrous gases under real test bench conditions. Further aspects such as urea conversion with Selective Catalytic Reduction (SCR) and NO_2/NO_X ratio are discussed. The study shows that QCL technology is capable of mastering the growing challenges facing emission testing.

Introduction

Motivation

Proposed legislation as well as new after-treatment devices that comply with recent regulations lead to the need for new analyzing capabilities in terms of new nitrogen exhaust components. Several after-treatment systems such as the Lean NO_X Trap (LNT) catalyst and Selective Catalytic Reduction (SCR) have been developed for reducing NO_X (NO: nitrogen monoxide / NO_2: nitrogen dioxide) emissions from both diesel and lean-burn gasoline engines to meet the recent stringent regulations for automobile exhaust emissions. However, to evaluate the performance of these new after-treatment devices, it is not sufficient to analyze the regulative nitrogen components such as NO and NO_2 only,[4] It is also important to monitor NH_3 (ammonia) slip from SCR catalysts during different engine running conditions.
In addition, proposed legislation such as EURO 6 and 7 or CFR 1065 and 1066 will substantially change test methods and instruments used for measuring toxic emissions. These emission standards stipulate the measurement and regulation of new exhaust gas components. To confront global warming, the United States Environmental Protection Agency (EPA) has issued a rule requiring greenhouse gases (GHG) including N_2O (nitrous oxide) to be reported.[10] Thus, an analyzer that can measure NO and NO_2 at the same time as NH_3 and N_2O is a key demand. Conventional methods used for measuring nitrogen compounds have problems mastering the growing challenges posed by interferences and detection limits. This has led to the development of new analyzers utilizing a Quantum Cascade Laser (QCL) to measure NO, NO_2, N_2O and NH_3.

Principles of Optical Spectroscopy

Like conventional gas analyzers, QCL devices are based on the principles of optical absorption spectroscopy:

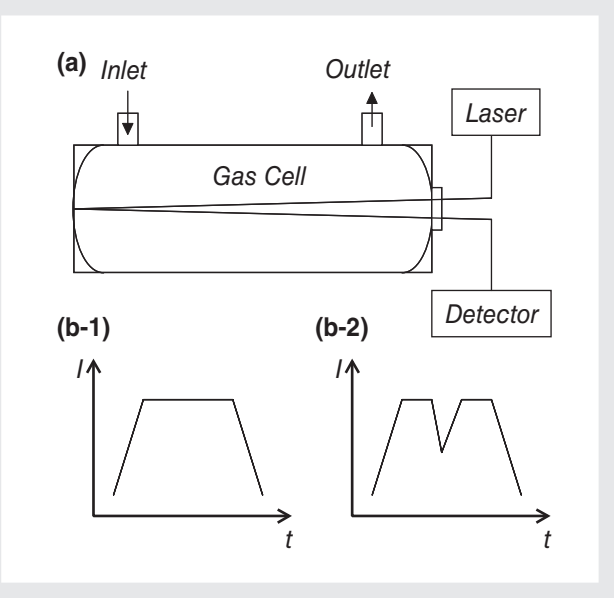

Figure 1 (a) Schematic setup of a Spectrometer; (b-1) the original pulse shape of the laser beam and (b-2) the characteristic absorption spectrum after transmission

substances such as, in this case, exhaust components absorb energy in the form of electromagnetic waves. The molecules are transformed to a higher energy state, while the energy absorbed represents the molecular structure of a specific substance. Each component therefore shows specific wavelengths at which its absorption tendencies are most pronounced. To record the specific absorption spectrum, a laser beam is passed through the sample gas as shown in Figure 1(a). The laser pulse is reflected by mirrors and hits a detector. When the frequency of the beam is the same as the vibrational frequency of an atomic bond (depending on factors such as element mass and bond strength), absorption occurs. An examination of the light transmitted shows how much energy the component has absorbed at each wavelength, and the absorption spectrum ascertained in this way characterizes the component as shown in Figure 1(b). According to the Beer-Lambert law, the absorbance is proportional to the gas concentration. Thus, the gas concentration can be obtained from the shape of the absorption spectrum according to library data.[6], [7]

QCL Technology

The difference between QCL and conventional exhaust gas analyzers lies in the laser technology used. QCL is a semiconductor laser based on two fundamental phenomena of quantum mechanics: tunneling and quantum confinement.[2], [3] With conventional diode lasers, the light originates from an energy gap existing between the valence and the conductance band. As shown in Figure 2(a), only one photon is released every time an electron undergoes relaxation. In contrast, a QCL element

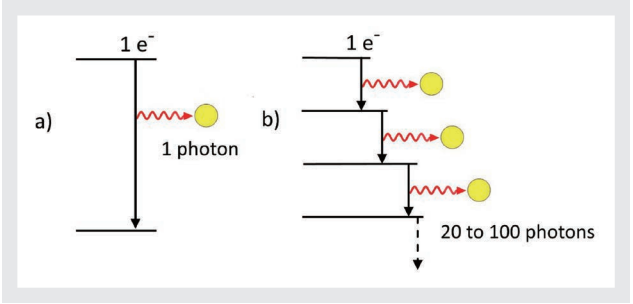

Figure 2 (a) Conventional lasers emit only one photon at one electron transition; (b) with QCL, the electron transits multiple layers, releasing several photons in the process

has several thin layers of semiconductors which create a multi-level band structure consisting of separate quantum wells. This results in the electrons "cascading" down through the layers while several photons are released. For this reason, the laser strength and intensity increase considerably, Figure 2(b).

Moreover, with QCL the wavelength no longer depends solely on the band gap of the semiconductor materials applied but also on the layer thicknesses. This allows QCLs with a wide range of emission wavelengths to be manufactured using the same well-known semiconductor material systems. QCLs are able to produce light in the whole Mid-Infrared (Mid-IR) and potentially in the Far-Infrared (Far-IR) spectrum. They can therefore emit strong beams in regions in which the relevant nitrogen compounds exhibit high extinction coefficients, whereas the absorption tendency of coexisting gases is low in these regions.

Operating Principles of QCL Spectroscopy

The principles of optical spectroscopy, which have already been discussed in Subsection of Principles of optical spectroscopy, also apply to QCL analyzers. There are, however, differences in their operation processes: supplied with electrical pulses at a constant interval, a QCL element generates light while the temperature of the laser element increases with the electric current applied. As the emitted wavelength depends on the QCL's temperature, the wavelength is tuned by its temperature and the electrical pulse.[5], [11], [12] This makes it possible to precisely adjust the wavelength to the region in which the compounds targeted for measurement absorb laser light. One pulse lasts several 500 ns and the wavelength changes with increasing temperature. The wavelength variation during a pulse of this kind is approximately 0.005 µm.

System Setup and Sample Handling

It took some effort to make the QCL working principle

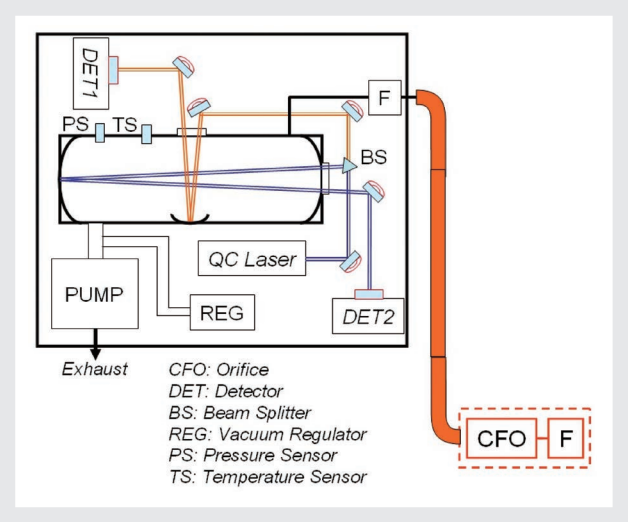

Figure 3 The MEXA-1400QL-NX system design allows NO, NO_2, N_2O, and NH_3 to be measured simultaneously at different concentrations

more viable and to meet the demands of legislation for exhaust gas measurement. The result is the HORIBA MEXA-1400QL-NX, which is already being used by several OEMs. The analyzer is capable of measuring the four most relevant nitrogen compounds simultaneously at different concentration levels, Figure 3.

Measuring at different concentration levels

The optical path length is absolutely crucial for the measurement results. A short laser path allows the use of small optical cells and leads to rapid responses. On the other hand, a very long path length enables very low detection limits but often extends the response time. For this reason, a sophisticated design of the cell and of the mirrors in particular has been implemented in the MEXA-1400QL-NX analyzer to allow for two different path lengths with one gas cell. A short path of 0.84 m is realized with a low number of light reflections (~ 25) while a high number of light reflections (~ 100) add up to a path length of 30 m. The combination of these two paths gives way to the measurement of both high and low gas concentrations in one system configuration.[4], [8], [9]

Measuring several gases simultaneously

To measure NO, NO_2, N_2O and NH_3 simultaneously, the system design uses four QCL elements at individual wavelengths. At the chosen wavelengths, the absorption tendency of coexisting gases is expected to be low. Each laser unit in turn emits pulse light while the detector receives the whole spectrum and for each QCL one after another.[4], [8], [9]

Compensation of coexistent gases

Firstly, with QCL the interference caused by the spectral overlap of co-existing gases is reduced due to the fine laser beam resolution of 0.001 cm^{-1}. Secondly, while an absorption spectrum expands under atmospheric pressure, a sharp peak of the absorption spectrum can be obtained under low pressure. The sample gas is therefore drawn into the gas cell by a vacuum pump which creates enough vacuum (25 kPa) to reduce this pressure broadening effect significantly. These two circumstances allow reliable mathematical compensation of the interference of co-existing gases such as CO, CO_2, CH_4, H_2O, and hydrocarbons.[4], [8], [9]

Rapid NH_3 measuring

The difficulty with NH_3 is that it tends to adhere to the surfaces of the sample cell and transfer lines due to its large electric dipole moment. To prevent water condensation and to minimize the dissolution of NH_3, the sample inlet, filter, vacuum regulator, and gas cell are heated to 113 °C. In addition to this, materials and surfaces of the transfer lines were optimized to reduce the response time to less than 5 s during NH_3 testing.[4], [8], [9]

Sample handling

The MEXA-1400QL-NX analyzer works with a sample flow of approximately 8 L/min. There are thus two ways of handling emission testing samples. Firstly, the exhaust gases can be directly sampled from the exhaust in the undiluted or raw state via a transfer line as shown in Figure 4(a). In this configuration, the system response is

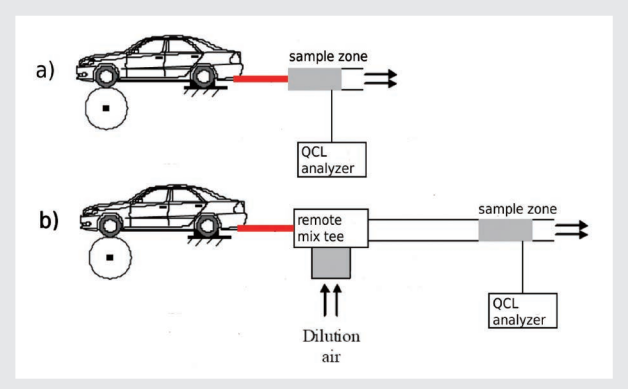

Figure 4 System diagram for vehicle tests on a chassis dynamometer. With the MEXA-1400QL-NX, the exhaust gases can either be measured directly, i.e. raw (a), or diluted with air (b).

Table 1 Synthetic gas tests performed for this study

Test	Low Range				High Range			
	NO	NO_2	N_2O	NH_3	NO	NO_2	N_2O	NH_3
Zero Noise	Y	Y	Y	Y	Y	Y	Y	Y
Span Noise	Y	Y	Y	Y	Y	Y	Y	Y
Linearity	Y	Y	Y	Y	Y	Y	Y	Y
Linearity	Y	Y	Y	Y	Y	Y	Y	Y
Rise Time	Y	Y	Y	Y	Y	Y	Y	Y
Interference Check	Y	Y	Y	Y				

very fast, and all four gases can be measured simultaneously at high concentrations. Secondly, it is possible to dilute the exhaust gases with ambient air to measure low and medium concentrations of NO, NO_2, and N_2O at the same time, as shown in Figure 4(b). For bag sampling, there will be modified analyzer versions which work at lower sample flow rate.

Test Results

The performance of MEXA-1400QL-NX was tested and verified using a variety of tests conducted at different locations within the HORIBA Group and at different end user laboratories. The following section shows some of the test results.

Synthetic Gas Tests

Synthetic gases - like any first step of gas analyzer verification – comprise gas blends of the target species based on either nitrogen or synthetic air at known concentrations. They also for example include blends of potentially co-existing gases in the exhaust. The absolute accuracy of any gas analyzer is determined via the items listed in Table 1.

Noise

The signal noise is defined here as two times the standard deviation during steady flow of a defined gas. For each component and range, the gases used here are nitrogen and the span gas, which is usually 95 % of the full-scale concentration. The zero noise results shown in Table 2 are of special importance as they determine the lower detection limit of an analyzer.

Linearization curve

The linearity of the instrument is examined for both the low range and the high range. In the linearity test, calibration gases of the required concentrations are generated by blending the calibration gas with N_2 at ten different blending ratios. A gas divider is used to do this automatically. The reference concentration of each sample gas is calculated from these blending ratios and the nominal gas concentration. Figure 5 shows a typical result of a linearity test. As a quality criterion, every measured point should deviate from the expected concentration by no more than 1 % of the full scale. All measurement ranges are calibrated separately and meet the criteria of the various regional regulations (ECE, EPA) or, for simplicity's sake, each measured point should be within 2 % of the expected concentration.

Table 2 Results of noise tests as well as the pass/fail criteria

	NO	NO_2	N_2O	NH_3
criteria (100 / 50 ppm range)	< 0.4 % F.S./100 ppm	< 0.4 % F.S./50 ppm	< 0.4 % F.S./100 ppm	< 0.4 % F.S./50 ppm
ZERO 2 σ	0.02	0.01	0.02	0.01
	NO	NO_2	N_2O	NH_3
criteria (5000 / 2000 ppm range)	< 0.4 % F.S./5000 ppm	< 0.4 % F.S/2000 ppm	< 1.0 % F.S./2000 ppm	< 0.4 % F.S/2000 ppm
ZERO 2 σ	1.3	0.25	0.62	0.16
	NO	NO_2	N_2O	NH_3
criteria (100 / 50 ppm range)	< 2.0 % F.S./100 ppm	< 2.0 % F.S./50 ppm	< 2.0 % F.S./100 ppm	< 2.0 % F.S./50 ppm
SPAN 2 σ	0.34	0.16	0.34	0.21
criteria (5000 / 2000 ppm range)	< 2.0 % F.S./5000 ppm	< 2.0 % F.S./2000 ppm	< 2.0 % F.S./2000 ppm	< 2.0 % F.S./2000 ppm
SPAN 2 σ	28.81	11.83	9.71	15.5

Figure 5 Screenshot showing typical results of a linearity test

Interference

The number of components emitted by internal combustion engines can generally be as high as 200. The concentration of each component depends largely on the type of fuel used, the chemistry of the combustion process itself and exhaust after-treatment. The major components at significant concentrations are tested for potential cross-interference with the target species of MEXA-1400QL-NX. They are listed with their criteria in Table 3.

Rise time

The rise time of the full measurement system can be divided into two parts: the sample handling system depends on the application and differs in the dimensions and material of the transfer line and the degree of soot contamination etc. However, the analyzer is the same from unit to unit. Hence, in a first step, the full system is measured without the influence of the sample handling system, Table 4(a). It is then tested including a typical

Table 3 Gases used for the interference check

Componets	NO	NO_2	N_2O	NH_3
criteria (for 5 ppm / 10 ppm range)	+/-0.2 ppm	+/-0.1 ppm	+/-0.2 ppm	+/-0.1 ppm
CO_2_16 vol%	-0.01	0.00	0.00	0.021
H_2O_16 vol%	-0.01	0.00	0.00	0.066
CH_4_5000 ppm	-0.01	-0.01	0.09	0.070
C_2H_4_500 ppm	-0.06	-0.00	0.00	0.073
C_2H_5OH_500 ppm	-0.01	0.02	0.16	0.069
C_2H_2_250 ppm	-0.03	-0.01	0.04	0.048
C_2H_6_250 ppm	-0.01	-0.00	0.00	0.057
NO_5000 ppm	–	–	–	-0.010
NO_2_2000 ppm	–	–	0.00	0.000
N_2O_2000 ppm	0.00	0.03	–	0.000
NH_3_2000 ppm	0.01	0.00	0.01	–

Table 4 (a) Rise time T_{10-90} of the sole analyzer; (b) rise time of the full measurement system including heated filter and transfer line

(a)

Range	NO	NO_2	N_2O	NH_3
criteria	< 1.5 s	< 1.5 s	< 1.5 s	< 2.5 s
100 / 50 ppm	0.8 s	0.7 s	0.9 s	0.8 s
5000 / 2000 ppm	1.0 s	0.8 s	1.4 s	0.9 s

(b)

Range	NO	NO_2	N_2O	NH_3
criteria	< 2 s	< 2 s	< 2 s	< 5 s
100 / 50 ppm	0.9 s	0.8 s	0.7 s	3.6 s
5000 / 2000 ppm	0.9 s	1.0 s	1.0 s	1.6 s

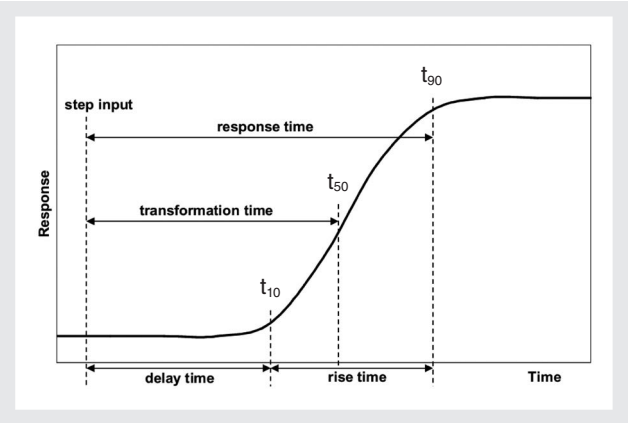

Figure 6 The rise time of a sensor is defined in ECE R49 and elsewhere

setup comprising a heated filter using a quartz glass fibre filter element and a 6 m long heated line. This is a common length which suits a high number of installations, Table 4(b).

The definition of the rise time as T_{10-90} represents the duration from 10 to 90 % of a sensor's response to a step-shaped input signal as shown in Figure 6.[1]

Engine Tests

The real engine exhaust tests shown here are examples of the possible applications of MEXA-1400QL-NX.

First the correlation to standard, well-known measurement systems in some selected applications is investigated. The reference systems chosen are Chemi-Luminescence (CLD) and Fourier Transform Infra-Red (FTIR) analyzers, Figure 7. Since MEXA-1400QL-NX has wider measurement ranges at both the lower and upper end of the scale, the correlation test can only cover part of the specification.

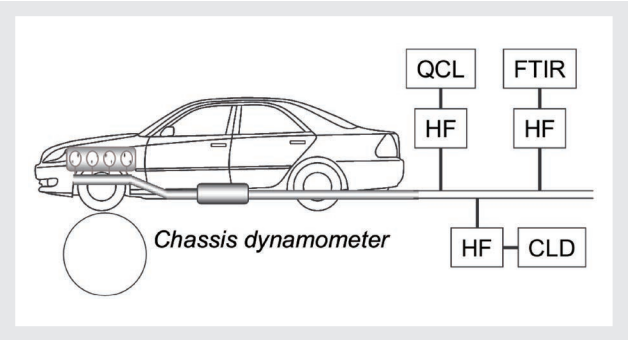

Figure 7 Setup of NO correlation test between QCL, CLD and FTIR at the sample position 'tailpipe'

The shapes of modal traces for tailpipe sampling are similar for all three methods under investigation. Also, the absolute level of emissions is almost identical and shows qualitatively good correlation of the systems for NO gas over a Federal Test Procedure 75 (FTP-75) driving cycle as shown in Figure 8.[3]

More tests are conducted between 1400QL-NX and two-channel CLD sampling via a full flow dilution tunnel.

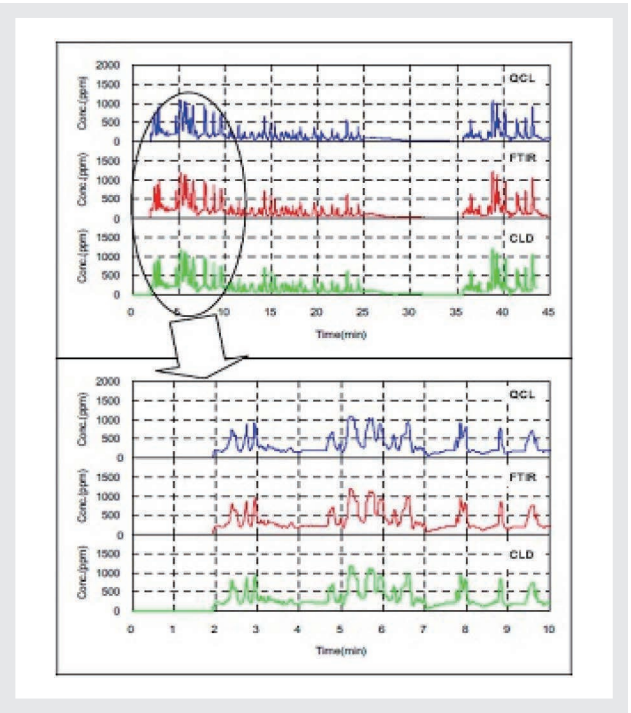

Figure 8 Comparison of MEXA-1400QL-NX with three analyzers that can be used for NO measurement at the concentration levels given

One channel of the CLD is set to NO mode and the other to NO_X. The parameter under investigation is the correlation between the two instruments at static speed conditions.

One important aspect must be considered when measuring NO_X gases using different systems: the sample handling systems can change the oxidation stage upwards or downwards depending on the temperature conditions and the presence of substances such as soot which for example reduce NO_2 to NO. This effect needs to be taken into account when only nitrogen oxide is compared. The instrument with higher temperature and soot contamination is likely to show the NO_X reduction effect. In the particular measurement shown in Figure 9, the averaged NO concentration is well within 3 %. This is a good agreement in view of the fact that both instruments

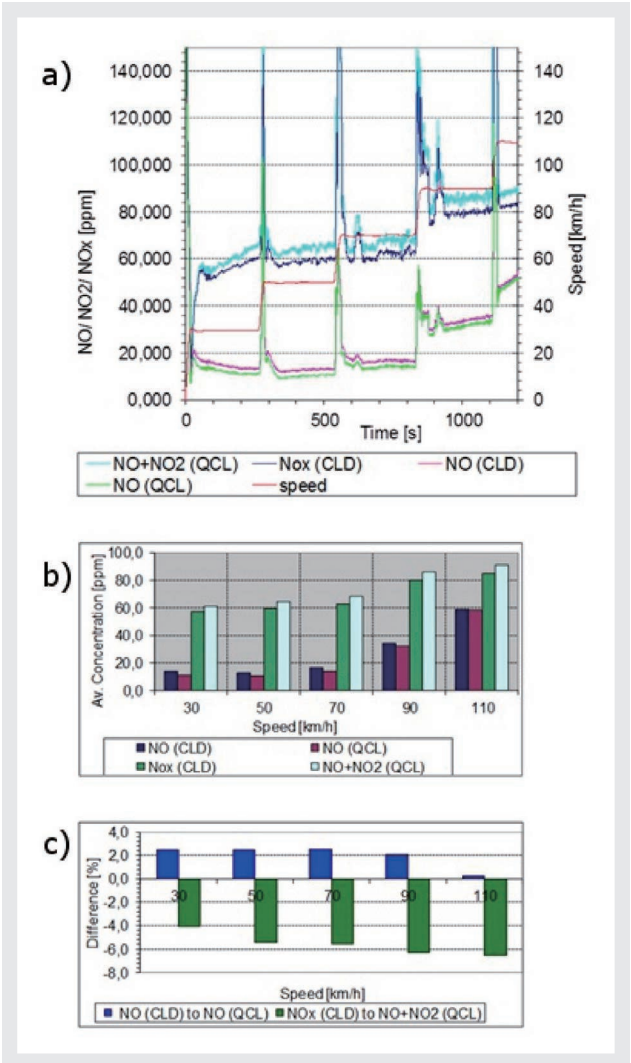

Figure 9 NO, NO_2 and NO_X compared at five different speeds:
(a) the modal traces follow the same trend;
(b) the average values;
(c) the differences of NO and NO_X to NO and NO_2

are calibrated using different span gas bottles and have different ranges and hence linearization curves. The NO_X value of CLD and the NO and NO_2 value of QCL deviate by between 4% and ~ 6%. As described above, this can be partly due to the individual calibrations and linearizations. Besides sample handling effects, another potential influence on NO_X measurements using CLD is the converter material. Its task is to reduce the entire NO_X to NO so it can be detected. The converter generally has an efficiency of less than 100%, and this typically causes underestimation of NO_X. For the results shown in Figure 9, the potential influences of sample handling and converter are not investigated further here.

Urea Conversion

The functional principle of a Selective Catalytic Reduction (SCR) catalyst is based on the conversion of NO_X to N_2 with the help of NH_3. The basic principle is as follows: the NH_3 is typically generated from an injected aqueous urea solution or – less commonly – directly applied as a gas. The injection of NH_3 needs to be performed in a controlled manner since a stoichiometric reaction is required in order to avoid NH_3 slip.
The urea is injected via a nozzle and then decomposes into iso-cyanic acid and ammonia at a temperature of more than 133 °C (Formula 1). The iso-cyanic acid is only an intermediate product which is further hydrolyzed into ammonia at 160 °C (Formula 2):

$$(NH_2)_2CO \rightarrow NH_3 + HNCO \quad \cdots\cdots (1)$$

$$HNCO + H_2O \rightarrow NH_3 + CO_2 \quad \cdots\cdots (2)$$

Besides the desired main reactions, a number of intermediate and unwanted substances are also produced at temperatures of 133 °C or above. These components are biuret, triuret, melamine and cyanuric acid. They are potentially dangerous due to the risk of instrument contamination and can cause false measurements. One application used during the research and development of SCR catalysts is NH_3 measurement directly upstream of the SCR catalyst. However, this measurement exhibits several difficulties. The urea → ammonia conversion as well as the ammonia/exhaust gas mixing may not be perfect and may create misleading results.

Figure 10 shows two examples of pre-SCR measurements with the 1400QL-NX and a FTIR instrument in parallel during a New European Driving Cycle (NEDC). In one

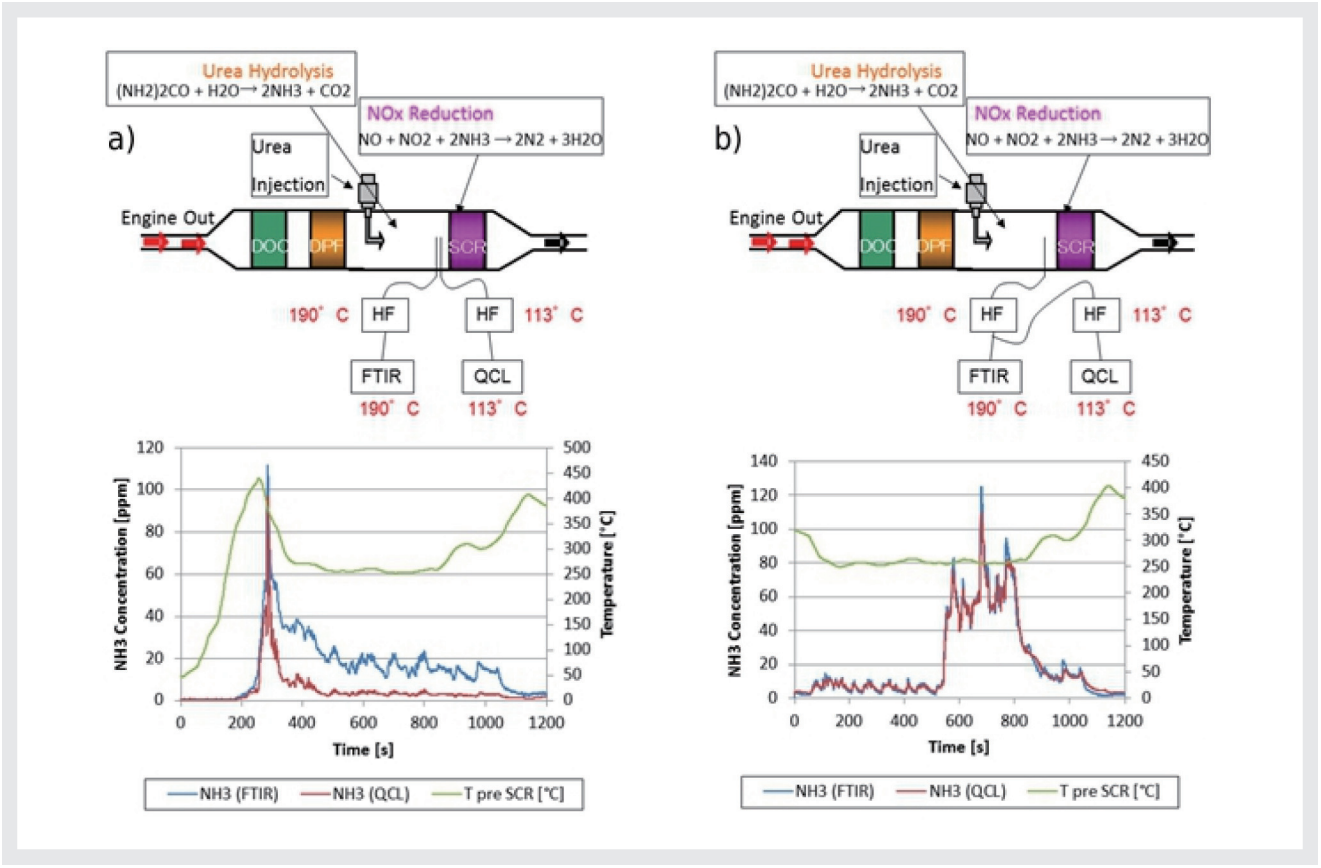

Figure 10 1400QL-NX (QCL) compared to a FTIR instrument with sampling upstream of the SCR: when two separate probes and independent sample handling systems of different temperatures are used (a), the NH_3 trace deviates strongly. When the QCL is connected behind the FTIR heated pre-filter (b), the traces are in good accordance.

configuration, both instruments, 1400QL-NX at 113 °C and the FTIR at 190 °C, sampled exhaust gas from different probes with a spacing of only about 5 cm in between,
Figure 10(a). The NH_3 traces showed large discrepancies. After further investigations, the 1400QL-NX was connected via a flow splitter downstream of the heated filter of FTIR, which was also heated to 191 °C. The sample handling of the 1400QL-NX itself was not changed. The measurement results showed a good correlation in this case.

It can be concluded from
Figure 10(b) that the instruments themselves are equivalent. On the other hand, the differences for the
Figure 10(a) configuration need to be explained. As far as it concerns non-perfect NH_3/exhaust mixing, this is an unlikely reason since the instrument shows no full accordance at all. The mixing behaviour should depend on flow conditions which vary throughout the test depending on the engine load etc. During idling phases of the test, the instruments would be expected to agree better. The more probable explanation for the disagreement in
Figure 10(a) is the production of NH_3 inside the FTIR sample handling system. The temperature conditions would allow this effect: if urea or iso-cyanic acid reached into the sample handling systems of an instrument, they would stay stable if the temperature was below their decomposition point. This is the case for 1400QL-NX since the temperature is below 133 °C. However, the FTIR heated to 191 °C may change the sample gas and allow reactions such as those shown in Formula 1 and Formula 2. It can measure ammonia plus potential ammonia in the form of precursors. In contrast, 1400QL-NX measures the real ammonia concentration present at the sample position.

QCL and NO_2/NO_X Ratio

The NO_X concentration of the engine exhaust has a wide range. It depends on the air-to-fuel ratio, the combustion temperature and the pressure – and on the after-treatment system too, of course. Also, the NO_2/NO_X ratio is variable between almost 0 and more than 50%.
QCL technology allows an accurate direct measurement of NO_2 which is useful for both low and high NO_2/NO_X ratios: at low ratios, a differential method such as dual CLD is very sensitive to time alignment and inter-channel variation. Those variations can result from linearization,

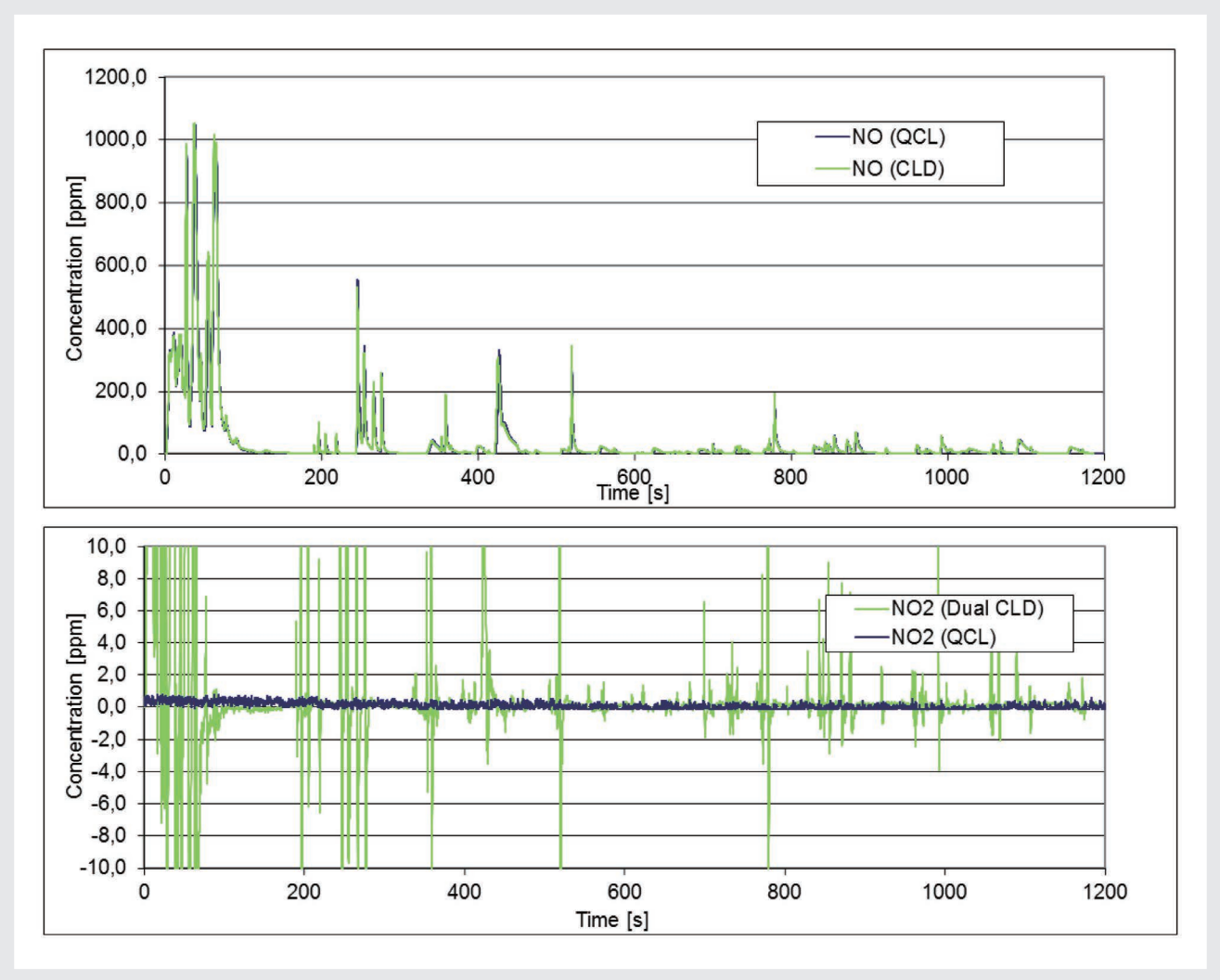

Figure 11 The direct injection gasoline vehicle (3 L, 6 cylinder) used for this study has almost no NO_2 emission (bottom) while NO emission (top) is relatively high

calibration, uncertainties of converter efficiency etc. Direct measurement using QCL absorption spectroscopy yields reliable results for NO_2 even at high NO calibrations as shown in Figure 11.

On the contrary, for high NO_2/NO_X ratios, any uncertainty in the $NO_2 \rightarrow NO$ conversion efficiency has a relatively large influence on the NO_X value compared to the case in which most of the NO_X consists of NO. QCL without the use of converters is not affected by this and is a reliable and robust method.

Conclusion

The working principle of absorption spectroscopy based on a Quantum Cascade Laser is shown in theory. A QCL device offers strong and highly monochromatic light of a defined wavelength which can be selected over a wide range during manufacturing of the laser and over a small range via its operating temperature.
MEXA-1400QL-NX uses four of these lasers to realize a four-component analyzer designed for negligible interference from co-existing gases and a low limit of detection. The analyzer performance is shown for both synthetic and real exhaust gases. It correlates well with conventional methods if gas concentrations are suitable for other methods. However, MEXA-1400QL-NX shows its unique strengths and advantages in the case of low concentrations and extreme mixtures. QCL technology can be used to measure many different gas components. Choosing the right wavelength area with a suitable coefficient of extinction and minimum interference is the key issue. As the next model of the QCL series, HORIBA will introduce the new MEXA-1100QL-N2O analyzer,

which was designed for an ultra-low N_2O detection limit in the order of a few ppb.

Acknowledgements / Danksagung

The authors appreciate the friendly cooperation and courtesy supplied by Umicore AG & Co. KG, Hanau, Germany during the preparation of this paper.

References

[1] ECE/TRANS/WP.29/GRPE/2009/12 *Regulation No.49.*

[2] Faist, J., Capasso, F., Sivco, D. L., Sirtori, C., Hutchinson, A. L., Cho, A. Y., Quantum Cascade Laser, *Science 264*, 1994, p. 553-556.

[3] Faist, J., Capasso, F., Quantum Cascade Laser Mc Graw-Hill , *Yearbook of Science and Technology* 1997, p. 265-267.

[4] Hara, K., Nakatani, S., Rahman, M., Nakamura, H., Tanaka, Y., Ukon, J., Development of Nitrogen Components Analyzer Utilizing Quantum Cas-cade Laser, *SAE Paper* 2009-01-2743, 2009.

[5] Hill, Cory J, Yang, Rui Q., Mid-IR Semiconductor Lasers for Chemical Sensing, *SAE Paper* 2003-01-2551, 2003.

[6] McCulloch, M. T., Normand, E. L., Langford, N., Duxbury, G., Newman, D. A., High sensitive detection of trace gases using the time-resolved frequency downchirp from pulsed quantum-cascade lasers, *Journal of the Optical Society of America* B 20, 1761, 2003.

[7] McCulloch, M. T., Normand, E. L., Langford, N., Duxbury, G., Real-time trace-level detection of carbon dioxide and ethylene in car exhaust gases, *Applied Optics* 44 (14), 2005, p. 288-294.

[8] Rahman, M., Development of an Ultra-Low Concentration N2O Analyzer Using Quantum Cascade Laser (QCL), *SAE Paper* 2010-01-1291, 2010.

[9] Rahman, M., Hara, K., Nakatani, S., Tanaka, Y, Emission Testing of N2O (Bag Sampling) from Diverse Vehicles by Laser Spectroscopic Motor Exhaust Gas Analyzer, *SAE Paper* 2011-01-1155, 2011.

[10] United States Environment Protection Agency, Climate Change, Green House Gas Emissions, 2010 Inventory of Green House Gas Emissions and Sinks, *http://www.epa.gov/climatechange/index.html.*

[11] Yang, Rui Q, Mid-IR III-V Semiconductor Diode Lasers for Trace Gas Monitoring, *SAE Paper* 2002-01-2451, 2002.

[12] Yang, Rui Q, et al., Development of Thermoelectric Cooled Single-Mode Distributed Feedback Mid-IR Interband Cascade Lasers for Chemical Sensing, *SAE Paper* 2007-01-3151, 2007.

Daniel SCHEDER
European Product Manager
Engineering Department
Automotive Test System
HORIBA Europe GmbH

Matthias SCHRÖDER
Manager Emission Engineering
Global Product Planning Group
HORIBA Europe GmbH

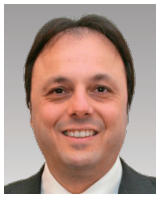

Marcus RIEKER
Director Academic Affairs
HORIBA Europe GmbH
Prof. Dr. Sc. Hum.

Hiroshi KAWAMURA
Junior Corporate Officer
HORIBA, Ltd.
Corporate Officer, Executive Vice President
HORIBA Europe GmbH

Feature Article

Development and Status of the Worldwide Harmonized Light Duty Vehicle Test Procedure

Les HILL

The globalisation of automotive exhaust emissions testing and measurement procedures has been in progress for a number of years and has already been introduced for vehicles such as motorcycles, on road heavy-duty vehicles (trucks/buses) and Non-Road Mobile Machinery (NRMM). The latest vehicle category for which a Global Technical Regulation (gtr) is to be developed in the Light Duty Vehicles. The paper reviews the history and current status of the Worldwide Harmonized Light Duty Vehicle Test Procedure (WLTP) program and the development of the new regulation for its world wide application. The document will also compare the draft WLTP requirements and procedures with those of the USA who have recently introduced their own draft procedures (CFR 1066) and highlight potential conflicts.

Introduction

In the past few years, there has been a large increase in activity in the development of new legislation, both in the reduction in the allowable mass limits of toxic and photo-chemical emission species and also in the development of new testing procedures, calculations and test system specifications. Coupled to this, there has also been a large increase in the variety and complexity of vehicle powertrain design including individual elements such as the internal combustion engine, potential of electrical/mechanical hybrization, transmissions and the exhaust after-treatment. Such diversity of powertrain design creates challenges to the emissions measurement systems, the test procedures and calculations.

The globalisation of automotive exhaust emissions testing and measurement procedures has been in progress for a number of years and regulations have already been introduced for vehicles such as motorcycles, on road heavy-duty vehicles (trucks/buses) and Non-Road Mobile Machinery (NRMM). The latest vehicle category for which a Global Technical Regulation (gtr) is to be developed is for Light Duty Vehicles (LDVs) for passengers and small commercial applications.

The paper summarises the progress and key elements of the Worldwide Harmonized Light Duty Vehicle Test Procedure (WLTP) program, as well as summarising other legislative developments in the LDV emissions measurement field.

Background

Whilst the amounts of permissible toxic, photo-chemical and Greenhouse Gas (GHG) emissions have been and are always likely to be decided by individual countries, the global harmonisation of emissions and fuel economy measurement methods, test procedures and calculations has been a long standing goal in order to simplify and streamline the certification process, test laboratory equipment and its calibration/verification.

The process for the WLTP was initiated at the UN-ECE WP29 meeting on the 4th June 2008 in Geneva. A target schedule for its development was presented at that meeting (Figure 1).

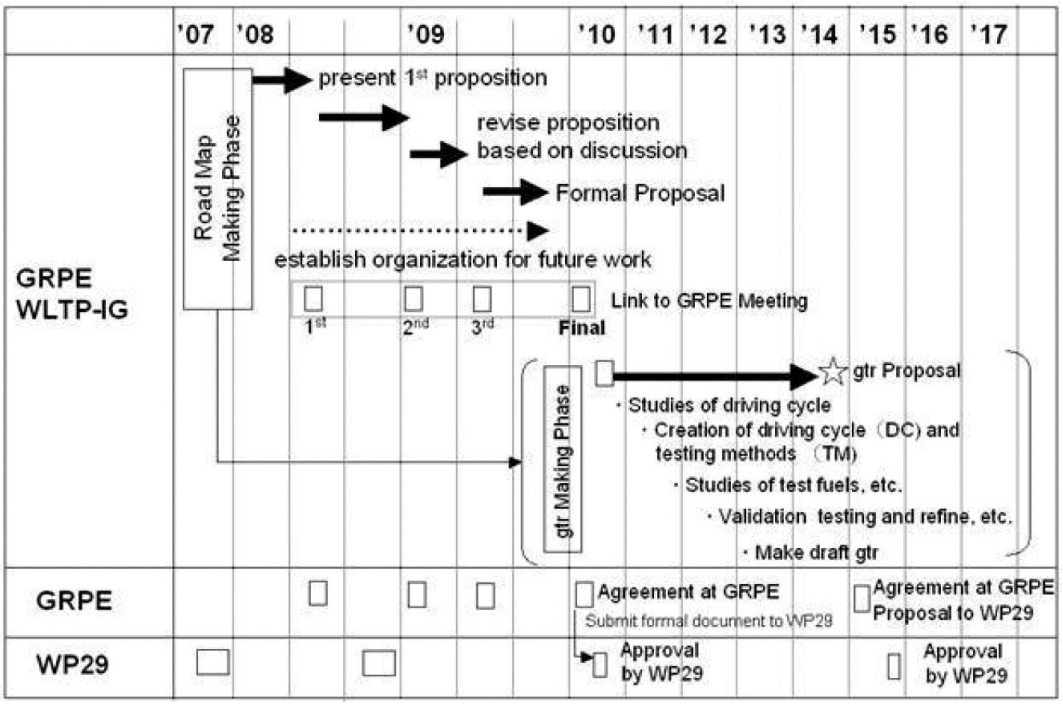

Figure 1 Original WLTP Development Schedule

WLTP Working Organisation and History

The development of the WLTP was passed to the GRPE (Group of Rapporteurs on Pollution and Energy) section of WP29 and organised into a number of Working Groups (WG).

- DHC : generation of the new vehicle speed/time drive cycle
- DTP : definition of the new test procedures, calculations and equipment specifications. The task of the DTP was further subdivided into smaller WGs.
  - PM/PN : procedures, specifications and calculations for the measurement of Particulate Matter (PM) mass and solid Particle Number (PN)
  - AP : new additional pollutants, their measurement procedures, calculations and equipment specifications
  - E-Lab : new test procedures, calculations and equipment specifications for electrified and hybrid electric vehicles
  - Reference Fuels : definition of the test fuels

The members of the various working groups are representative of the wide spectrum of interested parties and included light duty vehicle manufacturers, regional industry organisations, regional Technical Authorities, the USA EPA, the CARB, Environmental Monitoring/Study Groups and Equipment/Test System Suppliers.

These WGs report their status, open issues and future plans to the main WLTP organising committee primarily on a twice yearly basis at the UN-ECE GRPE meeting in Geneva. Individual working group meetings are scheduled as required by the activities either on a face to face basis or using web/phone conference.

Development of the New Drive Cycle (DHC WG)

The development of a new test drive cycle that can be applied globally for all countries and vehicle types has proven to be the big challenge of the WLTP program.
This task was given to the DHC Working Group whose primary goals were outlined as:

- Devise a methodology for the development of a worldwide harmonized light-duty driving test cycle
- Develop guidelines for in-use data collection;
- Develop and validate a worldwide Harmonized light duty vehicle driving test cycle (to include validation, confirmation and round robin tests).

Road trip data was supplied by several regions/countries

including the USA, Europe, Japan, China, India and Korea. This data was analysed and processed by the DHC WG and consolidated into a new drive cycle. The format of the new drive cycle followed the form of the schedules created for other gtrs where the speed/time trace is basically separated into urban, rural and highway phases. It was a request from the European Commission Directorate General for Enterprise and Industry (EU DG-ENTR) and the regional Technical Authorities that the drive cycle should be realistic of European driving and so an extra high speed phase was added with velocities above 130 km/h. It was recognised that such speeds would not be realistic for some countries or for some vehicle classifications with low power and so the test could be configured to eliminate the higher speed phases.

Version 1 of the Worldwide Harmonized Light Duty Vehicle driving Test Cycle (WLTC) was generated and subjected to evaluation in a Validation Phase by the various interested parties. As a result of the testing of various types of light duty vehicle, a series of modifications were made to improve the driveability and reproducibility of the drive cycle, culminating eventually in the version 5 of the WLTC that has been used in the current validation of the draft WLTP procedures, specifications and calculations (Figure 2).

The actual phases of the drive cycle to be used within the test depend on the power: weight ratio of the vehicle with the higher speed phases being eliminated if the vehicle is unable to meet the maximum speed in the phase. It is expected that further modifications will be made to the drive cycle as a result of the current validation program in progress.

In addition to the speed/time trace, another issue was that of the vehicle speeds at which the manual gear changes

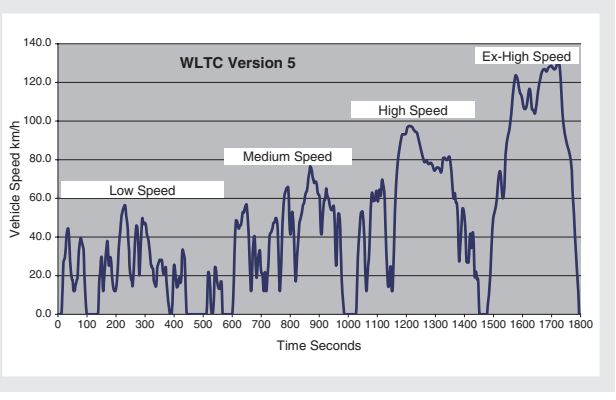

Figure 2 WLTC Version 5

are to be made. Currently, there are three proposed schemes under discussion:

- Fixed speeds
- Vehicle specific shift points: calculated based on the engine power, vehicle weight, number of gears, gear ratios, engine idle speed. This is the default method being used for the current Validation exercise.
- Alternative methods: such as vehicle Gear Shift Indicators (GSI) whose fitment is being made mandatory in Europe for all light duty vehicles fitted with manual transmissions. Their use will require a reliable solution on how these indicators can be made visible on the driver's aid used to display the speed/time trace to the test driver during the emissions test.

Development of the New Test Procedure (DTP)

The DTP Working Group started the draft process by reviewing and amalgamating the test procedures, calculations and specifications from the existing regulations from the USA (CFR 86), UN-ECE (Regulation 83) and JAPAN. A fundamental decision was, for the initial introduction of the new test procedure, to specify the full exhaust flow dilution technique using a constant volume sampler (CVS) as the only prescribed method of gaseous, particulate matter (PM) and solid particle number (PN) measurement. Other methods, such as partial flow dilution (for PM mass and gaseous compounds) and direct exhaust mass measurement (for gaseous compounds) were discussed but not included due to the technical unknowns/uncertainties and the lack of published correlation data on light duty vehicles. However, such alternative techniques could be included in the future once data is available.

The EU DG-ENTR and the Technical Authorities requested that the new test procedures should be more realistic and representative of the "real world" operation of the vehicle, particularly in the area of CO_2 and fuel economy determination. TUV Nord provided a report from their test program[1], comparing the vehicle manufacturers' CO_2 emissions data against data measured in their own laboratory. This outlined the key parameters that have an effect on the CO_2 emissions of the vehicle (Table 1). This resulted in lengthy discussions on a number of key topics such as the test cell/soak area temperature, the procedure and parameters for the vehicle road load determination and the vehicle mass to be used

Table 1 TUV Nord Summary of Factors Influencing CO_2 Emissions on LDVs
Influencing factors in the determination of CO_2 emissions and fuel consumption within the framework of passenger car type approval

Item	Parameter	Current status in Europe	Influence on CO_2 type test value	Recommendations for the WLTP
Test cycle "DHC"	Tolerance range	Use of tolerance to achieve lower CO_2 emissions is possible	- /+	Tolerances should be as narrow as possible; no smoothi ng out of the driving cycle curve and no excessive use of the accelerator pedal; option: driving robots
	Gearchange points	Gearchange points currently laid down for manual gearboxes: in case of optimisation, CO_2 reduction is possible	+++	GSI; alternatively, gear change point table based on vehicle parameters, automatic gearboxes in default mode
Measuring/ Test procedure "DTP"	Selection of test vehicle	Worst case for exhaust gas type test; minimum equipment for determination of CO_2 (overload) is possible	-- /++	Worst case variant wi th regard to vehicle weight and driving resistance
	Coast down test	Vehicle preparati on (tyre p ressure , toe angle), test track and ambient conditions influence the results	--- /+++	Setting of the vehicle (tyre pressures, toe angle) in accordance with the manufacturer's instructions; definition of the environmental conditions in accordance with ECE R83, average results in terms of forces, definition of the road surface
	nertia	Increments of 250 lbs, greatest inertia mass 5000 lbs	- /+	Halving o f the flywheel mass classes to 125 lbs, Adaptation of maximum flywheel mass to vehicle mass
	Test stand load setting	±10% at 20 km/h; ±5 % at 40 up to 120 km/h	- /+	Tolerances as narrow as possible; driving resistance on the road as set point
	Ambient conditions in the exhaust gas laboratory	20 °C to 30 °C	-	Conditioning at 22 °C +3 °C - 2 °C
	Battery charge state	Not defined, generally, battery is full at the start of the test	-	Measurement of the charging balance during the test, correction of emissions and consumption
	Auxiliary equipment	Auxiliary eq uipment is currently not taken into consideration	----	Auxiliary consumers in default mode; additional test for mobi le air condition, information regarding CO_2 and energy consumption o f optional auxiliary equipment
Type approval procedure	Conformity of production (CoP) testing	Random sample checks at the end of the production l ine		End-of-line check of production vehicles with regard to CO_2 and energy consumption
	In-service testing	Random-sample checks of the exhaust gas emissions of vehicles on the road.		In-service monitoring wi th regard to CO_2 and energy consumption

for testing; some of which are still to be finally resolved.

Measurement of PM Mass and PN

Relatively few changes were made to the existing procedures, calculations and specifications for these compounds. Some key modifications were:

- ability to use CVS systems applying double dilution of the vehicle exhaust (harmonizing the EU with the JAPAN/USA regulations) for PM mass measurement
- Changes to the PN equipment specifications to take account of the measurement of PN emissions when the vehicle particle trap is being regenerated (now included in the WLTP having been excluded in the current UN-ECE Regulation 83)

Measurement of Additional Pollutants (AP)

In addition to the current list of regulated or measurement compounds related to toxic, photo-chemical or fuel economy determination, other compounds have been specified for measurement under the WLTP procedures. These include:

- Nitrogen Dioxide (NO_2)
  NO_2 is already measured and controlled as it is a component of NOx (along with nitric oxide - NO). It has been identified as an individual component to be potentially measured as some combinations of vehicle/ exhaust after-treatment have been shown to generate NOx exhaust tailpipe emissions with a high proportion of NO_2 which is the more toxic of the NOx compounds. At this stage, it has not been decided at what basis (mass or percentage of NOx emissions) will be used to set the permissible NO_2 limits.

- Nitrous Oxide (N_2O)
  Identified as a greenhouse gas (GHG)

- Ammonia (NH_3)
  NH_3 is already measured and controlled under EURO VI for heavy duty vehicles that are using active NOx

reduction methods such as Selective Catalytic Reduction (SCR) that have the potential to generate significant excess amounts of NH_3 if incorrectly applied. Unlike the other compounds that are proposed for measurement in the new WLTP, which will be made exclusively from diluted exhaust gas (via CVS), the measurement of ammonia will be made directly from the vehicle exhaust tailpipe and will be compared against an average concentration limit in the same way as heavy duty vehicles.

- Ethanol (C_2H_5OH), Acetaldehyde (ethanal : CH_3CHO), Formaldehyde (methanal : CH_2O)
  These compounds were added specifically for the use of fuels containing ethanol. The current proposal of the working group is that their measurement will be required for 100 % ethanol fuel and for gasoline mixtures containing more than 21% ethanol by volume (> E21), although the option of using a proportional factor based on the content of ethanol and the mass of Non-Methane Hydrocarbons (NMHC) is also being considered.

The candidate methods of measurement and equipment for the above compounds have been summarised by the working group and will be confirmed during actual vehicle testing in the Validation Phases of the WLTP program.

Test Procedures for Electrified Vehicle Testing (E-Lab)

A separate working group was created to consider the test procedures, calculations and specifications for the testing of all types of electrified vehicles including Battery Electric Vehicles (BEV), plug-in type hybrids (known as On Vehicle Charged Hybrid Electric Vehicles - OVC-HEVs) and conventional hybrids that are able to recover the kinetic energy of the vehicle but do not have an externally Rechargeable Energy Storage System (RESS) which are known as Not On Vehicle Charged Hybrid Electric Vehicles (NOVC-HEVs).

The base method for the test procedure was adopted from the existing SAE J1711 June 2010 standard "Recommended Practice for Measuring the Exhaust Emissions and Fuel Economy of Hybrid Electric Vehicles, including Plug-in Hybrid Vehicles".

A large number of open issues remain to be resolved regarding the details of the necessarily complicated test procedure which are likely only to be resolved after actual testing of vehicles during the current validation program.

Future Issues for Light Duty Vehicle Emissions and Fuel Economy Testing

The overall certification of Light Duty Vehicles in Europe is under discussion at the present time. Updated testing procedures are under review for evaporative emissions testing and a new test to determine the CO_2 emissions impact of LDV air conditioning systems is under discussion (MAC - Mobile Air Conditioning). In addition to the WLTP development process, there are a number of other activities related to Light Duty Vehicle emissions and fuel economy measurement that will impact on the future development and testing of light duty vehicles.

The first is the development of emissions legislation in the USA

Having relinquished the co-chairmanship of the DTP Working Group in November 2010 because of the extensive commitments to domestic legislative demands, the US Environmental Protection Agency (EPA) has developed their own new draft test procedure, calculations and specifications for light duty vehicles called CFR 1066. This is based on their existing CFR 1065 regulations that are applied to all applications of internal combustion engines such as heavy duty on-road and off-road, locomotives, marine, recreational and small utility engines etc. It has been proposed that the CFR 1066 will be applied for PM mass measurement for the 2017 model year and to gaseous components for the 2022 model year and so will be used for the introduction on the newly approved California LEV III and EPA Tier III emissions standards. In their current draft forms, the WLTP and CFR 1066 test procedures are not mutually compatible in all aspects which obviously could undermine the objective of global acceptance of the WLTP. Currently automotive industry and other technical groups are working together with the EPA and the California Air Resources Board to resolve the differences and to harmonize the two sets of draft test procedures, calculations and specifications.

The second is a new initiative from Europe known as the Real Driving Emissions for Light Duty Vehicles (RDE-LDV)

The program was created following the measurement of emissions from light duty vehicles when being driven on the road under real world conditions by the EU Joint Research Centre (JRC) using portable emissions measurements systems (PEMS). These systems were originally developed to meet the requirements of heavy duty engine certification procedures for the USA and Europe, which require an on-road verification test of the vehicles into which the engines are installed. The results from the JRC testing was published[2] and identified that the NOx mass emissions from diesel (compression ignition) vehicles were higher than their certified levels, in some cases by a factor of four. In addition, the NO_2 content of these NOx emissions were significantly higher than the gasoline (spark ignition) equivalent vehicles.
As a consequence, the EU DG-ENTR initiated the RDE-LDV working group to evaluate these results and to consider test methods to determine real world emissions from light duty vehicles. It is anticipated that these test methods will be supplementary for European certification when the WLTP test procedure is introduced.

Conclusion

The development of the new Global Technical Regulation for Light Duty Vehicles is in progress and will be introduced for emissions and fuel economy certification during the last half of this decade. Its eventual adoption by all territories and countries should simplify the design and specifications of the test facilities and improve the efficiency of the vehicle certification process. However, further work is likely to be required in order to harmonize the specifications of the equipment, test procedures and calculations to be acceptable to the USA legislative authorities. HORIBA Automotive Test Systems continue to actively monitor and contribute to the development of the new regulations to ensure that our customers are supported with compliant instrumentation and test systems for their light duty vehicle programs in a timely manner.

References

[1] TUV Nord : Analysis of the relevance of influencing factors when determining CO_2 emissions and fuel consumption during type approval of passenger cars on behalf of the BASt
[2] On-road Emissions of Light-duty Vehicles in Europe - *ENVIRONMENTAL SCIENCE & TECHNOLOGY* vol. 45 no. 19 p. 8575-8581

Les HILL
Global Product Planning Group
Automotive Test Systems
HORIBA Limited

Feature Article

In-situ Monitoring of Hazardous Ammonia in Ambient Air: Optimizing HORIBA's APNA-370 with a New NH_3 Converter

Wilma TRAVNICEK, Stefan KARWISCH,
Grischa P. FEUERSÄNGER

The following article contains the modification of a NO_X-analyzer (APNA-370) for monitoring of hazardous ammonia in ambient air at agricultural sites. HORIBA's APNA-370 was originally designed to determine NO_X/NO/NO_2 in ambient air, using the reduced pressure Chemiluminescence (CLD) method with a cross flow modulation (according to EN 14211). With the implementation of an additional converter, ammonia is transformed into nitrogen monoxide at an efficiency rate of 95 %. Therefore the modified NO_X-analyzer is suitable for quantitative determination of ambient ammonia. The Hessen Agency for Environment and Geology (HLUG) used the method of ammonia permeation, which has been proven to produce a reliable span gas. The evaluation of the permeation method has revealed an error range of approximately 1 %. Currently a type approval for a NH_3-analyzer does not exist in Europe. Therefore we related to the next relevant criteria. The instrument was validated according to the conforming standards of the German (VDI 4202-1/4203-3) and European (EN 14211) type approval test.

Introduction

Legal Requirements in Germany

The World Health Organisation (WHO) defined an orientation value of 10 µg NH_3/m^3 for the assessment of sensitive ecosystems.[1] In Germany during licensing processes of agrian facilities the authorities check if the total NH_3 exposure of sensitive ecosystems lies below this value. The total exposure is the sum of the initial pollution level and the additional load caused by the intended facility. The initial pollution level can be determined by a standard value of 7 $\mu g/m^3$ that is the maximum ambient air level in the neighboring states (Netherlands, Denmark, Great Britain). Although this approach allows an additional load of 3 $\mu g/m^3$[2] more precise is the use of NH_3 data of ambient air monitoring stations. Unfortunately the number of NH_3 datasets is small due to a missing monitoring obligation in Germany.

Another reason for monitoring of ammonia in ambient air is the implementation of the Goteborg protocol that entered into force in 2005.[3] This protocol sets limits on emissions of sulfur dioxide (SO_2), Non-Methane Volatile Organic Compounds (NMVOC), Ammonia (NH_3) and Nitrogen Oxides (NO_x) in 2010. In the EU directive 2001/81/EF (NEC) the countries are committed to the same obligations. Aim is the control of the acidification, eutrophication, and ground-level ozone which are still problematic in spite of the emission reduction success.[4] The Goteborg Protocol and the NEC-directive are in an amendment process in which the regulations will be tightened.

Source and Sinks for ammonia

Main source for NH_3 in the atmosphere is agriculture especially the intensive animal husbandry and fertilization. A substantial amount is emitted by the traffic sector. The NH_3 main sink is the wet and dry deposition. Anthropogenic nitrogen contamination disturbs the nutrient balance of the ecosystem and results in an acidification of soil. Ammonia and other gaseous

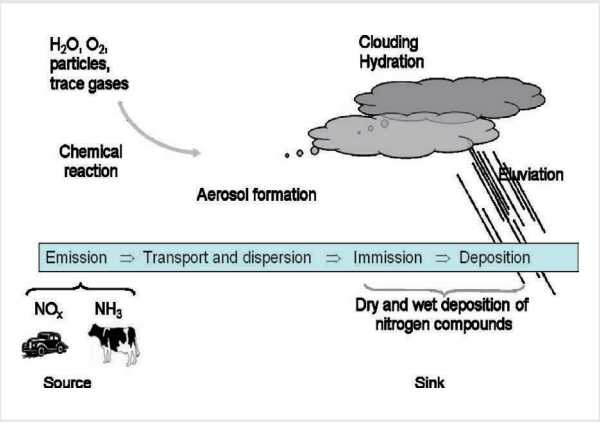

Figure 1 Atmospheric ammonia cycle.[5]

compounds such as SO_2 or NO_x compose to secondary aerosols that contribute significant to the background level of particles (PM_{10}*1, $PM_{2.5}$*2). Indirectly NH_3 acts as a greenhouse gas. It is converted partly to nitrous oxide that is a greenhouse gas. Figure 1 displays schematically the ammonia cycle in the atmosphere.[5]

*1: PM_{10}: Particulate matter with a aerodynamic diameter equal or less 10 μm

*2: $PM_{2.5}$: Particulate matter with a aerodynamic diameter equal or less 2.5 μm

Annual Ammonia Emissions in Germany

In Germany the ammonia emissions amount to 597 kt (2009) and stagnated during the last decade (Figure 2).[6] Due to the reduction of other acid pollutants such as SO_2 the NH_3-emissions become more important. Figure 3 shows the annual agrarian ammonia emissions of dairy cows taken from the ammonia cadastre of the Umweltbundesamt (UBA) in Germany. Hot spots are the regions Vechta and Cloppenburg in Lower Saxony and Münsterland in North Rhine-Westphalia. In the neighboring Netherlands a lot of stables for factory farming are installed, too. Their emissions are transported through the atmosphere and contribute to the NH3-pollution in Germany.

The data sets of the emission inventories are based on estimations. At present only few ambient air measurements exist in Germany due to the fact that no legal obligation for measuring ammonia exists. Most of them are done with discontinuously methods such as passive samplers or denuders. The NH_3 data base could be improved with ambient air measurements with a high time resolution.

Materials and Methods

Measurement Principle

The molecules of a gas sample containing Nitrogen Monoxide (NO) and Nitrogen Dioxide (NO_2) react with supplied Ozone (O_3). Part of the NO is oxidized to NO_2. The newly generated NO_2 is partly in an activated or excited state (NO_2*). It emits light, when it returns to its

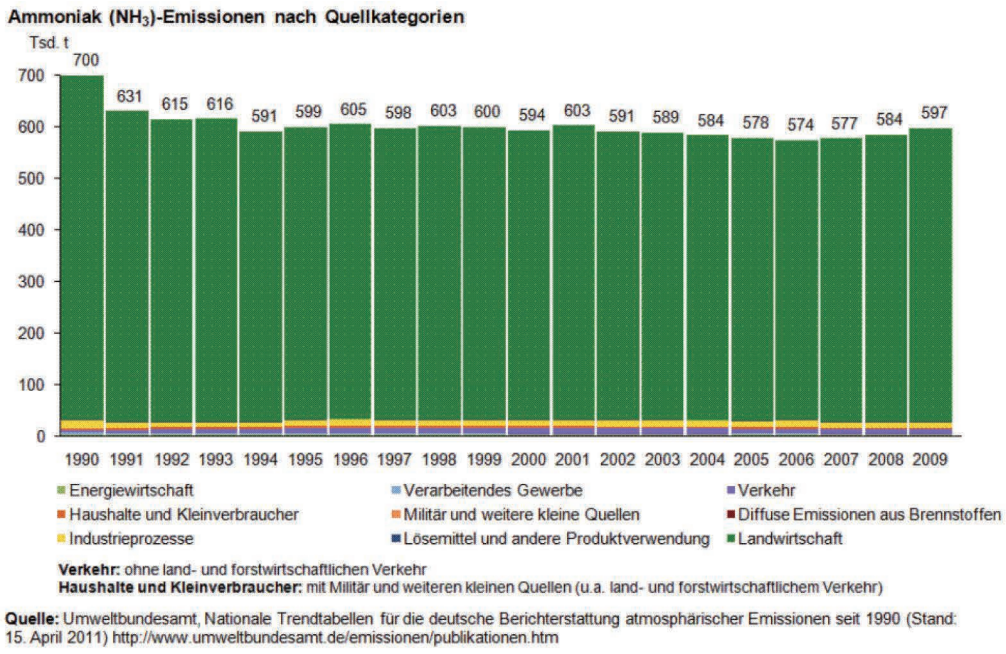

Figure 2 Ammonia emissions in Germany divided by sources.[6]

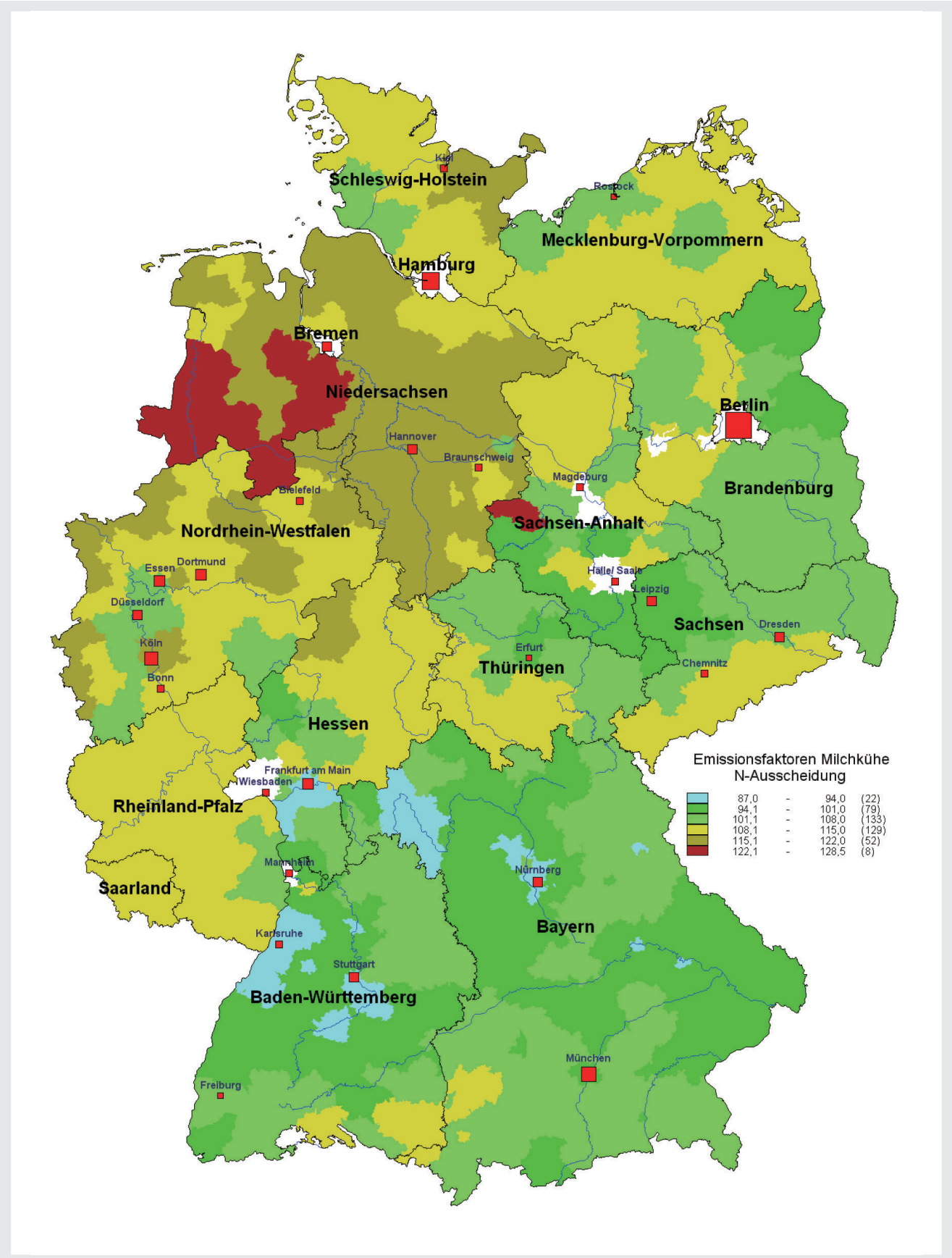

Figure 3 German ammonia inventory of emissions of dairy cows, Umweltbundesamt.[7]

original, lower energy level. This phenomenon is called chemiluminescence (CLD).

$NO + O_3 \rightarrow NO_2^* + O_2$
$NO_2^* \rightarrow NO_2 + h\nu$

This reaction is extremely fast and involves only NO. Coexisting gases in the sample are not affected at all. If the nitrogen monoxide is contained at low concentrations, the quantity of luminescence is proportionally low. Measuring nitrogen monoxide concentrations with this reaction is known as the CLD.[8] For measuring the ammonia concentration in the sample, NH_3 is oxidized to NO by a converter in the NH_3-measurement device (NH_3-converter). So the ammonia content is measured indirectly via the nitrogen monoxide determination, which is the original function of HORIBA's APNA-370 (Air Pollution Nitrogen Analyzer for NO_x). The sample gas passes a catalyst (Figure 4) that oxidises ammonia and reduces NO_x to NO. Afterwards this NO portion is analysed by HORIBA's APNA-370 as NO_y ($NO + NO_2 + NH_3$). Another portion passes merely the NO_2-converter and is reduced to nitrogen monoxide (Figure 4). This NO amount is also measured by APNA-370 as NO_x ($NO + NO_2$). HORIBA's APNA-370 analyses the NO concentrations in two lines and calculates the NH_3 concentration that is the difference between both channels ($NH_3 = NO_y - NO_x$).

Experimental Setup

The basic instrument HORIBA's APNA 370-NH_3 was developed by Junji KATO.[9] First tests yielded that the sensitivity was very low and the response time very high. Therefore the system was completely revised. In a first step the electronically devices were rearranged in order to shorten the way of sample flow. Redundant parts were removed and tube diameters changed. The permeation oven (calibration unit) was placed in the converter unit.

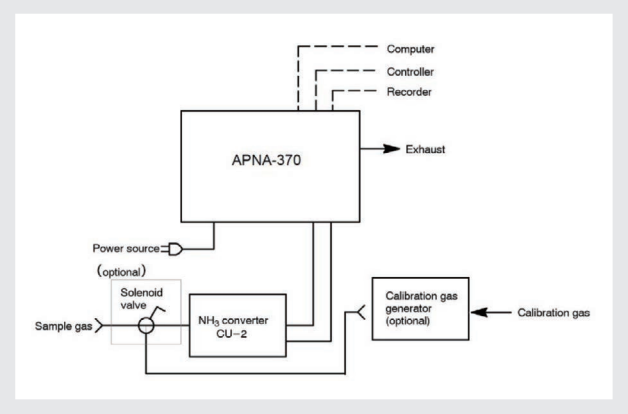

Figure 4 Flow Scheme of the NH_3-Converter Unit.

HORIBA's APNA 370 was not changed except of the removal of the calibration unit. Figure 5 gives an interior view on the converter unit.

In a second step every part and material used was overhauled and if necessary replaced by materials more suitable. A lot of parts consist of Polytetrafluoroethylene (PTFE). Unfortunately, this material strongly adsorbs ammonia. Better results are achieved with modified Perfluoroalkoxy Poylmer (MFA) and Perfluoroalkoxy polymer (PFA) in second place that are copolymers of Tetrafluroethylene and Perfluoroalkoxyvinyether. They have similar properties compared to PTFE. However the surface structure is less polar and smoother because of the ether groups.[10], [11] Therefore less wall effects of ammonia can be observed while using MFA instead of PTFE.

Essential is the quality of the thermal NH_3-converter who oxidises NH_3 to NO. It should have a high efficiency for ammonia (>98 %) and should be operated at low temperature <600 °C) due to a side reaction of nitrogen and oxygen to NO. The originally installed stainless steel helix converter has to be operated at 870 °C with an efficiency of 95 %. The stainless steel wears off after a while; it becomes porous and leaky. Since this moment the measured results are incorrect. Unfortunately this is a stealthy process, the exact date cannot be determined. Better results are achieved with a quartz glass pipe packed with stainless steel tubes (Figure 5). The efficiency is still 95 % by an operation temperature at 870 °C. Although the system remains air tight and produces reliable results. The low converter efficiency can be compensated by calibration in case it stays constant.

The stability of the system can be checked with an

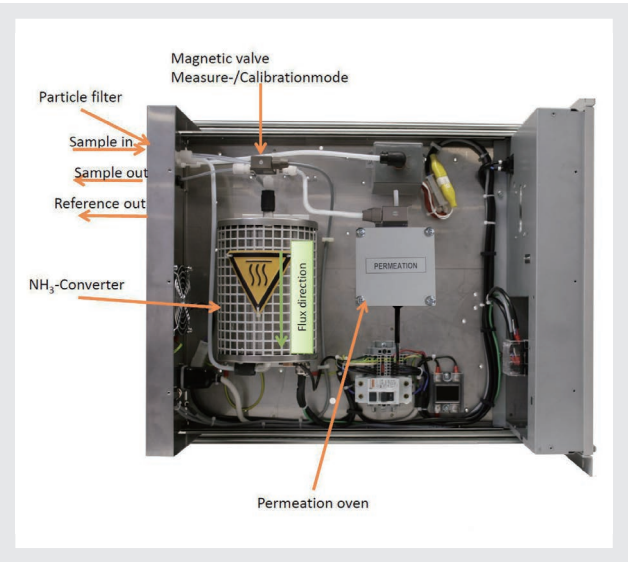

Figure 5 Interior View of the NH_3-Converter Unit.

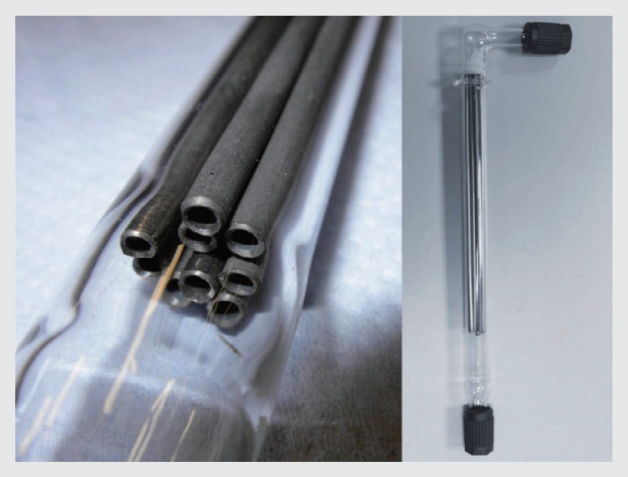

Figure 6 Catalyst glass pipe close-up view placed in the oven. The glass pipe is filled with 9 tubes of stainless steel (7301 SS, 1.4301). Each tube has a diameter of 3 mm with void of 2 mm.

internal standard. For this purpose, a NO_2 permeation tube is installed in a heated oven in the NH_3-converter unit. The analyzer can conduct an automated daily zero and span gas control (e.g. every 23 hours*3). NO_2 instead of NH_3 is used because NH_3 is a calculated value; the physical measurands are NO_x and NO_y (in this case represented by NO_2). Instrument drifts can be determined by a mismatch of the NO_x/NO_y-ratio and a NH_3-concentration different zero.

*3: Minimum requirement according to DIN EN 14211[12]

Span gas Production

For accurate measurements the calibration of the analyzer is required. HLUG established and validated a calibration standard for NH_3 in their lab. The method of static injection*4, standard method of HLUG for gaseous and liquid components, failed due to strong adsorption effects. The permeation method*5 (adding pure ammonia from a permeation tube to a constant carrier gas) produces a repeatable span gas. The validation of the permeation method results in a relative extended measuring uncertainty of approximately 1 %.

*4: DIN EN ISO 6144[13], VDI 3490-14[14], VDI 2100-4 [15]

*5: ISO 6145-10[16], VDI 3490-9[17], VDI 2100-4[15]

Results and Discussion

Validation

General

Type approval tests give the user the security that the measuring equipment is suitable for the use in automated ambient air monitoring network.[19] The test procedure is divided in two parts - the requirements on the construction and the evaluation of the performance characteristics.[20], [21] The modified instrument was validated according to the regulations of the German and European type approval test procedures.[12, 20, 21] For NH_3 no specific criteria are defined therefore the existing requirements for NO_2 are adopted. The analyzer meets all requirements on the construction such as a telemetric data transmission, the transmission of operation and error states or the possibility of an automatically function control. The validation includes a large number of system parameters. In the main the modified device passes the criteria. This article focuses on the most important.

Detection limit and measurement uncertainty

The detection limit is defined as the 3-fold standard deviation with a maximal value of 3 µg/m³.[20] The actual detection limit is 2 µg/m³. Therefore the requirements are fulfilled and the detection limit is sufficient for the measuring task. The data quality objectives request a relative expanded uncertainty of 15 % for inorganic components (e.g. NO_2) and 25 % for other compounds such as particles or benzene [22]. The uncertainty of the APNA 370 NH_3 amounts to 19.9 %. The criteria for NO_2 cannot be met yet; although the less strict requirements for benzene can be fulfilled.

Lack of fit

The lack of fit of linearity of the calibration function was tested. In the range of 0-300 ppbv NH_3 the detector is linear (Figure 7). The relative residuals of the linear regression function meet the criteria.

Response time

The response time is the time needed for the measured signal to reach 90 % of the nominal value. It may differ 5 % of the average determination; an average time of 3 min results in a response time of 9 s.[20] The instrument has a response time of 30 min; this result does not meet the

requirements. However this is a clear performance improvement.

Drift

The temporal change of the measured values at zero point shall not exceed 3 µg/m^3 (2.13 ppbv) during 24 hours.[20] The trend diagram (Figure 8) shows already a drift behavior although the requirements are passed except of the running-in phase. Figure 9 displays the absolute differences from the nominal value (zero) with the limits.

Interference

The interference of the device to the components NO_2, SO_2, and water moisture was tested. The results are seen in Table 1. The analyzer shows interferences to SO_2 in the region of 5 %. This discrepancy can be negligent because the SO_2-concentration of ambient air decreased strongly in the last years. The Hessian annual average for SO_2 is amounted to 6 µg/m^3 in 2007.[23] The recovery rate of a sample gas with a water content of 50 % is located at 13 %.

Field Measurements

Since 2004 respectively 2009 the Hessian ambient air monitoring network measures ammonia at three rural sites (Linden (2004), Spessart (2004), and Witzenhausen (2009)). The NH_3-pollution is low compared to other regions in Europe. The annual average amounts to 2-3 µg/m^3. Due to a close pig fatting establishment the location in Linden is most interesting. The nearby fields are under cultivation. As a result the background level is higher and high concentration peaks occur during fertilization. Figure 10 and 11 are examples for NH_3-trends at the monitoring site Linden. The blue line indicates the ammonia concentration while the red line shows the corresponding ambient air temperature.

Conclusions and Perspective

HORIBA's APNA 370 NH_3 was modified and validated according the German and European type approval tests by the Hessian Agency for Environment and Geology

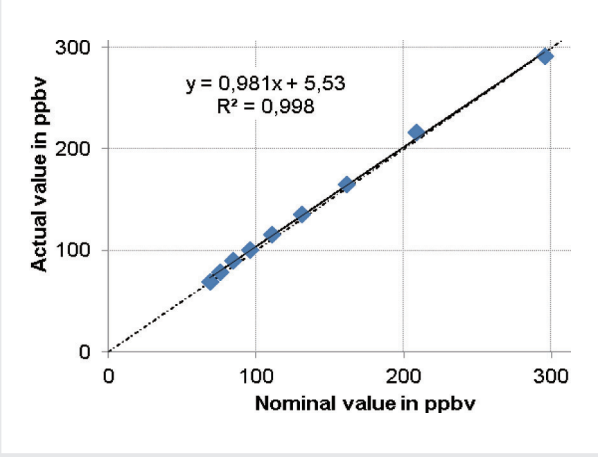

Figure 7 Lack of fit with the linear regression function

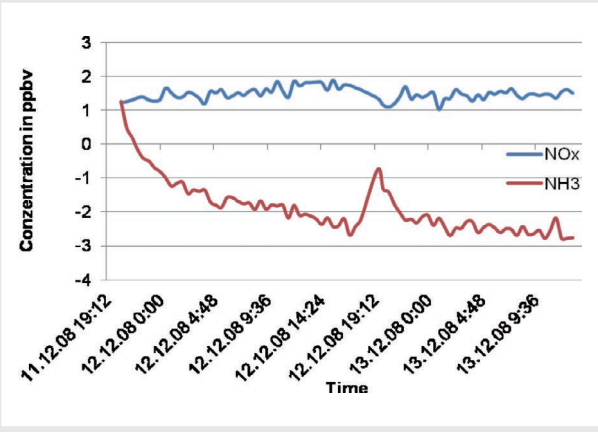

Figure 8 Zero Drift of the NH_3 and NO_x-Signals: Trend diagram

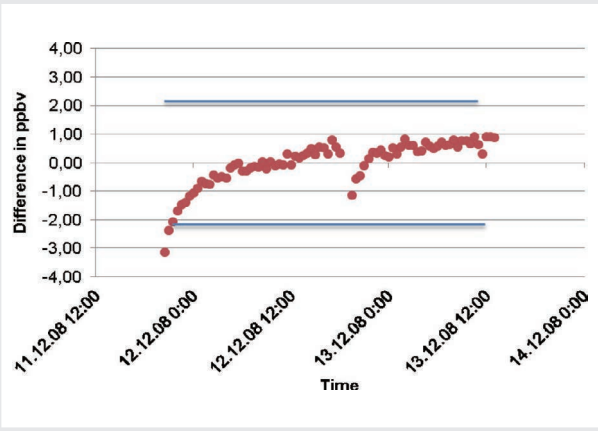

Figure 9 Zero Drift of the NH_3-Signal: Absolute differences of the nominal value

Table 1 Interferences at a test gas of 102 ppbv NH_3 (SO_2 100 ppbv, NO_2 100 ppbv, H_20 50 %)

Interference	NH3-Conc. ppbv	NH3-Conc. interference ppbv	with Difference ppbv	Difference %
SO_2	102	107	5	4.9
NO_2	102	102	0	0.0
H_2O	102	89	-13	-13.0

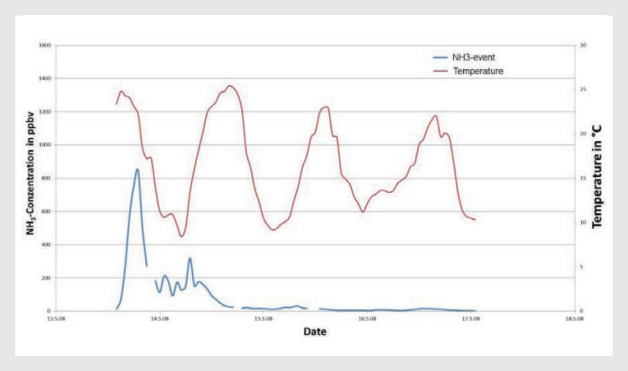

Figure 10 NH_3 trend at the ambient air monitoring site Linden, September 2007, Hessian ambient air monitoring cadastre (HLUG).[18]

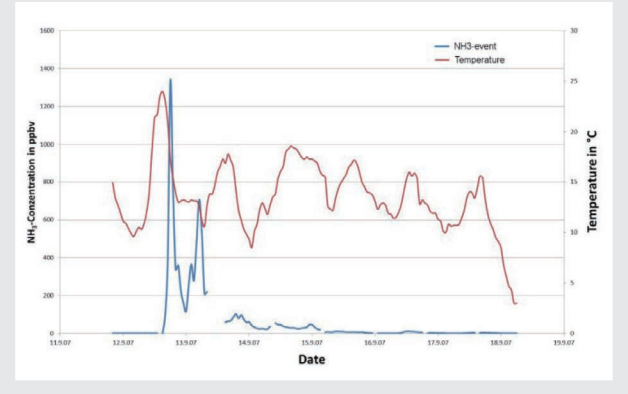

Figure 11 NH_3 trend at the ambient air monitoring site Linden, May 2008, Hessian ambient air monitoring cadastre (HLUG).[18]

(HLUG). After modification the system fulfills most of the requirements although there is still need for improvements.

Response time: At present the analyzer cannot be used in traffic related sites due to fast concentration changes. The pollution situation at agricultural locations can be monitored with an adequate resolution (see Field Measurements) although NH_3-monitoring at traffic related sites becomes more important due to changes in the motor technique of diesel-engine vehicles (SCR-cat).[24]

Drift: The criterion is met although the instrument drift should be improved.

Interference: To deal with interferences from high water moisture, you have to consider the following aspect: The unit consists of two separate, parallel installed conversion pathways. The first one is the NO_X converter operating at 230 °C and the second is the NH_3 converter running at 830-870 °C. As a conclusion and related to the temperature difference, there is a potential difference in air humidity. To avoid the cross sensitivity a molecular sieve with less than 3 Angstroem could be installed prior the converter pathways, just like dryer. It would be the optimal pore size due to the different molecular diameters of H_2O and NH_3. This application still needs to be tested.

Converter efficiency: Currently there are theoretical thoughts about exchanging the stainless steel tubes (Figure 6) by Molybdenum oxide (MoO) or a Platinum/Rhodium grid. Tests were performed with a molybdenum oxide granulate filling. First results display an efficiency of 98 % by 450 °C. This low temperature converter reduces measuring errors due to the effect of nitrogen combustion. Platinum/Rhodium grids are used in the industrial NO production (Ostwald process). There, NH_3 is selectively oxidized to NO.

References

[1] World Health Organisation (WHO), "Air quality guidelines for Europe", 2th Edition, *WHO Regional Publications*, European Series 91, ISBN 13563, Kopenhagen, 2000

[2] Erste Allgemeine Verwaltungsvorschrift zum Bundes-Immissionsschutzgesetz (Technische Anleitung zur Reinhaltung der Luft - TA Luft), 24. Juli 2002, GMBl. 2002, Volume 25 - 29, 511 - 605, 2002

[3] Protocol to abate acidfication, eutrophication and groundlevel ozone, United Nations Economic Commission for Europe, convention on long-range transboundary air pollution, signed by 27 member states am 1. December 1999 in Goteborg

[4] Directive 2001/81/EC of the European Parliament and of the Council of 23 October 2001 on national emission ceilings for certain atmospheric pollutants, THE EUROPEAN PARLIAMENT AND THE COUNCIL OF THE EUROPEAN UNION, *Official Journal L 309, 27/11/2001 P. 0022 - 0030*

[5] Bayrisches Landesamt für Umweltschutz (BLfU), "Ammoniak und Ammonium", BayLfU 2004 - PS1 / Umweltberatung Bayern, August 2004 [6] Umweltbundesamt, Umweltdaten, 2002

[6] Umweltbundesamt, Nationale Trendtabelle für die deutsche Berichterstattung atmosphärischer Emissionen seit 1990 (15.04.2011), http//www.umweltbundesamt.de/publikationen.htm, retrieved 2012-07-23

[7] Döhler, H., Eurich-Menden, B., Dämmgen, U., Osterburg, B., Lüttich, M.. Bergschmidt, A., Berg, W., Brunsch, R., BMVEL/UBA-Ammoniak-Emissionsinventar der deutschen Landwirtschaft und Minderungsszenarien bis zum Jahre 2010, UBA-Forschungsbericht 299 42 245/02, UBA-FB 00249, ISSN 0722-186X, P. 109

[8] Baumbach, G., Luftreinhaltung, Springer-Verlag, 1990

[9] Kato, J., Measurement technique and its application to trace components of atmospheric gas, HORIBA Readout 10, 30-35, 2006

[10] Falbe, J., Regitz, M. (issuers), Römpp Lexikon Chemie, 10th Edition, Volume 4, 3180f, Georg Thieme Verlag, 1998

[11] DuPont, http://www2.dupont.com/Teflon_Industrial/en_US/tech_info/techinfo_compare.html, retrieved 2012-07-23

[12] DIN EN 14211 “Luftqualität - Messverfahren zur Bestimmung der Konzentration von Stickstoffdioxid und Stickstoffmonoxid mit Chemilumineszenz”, Beuth Verlag, 2005
[13] DIN EN ISO 6144, “Gasanalyse - Herstellung von Prüfgasen - Volumetrisch-statisches Verfahren”, Beuth Verlag, 2006
[14] VDI 3490-14, “Messen von Gasen - Prüfgase - Herstellung von Prüfgasen nach der volumetrische-statischen Methode unter Verwendung von Glasbehältern”, Beuth Verlag, 1994
[15] VDI 2100-4, “Messen gasförmiger Verbindungen in der Außenluft - Messen von Innnenraumluftverunreinigungen - Gaschromatographische Bestimmung organischer Verbindungen - Kalibrierverfahren als Maßnahme zur Qualitätssicherung”, Beuth Verlag, 2004
[16] DIN EN ISO 6145-10 “Gasanalyse - Herstellung von Kalibriergasgemischen mit Hilfe von dynamisch-volumetrischen Verfahren - Teil 10: Permeationsverfahren”, Beuth Verlag, 2008
[17] VDI 3490-9, “Messen von Gasen - Prüfgase - Herstellung durch Permeation der Beimengung in einen Grundgasstrom”, Beuth Verlag, 1980
[18] Hessisches Landesamt für Umwelt und Geologie (HLUG), Ambient air monitoring cadastre
[19] VDI 4203-1, “Prüfpläne für automatische Messeinrichtungen - Grundlagen”, Beuth Verlag, 2001
[20] VDI 4202-1 “Mindestanforderungen an automatische Immissionsmesseinrichtungen bei der Eignungsprüfung - Punktmessverfahren für gas- und partikelförmige Luftverunreinigungen”, Beuth Verlag, 2002
[21] VDI 4203-3, “Prüfpläne für automatische Messeinrichtungen - Prüfprozeduren für Messeinrichtungen zur punktförmigen Messung von gas- und partikelförmigen Immissionen”, Beuth Verlag, 2004
[22] Directive 2008/50/EC of the European Parliament and of the Council of 21 May 2008 on ambient air quality and cleaner air for Europe, THE EUROPEAN PARLIAMENT AND THE COUNCIL OF THE EUROPEAN UNION, *Official Journal L 152,11/061/2008*
[23] Hessisches Landesamt für Umwelt und Geologie (HLUG), “Lufthygienischer Jahresbericht 2007, Teil 1: Kontinuierliche Messungen”, 2007
[24] Feßmann, J., Orth, H., Angewandte Chemie und Umwelttechnik für Ingenieure, *ecomed Sicherheit*, 2th Edition, 2002

Wilma TRAVNICEK
Master of Science in Physics
Department of Pollution Control and Radiation Protection
Hessian Agency for Environment and Geology

Stefan KARWISCH
Teamleader Service Engineering
Process & Environment
HORIBA Europe GmbH

Grischa P. FEUERSÄNGER
Marketing and Project Engineering
Process & Environment
Office Leichlingen
HORIBA Europe GmbH
Dr. Rer. Nat.

Feature Article

Modification of HORIBA's ENDA-5000 Continuous Emission Monitoring System in order to fulfill requirements of European standard EN 15267-3

Jaroslav LIBAL

HORIBA's ENDA-5000 Continuous Emission Monitoring System (CEMS) is used for continuous monitoring of NO_X, SO_2, CO, CO_2 and O_2 in stack gas, produced by stationary sources like power plants, boilers, gas turbines, furnaces, chemical plants, etc. Prior to the introduction of new CEMS to the European Market, the whole system must be tested and approved by the European certification agency, for example TÜV in Germany or MCERT in the U.K. There are lots of test procedures, which are applied to CEMS during the certification process in the laboratory as well as in the field under real process conditions. CEMS units must comply with the conditions that are specified in European standard EN 15267-3.[1] One of the most important items is the test for resistivity of CEMS system against disturbing or interfering chemical components.

Introduction

The industrial combustion of coal, oil, gas, waste and other combustion materials does not provide just energy, but also generates emission, gases like NO_X, SO_2, CO, CO_2, HCl, HF, and dust particles. These gases as well as the dust particles are subject of continuous monitoring. In present time, HORIBA provides several analyzer systems for the continuous monitoring of most important emissions gases, which are NO_X, SO_2, CO, CO_2, and of course O_2 as the reference component. In this year, HORIBA brings the ENDA-5000 analyzer system for continuous monitoring of NO_X, SO_2, CO, CO_2, and O_2 to the European market. The heterogeneous components NO, SO_2, CO, are determined by Non Dispersive Infrared (NDIR) combined with HORIBA's Cross Flow Modulation technology, while the oxygen concentration is measured by a magneto-pneumatic analyzer. Prior to entering the European market, the entire monitoring system, consisting of sampling probe, heated sampling line, sample conditioning unit and analyzer, must be approved by European certification agency. As mentioned in the preface, there are many test procedures that have to be conducted to CEMS during the certification, in laboratories as well in the field under real process conditions. The entire certification procedure is described by the European Standard EN15267-3 and includes tests of parameters like: response time, detection limit, standard deviation for zero and span point, linearity, zero and span drift, NO converter efficiency, influence of ambient temperature, sample flow rate and sample pressure, influence of vibration, fluctuation of voltage supply, and, probably the most important, the influence of specified disturbing and interfering components.

Combustion and various other production processes do not only generate gaseous emissions of NO, SO_2, CO, CO_2 as mentioned above, but also other gases like N_2O, HCl, NH_3, CH_4, and H_2O, according to fuel type and technology. The presence of these gases can have a significant influence for measurement of NO/NO_X, SO_2, CO, CO_2. This is the reason why any CEMS system is being approved by European Certification agency according to EN 15267-3 and must be resistive to the above mentioned, specified disturbing and interfering components. The infrared optical bench of the ENDA/CMA-5000 system is equipped with gas filters and compensation detectors to prevent the interferences

caused by N_2O, CH_4, H_2O and CO_2. Problems to overcome are not only caused by interfering components, but also by the SO_2 and NO_2 loss in the sample conditioning system. According to EN 15267-3 the total influence of interfering and disturbing components, including the loss of any tested component in sample conditioning system, must not exceed 4% of the measurement range. This is one major issue for all kinds of extractive analyzers and sample conditioning systems, which operate under dry (cold) conditions. In general they use electrical coolers (Peltier or compressor) to cool down the sample gas down to +5 °C dew point and remove the moisture. As SO_2 is well soluble in the water, we can expect a high loss of SO_2 in the electrical cooler, while cooling down wet sample gas containing up to 30 Vol.% of H_2O. As the standard configuration of the HORIBA ENDA-5000 sample conditioning system did not fulfill the requirements of EN 15267-3 at the German TÜV Certification agency, especially not the application of humid SO_2 test gas containing 30 Vol. % of H_2O, HORIBA Austria has decided to modify the sample conditioning system of ENDA-5000 in order to fully comply.

Materials and Methods

The ENDA-5000 is extractive analyzer system, measuring NO/NO_X, SO_2, CO, CO_2, O_2 at dry condition, i.e. the very first element of sample conditioning system is electrical cooler, which has to remove the moisture from the sample gas down to +5 °C dew point. As SO_2 is very well soluble in the water, we must expect high loss of SO_2 in the electrical cooler, while cooling down wet sample gas, containing up to 30 Vol.% of H_2O. The assembly of the primary cooler unit, used in the sample conditioning, should minimize the contact between sample gas and condensing water as much as possible. But there is still a big loss of SO_2 inside the cooler, significantly exceeding 4 % of measurement range. This is a critical issue especially in case of low concentration measurement for SO_2. The EN 15267 requires to test the SO_2 analyzer operating at measuring range 0 to 75 mg/m^3 (= 0 to 26.2 ppm).
One solutions to prevent the loss of SO_2 and NO_2 in first sample gas cooler is to establish a sufficient acidulous environment inside the cooler‘s heat exchanger, in order to replace the water condensate with weak acid. SO_2 and NO_2 as well as acid gases will not be affected in acidulous environment and will pass through the cooler without loss. A suitable acid for this purpose is diluted Ortho-phosphoric acid (H_3PO_4), injected in front of the primary cooler. Hence we have developed a special, electrically heated injection system, incorporated in front of first electrical cooler. A very small amount of weak ortho-phosphoric acid solution is injected by a peristaltic pump

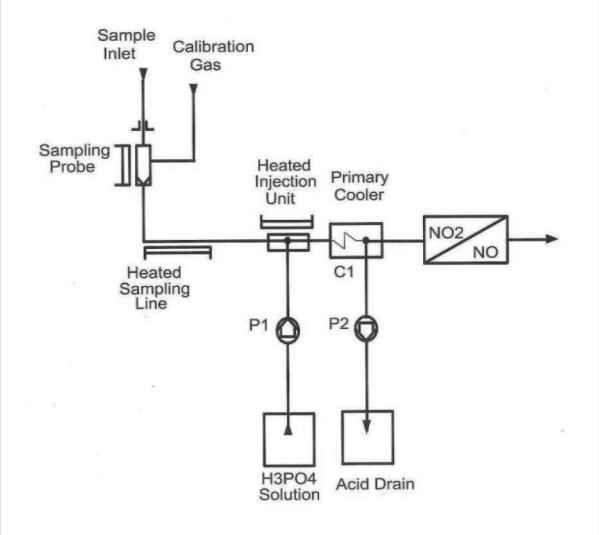

Figure 1 ENDA-5000 - front part of sample conditioning system – flow schematic with electrical cooler ECP1000-G, temperature set to +5 °C and heated H_3PO_4 injection section.

(Figure 1, P1) into the sample gas stream. The essential prerequisite is to inject the acid at a high temperature, at least 80 to 90 °C. Immediately after injection, the sample gas together with ortho-phosphoric acid flows into the primary cooler. Due to sufficiently acidulous environment inside the cooler‘s heat exchanger, saturated with ortho-phosphoric acid, the SO_2 and/or NO_2 cannot be additionally dissolved or absorbed. All the ortho-phosphoric acid solution is consecutively removed as acid condensate from the bottom part of electrical cooler by peristaltic pump (Figure 1, P2).

The heated acid injection unit is connected directly behind the sample line inlet port, inside of ENDA-5000 analyzer cabinet. (Figure 2) (The outlet of acid injection unit is connected directly to the primary cooler, which is set to +5 °C. The ortho-phosphoric acid solution is injected by the peristaltic pump, delivering 0.3 L/hour. The acid drain at the bottom of cooler is removed by similar peristaltic pump with capacity of 0.6 L/hour.

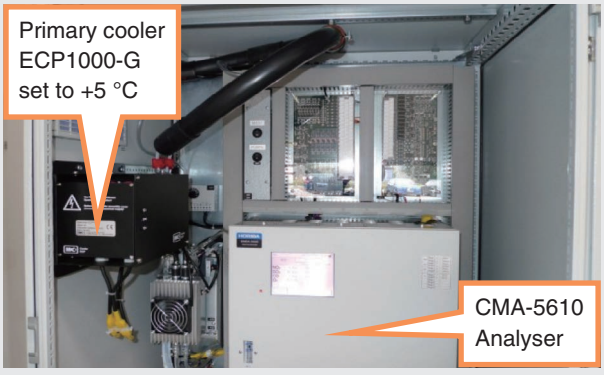

Figure 2 ENDA-5000 cabinet - upper part with electrical cooler ECP1000-G, temperature set to +5 °C and heated H_3PO_4 injection section.

Once the acid injection unit is started, the acidulous environment inside the primary cooler is created within several minutes. The measured loss of SO_2 is minimized to less than 1%.
If the acid injection is switched OFF, the acidulous environment remains for about 10 minutes, but then the SO_2 concentration will start to drop, as SO_2 starts to dissolve in the water condensate inside the cooler.

Results

In Figure 3 you can see the response characteristic of the ENDA-5000 analyzer, if dry sample gas (span gas containing 25 ppm SO_2 in N_2) is applied to ENDA-5000 Analyzer's inlet port. In this case, as sample gas is absolutely dry, the phosphoric acid (H_3PO_4) is not injected. The response efficiency is very high and this can be used for ZERO and SPAN calibration for the ENDA-5000. Dry sample gas therefore meets the requirements of EN 15267-3, as ZERO and SPAN gas must flow through the entire sample conditioning system during the calibration procedure. Under real process conditions the calibration gas must always be applied to the sampling probe.

The next chart (Figure 4) shows the behavior of the ENDA-5000 Analyzer, if the sample gas (same concentration of 25 ppm SO_2 in N_2) is applied under humid condition. In this case, sample gas contains additionally 13 to 15 Vol. % of H_2O.

As you can see in Figure 4, the response characteristic is, although a little noisy, similar to the one with dry gas application. This is caused by injection of acid in form of drops. However, the amplitude of the noisy signal is only 0.2 – 0.3 ppm of SO_2. Also the response time T90 is

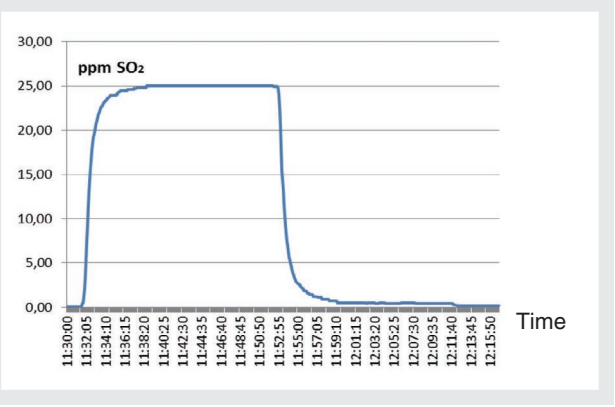

Figure 3 Response characteristic of ENDA-5610 Analyzer to 25 ppm SO_2– dry gas, dry conditions, H_3PO_4 not injected.

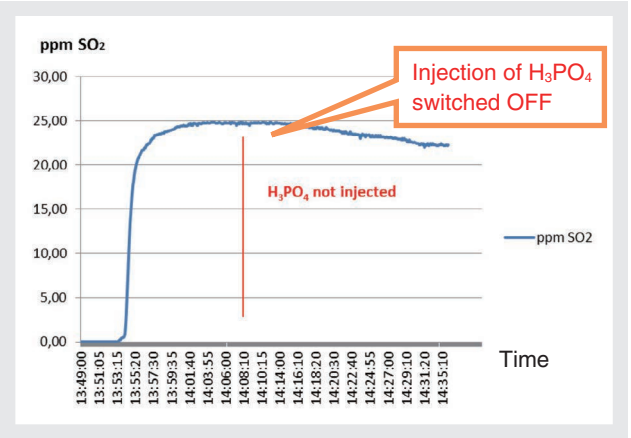

Figure 4 Response characteristic of ENDA-5000 Analyzer to 25 ppm SO_2 – humid sample gas, containing approx. 15 Vol. % of H_2O.

practically the same like the dry gas application.

Conclusions and Perspective

The modification of the ENDA-5000 sample conditioning system with above described phosphoric acid injection into the sample gas stream, has strongly improved the technical features of ENDA-5000 Analyzer System in case of low SO_2 concentration measurement. In the last few years we are facing the situation, that SO_2 concentrations, which are to be monitored, are strongly reduced. Due to restrictive laws, each production facility is presently equipped with flue gas desulfurization (FGD). 10 years ago, the situation was completely different and the combustion contained up to 1000 ppm. SO_2 is also measured in gas turbines powered by CNG (Compressed Natural Gas), where the SO_2 concentration is also very low, depending on the resource quality. Therefore the most requested measurement range for SO_2 lies within 20 to 50 ppm SO_2. Under the utilization of this application, ENDA-5000 Analyzer system as approved system for emission monitoring according to EN 15267-3 can be used for any technological application, where low SO_2 concentration measurement is required.

Reference

[1] World Health Organisation EN 15267-3 Air quality – Certification of automated measuring systems

Jaroslav LIBAL
Head Office
HORIBA Czech Office
HORIBA GmbH
Dipl. Ing

Feature Article

EV-140 P, New Emission Spectroscopic Product for Semiconductor Endpoint, Cleaning and Plasma Chambers Control.

Eric BLUEM, Jean-Philippe VASSILAKIS,
Mickael THIERCELIN, Michel AUBÉ, Harald BIRK

To address new requirements in semiconductor Dry Etch and PECVD (Plasma Enhanced Chemical Vapor Deposition) industry, HORIBA Semiconductor has introduced a unique generation of (Multi) Sensor dedicated to Fault detection, Chamber health monitoring and Advanced Process Control. Hardware and Software issues are developed so that EV-140 P may be adapted to all etchers (clusters and single chambers) and to help researchers, engineers and Fab's to manage actual but also future products and technologies. Based on innovative technologies like smart sensors, unique software architecture, including analytical methodology and sophisticated signal processing, this platform allows satisfying all the needs of in-situ plasma process control. Our paper describes, first, Recipe Designer engineering flow and then results obtained in Fab's for Endpoint and chamber health monitoring applications, like immediate Misprocessing detection, Preventive maintenance setting, Statistics and Multi-run Viewer for quality control in order to secure wafers during critical process.

Introduction

Plasma etching is a widely used technique in the semiconductor industry and the need for in-situ process monitoring is becoming greater as the technology advances. Extremely tight control of key process parameters must be maintained to increase throughput and reproducibility. The greatest need for plasma process monitoring arises in the determination of EndPoint (EPD) for critical ETCH process, which reduces the degree of over/under etching, but also now to control cleaning step and process stability.

For Endpoint detection and plasma reactor diagnosis, Optical Emission Spectroscopy (OES) is the most commonly used method in the industry today. As the open area becomes smaller and the device density becomes greater, select the relevant wavelengths with sufficient robustness in manufacturing environment represents a big challenge for process engineers: even if a new process development often means complex plasma spectra analysis, Process Engineer needs to setup "immediately" a production recipe.

The OES tool we present, EV-140 P, handles this complexity and allows to develop/optimize quickly and quite automatically any process:

- Selection of the relevant wavelengths that carry the information about the transition with the engineering software, Recipe Designer.
- Real-time data filtering (in the broad sense) and construction of an ENDPOINT indicator with the real-time software, Sigma_P.
- Series of tests to confront the algorithm to the reality of production fluctuations.

In this paper, after a short introduction about methods of analysis, two complementary types of OES in-situ metrology are presented: Endpoint detection and Health Monitoring based on real production applications.

With the help of Altis, historically IBM-Infineon Company, we present a method to monitor plasma during contact etch with low open area and high Polymerizing chemistry. This method uses Optical Emission Spectroscopy to improve plasma monitoring using wavelengths emission intensity of different species. When EPD is too much difficult to find or not a key parameter, Health monitoring on specific wavelengths ratio between polymer depositions and etch can be a good alternative. As a complement, typical characteristic wavelengths can be used to catch any equipment failure.

In this experiment it was shown that the optical spectrometer can be used for EPD and Health monitoring to enhance etch process monitoring and secure wafers etching.

Method for Endpoint Detection and Health Monitoring

Optical emission spectroscopy

Optical emission spectroscopy is a spectral analysis of the light emanating from plasma. For EPD and plasma diagnosis measurements, Optical Emission Spectroscopy is the most commonly used method in the industry today. Plasma emission results from the excited species relaxation in plasma. The direct electronic impact is the main excitation source. The spectral domain, 200 to 800 nm, is the main region being able to be observed by OES. And OES has the big advantage of being an external diagnosis from the reactor. So, plasma is not disturbed by this system. As we can see on Figure 1, EV-140 P gives access to many spectra (down to every 20 ms) and then to huge data along process. The question now is: how to select relevant process wavelengths from spectra?

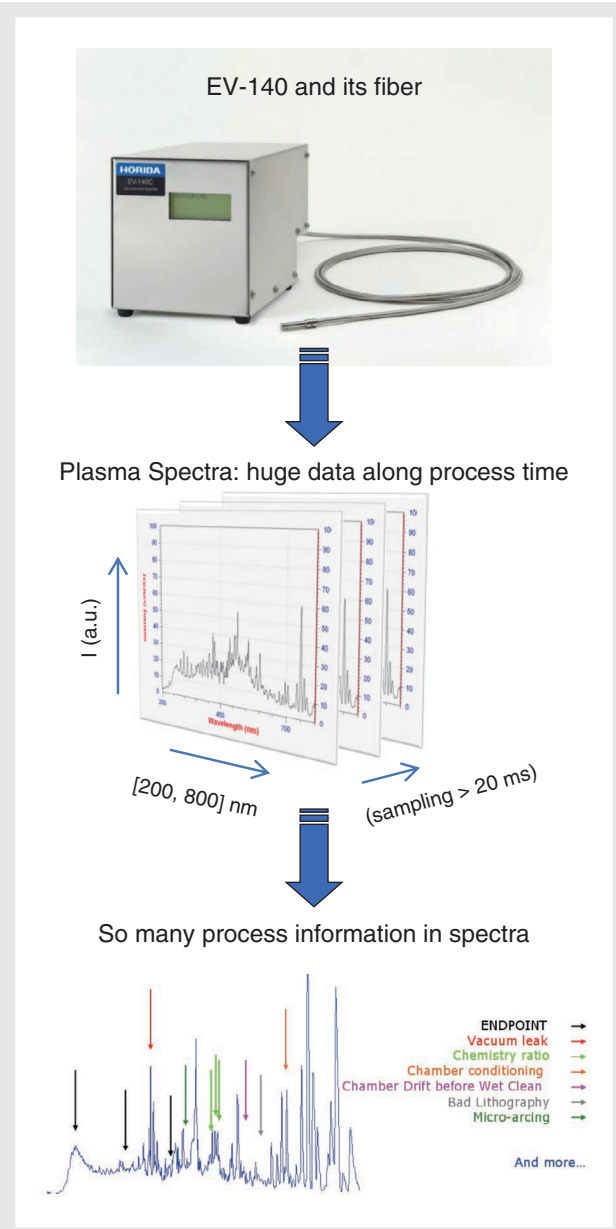

Figure 1 Ev-140 P spectra acquisition

Endpoint detection

By monitoring the emission intensity of selected wavelengths, the system tracks the amount/loss of material in the plasma, as when a particular material has been completely removed from the etch surface. Thus, based on the changes in the spectrum of radiation emitted by the plasma, the Endpoint is detected: due to non-uniformity on wafers, EPD is characterized by two ruptures as described Figure 2.

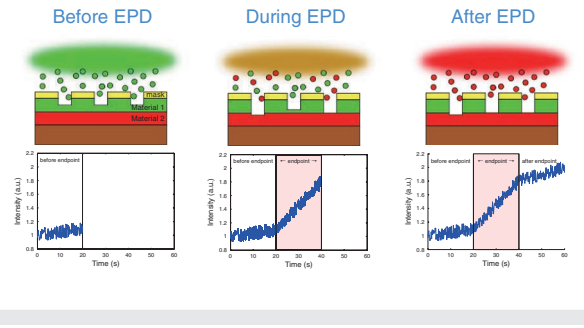

Figure 2 Principle of Endpoint detection

From endpoint to health monitoring

Sigma_P contains a large SQL database to allow:
- General monitoring for plasma dry Etch and PECVD:

Spectra Data collection (using Fab's logistics information), analysis, comparison using internal emission library and spectra reference, process

identification, uniformity control. Various functions like trends, ratios, differences, average, standard deviation.... can be used.

- Advanced Endpoint Process Control:
  Fully Automated Endpoint/Run to run control/Fault Detection Classification to improve yield and increase productivity in semiconductor manufacturing.
- Chamber Health Monitoring:
  - Chamber qualification and cleaning.
  - Chamber conditioning to avoid first wafer effect.
  - Matching and troubleshooting.
  - Chamber gas leak detection or gas purity control.
  - Preventive maintenance.
  - Failure analysis.

Hardware and fab's logistics

The HORIBA cluster system is used to collect the plasma emission during any etching or PECVD process. This system is equipped with a sturdy optical fiber which can be easily mounted on the side window of the plasma chamber. It uses 2048 CCD sensors. EV-140 P provides process automation for in-line integration in a production environment. It offers RFon, PIO remote, stop etch management, RS232 with the tool, TCP/IP/SECS/HSMS with network...

Softwares

Endpoint detection and Health Monitoring are available thanks to Recipe Designer and Sigma_P software.

Recipe designer, engineering flow

Based on new advanced mathematical treatment like wavelet and rupture probability, including analytical methodology and sophisticated signal processing, **Recipe Designer** allows satisfying all the needs of in-situ plasma process control.

On the Figure 3, the principle of Endpoint detection using Recipe Designer is illustrated. This software permits to extract *semi-automatically* relevant wavelengths contained on raw spectra, characteristic of

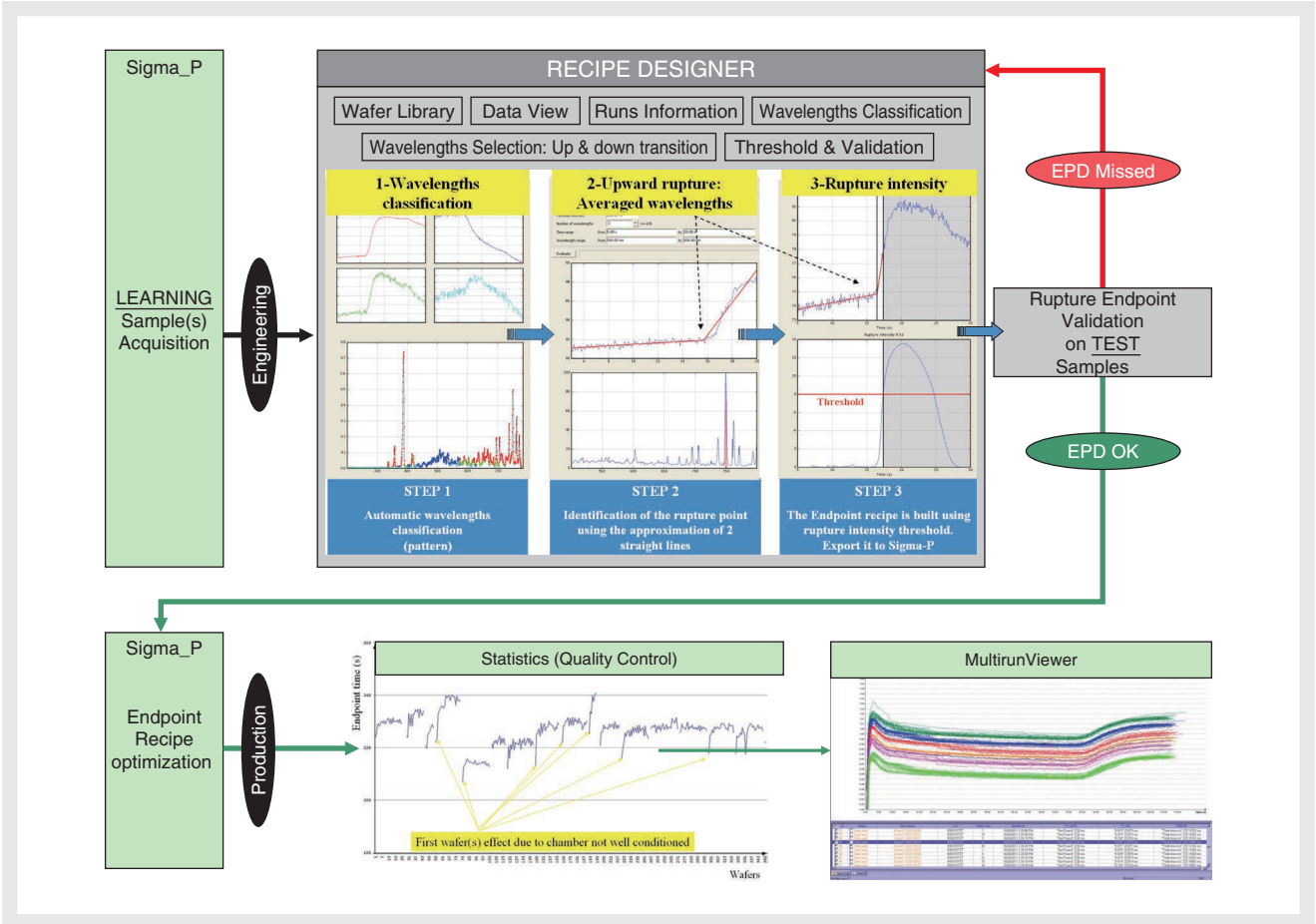

Figure 3 Recipe designer engineering flow: From spectra acquisition to Endpoint on Production

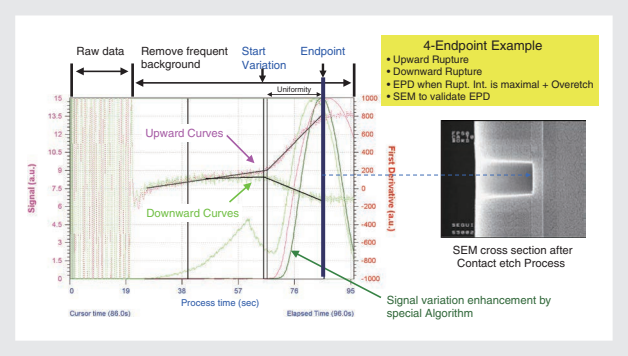

Figure 4 Sigma_P endpoint with SEM confirmation

plasma change like interface achieved, impurities detection, and Endpoint found...

Rupture slope may be "upward" or "downward". Working simultaneously on several runs result, Recipe Designer defines a threshold on the best rupture intensity and then check validity over those samples, as shown on Figure 3.

Real –time acquisition & EPD

Recipe Designer creates an Endpoint recipe directly exported to Sigma_P. Exposing the algorithm to the reality of production environment, this recipe is enhanced with reprocessing, optimizing parameters like derivative, filtering, conditions/decisions.

Then, EPD has to be confirmed using, for example:
- Scanning Electron Microscope (SEM cross section) measurement (Figure 4).
- Prepared wafers with varying thickness to show the correlation versus endpoint time.

As Endpoint management is done, it remains now to be sure that chamber and process stay on a safe mode to protect samples, wafers, masks, flat panel display...

Engineering tools to help process engineer to develop health monitoring algorithms

To achieve preventive and comparative actions, Sigma_P contains a Health Monitoring Toolbox:
- Statistics (Figure 3): EPD stability, EPD missed, 1st wafer effect…
- Spectrum and kinetics comparator with pattern envelop models, trends, Process Tags.
- Fingerprinting using references.
- Multi-runs Viewer (Figure 3): 1 color = 1 batch of 25 wafers.
- Real time action: Health Warning, Health Stop, continuation until Default time to avoid under etch, Emails...

Experiment

In this study, Dual damascene etch process, MXVX, is performed in a TEL (Tokyo Electron Ltd) SCCM (Super Capacitively Coupled Module) etch chamber (dual source) while Contact Etch, CA, is done on Applied Materials.

MXVX process has many etch steps with:
- ARC open (Anti reflective Coating) and Nitride etch (SiN) with endpoint detection possibility (ARC to Oxide (SiO) and SiN to Copper interface).
- VIA etch which uses a very high selective chemistry oxide to SiN with low open area (less than 2%), and over etch is minimum on actual production wafers, so endpoint detection is very difficult.
- Trench etch which has no stop layer, so the goal is to control these two steps using Health Monitoring.

First we decide to evaluate:
- EPD on the Arc open step which has low open area but with a low polymerizing effect.
- Health monitoring on the Partial VIA step with same open area (2%) but with a high polymerizing effect.

EPD on MxVx etch process

On this process, we want to detect one endpoint at the ARC/SiO interface (Figure 5). This step exists with two types of integrations. One with a 193 nm resist and one with a 248 nm resist. With a 193 nm resist, ARC is less thick than ARC with a 248 nm resist. This difference of thickness is visible with endpoint time on the Figure 5. With a 193 nm resist, we found an endpoint earlier than with a 248 nm resist. For both types of resist, statistic results show a good reproducibility on endpoint time.

Then, this endpoint has been validated with a SEM cross section:

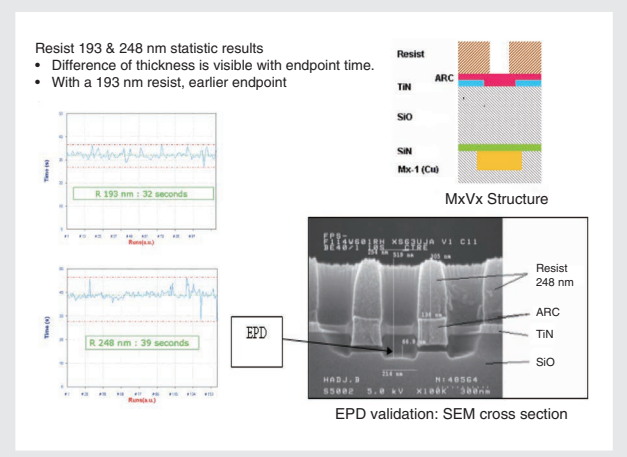

Figure 5 Arc open structure: EPD validation

ARC is open in 45 seconds with 248 nm resist (with an overetch).

Health monitoring on MxVx etch (Partial VIA step)

In this part, we want to detect all wafers considered as abnormal on the Partial VIA (2% open area) step from MxVx process. Thus, various defects into production recipes have been simulated. These defects are resumed below (Figure 6). The wafer ENG1 simulates a GAP (inter electrodes) problem, the ENG2 and ENG3 simulate an abnormal quantity of O_2 gas, the ENG4 and ENG5 feign a power problem, the ENG6 and ENG7 simulate a pressure problem, and the last ENG8 and ENG9 simulate an abnormal quantity of C_5F_8 gas.
Depending on equipment capability, these parameter's drifts are chosen for their sensitivity to the process (etch stop or less selectivity):
- Etch stop: too much polymers, ratio CF2/SiF4 increases
- Loss selectivity: less polymers, ratio CF2/SiF4 decreases

The aim was to develop an algorithm able to detect all these misprocessing. The algorithm integrates a superior and an inferior threshold in order to constitute an envelope (Figure 6: green dotted). When the signal characteristic of these wafers crossed the envelope, the signal has to be stopped. Monitored signals are the ratio between ENGX intensity and reference intensity (so reference is at 1). This reference, ENG10, was realized from a standard wafer during a standard process. On the Figure 6, there are the results. In x-axis, the time in second, and in y-axis, the ratio intensity. All the signals characteristics of these wafers (ENG 1 to 9) are stopped. Hence, Health Monitoring algorithms are able to discriminate Misprocessing even without managing endpoint.

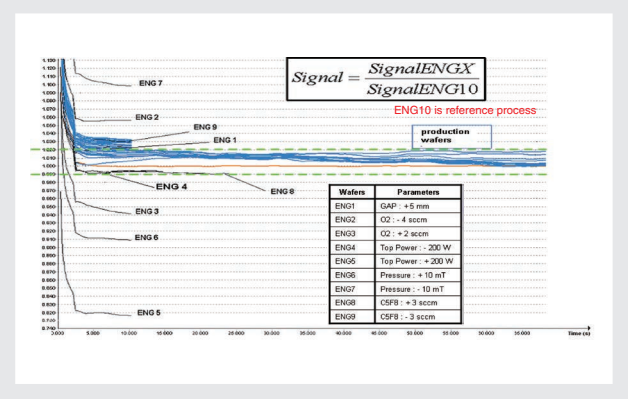

Figure 6 Multi Runs Viewer, Health Monitoring on MxVx

Furthermore, in order to give more realism to this study, several batches from production (Figure 6: the long blue curves) are inserted to check if Health Monitoring algorithm is strong enough to deal with classical wafers. But some lots are rejected due to Health Monitoring reason. After analysis, result is that wafers with too different open area cannot be monitored with this recipe. To go further, each technology has to be monitored with a dedicated recipe containing a relevant reference.

Health monitoring on CA etch process

On contact etch (CA), Health Monitoring (HM) target is to fit tool evolution (polymerization) between two wet cleans and monitor the tool drifts (Figure 7).
On this picture, the N_2 leak causes the instability of the electric signal. HM action wanted is to stop before the first abnormal wafer of the batch.

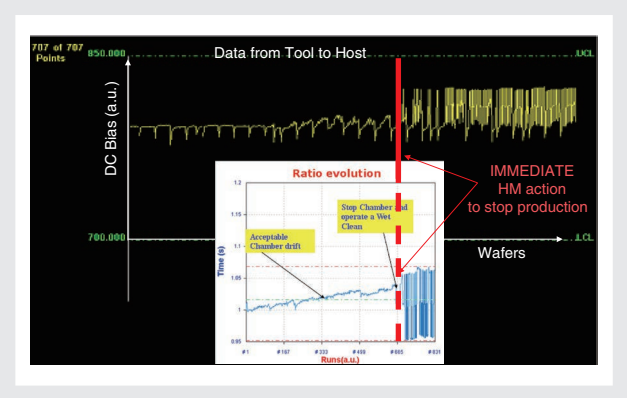

Figure 7 Tool drift and stop at the batch

This process is very sensitive at N_2 gas leaks which change the plasma composition and destroy the wafers. The aim is to detect the leaks before wafers degradation. Before the use of EV-140 P system, these leaks were detected too late because the time between the tool drift and the warning mail sent to the engineer is about 3 hours. And with this system we are able to detect very quickly these leaks and act on the tool during the production. So, the destruction of several batches is avoided. The engineers are able to act immediately after the drift because the system is configured to warn engineers at the first signs of drift (Email sent by EV-140 P from the clean room) and/or stop immediately the tool.

Health monitoring on wet clean recovery

Another application of Health Monitoring is the analysis of the production. On the Figure 8, there are the statistic results on about 7500 wafers (over 6 wet cleans). In x-axis

there is the number of wafers and in y-axis there is the signal intensity (real time spectra/reference spectra ratio).

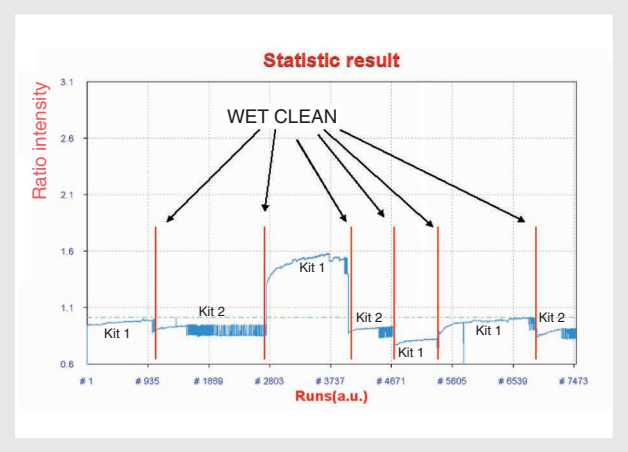

Figure 8 Health Monitoring on CA etch process

The Figure 8 gives us two important results:
- After each Wet Clean, the signal doesn't start with the same intensity, so Wet Clean procedure must be modified to obtain better reproducibility.
- Depending on Kits used, chamber life duration is different. We can see that Kit 2 is not adapted to this production.

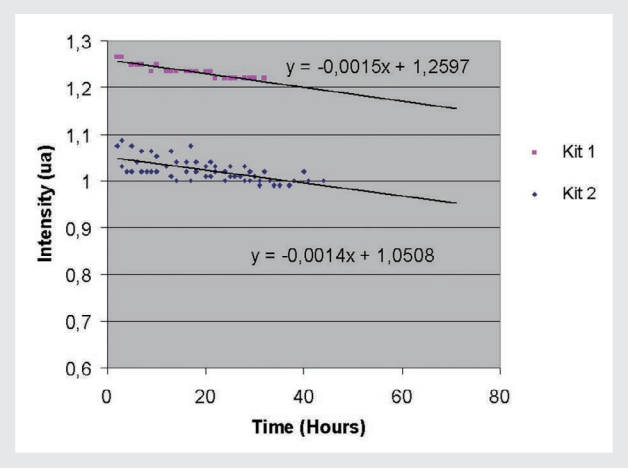

Figure 9 Chamber evolution with two different Tool Kits

On Figure 9, two Tool Kits have been emphasized with two groups of points. We note there are two similar trends (same slope) for two different Tool Kits.

Analyzing CF2/SiF4 ratio, we see that the polymerization (the equipment's clogging) is linear. Thus, we can follow the tool's clogging, and predict the wet clean depending on Tool Kit installed.

Conclusion

Monitoring the MxVx and CA process was extremely challenging due to low open area (2%), high selectivity chemistry, wet clean management and polymerization.

Endpoint detection using OES method proves to be a powerful technique that meets the plasma etching needs of the next generation of logic chips. Even if endpoint cannot be raised (especially for PECVD), Health Monitoring permits to manage chamber life duration and process drift to avoid Misprocessing and also raise alarm if necessary. But to do that on production environment, optical setup from chamber to OES system must be well known and reproducible chamber to chamber and Wet Clean after Wet Clean. It is so important for process engineer to have an up-to-date toolbox to enter into plasma information that a new version of Recipe Designer, RD7, will be soon out.

Besides EV-140 P, as soon as a top window exists on tool chamber, LEM-CT permits with Interferometric camera to obtain Etch rate, thickness Etched/deposited, Endpoint.

Eric BLUEM
Application Engineer
Process Control R&D Dept.
HORIBA Europe GmbH, France
Ph. D

Jean-Philippe VASSILAKIS
Software Manager
Process Control R&D Dept.
HORIBA Europe GmbH

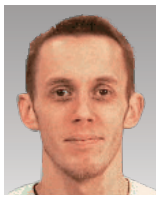

Mickael THIERCELIN
Process Engineer
Dry Etch Division
Altis International
Ph. D

Michel AUBÉ
Engineer
Process Expert
Dry Etch Division
Altis International

Harald BIRK
Business Line Manager
Semiconductor Systems
HORIBA Europe GmbH

Product Introduction

A New Generation of High End Instruments

Pierre BACHELIER

High end instruments for Hematology market is a tremendous request both from hospitals and screening platforms where high reliability and throughput are required. To address this challenging market, the Nexus product was designed and manufactured as an improvement of the existing Pentra DX120 blood analyzer. The main improvements concern hardware and software, including the use of a new laser technology, some pneumatic improvements, additional functionalities in the Pentra ML Data Management and an ergonomic evolution including a new cover integrating a color touch screen. The Pentra Nexus comes out in two versions, the Pentra DF Nexus, making cell blood count, and the Pentra DX Nexus adding the 5 diff formula, erythroblast and reticulocyte parameters to the cell blood count (Figure 1). This article sets out the major technical developments of the Pentra DX Nexus.

Aim of the Project

Before launching the teams on such a development and fixing the project planning, it was necessary to define the project framework. The main needs to make a new product were clear, but it was necessary to define details, to be sure they could be achieved within the project constraints. Three main changes were set out, improving reliability, adding new features on Data Management and changing the look & feel of the instrument.

The reliability of a product is extremely important, for our customers who use our products every day as well as to reduce field service costs. It was necessary to identify possible changes that would improve the product reliability. A study was conducted on the most common

Figure 1 Pentra DX Nexus with Pentra ML Data Management

machine failures reported from the field. Each type of failure was analyzed so as to identify its cause and find a technical solution to reduce or correct the defect. The study showed a possible gain on MTBF (Mean Time Between Failure). Seven possible improvements were identified and could be tackled within the project constraints. Some feasibilities were made to validate the solutions. The effective gain on MTBF was dependent on the efficiency of each modification, but some of those MTBF can only be observed after some use. Indeed, some failures occur after several months of use. Verification of this efficiency can only intervene at the end of the project through reliability tests on the product and then through measurement directly on the field, on installed machines.

The Pentra ML Data Management is a validation station of test results. Several high range instruments can be connected to the Data Management. The test results are automatically validated according to given rules before being transmitted to the LIS (Laboratory Information System) that centralizes all the prescription results. The validation rules exploit the patient's historical antecedents if any, to carry out a rerun or reflex (additional tests) following according to specific conditions. Finally, the results that cannot be automatically validated are manually validated through a man-machine interface that gives the biologist the necessary information to make a decision. Among the changes, it was requested to add information on the reagents used to obtain the result, such information being needed for analysis traceability. The other major change was to improve the QC management by centralizing information on Pentra ML. Detailed specifications of these new functions have been defined with the Marketing and Development.

The requested Look and Feel change resulted in major design changes. The instrument cover is a molded part of a size of the instrument, modifying its shape implies the creation of a new mold composed of two steel parts and weighing 10 tons. Replacing a screen by another implies mechanical changes but also electronics and software evolutions. In both cases, changes had to remain consistent with the target to release a new product within one year.

Design Elements

Right away, realization of a new cover was considered critical in the project. It was necessary to define a new cover shape as soon as possible. To do so, we used a designer who proposed several sketches, from classic to modern, taking into account technical constraints, such as the opening of the cover, loading or ejecting racks. Communication and Marketing departments chose the final design among those proposed. At this point, the hardware department was able to start designing the cover and all associated changes such as incorporating a PC subset, USB ports in front and back, and upgrading the loading chimney to accept open racks, yet another expected development. These racks can be used in laboratory pre- and post-analytical systems, to automatically load or unload tubes. Once the cover design was completed and verified, a prototype was developed with FDM (Fused Deposition Modeling) technology. This prototype cover was assembled on a machine frame and it allowed checking each part of this new mechanical part in detail. Minor changes were proposed on the drawing (3D) before starting the mold design and its validation. The mold was made in China. Once completed, the first injected parts were tested again to validate the covers themselves and the injection process. Our supplier was ready to produce the first series.

The Pentra DX Nexus is an evolution of an existing product, the Pentra DX120 which was designed around 1995. Replacing the black and white LCD screen by another compatible screen or any other system was not easy since it was specified that the electronic design would not be reconsidered. This instrument has an architecture based on an MOTOROLA 68000 microprocessor electronic board and a set of dedicated electronic boards equipped, for some of them, with HC11 microcontrollers. These boards are grouped on a G96 bus, each having a specific function such as input/output management, acquisition management, stepper motor management, and communication management (RS232, parallel port). From a software perspective, the operating system is OS9 from MICROWARE, a real-time multitasking system. The software has a multi-process architecture, each process having a specific responsibility and a limited interface with other processes. Communication between processes is done through a mail. A signal system, implemented in the OS9 operating system allows to cadence actions of the analytical process and rack automation process.

This initially well-thought architecture allowed many Pentra DX120 product changes since its launch, and it will facilitate replacement of the screen. Besides this change of look and feel and user interface, we had to solve problems of electronic component obsolescence. This was the case with the LCD screen. The first solution was to replace the reference by an equivalent. Unfortunately, there was no component strictly equivalent without changing the display controller. Hardware changes to this LCD controller would have led to mandatory changes of

Product Introduction A New Generation of High End Instruments

its embedded software. The strong time constraint did not allow imagining a long and complex software development. We had to limit software development workload and the associated validation tests.

In the software architecture of this product, a process (A) is dedicated to management of the user interface and its behavior. It manages menus, organization of the user interface, keyboard inputs and interfaces with other processes. Graphic display is managed by another process (B). Its role is quite simple, it receives requests displaying high-level, like opening a window, writing a string to an X, Y coordinates, displaying a bitmap ... This displaying process addresses the LCD through its controller in order to draw on the screen each request sent by the management process (A) of the man-machine interface. The number of requests is quite low, about 20 display queries. The function of each query is easily transferable to another software environment.

Thanks to the software modular architecture, and the theoretical study performed, it became possible to redirect the graphical management of postings on another system with a standard screen.

A software feasibility was required to validate this principle. Display queries normally received by the process (B) could be sent to another process (B') installed on a PC via a serial RS232. From PC side, a program (process B') functionally equivalent to the process (B) side view OS9, receives display queries and redraws them on the PC screen (Figure 2). This software mockup also allowed verifying that the flow of information sent by RS232 had performances consistent with a display process. The reactivity of the display had to be similar to that existing on the Pentra DX120.

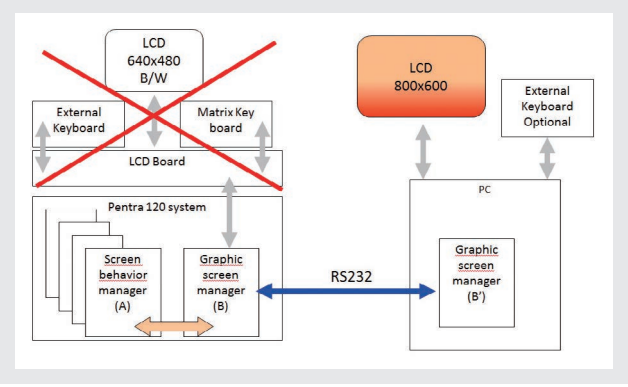

Figure 2 Software Architecture

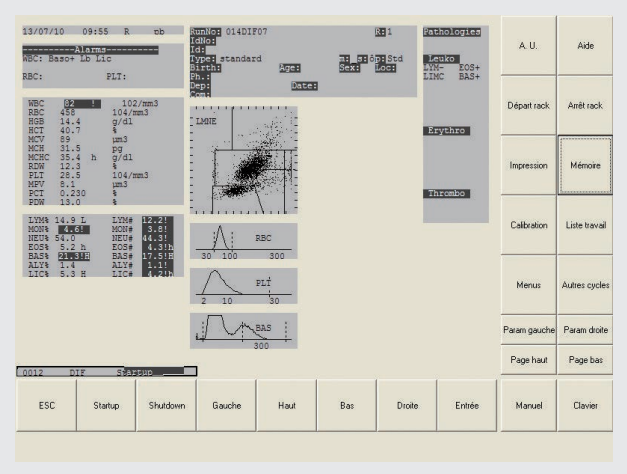

Figure 3 First Software Mockup

The first software mockup (Figure 3) confirmed that this new hardware architecture, although a little more expensive, allowed management of a new color screen. A touch screen was easy to integrate from a mechanical point of view and allowed to improve the software ergonomics. This new color "touch screen" provides an innovative solution to the Pentra DX Nexus.Choosing a PC platform allowed the use of standard electronic components, already used on other products, without having to make a new electronic design. Only the mechanics part of this subset would have to be designed so that it could be integrated into the new cover.

The Pentra DX120 software ergonomics is based on its black and white LCD screen, a front panel keyboard positioned on the instrument and a standard keyboard. Navigation in the man-machine interface is done through these two keyboards.

Replacing 640×480 pixels black and white screen and two keyboards with an 800×600 pixels bigger screen and "touch screen" allowed modern ergonomics. Unfortunately, software usability is linked to hardware interfaces such as screen and keyboard but also mainly to the functional behavior which defines that of the user interface, access to the menus and software functions.

The time constraint limited the opportunities for major changes in the functional organization of software and menus. To help us in this task, we contacted an outside company, specialist in ergonomics. After a training on how to use the Pentra DX120 product, the consultant led a user survey, and took into account technical constraints. At the end of this first study, several areas for

improvement were proposed with regard to the technical constraints: Enlarging interline menus, creating a path of menus, creating a virtual keyboard, using standardized icons.

The second step was to propose a functional mockup to represent the operating principles of the new man-machine interface. This type of mockup does not take into account graphical aspects (Figure 4). A new model was then proposed with a graphical design in conjunction with our marketing and communication departments. The reuse of icon libraries allows standardizing man-machine interfaces for our products.

Several user tests were performed with this new interface and proved to be easy to use. The latest mockup (Figure 5) was validated and used to define graphic specifications needed to develop the final software (Figure 6).

The positive test results of this new hardware and software architecture were encouraging, but we had to verify that adding a PC subset in the cover of the new product would not degrade the analytical performance of the product, and that this new design would comply with the EMC (Electro Magnetic Compatibility) standards. A Pentra DX Nexus mockup was built and showed through clinical tests that there was no disturbance due to addition of a PC measured performances met product specifications. In addition, EMC testing performed showed the precautions to be taken in the final design.

At this stage, with the studies conducted since the beginning of the project, the scope was defined, hardware and software architecture were defined and validated, key feasibilities were performed and gave a good level of reliability. It remained to organize the rest of the project so that all necessary activities to achieve it are established, and resources reserved.

Project Management

To carry out product development, it is necessary to follow up a method that ensures that all activities necessary to achieve a goal like the one proposed here, are effectively implemented and monitored at each milestone.HORIBA Medical has its own development process based on the PMI (Project Management Institute). This process is based on five distinct phases (Figure 7).

Each phase has a clear objective. Phase 0 is the study of the concept, it is to define essential requirements of the product, ask for a business strategy and assess the project's potential.

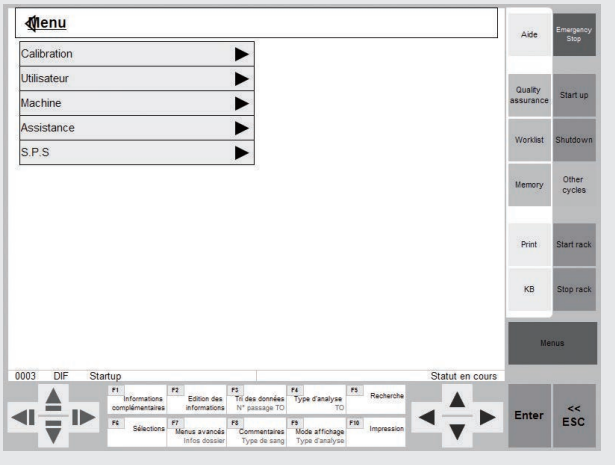

Figure 4 Functional Mockup

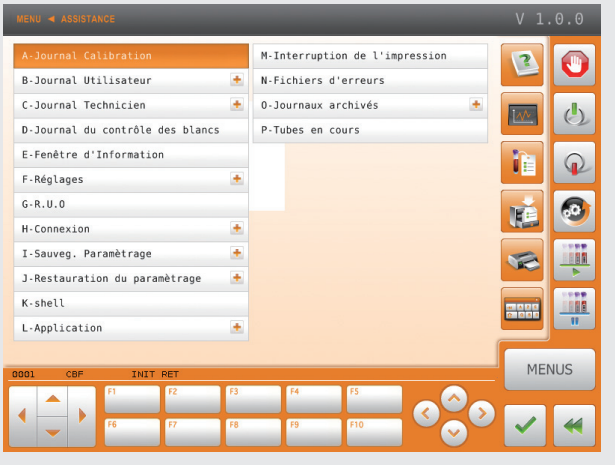

Figure 5 Graphics Mockup

Figure 6 Final Graphic User Interface

Phase 1 sets up feasibility and planning, it reduces the unknowns by technical feasibility, and verifies that the project is viable within identified constraints. It also helps define the regulatory requirements applicable to the product (21 CFR 820, CMDCAS, UL, TUV, IVD...). Finally, this phase permits to plan all activities of the various phases. In the Nexus project, given the nature of modifications and project risk level, it was decided from the beginning to provide comprehensive planning only at

Product Introduction A New Generation of High End Instruments

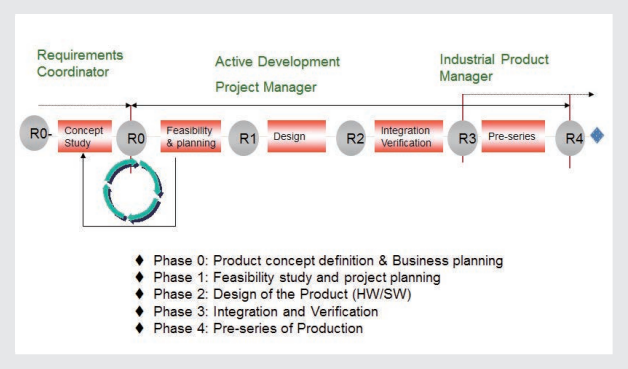

Figure 7 Development Process

the end of phase 2. This choice allowed increasing confidence level of project planning, thanks to feasibility results and to definition of the initial design elements.

Phase 2 is the design that defines all elements of the new product, 3D files, drawings, schemes of electronic charts, technology. These drawings or files will enable production of prototypes and series parts. At this stage, the expected functions are reflected in the design, taking into account constraints of the project especially expected cost of the product. This phase allows design validation through the prototype that will be realized in phase 3.

Phase 3 allows integration of one or more prototypes, which will allow verifying the prototype compliance with the specifications of the expected product. At this stage, design is completed and validated, production must be prepared through a pre-production.

Phase 4 is the last phase, it is dedicated to verify the possibility to mass produce within the cost limits, and that the product of the pre-series meets these specifications. The product requirements are validated, in particular through one or more beta sites, allowing the use of the product in customer conditions. At the end of phase 4, product liability is transferred to operations.

Each phase is sanctioned by a phase review that evaluates discrepancies that may exist and determines action plans to reduce them. Depending on the nature of differences, a phase is closed with or without limitations, and sometimes it can be extended to find a solution to a major problem. It is difficult to launch a pre-production if the design is not completed or verified. Phase closure is decided by the Steering Committee. The development process provides a list of documents needed to define the project, its specification, planning, and control activities. These deliverables are documentary or physical. Each phase defines its specific deliverables. They are expected and approved at the end of each phase at the latest. Stating here an exhaustive list of deliverables would be too long, a project like Nexus gathers approximately 350 deliverables for all five phases.

Conclusion

The Pentra DX Nexus is an example of product evolution developped from an existing product. The expected needs in the project were clear and limited. A detailed specification was established, taking into account technical constraints. The initial hardware and software architecture of the Pentra DX120 was modular enough to implement the requested changes without deeply challenging initial design of the instrument. Feasibilities were needed to confirm possible technical solutions and raise technical uncertainties.

The project management set up an organization and some follow-up activities, this allowed achieving the expected goal. This project involves several departments of the company, with different skills and organizations. Despite daily difficulties, problems to be solved, solutions to be imagined, a project is a great teamwork. At their respective levels, with their skills and work, each team member contributes to the project. About 120 people have worked on implementation of this new product. When the first Pentra DX Nexus will come out of production, everyone should be proud.

We are drafting the next evolution of the Nexus which will integrate additional functionalities, new analytical features fully compliant with extended regulations.

Pierre BACHELIER
Project Manager
HORIBA ABX SAS

HORIBA World-Wide Network

JAPAN

HORIBA, Ltd.
2, Miyanohigashi-cho, Kisshoin, Minami-ku, Kyoto 601-8510
Phone : (81)75-313-8121 Fax : (81)75-321-8312

HORIBA Advanced Techno Co., Ltd.
31, Miyanonishi-cho Kisshoin, Minamiku, Kyoto 601-8306
Phone : (81)75-321-7184 Fax : (81)75-321-7291

HORIBA STEC, Co., Ltd.
11-5, Kamitoba Hokodate-cho, Minami-ku, Kyoto 601-8116
Phone : (81)75-693-2300 Fax : (81)75-693-2350

Aso Factory
358-11 Toriko, Nishihara-mura, Aso-gun, Kumamoto, 861-2401
Phone : (81)96-279-2921 Fax : (81)96-279-3364

HORIBA TECHNO SERVICE Co., Ltd.
2, Miyanohigashicho, Kisshoin, Minamiku, Kyoto 601-8305
Phone : (81)75-325-5291 Fax : (81)75-315-9972

BRAZIL

HORIBA Instruments Brazil, Ltda
Avenida das Nacoes Unidas, 21.735 PT QD 17 - Jurubatuba - Sao Paulo -SP - CEP 04795-100
Phone : (55)11-55-45-1500 Fax : (55)11-55-45-1570

CANADA

HORIBA Canada, Inc.
Unit102, 5555 North Service Road Burlington, Ontario, L7L 5H7
Phone : (1)905-335-0234 Fax : (1)905-331-2362

U.S.A.

HORIBA Instruments Corporated
17671 Armstrong Avenue, Irvine, CA 92614
Phone : (1)949-250-4811 Fax : (1)949-250-0924

HORIBA International Incorporation
17671 Armstrong Avenue, Irvine, CA 92614
Phone : (1)949-250-4811 Fax : (1)949-250-0924

Austin Office
9701 Dessau Road, Suite 605, Austin, TX 78754
Phone : (1)512-836-9560 Fax : (1)512-836-8054

Chicago, IL Field Office
1725 Roosevelt Rd #115, West Chicago, IL 90185
Phone : (1)630-562-2298 Fax : (1)630-562-2324

Edison Office
3880 Park Avenue, Edison, NJ 08820
Phone : (1)732-494-8660 Fax : (1)732-549-5125

Houston, TX Field Office
240 Springhills Drive, Suite 410, Spring, TX 77386
Phone : (1)281-367-7422 Fax : (1)281-367-7423

Irvine South Office
34 Bunsen Drive, Irvine, CA 92618
Phone : (1)949-453-0500 Fax : (1)949-453-0600

New Hampshire Office
315 Derry Road, SUITE 13 Hudson, NH 03051
Phone : (1)603-886-4167 Fax : (1)603-886-4267

Portland Office
10110 SW. Nimbus Avenue, Suite B-11, Portland, OR 97223
Phone : (1)503-624-9767 Fax : (1)503-968-3236

Reno Office
605 Spice Island Drive, #5, Sparks, NV 89431
Phone : (1)775-358-2332 Fax : (1)775-358-0434

Santa Clara Office
3265 Scott Blvd.Santa Clara, CA 95054
Phone : (1)408-730-4772 Fax : (1)408-730-8975

AnnArbor Facility
5900 Hines Drive, Ann Arbor, MI 48108
Phone : (1)734-213-6555 Fax : (1)734-213-6525

Troy Facility
2890 John R Road, Troy, MI 48033
Phone : (1)248-689-9000 Fax : (1)248-689-8578

AUSTRIA

HORIBA (Austria) GmbH
Kaplanstrasse 5, A-3430 Tulln
Phone : (43)2272-65225 Fax : (43)2272-65230

BELGIUM

HORIBA ABX SAS
Belgium Branch
Luchthavenlei 7A, 2100 DEURNE
Phone : (32)3-281-49-08 Fax : (32)3-281-65-04

CZECH

HORIBA Czech
Prague Office
Petrohradska 13, CZ-10100 Praha 10
Phone : (420)2 7174 6480 Fax : (420)2 7174 7064

Olomouc Factory
Zeleznicni 512/7, 772 00 Olomouc
Phone : (420)585 208 763 Fax : (420)585 208 760

FRANCE

HORIBA ABX SAS
Parc Eurom decine, rue du Caduc e, BP7290, 34184 Montpellier Cedex 4
Phone : 33(0)4 67 14 15 16 Fax : 33(0)4 67 14 15 17

HORIBA France SARL
12. Av des Tropiques Hightec Sud, F-91955 Les Ulis
Phone : (33)1-69-29-96-23 Fax : (33)1-69-29-95-77

Grenoble Office
BUROCLUB 2 Av de Vignate, Gieres 38610
Phone : (33)4-76-63-49-15 Fax : (33)4-76-54-03-99

HORIBA Jobin Yvon SAS
16-18, rue du Canal, 91165 Longjumeau Cedex
Phone : (33)1-64-54-13-00 Fax : (33)1-69-09-07-21

Chilly Mazarin Office
5 avenue Arago, ZI de la Vigne aux Loups, 91380 Chilly Mazarin
Phone : (33)1-69-74-88-60 Fax : (33)1-69-74-88-61

Villeneuve d'Ascq Office
231 rue de Lille, 59650 Villeneuve d'Ascq
Phone : (33)3-20-59-18-00 Fax : (33)3-20-59-18-08

GERMANY

HORIBA Europe Automation Division GmbH
Zabergaeustr. 3, D-73765 Neuhausen
Phone : (49)7158-933-300 Fax : (49)7158-933-399

HORIBA Europe GmbH
Oberursel Office
Hans-Mess-Str.6, D-61440 Oberursel
Phone : (49)6172-1396-0 Fax : (49)6172-1373-85

Berlin Office
Fichtestr. 32, D-10967 Berlin
Phone : (49)30-61625581 Fax : (49)30-61625584

Darmstadt Office
Landwehrstrasse 55, D-64293, Darmstadt
Phone : (49)6151-5000-0 Fax : (49)6151-5000-3865

Dresden Office
Zur Wetterwarte 10, Haus 109, 01109 Dresden
Phone : (49)351-8896807 Fax : (49)351-8896808

Hanover Office
Bayernstr. 29, D-30855 Langenhagen
Phone : (49)511-7410-95 Fax : (49)511-7410-53

Korschenbroich Office
Friedrich-Ebert-Str. 9-11, D-41352 Korschenbroich

Leichlingen Office
Julius-Kronenberg-Str. 9, D-42799 Leichlingen
Phone : (49)2175-8978-0 Fax : (49)2175-897850

Munich Office
Putzbrunner Str. 89, D-81739 Munich
Phone : (49)89-634970-10 Fax : (49)89-67070-29

Potsdam Office
Dennis-Gabor-Str. 2, D-14469 Potsdam
Phone : (49)3316-4900-70 Fax : (49)3316-4900-74

Stuttgart Office (Boeblingen)
Hans-Klemm-Str. 56, D-71034 Boeblingen
Phone : (49)7031-677-9440 Fax : (49)7031-677-9450

Stuttgart Office (Neuhausen)
Zabergaeustr. 2, D-73765 Neuhausen
Phone : (49)7158-933-800 Fax : (49)7158-933-899

Wolfsburg Office
John - F. - Kennedy - Allee 64 38444 Wolfsburg
Phone : (49)5361-27648-11 Fax : (49)5361-27648-24

HORIBA Jobin Yvon GmbH
Hauptstr. 1* D-82008 Unterhaching
Phone : (49)89-46-23-17-0 Fax : (49)89-46-23-17-99

Bensheim Office
Neuhofstrasse 9, D_64625, Bensheim
Phone : (49)89-62-51-84-750 Fax : (49)89-62-51-84-7520

ITALY

HORIBA Jobin Yvon SRL
Via Cesare Pavese, 19/21 20090 Opera Millano
Phone : (39)2-57-60-30-50 Fax : (39)2-57-60-08-76

Torino Office
Europalace, Corso, Torino 43/45, 10043 Orbassano, Torino
Phone : (39)11-904-0601 Fax : (39)11-900-0448

HORIBA ABX SAS
Italy Branch
Via Le Luca Gaurico 209/211, 000143 Roma
Phone : (39)6-51-59-22-1 Fax : (39)6-51-96-43-34

NETHERLANDS

HORIBA Europe GmbH
Netherlands Branch
Science Park Eindhoven 5080 (Industrial park "Ekkersrijt") 5692 EA, Son
Phone : (31)40-2900240 Fax : (31)40-2900624

POLAND

HORIBA ABX Sp. zo. o.
Wal MIEDZESZYNSKI 598 - 03 994 Warzsawa
Phone : (48)22-673-2022 Fax : (48)22-673-2026

PORTUGAL

HORIBA ABX SAS
Portugal Branch
Alfrapark - Estrada de Alfragide n 67, Edificio F - Piso 0 Sul, 2610-008 Amadora
Phone : (35)12-14-72-17-70 Fax : (35)12-14-72-17-89

ROMANIA

HORIBA (Austria) GmbH
Romania Branch
Pitesti, B-dul Republicii Nr.38, Bloc 2 IRTA, Scara A, Etaj 3, Ap.11 Judetul Arges 110011 Pitesti
Phone : (40)348-807117 Fax : (40)348-807118

RUSSIA

HORIBA OOO
Altufievskoe shosse, 13, building 5, 127106, Moscow

HORIBA, Ltd.
Moscow Office
Build 5, h.13, Altuf'evskoe shosse, Moscow, 127106, Russia.
Phone : 7(495)221-87-67 Fax : 7(495)221-87-68

SPAIN

HORIBA ABX SAS
Spain Branch
Avenida Caidos de la Division Azul 16, 28016 Madrid
Phone : (34)91-353-30-10 Fax : (34)91-353-30-11

HORIBA Jobin Yvon
Spain Branch
PAE Neisa Norte Ed. II, Avenida Valdelaparra, 27, 28018 Alcobendas/Madrid Spain
Phone : (34)91-490-23-34 Fax : (34)91-724-13-73

SWEDEN

HORIBA Europe GmbH
Sweden Branch (Gotehnburg)
Kaerrlyckegatan 21, S-418 78 Gothenburg
Phone : (46)31-644268 Fax : (46)31-644269

Sweden Branch (Sodertalje)
Sydhamnsvagen 55-57, SE- 151 38 Sodertalje, Sodertalje
Phone : (46)8-550-80701 Fax : (46)8-550-80567

U.K.

HORIBA Instruments Limited
Kyoto Close, Summerhouse Road, Moulton Park, Northampton, NN3 6FL
Phone : (44)1604-542-500 Fax : (44)1604-542-699

HORIBA Jobin Yvon IBH Ltd.
Skypark 5, level 1, The Clydeway Centre, 45 Finnieston Street, Glasgow G3 8JU
Phone : (44)141-229-67-89 Fax : (44)141-229-67-90

HORIBA Jobin Yvon Ltd.
2 Dalston Gardens, Stanmore, Middx HA7 1BG GREAT BRITAIN
Phone : (44)208-204-8142 Fax : (44)208-204-6142

SRH Systems Ltd.
Evesham House, Whittington Hall, Whittington Road Worcester, WR5 2ZX
Phone : (44)1905-359359 Fax : (44)1905 359332

HORIBA ABX SAS
U.K. Branch
Kyoto Close Moulton Park NORTHAMPTON NN3 6FL
Phone : (44)146-281-4400 Fax : (44)146-285-1004

HORIBA World-Wide Network

CHINA

Beijing HORIBA METRON Instruments Co., Ltd.
Chaoyang District, Bei Yuan Road 40, Beijing

HORIBA INSTRUMENTS (SHANGHAI) CO., LTD
No.200, Taitao Rd, Anting Town, Jiading District, Shanghai 201814
Phone : (86)21-6952-2835 Fax : (86)21-6952-2823

HORIBA (China) Trading Co., Ltd.
Room 1701, United Plaza, 1468 Nanjing, Rd. West, Shanghai, 200040
Phone : (86)21-6289-6060 Fax : (86)21-6289-5553

Beijing Branch
Room 1801, SK Tower, Tower 1, No. 6 Jia, Jianguomenwai Ave., Chaoyang District, Beijing 100022
Phone : (86)10-8567-9966 Fax : (86)10-8567-9066

Guangzhou Branch
Room 1611/1612, Goldlion Digtal Network Center, 138Tiyu Road East, Guangzhou 510620
Phone : (86)20-3878-1883 Fax : (86)20-3878-1810

INDIA

HORIBA India Private Limited
246, OKHLA INDUSTRIAL ESTATE, PHASE 3 NEW DELHI - 110020
Phone : 91-11-4669-5001/91-11-4646-5000
Fax : 91-11-4669-5010/91-11-4646-5020

Bangalore Office
Kamadhenu, No.17/1 - 32, Bannerghatta Road, Audugodi, Bangalore - 560030
Phone : (91)80- 22210071

Pune Office
502, 5th Floor, Purushottam Plaza, Baner Road, Baner, Pune - 411045
Phone : (91)20-40766000 Fax : (91)20 40766010

INDONESIA

HORIBA Instruments (Singapore) Pte Ltd.

Jakarta Office
Jl. Jend. Gatot, Subroto, Kav 71-73, Menara Bidakara 2, Unit 11-04, Jakarta Selatan, 12870
Phone : (62)21-2906 9419/2906 9420
Fax : (62)21-2906 9421

KOREA

HORIBA Automotive Test Systems Ltd.
Room #906, World Meridian Venture Centre I, 60-24 Gasan-Dong, Geumcheon-Gu, Seoul, 153-781
Phone : (82)2-562-7706 Fax : (82)2-562-7630

HORIBA KOREA Ltd.
202-501, Pucheon Techno Park, 192, Yakdae-Dong, Wonmi-ku, Pucheon Kyunggido
Phone : (82)32-621-0100 Fax : (82)32-621-0105

Seoul Branch
112-6, Sogong-Dong, Choong-Ku, Seoul
Phone : (82)2-753-7911 Fax : (82)2-756-4972

Suwon Office
D2f Hae Sung Bldg 307-9 Yuljun-Dong Changan-Ku Suwon, Kyunggi-Do
Phone : (82)31-296-7911 Fax : (82)31-296-7913

Ulsan Office
601, Kaya Bldg, 193-5, Sinjeong 3Dong, Nam-Ku, Ulsan
Phone : (82)52-275-0122 Fax : (82)52-276-0136

HORIBA STEC KOREA, Ltd.
110, Suntech-City, 513-15, Sangdaewon, Jungwon-Ku, Sungnam-City, Kyungki-Do
Phone : (82)31-777-2277 Fax : (82)31-777-2288

SINGAPORE

HORIBA Instruments (Singapore) Pte Ltd.
10, UBI CRESCENT #05-11/12 UBI TECHPARK (408564)
Phone : (65)6-745-8300 Fax : (65)6-745-8155

TAIWAN

HORIBA Taiwan, Inc.
3F., No.18, Ln. 676, Zhonghua Rd, Zhubei City, Hsinchu County 302
Phone : (886)3-656-1160 Fax : (886)3-656-8231

Tainan Office
1F., No.117, Chenggong Rd., Shanhua Township, Tainan Country 741
Phone : (886)6-583-4592 Fax : (886)6-583-4592

THAILAND

HORIBA ABX Diagnostics (Thailand) Ltd.
393, 395, 397, 399, 401, 403 Ladyah Road, Somdejchaopraya Sub-district, Klongsan District, Bangkok 10600
Phone : (66)2-861-59-95 Fax : (66)2-861-52-00

HORIBA ABX (Thailand) Ltd.
395, Latya Road, Somdejchaopraya Sub-district, Klongsan District, Bangkok 10600
Phone : (66)2-861-59-95 Fax : (66)2-861-52-00

VIETNAM

HORIBA Instruments (Singapore) Pte Ltd.

Hanoi Office
Unit 10, 4 Floor, CMC tower, Dich Vong Hau Ward, Cau Giay district, Hanoi
Phone : (84)4-3795 8552 Fax : (84)4-3795 8553

Readout **HORIBA Technical Reports English Edition No.39**

Publication Date : September 24th, 2012
Publisher : Kozo ISHIDA
Associate Editor : Masayuki ADACHI
Publication Member : Marcus RIEKER, Olivier ACHER,
Sebastien SR. RAIMBAULT, Marianne BOURGEOIS,
Satoshi NOMURA, Hideyo SEKI
DTP, Printing : SHASHIN KAGAKU Co., Ltd.
Information : R&D Planning Center, Research & Development Division, HORIBA Ltd.
2, Miyanohigashi-cho, Kisshoin, Minami-ku, Kyoto 601-8510, Japan
Phone : (81)75-313-8121 Fax : (81)75-321-5648
E-mail : readout@horiba.co.jp
http://www.horiba.com/publications/readout/

HORIBA

Explore the future

R100
Printed on 100% recycled paper.

This article is printed using environment-friendly process qualified as SILVER status by E3PA.
E3PA : Environment Pollution Prevention Printing Association http://www.e3pa.com